A THEORETICAL AND EXPERIMENTAL STUDY OF THE TRIBOLOGY OF A CAM AND FOLLOWER

by

Guangrui Zhu M.Eng.

Submitted in accordance with the requirements
for the degree of Doctor of Philosophy

Institute of Tribology
Department of Mechanical Engineering
The University of Leeds

May, 1988

ABSTRACT

The development of more fundamental knowledge of the tribology of the cam and follower mechanism calls for a more comprehensive theoretical analysis and experimental investigation than has been previously reported. A mixed lubrication analysis has been applied to the problem to give an estimation of the nominal minimum film thickness and friction force associated with the contact in such mechanisms. The analysis showed that the roughness height and the distribution of the roughness between the two contacting surfaces had important effects on the lubrication performance of the contact. A full numerical transient EHL analysis was carried out allowing the normal velocity to vary along the conjunction. This revealed that local squeeze film velocity provided an increased damping effect which contributed to the persistence of the minimum film thicknesses in the two zero entraining velocity regions. An approximate technique for determining the minimum film thickness of a transient EHD line contact associated with rough surfaces was developed and applied to the mixed lubrication analysis of a four-power polynomial cam and non-rotating flat faced follower arrangement. The results demonstrated that under certain circumstances mixed lubrication predominated in the conjunction of the cam and follower with the surfaces being separated by an EHL film on the cam flanks.

Existing experimental apparatus was improved to test the effects of altering the bulk temperature and camshaft rotational speed by measuring the friction torque and electrical resistivity across the contact. By adopting advanced techniques for data sampling and processing the instantaneous friction torque was successfully obtained with the camshaft rotational speed exceeding (2000 rpm). The wear characteristics were also examined. The bulk temperature showed a mild effect on the wear characteristics of the cam and follower as it was increased from (75°C) to (105°C), whilst, a substantial influence was found as the temperature was further increased to (120°C). Increasing the bulk temperature caused an increase in both the friction torque and power loss of the valve train, but this increase was not considerable.

Based upon the theoretical analyses and experimental observations, a theoretical model for evaluating the tribological performance of the valve train was developed. A multi-aspect comparison between theoretical and experimental results was made. The excellent agreement between theoretical and experimental results showed that the model provided a reliable prediction of the tribological characteristics of the cam/flat faced follower. Three critical portions of the cycle could be identified – one over the cam nose and two in the vicinity of the zero entraining velocity regions. The minimum separation between the cam and follower occurred near the falling flank of the cam.

ACKNOWLEDGEMENTS

I would like to express my sincere appreciation to my supervisors, Professor D. Dowson and Dr. C.M. Taylor, whose enthusiasm and example have been a constant source of inspiration throughout the course of this work.

Thanks are also due to Mr. R.T. Harding for his advice with the improvement of the experimental apparatus and the technical help of the technicians in the Tribology Laboratory, Mr. L. Bellon, Mr. A. Bartlett and Mr. B.S. Randhawa.

I would also like to thank my fellow research students, Mr. A.D. Ball and Mr. N.P. Sheldrake, who have helped with my proof reading.

I wish to acknowledge, with gratitude, Xian Jiaotong University for funding part of the research assistantship and the Committee of Vice-Chancellors and Principals of the United Kingdom for providing an ORS award. The financial and technical support of the Ford Motor Company Ltd. is also gratefully acknowledged.

Finally, I would like to express my deep appreciation to my wife, Benyu Jiang, who has provided continual support and encouragement in the completion of this task.

CONTENTS

NOMENCLATURE

a	follower acceleration
A	apparent area of contact
A_r	real area of contact
b	half Herztian contact width
B	dimensionless half Herztian contact width
e	eccentricity or offset value of two contacting cylinders
E	Young's modulus
$E<>$	expectancy operator
E'	equivalent elastic constant $[E'=2/\{(1-\nu_1^2)/E_1+(1-\nu_2^2)/E_2\}]$
F_a	friction force due to asperity interaction
$F_2, F_{5/2}$	integrals for Gaussian height distribution
g	gravitational acceleration
G	dimensionless materials parameter, $[\alpha E']$
h	nominal film thickness
h_c	central oil film thickness
h_o	film thickness on line of centres
h_t	local film thickness
H	dimensionless film thickness, $[h/R]$ or $[h/\sigma]$
H_c	dimensionless central film thickness, $[h_c/R]$
H_o	dimensionless film thickness on line of centres
H_v	Vickers hardness number
K	spring stiffness
L	cam lift
M	reciprocating mass
M_e	equivalent reciprocating mass
m	valve spring mass
n	camshaft rotational speed
p	mean hydrodynamic pressure
p, q, r, s	powers associate with cam law
p_a	mean asperity pressure per unit width
P_x	hydrodynamic force per unit width in x direction
P_z	load on cam
q	reduced pressure
Q	dimensionless reduced pressure, $[q/E']$
r	ratio of normal velocity to entraining velocity

R	effective radius of cylinder
R_c	radius of curvature of nominal contact point on cam
R_b	cam base circle radius
t	time
u	surface velocity or mean entraining velocity $[(u_1+u_2)/2]$
U	dimensionless speed parameter, $[\eta_o u/(RE')]$
v	normal velocity or elastic deformation
V	dimensionless normal velocity, $[\eta_o v/(RE')]$
V_r	variance ratio
w	total load acting on unit width of cam
W	dimesionless load parameter, $[w/(RE')]$
W_a	asperity load per unit width
W_h	hydrodynamic load per unit width
x, y, z	coordinate axes
α	rate of change of shear stress with pressure or pressure viscosity coefficient
β	asperity radius of curvature or pressure viscosity coefficient
δ	roughness amplitude
η	dynamic viscosity or asperity density
η_o	reference viscosity (at inlet)
$\bar{\eta}$	dimensionless viscosity, $[\eta/\eta_o]$
λ	film thickness ratio $[h/\sigma]$ or film parameter $[h_{min}/\sigma]$
θ	cam angle
ν	Poisson's ratio
σ	composite roughness height
τ	shear stress acting on solid
τ_a	shear due to asperity interaction
τ_o	shear stress constant
τ_s	boundary film shear stress
$\phi_x, \phi_s, \phi_f, \phi_{fs}, \phi_{fp}$	factors in average flow model
Ω	camshaft rotational frequency

Subscripts

1	cam body
2	follower body
a	asperity
x, y, z	coordinate system

CHAPTER 1

INTRODUCTION

1.1 CHALLENGES TO BE FACED

1.2 SUMMARY OF PRESENT WORK

1.1 Challenges to Be Faced

Since the oil crisis in the 1970's an increasing effort has been devoted to the improvement of the efficiency of the internal combustion engine. Although the major losses are due to the thermal inefficiency, there are still large benefits to be gained from reducing the mechanical losses which broadly speaking may approach (15%) of the fuel energy. Most of the mechanical losses can be attributed to the friction associated with the piston ring assemblies, the bearings and the valve train system. Reducing the mechanical power loss in the internal combustion engine requires a more fundamental knowledge of the operation of these mechanisms. Developments in the understanding of the tribological characteristics of dynamically loaded engine bearings and piston rings are more advanced than studies on the valve train, particularly on the cam and follower.

Over the years the understanding of valve train dynamics has increased and cam profiles have been refined to give a smoother operation, less vibration and lower noise. Unfortunately some of these improved profiles are inherently difficult to lubricate adequately. In recent years more and more car engine manufacturers have been running into problems of severe wear of cams and followers, and no doubt many operators will have encountered excessive wear. The cam and follower contact is the most severely tested tribological component in the internal combustion engine, operating, it is believed, with a degree of surface interaction for virtually the whole of its cycle. An important feature in the consideration of ways to reduce wear and failure is the recognition that the mechanism of lubrication involved in the conjunction of the cam and follower includes both surface contact and elastohydrodynamic influences. To understand the lubrication phenomenon existing in the cam and follower conjunction a theoretical model, known as the mixed lubrication model, which includes the influences of surface elastic deformation, asperity interactions and squeeze film action, should be developed. Moreover, reliable theoretical models which are much less costly to implement and study than experimental programmes can provide us with useful information for predicting the tribological performance of the cam and follower as well as the valve train. The difficulty here is the substantial computing time required to obtain a convergent solution to a transient elastohydrodynamic lubricated line contact problem; sometimes this is not even possible. Therefore, the

development of a technique which enables a quick and reliable estimation to be made of the minimum oil film thickness in a transient elastohydrodynamic line contact has been required for many years. This technique will be applicable to the lubrication analysis of a number of machine elements, such as gears, rolling bearings and cams and followers which involve heavily loaded counterformal contacts. However, up to now, such a reliable technique has not previously been available.

In recent years operating conditions for engines have also changed. In the search for efficiency, oil temperatures have risen, and because of the widespread adoption of electic fans which only operate intermittently, the average temperatures, particularly in the top of the engine, have risen considerably. Thus we have to face a new challenge arising from the increase in the bulk temperature surrounding the cam and follower. This relates to the influence of thermal effects on the tribological performance of the cam and follower. In addition, the camshaft rotational speed has some important influence on the performance of the valve train, including aspects associated with the dynamic characteristics. Although both thermal and dynamic effects can be studied by developing theoretical models, it is believed that an experimental programme for investigating the tribological performance at different bulk temperatures and different camshaft rotational speeds is still of great value. A comprehensive comparison between theoretical predictions and experimental data will put the theoretical model on a firm foundation and consequently the model can be used for design purposes with great confidence.

1.2 Summary of Present Work

As part of the continuing effort to understand the tribological performance of the cam and follower, the present study consisted of three main parts; these are theoretical analyses, experimental investigations and experimental and theoretical comparisons, which are presented separately in this thesis.

In the first part of this work, as an initial consideration of surface roughness effects, a mixed lubrication analysis of the cam and follower was undertaken with the assumption that the bounding solids were rigid. Then, a complete numerical analysis of the cyclic variation of the minimum film thickness in the whole cam cycle was carried out to estimate the influence

of squeeze film action. This analysis was based upon a numerical solution to the transient elastohydrodynamic line contact problem by allowing the normal velocity to vary along the conjunction. Finally, an approximate technique for estimating the minimum film thickness of a transient elastohydrodynamic line contact associated with rough surfaces was developed and applied to the mixed lubrication analysis of a four-power polynomial cam and non-rotating flat faced follower arrangement.

In the second part of this research existing experimental apparatus was improved and equipped with thermostatic control facilities to investigate the influence of different bulk temperatures and camshaft rotational speeds on the tribological performance of the cam and follower. Several important variables including the friction torque, power loss, electical resistivity across the contact of the cam and follower and temperatures at the cam nose and in the valve stem guide were measured. At the same time surface characteristics were also examined by measuring the surface roughness values, surface profile and material hardness of the cam and follower both prior to and subsequent to each test.

In the third part of the study, based upon the experimental observations, a theoretical model was developed to estimate the tribological performance of the valve train which includes the cam/follower interface, follower/guide interface and camshaft support bearings. Then a widespread comparison was made between the theoretical and experimental results to examine the reliability of the theoretical model.

It is believed that the present work including both theoretical analyses and experimental investigations has improved the understanding of the tribological performance of the cam and follower and provided a reliable theoretical model for design purposes.

PART I

A THEORETICAL STUDY OF THE TRIBOLOGY OF A CAM AND FOLLOWER

CHAPTER 2

BACKGROUND TO THE THEORETICAL ANALYSIS

2.1 INTRODUCTION

2.2 A SURVEY OF CAM AND FOLLOWER LUBRICATION ANALYSIS

2.3 CAM AND FOLLOWER KINEMATICS AND CONTACT LOADING

2.4 REYNOLDS' EQUATION

2.5 ELASTICITY EQUATION

2.6 PRESSURE-VISCOSITY RELATIONSHIP

2.7 REDUCED PRESSURE (q)

2.8 AVERAGE REYNOLDS' EQUATION OF ROUGH SURFACES

2.9 ASPERITY INTERACTIONS

2.1 Introduction

The limit to the availability and high price of organic fuels has spurred manufacturers to improve the efficiency of the internal combustion engine. The need for reducing the power loss arising from the valve train has meant a requirement for a more fundamental understanding of the lubrication mechanism between the cam and follower. To understand the lubrication phenomenon existing in the cam and follower conjunction a theoretical model, known as the mixed lubrication model, which includes the influences of surface elastic deformation, asperity interactions and squeeze film action, should be developed.

A literature survey of the theoretical analysis on cam and follower lubrication is given at the beginning of this chapter, and then the theoretical background on which the mixed lubrication model is based is introduced in detail. The equations and empirical relationships described in this chapter are expressed in their common forms although they might be slightly different from those adopted in the next three chapters which deal with theoretical studies of the tribology of a cam and follower. The analysis of the kinematics and contact loading of the cam and follower is also described in this chapter.

2.2 A Survey of Cam and Follower Lubrication Analysis

Early theoretical studies considering the cam mechanism resulted from excessive noise at a time when engine speeds and load were being increased. Bishop (1950-51) realised that theoretical instantaneous changes of the acceleration were responsible for the noise. He developed an improved cam with a profile defined by a number of sine wave functions, which negated the discontinuities of the acceleration and led to improved engine efficiency and quieter action. A similar conclusion was reached by Dudley (1948).

Although new cam forms did prevent high noise levels and resulted in more efficient engine breathing, the increased cam loads caused failure of the cam and followers. The types of failure which were found to be common in cam and follower pairs were pitting, scuffing and polishing wear. Due to the apparent effects of load on failure an early design criterion for the cam mechanism was that the Herzian stress at the cam nose should be less than the critical stress for the materials employed. Even then, failures of cam and

follower pairs happened from time to time. This promoted more research into the effects of metallurgy, lubricants and driving conditions on the performance of the cam mechanism. A vast amount of experimental study was carried out over the years between 1950 and 1970. A detailed survey on the previous experimental studies is given in Chapter (6).

The first attempt to understand the mechanism of the scuffing failure was made by Dyson and Naylor (1960-61) who introduced the flash temperature concept into the cam and follower analysis. The results showed that the maximum temperatures (that is to say the instantaneous rise in temperature occurring when two asperities collide), took place at the nose of the cam and the points of zero acceleration where the predicted film thickness might be expected to be small. Dyson and Naylor concluded that polishing might be expected on a surface where there was a high velocity relative to the point of contact and scuffing where a low velocity relative to the point of contact occurred. Due to the lack of sophisticated technology to estimate the friction coefficient and asperity load, two very important parameters, this model could be improved by giving consideration to the surface elastic deformation and asperity interactions.

Another attempt to apply analytical method to cam design was undertaken by Muller (1966) who compared two cams of the three-arc type, one having a large nose radius and the other a small one. The film thickness was predicted for each cam. The cam with the smaller nose radius showed a considerably larger film thickness, despite a greater Herzian stress, than the cam with the larger nose radius. These findings were supported by an experimental investigation which showed that the cam with the large nose radius and small predicted film thickness suffered severe scuffing and eventually pitted, whilst the cam with the small nose radius and large predicted film thickness operated satisfactorily. Since then, there has been an increasing realization that the lubrication also has important effects on the cam and follower performance.

The importance of the squeeze film action for the operation of the cam mechanism was first reported by Vichard and Godet (1967–68), and later Vichard (1971) showed, theoretically, that the squeeze film action contributed to the persistence of the oil film. In two papers, Holland (1978) developed an elastohydrodynamic theory to include the squeeze film action. As a result of some unreasonable mathematical assumptions upon which the

model was based, the squeeze film action predicted by Holland was proved to be exaggerated by Bedewi et al (1985) who performed a transient elastohydrodynamic lubrication analysis on a modified cam in the nose and flank regions, although some of the conclusions arrived at by Bedewi et al seem to be quite doubtful. A detailed discussion is to be given later.

Since the oil crisis in the 1970s, manufacturers have realised the importance of an efficient engine. Thus, more and more effort has been made to reduce the energy consumption of the valve train. In order that the efficiency of the valve train can be increased the model of friction must be understood. Staron and Willermet (1983) developed a simple model of friction in a valve mechanism which included the effects of the cam and follower interface, the support bearings and the rocker arm. A very low value of the film thickness ratio ($\lambda<1$) was taken as a full elastohydrodynamic film and a value of ($\lambda\approx 0$) was taken as evidence of boundary lubrication. The film thickness was calculated in steps of (5°) throughout the cycle thus missing the most important areas where the entraining velocity and hence film thickness approaches zero. Using the above hypothesis it was suggested that the cam operated in a mixed lubrication regime and a simple model was developed on the assumption that part of the load was carried by the asperities. Although the results showed good agreement with those found in experiments, the assumptions upon which the model is based should be theoretically verified with a more realistic model to include squeeze film action, elastic deformation and asperity interactions.

It has often been suggested (e.g. Barwell and Roylance, (1978)) that the film thickness ratio is an important factor in the design of mechanisms if surface failure is to be avoided. A mixed lubrication model developed by Patir and Cheng (1978) made it possible to predict the cyclic variation of the film thickness ratio in the cam and follower interface. Unfortunately this analysis has received little attention.

Based upon existing technology, computer software for cam design with graphic output was established by Dowson et al (1985). At the same time, a parametric study of the behaviour of a four power polynomial cam was completed to assess the influence of the important variables. This gives cam designers great convenience in predicting the cam performance when they modify parameters. The cyclic variation of the minimum oil film thickness was predicted for the rigid cam and follower pair with the consideration of

the squeeze effect, which showed that the film thickness did not decrease to zero due to the squeeze film action as the entraining velocity was decreasing to zero. The minimum separation between the cam and follower occurred at the point of zero entraining velocity as the cam was leaving the follower. However, the results given by Bedewi et al (1985) from the transient elastohydrodynamic lubrication analysis showed that the minimum separation between the cam and the follower took place at the point of zero entraining velocity as the cam was approaching the follower. These contradictory findings require further analysis.

2.3 Cam and Follower Kinematics and Contact Loading

2.3.1 Cam and Follower Kinematics

Consider the situation shown in Figure (2.1) with the contact point on the rising flank of the cam. The cam is designated component number one and the follower, which is taken not to rotate, number two. The cam rotates about (O) whilst (O') is the centre of curvature of the cam surface at the instantaneous contact point (C). The absolute velocities of the follower in the (x, z) coordinate directions are determined simply as,

$$u_2 = 0 \tag{2.1}$$

and

$$v_2 = \frac{dL}{dt} = e\,\Omega \tag{2.2}$$

The acceleration (a) of the follower may be calculated as

$$a = \frac{d^2L}{dt^2} = \Omega\frac{de}{dt} \tag{2.3}$$

The x-velocity of the point on the cam in contact with the follower is,

$$u_1 = (R_b + L)\,\Omega \tag{2.4}$$

The velocity of the contact point along the cam surface (ds/dt) may be calculated as follows with due regard to sign,

$$\frac{ds}{dt} = u_1 + \frac{de}{dt} = (R_b + L)\,\Omega + \frac{de}{dt} \tag{2.5}$$

The instantaneous radius of curvature of a point moving along a cam with velocity (ds/dt) such that the angular velocity of the tangent to the contact point is (γ) is given by,

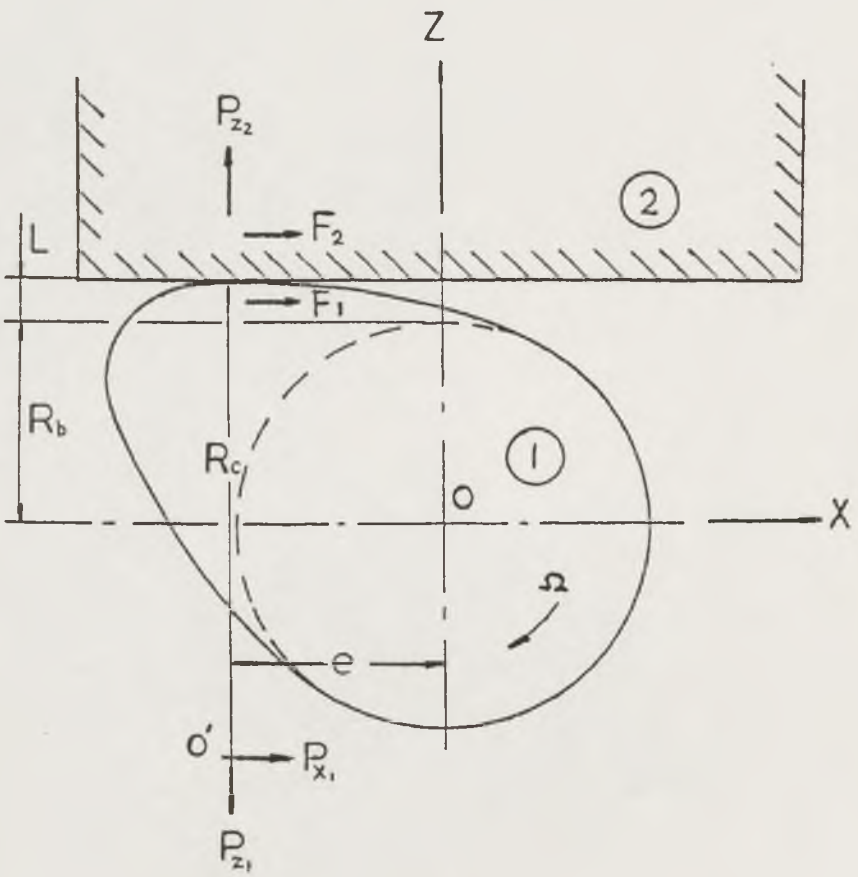

Figure (2.1) General View of cam and follower contact

$$R_c = \frac{ds}{dt}\frac{dt}{d\gamma} = \frac{ds}{d\gamma}$$

For the flat follower

$$R_c = \frac{1}{\Omega}\frac{ds}{dt} \qquad (2.6)$$

Combining equations (2.3), (2.5) and (2.6) we find

$$R_c = R_b + L + \frac{1}{\Omega}\frac{de}{dt} = R_b + L + \frac{a}{\Omega^2} \qquad (2.7)$$

2.3.2 Contact Loading

The precise determination of the load to be carried by a cam and follower contact during a cycle is a complex matter. In general the forces associated with the operation of the mechanism are the inertia force, the spring load arising as a result of relative motion between the contacting parts and the forces resulting from the stiffness and damping characteristics of the overall structure. For the purpose of the present study the valve train arrangement to be modelled was that of the experimental apparatus to be described in Chapter (6). Frictional forces were neglected in the determination of contact loading and by taking the mechanism to be rigid, the stiffness and damping characteristics were also omitted.

The inertia force is a product of the mass and the acceleration of the moving parts. Its direction opposes that of the acceleration. The inertia force of the spring is equivalent to adding one third of the mass of the spring concentrated at the end of the valve. Hence the total mass of the system (M_e) is given by the expression,

$$M_e = M + \frac{m}{3} \qquad (2.8)$$

and the inertia force by

$$I = a M_e \qquad (2.9)$$

A purely static evaluation of the spring force gives

$S = K d$ at no lift

and $S = K (L + d)$ when the lift is equal to (L)

where (d) is the initial compression of the spring. The function of the initial compression of the spring is to generate a force which is large enough to

prevent the valve being forced open by the pressure differential between the combustion chamber and the valve port when there is no contact between the cam and the follower. Therefore the total load on the cam is,

$$W = I + S + g M_e \tag{2.10}$$

2.4 Reynolds' Equation

As with many lubricated machine contacts in engineering the cam mechanism can be represented as a cylinder acting on a plane, as shown in Figure (2.2a), where the parameters of the contact vary with time. The cylinder was assumed to be infinitely wide, thus neglecting any side leakage effect. If the lubricant density with respect to temperature and pressure is considered constant through the thin film, the one dimensional Reynolds equation for an incompressible fluid is,

$$\frac{d}{dx}\left[\frac{h^3}{12\eta}\frac{dp}{dx}\right] = u\frac{dh}{dx} + v_1 - v_2 + u_2\frac{dz_2}{dx} - u_1\frac{dz_1}{dx} \tag{2.11}$$

where $u = (u_1 + u_2)/2$. Considering the situation shown in Figure (2.2a) we have

$$v_1 = u_1\frac{dh}{dx} + \frac{\partial h}{\partial t} \qquad v_2 = 0$$

$$\frac{dz_1}{dx} = \frac{dh}{dx} \qquad \frac{dz_2}{dx} = 0$$

Therefore equation (2.11) becomes,

$$\frac{d}{dx}\left[\frac{h^3}{12\eta}\frac{dp}{dx}\right] = u\frac{dh}{dx} + \frac{\partial h}{\partial t} \tag{2.12}$$

Reynolds boundary condition is adopted in the present analysis for determining the film rupture and the boundary conditions on pressure are,

$$p(-\infty) = 0 \quad \text{and} \quad \frac{dp}{dx}(x_m) = p(x_m) = 0$$

The assumption of a parabolic profile is valid when the magnitude of (x/R_c) is small compared to unity. From Figure (2.2a) we find

$$h = h_0 + R_c - R_c\left[1 - \left(\frac{x}{R_c}\right)^2\right]^{1/2}$$

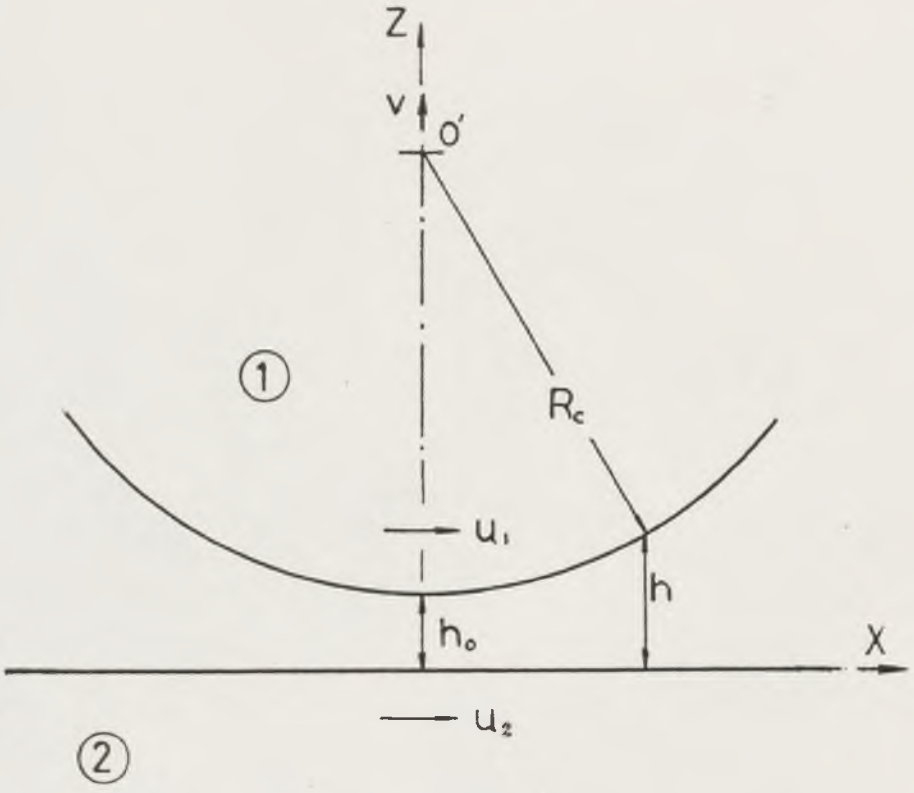

Figure (2.2a) Cam and follower represented by a cylinder and a plane

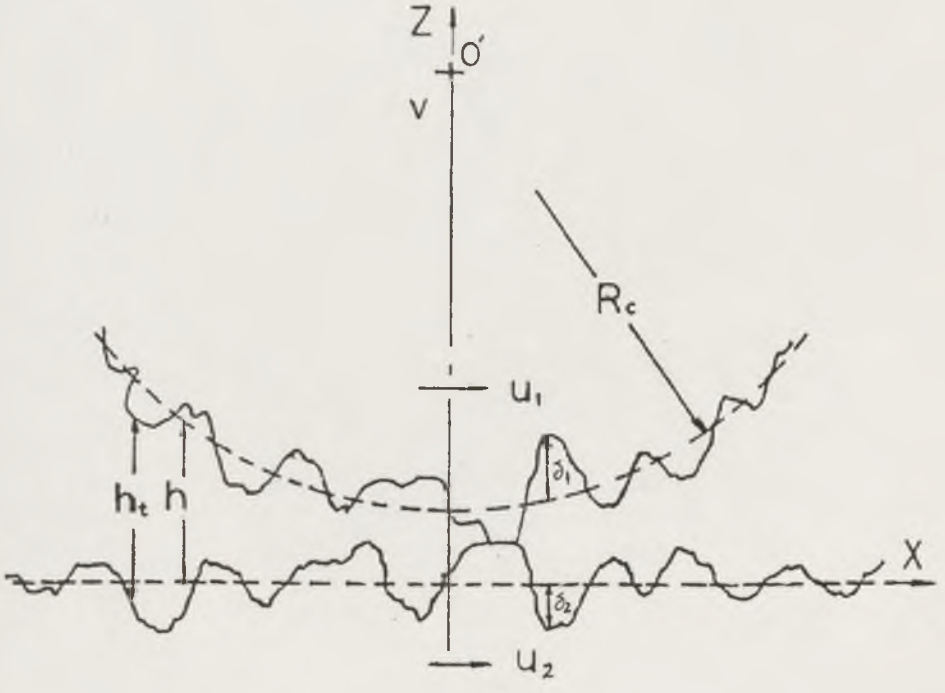

Figure (2.2b) Geometry of the surfaces in the vicinity of the contact point of cam and follower

Expanding the term in the brackets and neglecting the fourth and higher powers gives

$$h = h_o + \frac{x^2}{2R_c} \tag{2.13}$$

2.5 Elasticity Equation

In practice, cam and follower surfaces subjected to heavy loads are deformed elastically. In typical conditions for a nominal line contact, the contact region is very small compared with the radius and length of the cylinder. Hence the displacement is a state of plane strain uniform along the length, except near the ends. Furthermore tangential displacements can be neglected because they do not have significant effects on the lubricated contact. The normal displacement caused by the pressure generated in the fluid film is calculated for a semi-infinite plane and then added to the rigid geometrical separation of the equivalent cylinder.

Considering Figure (2.2a) and the corresponding coordinate system, the elastic deformation at a point at a distance (x) from the origin on the surface of a semi-infinite solid subjected to a strip of non-uniform pressure (p(s)) between ($s = -s_1$) and ($s = s_1$) can be written as (see Dowson and Higginson (1966)),

$$v(x) = -\frac{2}{\pi E'} \int_{-s_1}^{s_1} p(s) \ln(x - s)^2 \, ds + C \tag{2.14}$$

where (E') is the equivalent elastic constant related to both cam and follower surfaces. The constant (C) can be eliminated by including it in the central film thickness (h_c). Thus the displacement is not an absolute, but a relative quantity.

2.6 Pressure–Viscosity Relationship

In many engineering situations extremely high pressures may occur, especially in heavily loaded lubricated contacts. The very high pressures dramatically affect the viscosity of the fluid. A widely used relationship, proposed by Barus, for the effect of pressure on the viscosity in the isothermal case, particularly for lubricating oils, is

$$\eta = \eta_o \exp(\alpha p) \tag{2.15}$$

where (α) is known as the pressure-viscosity coefficient and depends on temperature only, and (η_o) is a reference viscosity at atmospheric pressure for the specific lubricant. Equation (2.15) is valid only for a moderate pressure region.

To overcome the difficulty encountered at high pressures, a composite pressure-viscosity relationship introduced by Allen et al (1970) was adopted in the present analyses. This relationship is valid not only for moderate pressure but also for very high pressures and can be expressed as,

$$\eta = \begin{cases} \eta_o \exp(\alpha p) & \text{for} \quad p \le p_1 \\ \eta_o \exp[\alpha p_1 + \beta(p-p_1)] & \text{for} \quad p > p_1 \end{cases} \tag{2.16}$$

where (β) is a pressure-viscosity coefficient of the lubricant when the pressure is greater than the critical pressure (p_1).

2.7 Reduced Pressure (q)

Introducing the pressure-viscosity relationship (2.16) into Reynolds equation (2.12) results in a non-linear equation which cannot be solved by simple integration. Therefore, an alternative parameter (q) was adopted, namely the reduced pressure, which is mathematically expressed as,

$$q = \begin{cases} \dfrac{1}{\alpha}[\,1 - \exp(-\alpha p)\,] & \text{for } p \le p_1 \\ \dfrac{1}{\beta}[1 - \exp(-\{\alpha p_1 + \beta(p-p_1)\})] + \dfrac{\beta-\alpha}{\alpha\beta}[1 - \exp(-\alpha p_1)] & \text{for } p > p_1 \end{cases}$$

Replacing (p) in Reynolds equation (2.12) by (q), a reduced Reynolds equation was obtained,

$$\frac{d}{dx}\left(h^3 \frac{dq}{dx} \right) = 12\eta_o \left(u \frac{dh}{dx} + \frac{\partial h}{\partial t} \right) \tag{2.17}$$

which represents Reynolds equation for an isoviscous lubricant of viscosity (η_o). The reduced pressure (q), the solution of equation (2.17), can be converted into a piezoviscous solution by substituting (q) into the followering equations,

$$p = \begin{cases} -\frac{1}{\alpha} \ln[\,1 - \alpha q\,] & \text{for} \quad q \le q_1 \\ p_1 - \frac{1}{\beta} \ln[1 - \beta(q - q_1)\exp(\alpha p_1)] & \text{for} \quad q > q_1 \end{cases} \tag{2.18}$$

where $q_1 = \frac{1}{\alpha}[1 - \exp(-\alpha p_1)]$.

2.8 Average Reynolds' Equation of Rough Surfaces

In more realistic conditions, the contact situation between the cam and follower can be represented by the contact of an infinitely wide rough cylinder with a rough plane as shown in Figure (2.2b). Thus a one dimensional form of the average Reynolds equation developed by Patir and Cheng (1978) was adopted to evaluate average hydrodynamic behaviour with the Reynolds boundary condition for determining the film rupture. This equation is applicable to any general roughness structure and takes the form

$$\frac{d}{dx}\left(\phi_x \frac{h^3}{12\eta} \frac{d\bar{p}}{dx}\right) = \frac{(u_1+u_2)}{2} \frac{d\bar{h}_t}{dx} + \frac{(u_2-u_1)}{2} \sigma \frac{d\phi_s}{dx} + \frac{\partial \bar{h}_t}{\partial t} \tag{2.19}$$

The boundary conditions on pressure are

$$\frac{d\bar{p}}{dx}(x_m) = \bar{p}(x_m) = 0, \qquad \bar{p}(-\infty) = 0.$$

and $h_t = h + \delta_1 + \delta_2$.

The empirical pressure and shear flow factors, (ϕ_x) and (ϕ_s), enable the average lubricant flow to be related to average quantities, such as mean pressure and nominal film thickness. The pressure and shear flow factors were obtained by numerical flow simulation.

The approach adopted by Patir and Cheng assumed the bearing was approximated by a number of small rectangular bearings of an area which was small relative to the dimensions of the bearing but large enough to include a large number of asperities. The nominal film thickness was assumed to be constant within each small bearing as shown in Figure (2.3). For each rectangular bearing with a given roughness structure, the flow

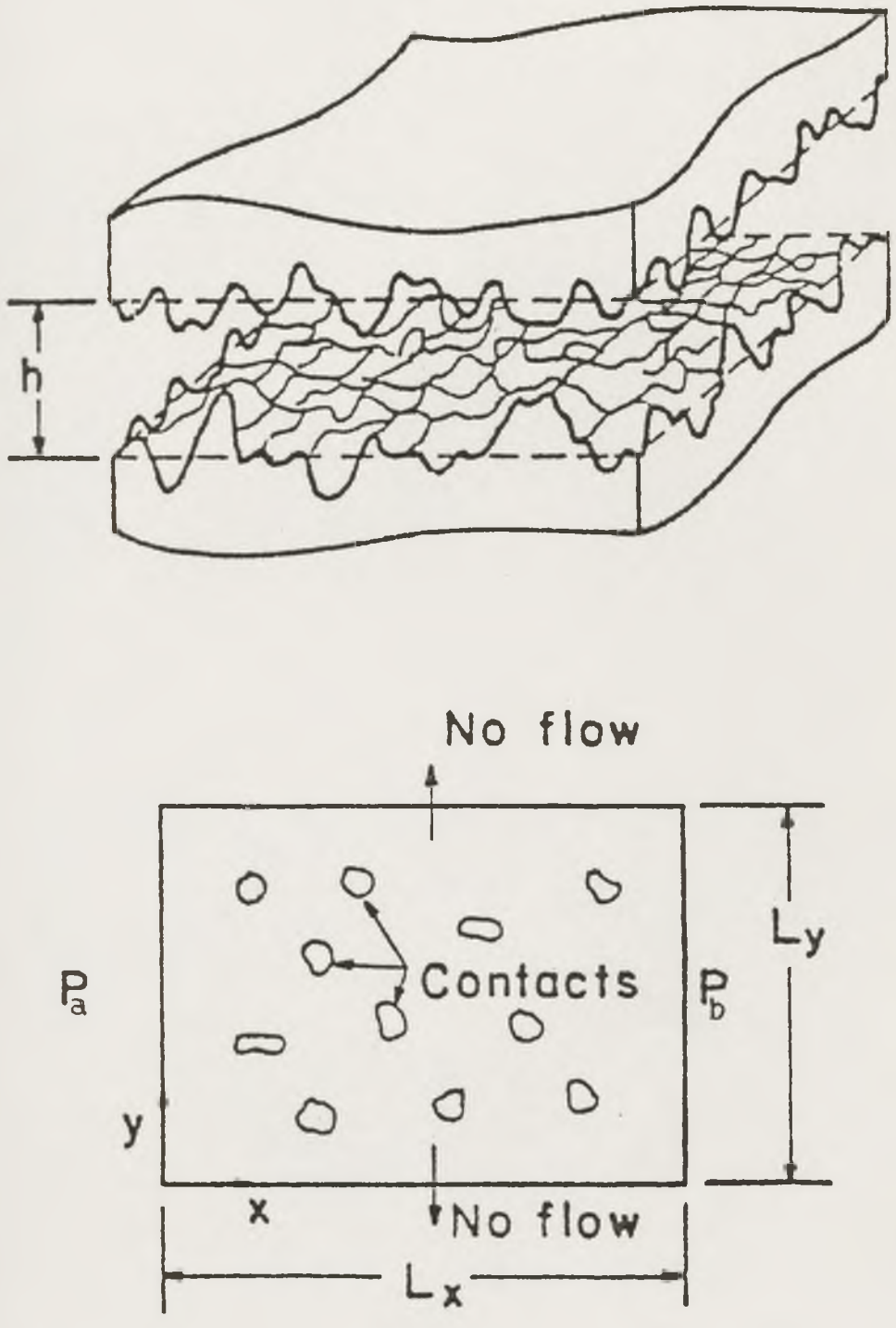

Figure (2.3) Small rectangular bearing for simulating

factor (ϕ_x) could be calculated by applying an arbitrary pressure gradient ($\partial p/\partial x$) on the model bearing boundaries. The pressure flow of the model bearing now was expressed as,

$$\frac{\partial}{\partial x}\left(\frac{h_t^3}{12\eta}\frac{\partial p}{\partial x}\right) + \frac{\partial}{\partial y}\left(\frac{h_t^3}{12\eta}\frac{\partial p}{\partial y}\right) = 0 \qquad (2.20)$$

with boundary conditions

$$p(0,\ y) = P_a, \quad p(L_x,\ y) = P_b$$

$$\frac{\partial p}{\partial y}(x,\ 0) = \frac{\partial p}{\partial y}(x,\ L_y) = 0$$

and no flow at contact points.
Solving the pressure flow from equation (2.20) with a numerical method, then comparing this flow to that of a similar smooth bearing by the following equation

$$\phi_x = \left(\frac{1}{L_y}\int_0^{L_y}\left(\frac{h_t^3}{12\eta}\frac{\partial p}{\partial x}\right)dy\right) \div \left(\frac{h^3}{12\eta}\frac{\partial \bar{p}}{\partial x}\right)$$

where $$\frac{\partial \bar{p}}{\partial x} = \frac{P_b - P_a}{L_x}$$

and finally considering such bearings with different nominal gaps, (ϕ_x) could be obtained as a function of the nominal gap.

Surface orientation (γ) used to study the surface roughness with directional properties can be considered as the length-to-width ratio of a representative asperity. Figure (2.4a) shows the typical contact areas for longitudinally oriented ($\gamma > 1$), isotropic ($\gamma = 1$) and transversely oriented ($\gamma < 1$) surfaces.

The shear flow factor (ϕ_s) was also obtained by numerical flow simulation on a model bearing similar to that used for (ϕ_x) but without any mean pressure gradient on the modelled bearing boundaries. The rolling speed was taken as zero. The model problem for (ϕ_s) then becomes pure sliding of two nominally parallel surfaces.

$$\frac{\partial}{\partial x}\left(\frac{h_t^3}{12\eta}\frac{\partial p}{\partial x}\right) + \frac{\partial}{\partial y}\left(\frac{h_t^3}{12\eta}\frac{\partial p}{\partial y}\right) = \frac{\partial h_t}{\partial t}$$

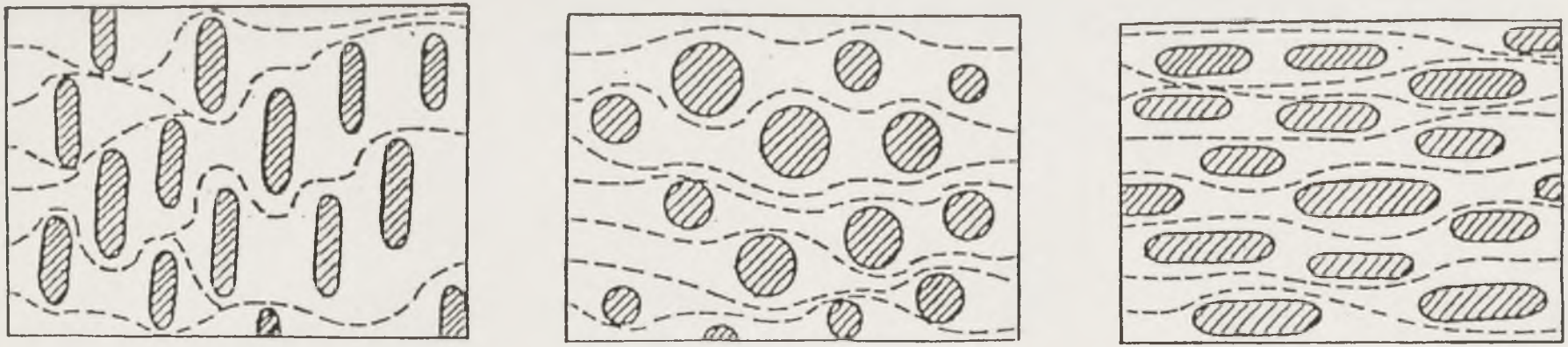

Transverse roughness $\gamma < 1$ | Isotropic roughness $\gamma = 1$ | Longitudinal roughness $\gamma > 1$

Figure (2.4a) Typical contact area for oriented roughness

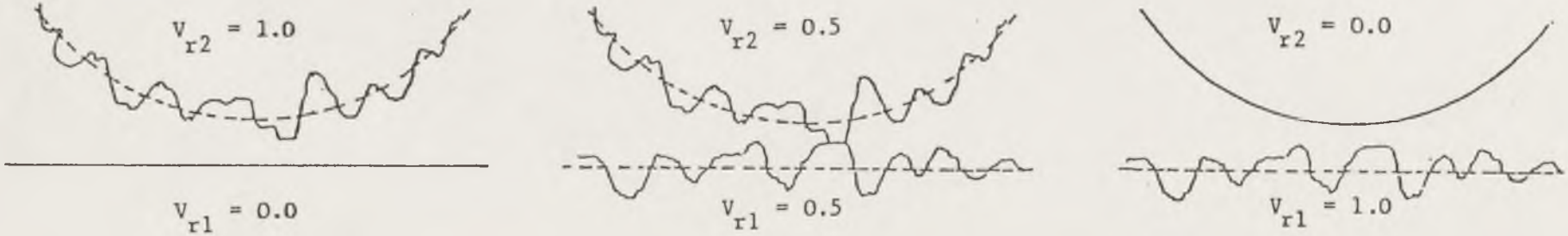

Figure (2.4b) Typical surface roughness variance ratio

with boundary conditions

$$p(0, y) = p(L_x, y) = 0$$

$$\frac{\partial p}{\partial y}(x, 0) = \frac{\partial p}{\partial y}(x, L_y) = 0$$

and no flow at contact points.

The combined effects of roughness and sliding results in a net flow which can be calculated by

$$Q_x = E\left\langle -\frac{h_t^3}{12\eta}\frac{\partial p}{\partial x}\right\rangle = \frac{1}{L_x L_y}\int_0^{L_y}\int_0^{L_x}\left(-\frac{h_t^3}{12\eta}\frac{\partial p}{\partial x}\right) dxdy$$

Since the mean pressure gradient was zero, and there was no rolling velocity and the net mean flow (Q_x) was equal to the calculated flow transport due to sliding. Thus,

$$\phi_s = \frac{2}{\sigma U_s} E\left\langle -\frac{h_t^3}{12\eta}\frac{\partial p}{\partial x}\right\rangle$$

where $$U_s = \frac{u_2 - u_1}{2}$$

The empirical formulae fitting to the factors of (ϕ_x) and (ϕ_s) were given by Patir and Cheng (1978 and 1979) as a function of the nominal gap listed below,

$$\phi_s = \begin{cases} 1 - C\exp(-aH) & \text{for } \gamma \le 1 \\ 1 + C H^{-a} & \text{for } \gamma > 1 \end{cases} \qquad (2.21)$$

and

$$\phi_s = V_{r1}\Phi_s(H,\gamma_1) - V_{r2}\Phi_s(H,\gamma_2) \qquad (2.22)$$

where

$$\Phi_s = \begin{cases} A_1 H^{a1}\exp(a_2 H + a_3 H^2) & \text{for } H \le 5 \\ A_2\exp(-0.25 H) & \text{for } H > 5 \end{cases} \qquad (2.23)$$

(V_{r1}) and (V_{r2}) are variance ratios and defined as,

$$V_{r1} = \left(\frac{\sigma_1}{\sigma}\right)^2 \quad \text{and} \quad V_{r2} = \left(\frac{\sigma_2}{\sigma}\right)^2 = 1 - V_{r1} \qquad (2.24)$$

They are adopted to describe the surface roughness location. Three typical situations of the surface roughness location are shown in Figure (2.4b).

2.9 Asperity interactions

The asperity interaction model used in the present analysis was that developed by Greenwood and Tripp (1970-71). The model assumed a Gaussian distribution of asperity heights and contact radius of curvature of the symmetric asperities. For the purpose of the study recorded in this thesis elastic asperity deformation was assumed for which the asperity contact force is given by

$$W_a = \frac{16}{15}\sqrt{2}\,\pi\,(\eta\beta\sigma)^2\,E'\,\left(\frac{\sigma}{\beta}\right)^{1/2}\,A\,F_{5/2}\left[\frac{h}{\sigma}\right] \qquad (2.25)$$

The real area of contact (A_r) is related to the apparent area of contact (A) through the relationship

$$A_r = \pi^2\,(\eta\beta\sigma)^2\,A\,F_2\left[\frac{h}{\sigma}\right] \qquad (2.26)$$

The integrals of the Gaussian distribution (F_n) were also given by Greenwood and Tripp. The total contact extent was divided into small regions of nominal constant height enabling the following interpretations,

$$A\,F_{5/2}\left[\frac{h}{\sigma}\right] = w\int_{-\infty}^{\infty} F_{5/2}\left[\frac{h}{\sigma}\right]dx \qquad (2.27)$$

$$A\,F_2\left[\frac{h}{\sigma}\right] = w\int_{-\infty}^{\infty} F_2\left[\frac{h}{\sigma}\right]dx \qquad (2.28)$$

Rohde (1981) has provided curve fitted formulae for the asperity contact functions (F_n). These lacked adequate accuracy particularly in the region of ($h/\sigma<1$) and improved curve fits have been undertaken. These are detailed in Appendix (A1) where it can be seen that the maximum error between the numerical results and new formulae is less than (1%).

CHAPTER 3

A MIXED LUBRICATION ANALYSIS OF A CAM AND FOLLOWER

3.1 Introduction

An analytical model for the mixed lubrication of a cam and flat faced follower is presented and results indicating the influence of surface roughness detailed in this chapter. This is the first such analysis for a cam and follower and the assumption that the bounding solids are rigid has been made (elastic deformation of the asperities is of course considered). The results of this chapter have already been published in the learned society literature (see Dowson et al (1986)). The next two chapters will deal with a mixed lubrication analysis incorporating elastohydrodynamic effects and the early indications are that the effect upon film thickness compared with the predictions of the present model is significant. This would be expected but it is still important to lay the foundation of rigid surface analysis in order to provide a benchmark for future studies.

The model developed uses approaches for rough surface hydrodynamic lubrication and the contact between rough surfaces developed by other workers. Analyses for the lubrication of the piston ring seal which are analogous to that given here have been undertaken by Rohde (1981) and Ruddy et al (1982). The investigation has concentrated on the effects of surface roughness height and the distribution of roughness between the cam and follower. Results for the variation of nominal film thickness, power loss and load carried by asperity contacts are presented.

3.2 Theoretical Basis

3.2.1 Cam and Follower Kinematics and Loading

Figure (2.1) shows the contact between a cam and flat faced follower and Figure (2.2b) illustrates the detailed geometry of the surfaces in the vicinity of contact with rough surfaces. The cam is designated component number one and the follower number two. The kinematical analysis of this arrangement has already been presented in Chapter (2), such analysis being valid for a general cam profile in contact with a flat faced follower. By consideration of the surface velocities in the x-coordinate direction relative to the contact, which is moving in this direction with velocity $(-a/\Omega)$ as can be seen from equation (2.3), the surface velocities of the cam and follower relative to the contact becomes respectively, from equations (2.4) and (2.7),

$$u_1 = R_c\Omega \qquad (3.1)$$

$$u_2 = \frac{a}{\Omega} \tag{3.2}$$

The mean entraining velocity now is given by,

$$u_2 = \frac{u_1 + u_2}{2} = [R_c + \frac{a}{\Omega^2}] \frac{\Omega}{2} \tag{3.3}$$

Details of the determination of the loading on cam and follower have also be given in Chapter (2).

3.2.2 Hydrodynamics of Rough Surfaces

The one dimensional form of the averaged Reynolds equation developed by Patir and Cheng (1978) was adopted in the determination of the hydrodynamic effects associated with the contact. This equation (2.19) has been detailed in Chapter (2). Only isotropic surfaces were considered due to the limitation of the asperity interaction model adopted.

3.2.3 Asperity Interactions

The asperity interaction model used in the present analysis was developed by Greenwood and Tripp (1970-71). A detailed introduction to this model has been given in Chapter (2).

3.2.4 Total Load

The total load (W) acting on unit width of the cam at any instant during the cycle was taken to be the sum of the hydrodynamic component (W_h) – estimated by integration of the pressure distribution obtained from the solution of equation (2.19) – and the asperity contact force (W_a).

$$W = W_h + W_a \tag{3.4}$$

3.2.5 Friction Force and Power Loss

The total friction force acting on the surfaces involves three components due to (a) the mean viscous shear flow, (b) the local pressure on asperities and (c) the force due to pressures acting on the nominal geometry. In their calculations associated with piston ring performance Rohde (1981) and Ruddy et al (1982) omitted consideration of the third of these components, which for rigid surfaces may not be valid. It is also important for rigid surfaces to include the contribution of terms arising from pressure effects.

The analysis here has incorporated all three components. The x-direction stresses on the cam (Figure (2.1)) were given by Patir and Cheng (1979),

$$\tau_a = \frac{\eta(u_2 - u_1)}{h}(\phi_f - \phi_{fs}) - \phi_{fp}\frac{h}{2}\frac{d\bar{p}}{dx} \qquad (3.5)$$

(mean viscous shear)

$$\tau_b = V_{r1}(\phi_{fp} - \bar{h}_t)\frac{d\bar{p}}{dx} - \frac{2\eta(u_2 - u_1)}{h}\phi_{fs} \qquad (3.6)$$

(local pressure on asperities)

$$\tau_c = \bar{p}\frac{dh}{dx} \qquad (3.7)$$

(pressure on nominal geometry)

$$\text{and } \tau_1 = \tau_a + \tau_b + \tau_c \qquad (3.8)$$

The determination of shear stress factors (ϕ_{fs} and ϕ_{fp}) has been achieved by numerical simulation. The (ϕ_f) factor has also been evaluated by Patir and Cheng (1979),

$$\phi_f = h\int_{-h+\varepsilon}^{\infty}\frac{f(y)}{(h + \delta_1 + \delta_2)}\,dy \qquad (3.9)$$

In their calculations (ε) was arbitrarily set to ($\sigma/100$) and analytical integration was possible using a polynomial density function for (f(y)) which closely approximated to a Gaussian distribution. The same analysis is adopted in the present chapter as that detailed by Patir and Cheng (1979). The small film thickness (ε) represents the value below which a hydrodynamic shear stress is taken not to exist, and for which boundary friction is assumed. Results are presented here for a value of ($\varepsilon = 10^{-9}$ μm); a physical interpretation is that this represents the approximate thickness of a boundary layer of molecules. Small variations in the value of (ε) were found to be insignificant.

When the total x-direction stress on the cam (τ_1) exceeded the shear strength of the boundary film, the latter was adopted in computing friction force. The boundary film shear stress was taken to be given by,

$$\tau_s = \tau_o + \alpha p \qquad (3.10)$$

The total friction force associated with asperity interaction was estimated from the integration of the shear stresses over the real contact area, assuming that the shear strength of the surface film was given by,

$$\tau_a = \tau_o + \alpha p_a \tag{3.11}$$

where (p_a) is the asperity pressure. Integration over the real area of contact gives the friction force due to asperity contact as,

$$F_a = \tau_o A_r + \alpha W_a \tag{3.12}$$

In evaluating the total torque and power loss associated with the cam care must be taken. The total load acting due to normal mean pressure may be equated to a force system acting at the instantaneous centre of curvature (Figure (2.1)). This will assist in determining cam torque for the case of rigid surfaces.

3.3 Numerical Analysis

The method adopted for the determination of the cyclic variation of film-thickness between cam and follower has been well established (e.g. Rohde (1981)). An initial value of the nominal central film thickness (h_o) at some instant during the cycle was estimated, and the normal velocity ($\partial h_o/\partial t$) determined such that applied load balanced the sum of the asperity and hydrodynamic components. A time step could then be marched out according to the Eulerian method such that,

$$h_o(t + \Delta t) \approx h_o(t) + \frac{\partial h_o}{\partial t} \Delta t \tag{3.13}$$

It was clearly necessary to proceed beyond one complete cycle to achieve convergency. The starting value of nominal central film thickness had little influence upon convergency, this being achieved with only a few steps after the complete cycle. The criterion for convergence was that the nominal central film thickness should be within (0.1%) of its value on the previous cycle at same point.

3.4 Results

The results presented here relate to the four power polynomial cam which had the following lift characteristic Chen (1982)

$$L = L_r + L_c + C_p\left[\frac{\theta}{\theta_t}\right]^p + C_q\left[\frac{\theta}{\theta_t}\right]^q + C_r\left[\frac{\theta}{\theta_t}\right]^r + C_s\left[\frac{\theta}{\theta_t}\right]^s \qquad (3.14)$$

with $p = 2$, $q = 9$, $r = 78$, $s = 80$

and $C_p = -11.691841$, $C_q = 2.8498942$,

$C_r = -0.5894568$, $C_s = 0.5314033$.

Details of the determination of lift, velocity and acceleration with the cam has been given by Harrison (1985). Important data relating to the arrangement is given below,

Cam action angle (θ_t)	60°
Base circle radius	18.0 mm
Maximum lift	9.40 mm
Cam width	12.0 mm
Spring stiffness	38.5 kN/m
Spring mass	0.045 kg
Bucket and valve mass	0.15 kg

The following operating conditions and values were chosen as a reference case.

Camshaft rotational frequency (Ω)	50 Hz
Equivalent elastic constant of both surfaces (E')	$2.3X10^{11}$ Pa
Lubricant viscosity (η_o)	0.01 Pas
Composite roughness height of both surfaces (σ)	0.2 μm
Variance ratio ($V_{r1}=V_{r2}$)	0.5
Ratio (σ/β)	0.0001
Product ($\eta\beta\sigma$)	0.05
Shear stress constant (τ_o)	$2X10^6$ Pa
Rate of change of shear stress with pressure (α)	0.08

The load at the cam nose at this rotational frequency was (240 N) and it should be noted that there was a cam/follower clearance on the base circle of the cam, with a ramp between the base circle and the action profile which extended (60°) from the nose.

Results are presented in Figures (3.1) to (3.9). Cam angle is taken as the

abscissa variable and the following parameters are plotted.

(a) nominal minimum film thickness

(b) load carried by the asperities (and the percentage this represented of the total)

(c) power loss and the percentage of this due to asperity contact.

The influence of variable composite surface roughness, lubricant viscosity, camshaft rotational frequency and distribution of roughness between surfaces are investigated.

3.5 Discussion

Figure (3.1) shows the variation of the nominal minimum film thickness during the cam cycle for the reference case and a series of other composite surface roughnesses. The reference case, with a composite surface roughness of (0.2 μm), reflects a typical surface finish to be found in practice. The predictions for the smaller values of roughness have been included because the theoretical approach adopted is more sound at the values of nominal film thickness to composite surface roughness (λ) obtained. This aspect will be discussed later. The results are all for the case of an equal distribution of roughness between the surfaces and the case of smooth surfaces was computed by adopting an extremely small composite roughness height of (0.001 μm).

The film thickness variations of Figure (3.1) exhibit the well known features, namely,

(1) Two portions of the cycle where substantial thicknesses of lubricant film are generated. These correspond to the rising and falling flanks of the cam where the entraining velocity of the lubricant into the contact and the contact effective radius of curvature are large.

(2) Two regions of extremely small film thickness at times where the entraining velocity of lubricant into the contact drops to zero for an instant. On the basis of quasi-static analysis the minimum film thickness at these two points would be zero, however, here the squeeze film analysis which has been undertaken reveals the protective action of squeeze film lubrication. Although the film thickness values predicted at these two points are extremely small (about (0.03 μm) for the reference case) it is interesting to note that for all the cases depicted the film thickness on the rising flank as the nose of the cam moves onto the follower is greater than that as the nose leaves the falling flank. This is in agreement with the results according to

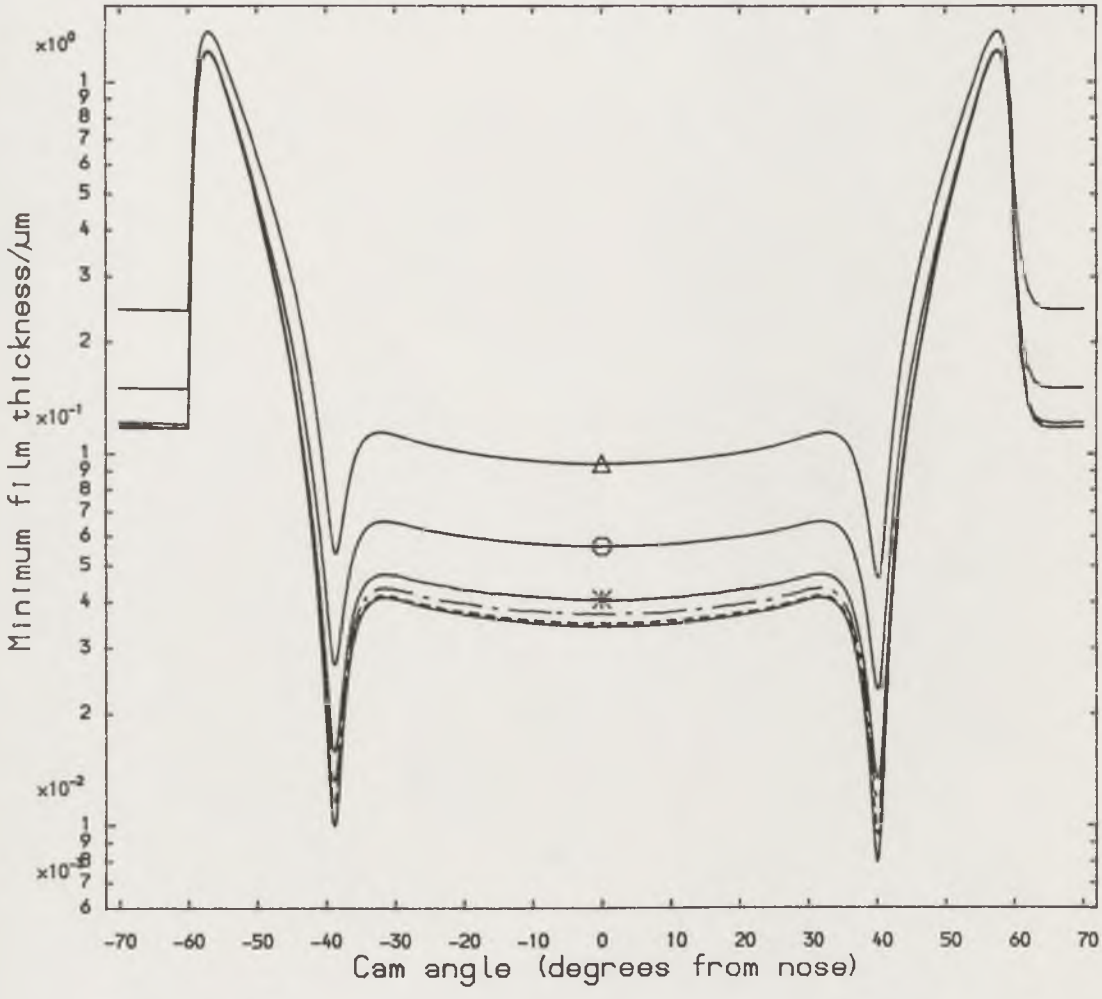

Figure (3.1) The effect of composite surface roughness height on minimum film thickness.

——— Smooth surface
-------- Composite surface roughness 0.01μm
—·—·— Composite surface roughness 0.02μm
—*— Composite surface roughness 0.04μm
—o— Composite surface roughness 0.20μm
—△— Composite surface roughness 1.00μm

the smooth, rigid surface analysis presented in the paper of Dowson et al (1985) but contrary to the elastohydrodynamic analysis presented in the paper of Bedewi et al (1985). Since the rough surface analysis presented here is for rigid bulk components there is a consistency in the comparison.

(3) A period in the vicinity of contact of the cam nose where the minimum film thickness is small and fairly constant, corresponding to a region where the entraining velocity and cam radius are small and vary only slowly.

The effect upon nominal film thickness of the introduction of surface roughness into the analysis film thickness is clearly evident from Figure (3.1). For the reference case the nominal minimum film thickness at the nose increases by about (65%) with respect to the smooth surfaces prediction whilst the increase approaches (200%) for a composite surface roughness of (1.0 μm). It should be noted that the film thickness ratio (λ) decreases from about (0.17) to (0.1) with the increase in composite surface roughness from (0.2 μm) to (1.0 μm). This serves as a reminder that the basis of the analysis undertaken is brought into question at such low values of film thickness ratio. The curve fitted data of Patir and Cheng (1978) and (1979) obtained by numerical experiment is limited to a film thickness ratio of (0.5). For the case with a composite surface roughness of (0.04 μm) the value of film thickness ratio at the nose is about (1.0). Particular care must be taken, therefore, in interpreting data for the two larger values of composite surface roughness adopted.

The load carried by the asperities and the proportion this represents of the total load is detailed in Figure (3.2). Only the reference case and details for a composite surface roughness of (1.0 μm) are presented. This is because for smaller roughnesses the load carried by the asperities becomes extremely small. The total load at the nose is (240 N) and that carried by the asperities is about (3 N) and (12 N) for the composite surface roughnesses of (0.2 μm) and (1.0 μm) respectively. Thus the asperity load is only a small percentage of the total load, a situation which has been noted for the piston ring/cylinder liner contact (see Rohde (1981)). Indeed the present geometry is significantly less conformal than that of the piston ring and cylinder liner contact considered by Rohde and the proportion of load taken by the asperities is somewhat less. At times of significant squeeze film action the percentage of load carried by the asperities increases but still only represents about (8%) of the total load for the highest composite surface

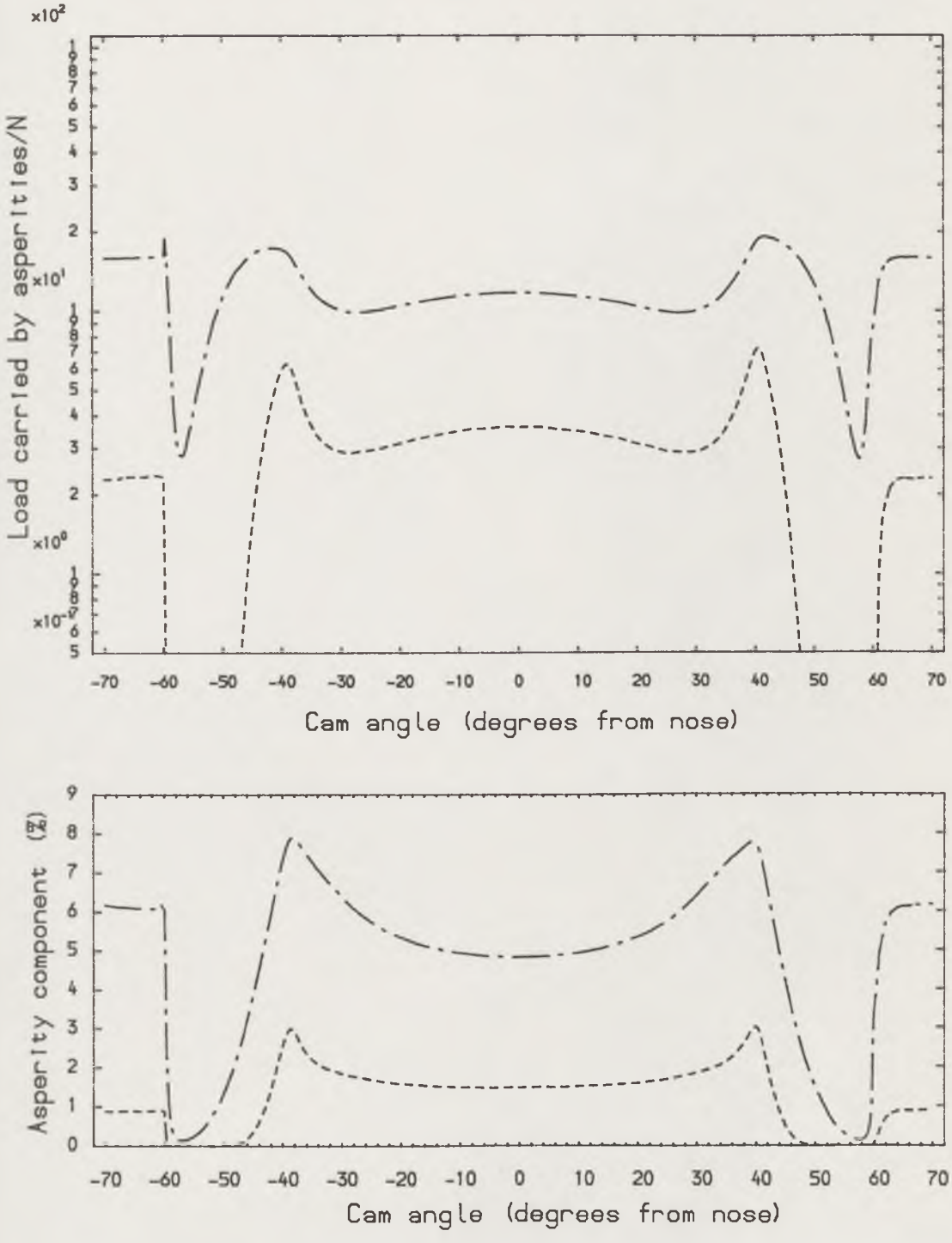

Figure (3.2) The effect of composite surface roughness height on load carried by the asperities and the percentage this represents of the total load.

--------- Composite surface roughness 0.2μm

—·—·— Composite surface roughness 1.0μm

roughness.

The small load carried by the asperities is a direct consequence of the non-conformal geometry of the cam and follower contact. It is interesting to contrast the predicted small percentage of the total load carried by the asperities with the significant increase in nominal minimum film thickness from the smooth surface case, which for the reference case (σ = 0.2 μm) was about (65%). This is as a result of the small value of the pressure flow factor (ϕ_x) at the low values of film thickness ratio. Physically this implies a considerable restriction to the lubricant flow (which is only in the direction of surface motion for the analysis here) and a consequent enhancement of nominal minimum film thickness for the same applied load.

In Figure (3.3) the power loss and the proportion of this due to asperity contact are presented. Data for the smooth surface situation and composite surface roughnesses of (0.01 μm), (0.02 μm) and (0.04 μm) are given (again with the same isotropic roughness on both surfaces). The results for the higher values of composite surface roughness have been omitted. This is because predictions which were inconsistent with physical reality, in which power loss decreased with increasing roughness, were made. This resulted from the curve fitted data for (ϕ_f) proving unsatisfactory at the low values of film thickness ratio for which it was not strictly applicable. For a composite surface roughness of (0.04 μm) the power loss at the nose position was some (35) watts, an increase of about (50%) from the smooth surface case. The proportion of this increase due to asperity interaction is extremely small, as was the proportion of load carried by asperity contact. Once again this reflects the low degree of asperity interaction because of the non-conformal geometry coupled with the larger nominal film thickness. The latter affects the factor (ϕ_f) of the mean viscous shear and the asperity loading in the direction of surface motion due to local pressure (see section (3.2.5)) causing the significant increase in power loss. The increase is almost entirely derived from hydrodynamic effects.

Figures (3.4) and (3.5) show the effect of the variation of lubricant viscosity and camshaft speed upon the nominal minimum film thickness during the cycle. Apart from the applied variables other factors remain as for the reference case detailed previously, with the composite surface roughness taken as (0.2 μm). The results of these two figures are physically consistent. A five-fold increase in lubricant viscosity causes an increase in

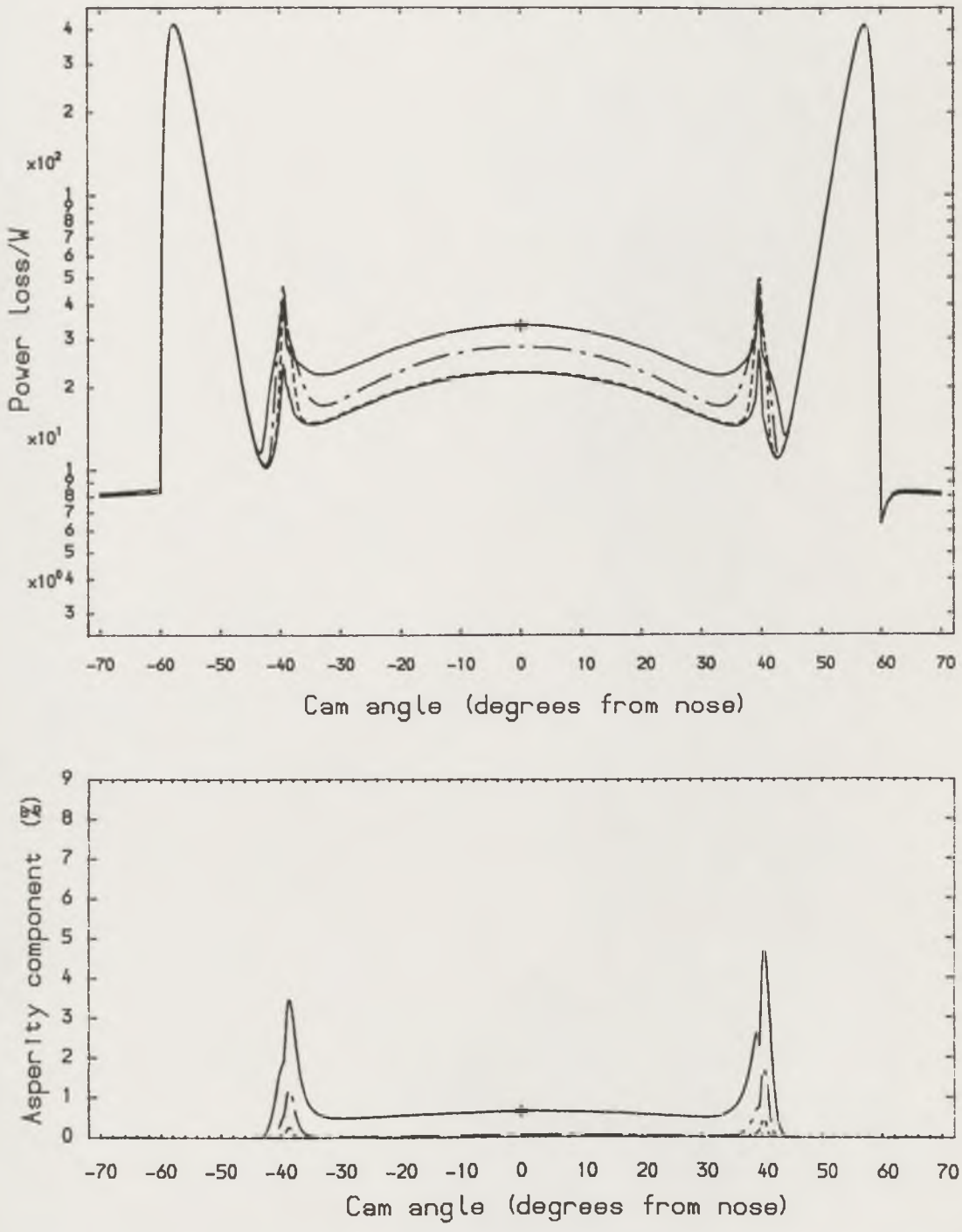

Figure (3.3) The effect of composite surface roughness height on power loss and the percentage of this connected with asperities.

———— Smooth surface

--------- Composite surface roughness 0.01μm

—·—·— Composite surface roughness 0.02μm

———*——— Composite surface roughness 0.04μm

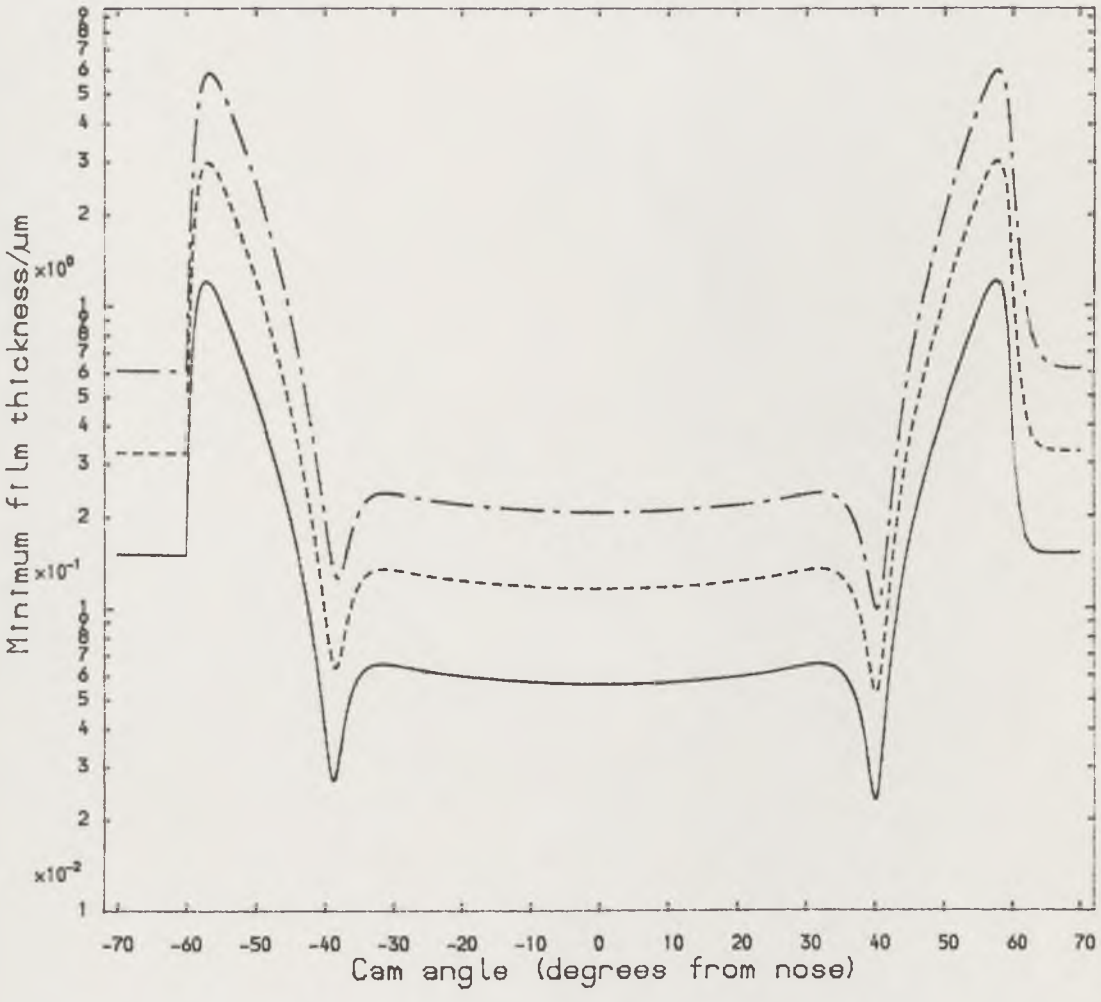

Figure (3.4) The effect of lubricant viscosity on minimum film thickness.

————— Lubricant viscosity 0.010 Pas.

--------- Lubricant viscosity 0.025 Pas.

—·——·— Lubricant viscosity 0.050 Pas.

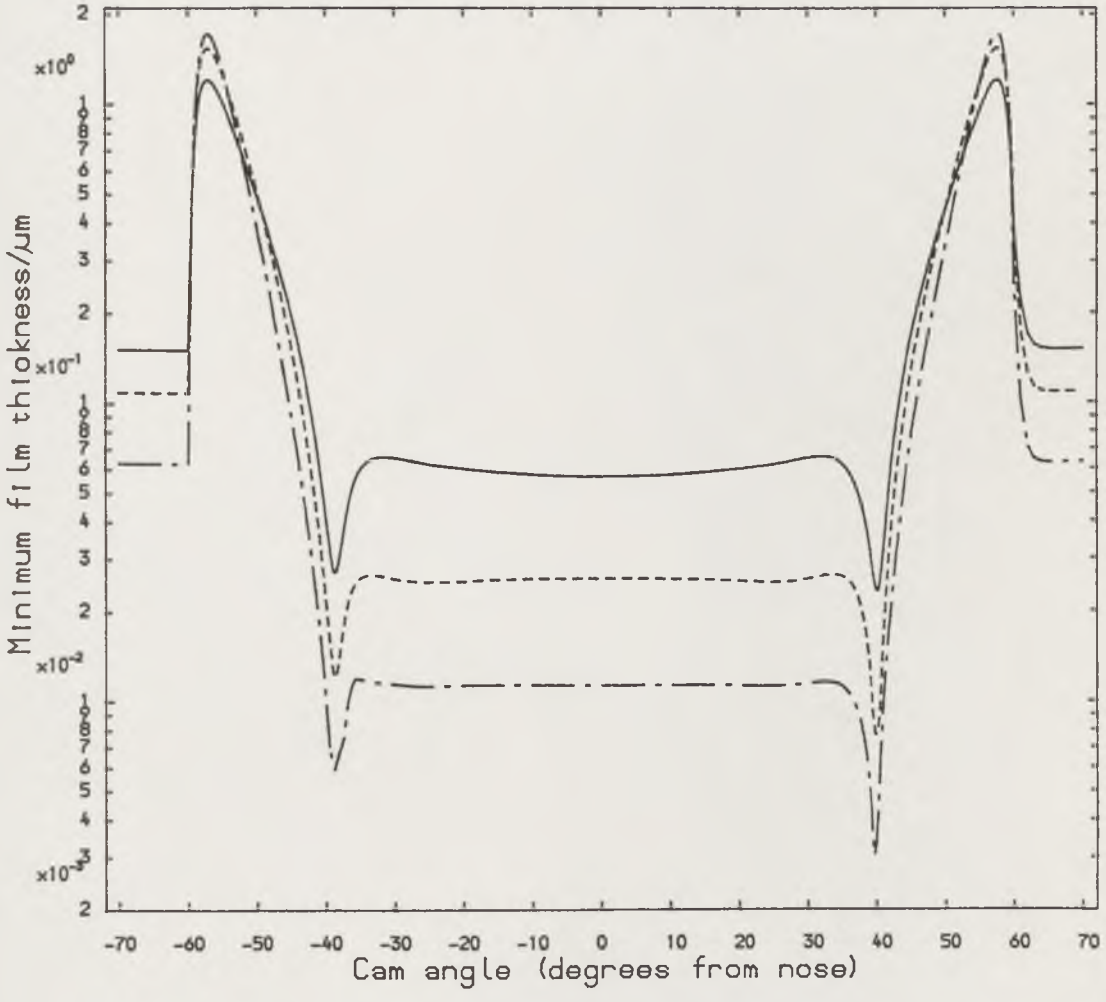

Figure (3.5) The effect of camshaft rotational speed on minimum film thickness.

———— Camshaft rotational speed 3000 r/min (50.0Hz)

--------- Camshaft rotational speed 2000 r/min (33.3Hz)

—·—·— Camshaft rotational speed 1000 r/min (16.7Hz)

the nominal minimum film thickness at the nose by a factor of about (3.8), whilst a reduction in camshaft rotational frequency from (50 Hz) to (16.7 Hz) is reflected in a drop in this film thickness from (0.058 μm) to (0.011 μm).

A consideration of the effect of the distribution of roughness between the cam and the follower is presented in the remaining Figures. The results detailed thus far have related to situations with the same isotropic roughness on both surfaces. In such situations the second term on the right hand side of averaged Reynolds equation (2.19), representing fluid transport due to sliding in a rough bearing, is not influential as regards generation of the mean pressure since (ϕ_s) becomes zero. If, however, the surfaces have different isotropic roughnesses this term becomes important because there is a net fluid transport resulting from the combination of sliding and roughness. The shear flow factor (ϕ_s) depends not only upon the film thickness ratio and the orientation of surface roughness, but also on the roughness heights of the individual surfaces. The analysis was restricted to cases of isotropic roughness.

In the case of the cam and follower situation the influence of fluid transport resulting from sliding and roughness is further complicated by the fact that the lubricated contact is moving through space. The entraining velocity of lubricant into the contact changes direction whilst the sliding velocity with respect to the contact does not. Care is needed therefore in specifying the appropriate sign to the velocities and shear flow factor (ϕ_s) when solving Reynolds' equation.

Two cases showing the effect of isotropic surface roughness distribution upon the nominal lubricant minimum film thickness are presented in Figures (3.6) and (3.7). In Figure (3.6) the composite surface roughness is kept fixed at (0.2 μm) and in addition to the reference case, where both surfaces have the same roughness, results for a smooth cam and rough follower and smooth follower and rough cam are presented. The data of Figure (3.7) is for a fixed composite surface roughness of (0.04 μm) with otherwise the same situation. The contrast between the relative predictions of minimum film thickness at the nose dependent upon roughness distribution for the two cases is apparent.

For the composite surface roughness of (0.2 μm), Figure (3.6) shows that the case of a smooth cam and rough follower would result in a higher

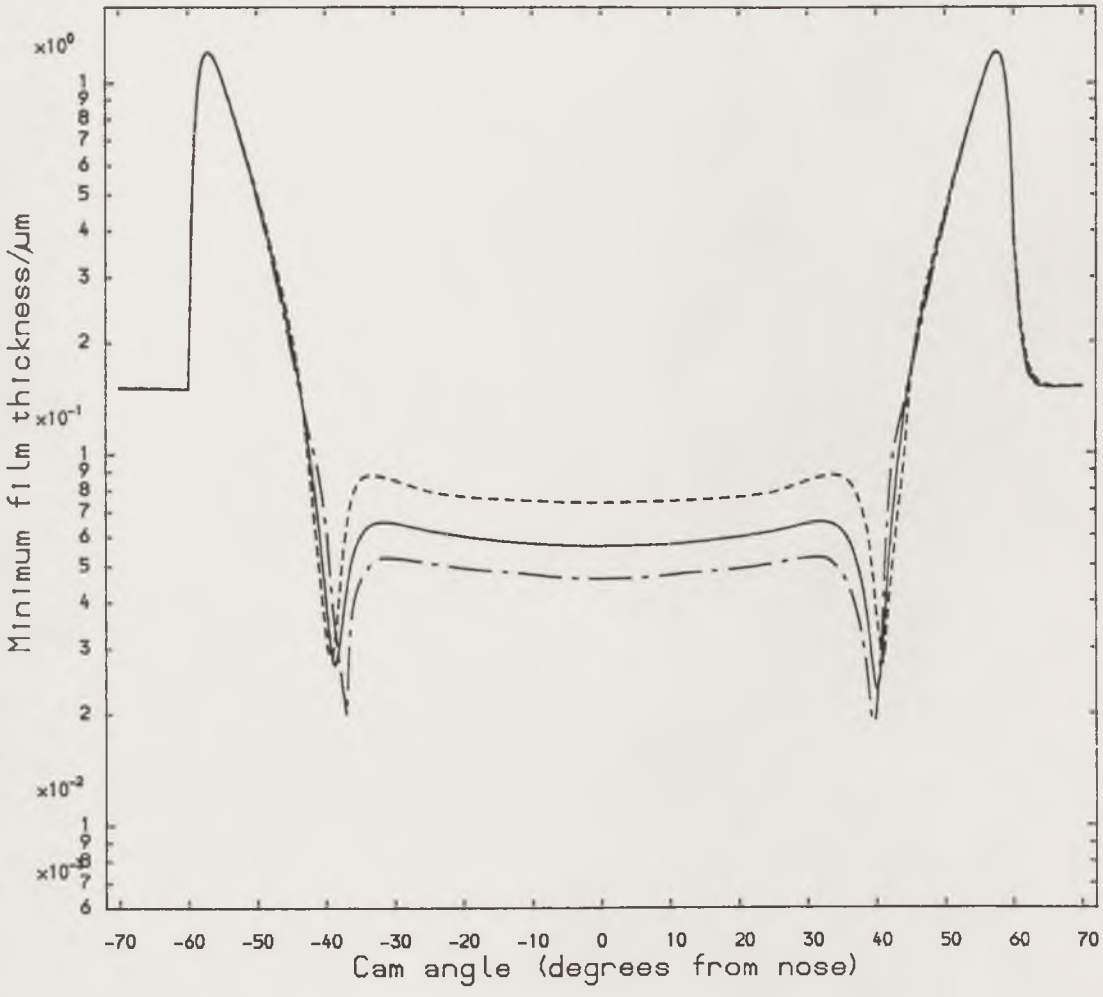

Figure (3.6) The effect of distribution of roughness between cam and follower surfaces on minimum film thickness.

———— Same roughness on cam and follower

--------- Smooth cam and rough follower 0.2μm

—·—·— Smooth follower and rough cam 0.2μm

nominal minimum film thickness at the nose than for equal roughnesses on the surfaces. With a smooth follower and rough cam the converse is true, the film thickness being less than for the case of the same roughness on cam and follower. The trend of this variation is reversed for a fixed composite surface roughness of (0.04 μm) as may be seen on Figure (3.7). The difference between the two cases is explained by the way in which the shear flow factor (Φ_s) varies with the film thickness ratio (λ). As (λ) is reduced (from say (3) or (4)) the value of (Φ_s), or more strictly its modulus, increases. However, it reaches a peak and then decreases rapidly towards a value of zero. This is because the number of asperity contacts and the real area of contact increases and as the total contact area approaches the apparent contact area the shear flow factor must tend towards zero since it reflects a mean flow. The restrictions on the data at low values of film thickness ratio which have already been mentioned must here be borne in mind.

For the case of a fixed composite surface roughness of (0.2 μm) the modulus of (Φ_s) exhibits an increasing trend with increasing film thickness ratio (λ) at the values of (λ) in the region of the nominal minimum film thickness at the nose. The sign of (Φ_s) then depends upon the distribution of roughness. With a composite surface roughness of (0.04 μm) the minimum film thickness ratio at the nose is of order unity and the appropriate values of (Φ_s) are around the turning point on the (Φ_s–λ) curve. The two situations result in different trends reflecting the tendency of the fluid in the valleys of the rough surface either to help or to impede the transport of lubricant in the gap between the components. The changes in the nominal minimum film thickness at the nose due to the variation in distribution of isotropic roughness investigated are not insignificant. For the fixed composite roughness height of (0.2 μm) (Figure (3.6)) the increase with a smooth cam and rough follower is (30%), whilst the decrease with a smooth follower and rough cam is (21%).

A further interesting feature of the results is that the trend of the influence of the distribution of surface roughness upon minimum film thickness at the nose is reversed on the flanks at locations around (40°) from the nose. This is because although the direction of relative sliding remains the same, the direction of lubricant entrainment into the contact has altered. The effect of the shear flow factor through the second term on the right hand side of the Reynolds' equation (2.19) is therefore changed in

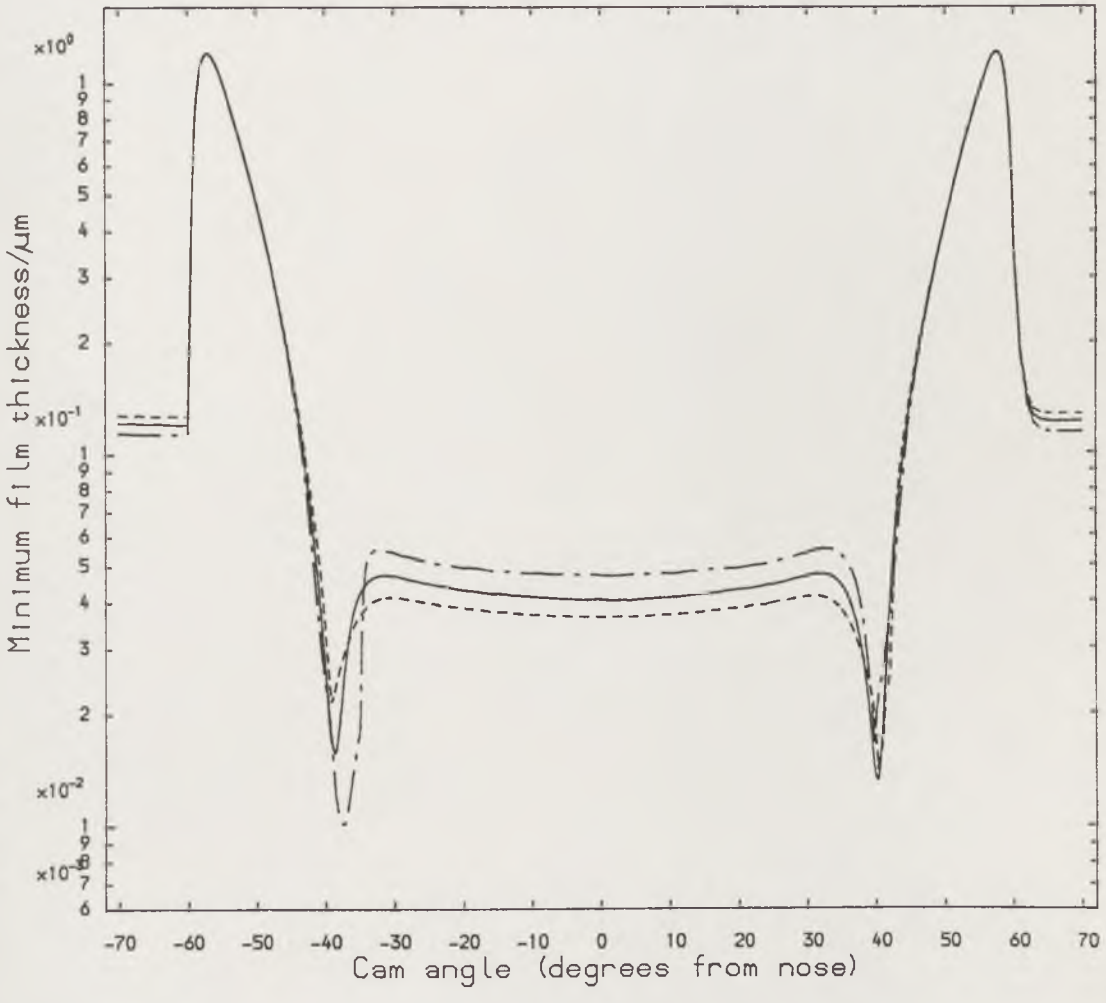

Figure (3.7) The effect of distribution of roughness between cam and follower surfaces on minimum film thickness.

———— Same roughness on cam and follower

--------- Smooth cam and rough follower 0.04μm

—·—·— Smooth follower and rough cam 0.04μm

sense.

The effect of the distribution of roughness between surfaces upon load carried by the asperities and the percentage this represents of the total is shown in Figure (3.8) for a fixed composite surface roughness of (0.2 μm). The influence is small and this would be expected from the results for the case of the same roughness on the cam and follower presented already (Figure (3.2)). The trend of the variations is consistent with that which would be expected from the graph of minimum film thickness shown in Figure (3.6). With a smooth cam and rough follower, for which there was an increase in nominal minimum film thickness at the nose, Figure (3.8) shows there is a corresponding reduction of the load carried by the asperities. The converse is true for the smooth follower and rough cam.

In the final figure, Figure (3.9), the influence upon power loss and the proportion associated with asperity contact of the distribution of roughness is presented. As has already been discussed the contribution of asperity friction to the overall power loss is small. The data presented is for a fixed composite surface roughness of (0.04 μm) and the situations of both a smooth cam and rough follower and a smooth follower and rough cam cause an increase in power loss at the nose in comparison with the case of equal distribution of roughness. However, the contribution to the power loss of asperity friction as a percentage of the total is greater for the smooth cam and rough follower than the case of equal distribution of roughness, whilst the opposite is true for the smooth follower and rough cam. A simple explanation of these observations is difficult because of the complexity of the various influences upon friction and power loss but the extremely small contribution of asperity interaction to the total power loss will once again be noted.

The study of mixed lubrication in a cam and flat faced follower presented here has considered a model in which the bulk solids are taken to be rigid although elastic deformation of asperities has been considered. As a result of this, predicted values of the nominal minimum lubricant film thickness are substantially less than would be expected for the practical situation in which elastohydrodynamic lubrication plays an important role. A consequence of this is that for realistic surface roughness values of (say (0.2 μm)) the predicted film thickness ratio is less than (0.5) at the nose position. The data of Patir and Cheng is only valid for film thickness ratios greater

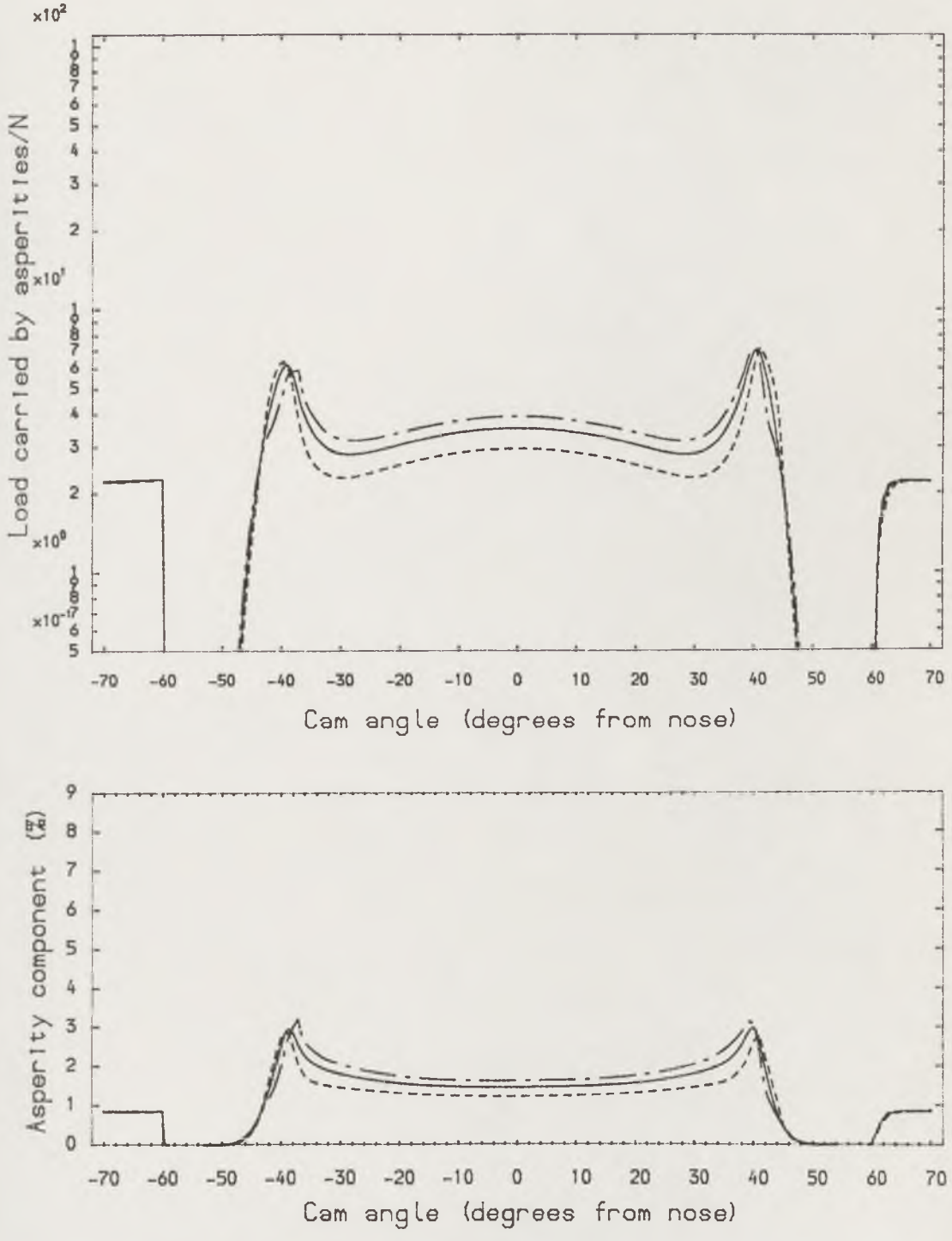

Figure (3.8) The effect of distribution of roughness between cam and follower surfaces on load carried by asperities and the percentage this presents of the total load.

———— Same roughness on cam and follower

--------- Smooth cam and rough follower 0.2μm

—·—·— Smooth follower and rough cam 0.2μm

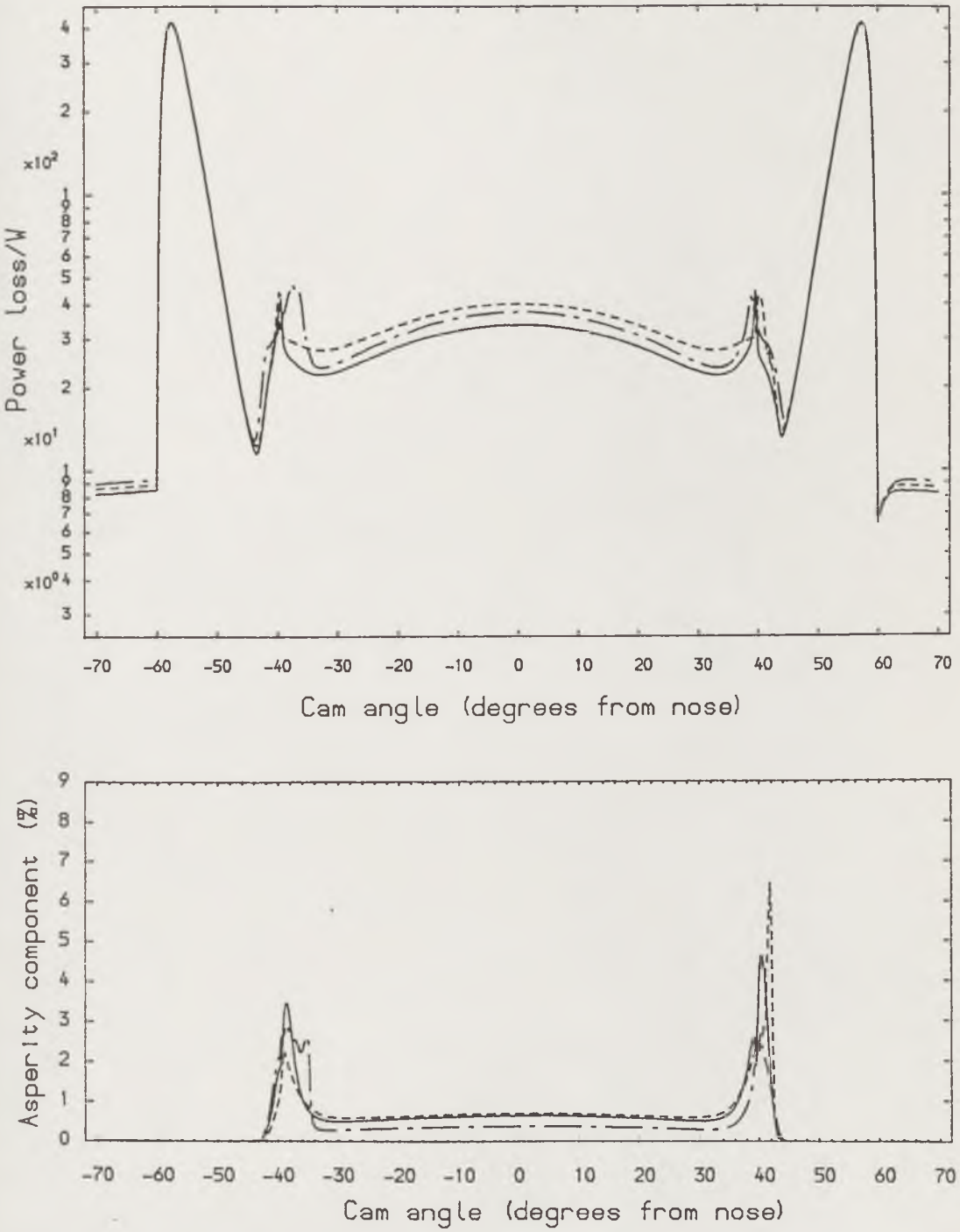

Figure (3.9) The effect of distribution of roughness between two surfaces on power loss and the component of this connected with the asperities.

———— Same roughness on cam and follower

--------- Smooth cam and rough follower 0.04μm

—·—·— Smooth follower and rough cam 0.04μm

than (0.5) and hence caution must be exercised when interpreting results for such situations. With adopted values of composite surface roughness less than those likely to be encountered in practice a situation for which the model used is valid has been created.

Analysis of the mixed lubrication of a contact in which values of film thickness ratio less than (0.5) are encountered is extremely difficult. For such a situation the deformation of asperities would be expected to influence the nominal geometry and this and other factors at the moment means that such cases have not yet satisfactorily yielded to analysis. In the analysis presented here fixed values of the quantities (σ/β) and $(\eta\beta\sigma)$ have also been taken and a further investigation of the influence of these parameters based upon experimental data would be valuable. In addition no results have been presented for the case of non-isotropic roughness. Whilst the analysis of Patir and Cheng for the hydrodynamics of rough surfaces can accommodate non-isotropic roughness, the Greenwood and Tripp model for the contact of rough surfaces cannot. It is interesting to note, however, that despite this, Rohde (1981) did investigate non-isotropic roughness, using the same model for the piston ring/cylinder liner contact.

Despite the limitations of the results presented here they do provide a useful assessment of the influence of surface roughness upon cam and follower lubrication. The development of the model to consider conditions of elastohydrodynamic lubrication will be the subject of the next two chapters.

3.6 Conclusions

A mixed lubrication analysis of a cam and flat faced follower has been presented. For the case of the same isotropic roughness on both surfaces it has been shown that,

(1) An increase in composite surface roughness results in an increase in nominal minimum film thickness.

(2) The proportion of the load carried by the asperities is small because of the nonconformal nature of the contact.

(3) For small values of the composite surface roughness the power loss increases with increasing roughness. The asperity component of power loss

is small the major effects being hydrodynamic.

With an equal distribution of isotropic roughness between the cam and follower surfaces it has been demonstrated that the trend of variations is influenced by the magnitude of the composite surface roughness. For a larger fixed composite roughness the situation of a smooth cam and rough follower will result in a larger nominal minimum film thickness at the nose than for the case of the same roughness on both surfaces. However, for a smaller fixed composite surface roughness the situation can be reversed.

The analysis has been undertaken for the case of rigid bulk components. This has resulted in the prediction of small values of nominal film thickness and the ratio of this to surface roughness height for which in some cases the data used has been extrapolated beyond the limit for which it was established. Whilst this is recognized as a limitation the results presented will be of value and interest to designers. The studies described in the next two chapters will extend the analysis to cover the elastohydrodynamic lubrication of the cam and follower with considerations of surface roughness.

CHAPTER 4

A FULL NUMERICAL ELASTOHYDRODYNAMIC LUBRICATION ANALYSIS OF A CAM AND FOLLOWER WITH CONSIDERATION OF LOCAL SQUEEZE VELOCITY EFFECTS

4.1 Introduction

The mixed lubrication analysis of the cam and follower, which has been detailed in Chapter (3), has been used for an initial consideration of surface roughness effects whilst taking the bulk solid to be rigid. It is well recognized that the lubrication conditions encountered in an automotive cam and follower contact involve significant bulk elastic distortion of the boundary surfaces. As the dominant requirement in the operation of cams and followers is to reduce the probability of premature surface failure, an important feature in the consideration of ways to reduce wear and failure is the recognition that the mechanism of lubrication is essentially elastohydrodynamic. The elastohydrodynamic lubrication theory was described and related to the mechanisms of pitting and scuffing, as well as the flash temperature concept, by Naylor (1967-68).

In addition, the operation of lubricated cams and followers introduces a squeeze film action between cam and follower surfaces. This arises as a result of the variations of the load, relative radius of curvature and entraining velocity with time. The lubrication analysis with considerations of both squeeze film action and bulk elastic distortion of the boundary surfaces is known as a transient (or non-steady state) elastohydrodynamic lubrication analysis. The transient elastohydrodynamic lubrication analysis has shown that the squeeze component can act effectively as a viscous damping phenomenon in which the effects from the variations of external parameters such as the load and the entraining velocity are damped down. This, in turn, contributes to the maintenance of the persistence of lubricated thin films when subjected to sudden variations.

Previous transient lubrication analyses of the cam and follower were all based upon the assumption that the normal velocity is constant. In fact, due to the elastic deformation of the surfaces, the normal velocity varies along the conjunction of cam and follower surfaces. The normal velocity arising from the elastic deformation is termed local squeeze velocity. The local squeeze effect was investigated by Dowson et al (1983) in an elastohydrodynamic analysis of piston rings in combined normal and entraining motion. Their general findings showed that the wave of elastic deformation, which ripples up and down the liners of engine cylinders several times each second, together with the associated deformations on the piston ring itself, combined with the direct effect of pressure upon

lubricant viscosity promoted elastohydrodynamic lubrication. Obviously the local squeeze effect should be incorporated in the transient elastohydrodynamic analysis of the cam and follower. However, such an analysis has not yet received any attention.

The purpose of the present chapter is to offer an assessment of the role of elastohydrodynamic lubrication on the tribological performance of the cam and follower. This chapter presents a transient elastohydrodynamic lubrication analysis of the cam and follower by a straightforward iterative procedure, in which elastohydrodynamic effects were introduced into the numerical procedure by allowing the lubricant viscosity to vary with the pressure, and by taking into account the local squeeze velocity effect. This is the first time that such an analysis has been performed on the cam and follower pair. The investigations have concentrated on the influence of the surface elastic deformation and local squeeze velocity effects on the cyclic variations of the minimum film thickness, film shape and pressure distribution.

4.2 Theoretical Basis

The following dimensionless groups are adopted in the present analysis.

B	dimensionless half Hertzian contact width	[b/R]
H	dimensionless film thickness	[h/R]
P	dimensionless pressure	[p/E']
Q	dimensionless reduced pressure	[q/E']
r	ratio of normal to entraining velocity	[v/u]
U	entraining velocity parameter	$[(\eta_0 u)/(E'R)]$
W	load parameter	[w/(E'R)]
X	dimensionless coordinate in x direction	[x/b]

4.2.1 Hydrodynamic Equation

Reynolds' equation for fully flooded lubrication of two cylinders in combined 'entraining' and 'normal' motion has been given by equation (2.12) in which the normal velocity term $(\partial h/\partial t)$ of the cylinders can be assumed to be either constant or variable along the whole conjunction region. By introducing the dimensionless groups into Reynolds equation (2.12), a dimensionless Reynolds equation is obtained;

$$\frac{d}{dX}\left(\frac{H^3}{\bar{\eta}}\frac{dP}{dX}\right) = 12UB\left[\frac{dH}{dX} + B\,r(X)\right] \qquad (4.1)$$

with boundary conditions

$$P(-\infty) = 0, \qquad \frac{dP}{dX}(X_m) = P(X_m) = 0.$$

4.2.2 Pressure–Viscosity Relationship and Reduced Pressure

The composite exponential pressure-viscosity relationship under isothermal condition has been given by equation (2.16). Non-dimensionalizing the equation with the dimensionless groups leads to the expression for the dimensionless pressure-viscosity relationship;

$$\bar{\eta} = \begin{cases} \exp(GP) & \text{for } P \le P_1 \\ \exp(GP + G_1[P - P_1]) & \text{for } P > P_1 \end{cases} \qquad (4.2)$$

Thus, the dimensionless reduced pressure (Q) takes the form;

$$Q = \begin{cases} \dfrac{1}{G}[1 - \exp(-GP)] & \text{for } P \le P_1 \\ \dfrac{1}{G_1}\{1 - \exp[-GP_1 + G_1(P-P_1)]\} + \dfrac{G - G_1}{G\,G_1}[1 - \exp(-GP_1)] & \text{for } P > P_1 \end{cases} \qquad (4.3)$$

4.2.3 Film Thickness

With the parabolic approximation, the separation between two rigid cylinders can be represented by that between a cylinder having an equivalent radius (R) ($1/R = 1/R_1 + 1/R_2$) and a plane. The separation between the cylinder and the plane has been given by equation (2.13). For an elastic equivalent cylinder, if the local elastic deformation relating to some datum mark is (v), the separation between the elastic cylinder and the elastic plane is given by:

$$h(x) = h_o + \frac{x^2}{2R} + v(x) \qquad (4.4)$$

4.2.4 Elasticity Equation

For plane strain the elastic deformation at a location distance (s) from the origin resulting from a pressure distribution (p(x)) is calculated by equation (2.14). If (h_c) is the central film thickness in the elastohydrodynamic conjunction, it can be seen from equations (4.4) and (2.14) that;

$$v_c(0) = -\frac{2}{\pi E'} \int_{-\infty}^{\infty} p(s) \ln(s)^2 \, ds + C$$

so we have

$$h(0) = h_c = h_o + v_c(0)$$

and

$$h_o = h_c - v_c(0) = h_c + \frac{2}{\pi E'} \int_{-\infty}^{\infty} p(s) \ln(s)^2 \, ds - C \qquad (4.5)$$

Substituting (h_o) in equation (4.4) with equation (4.5) gives;

$$h(x) = h_c + \frac{x^2}{2R} - \frac{2}{\pi E'} \int_{-\infty}^{\infty} p(s) [\ln(x-s)^2 + \ln(s)^2] \, ds \qquad (4.6)$$

Equation (4.6) was used for evaluating the elastohydrodynamic film thickness between the equivalent cylinder and the plane. Thus the dimensionless film thickness is given by the expression;

$$H(X) = H_c + B^2 \frac{X^2}{2} - \frac{2}{\pi} B \int_{-\infty}^{\infty} P(S)[\ln(X-S)^2 + \ln(S)^2] dS \qquad (4.7)$$

4.3 Numerical Procedure

4.3.1 Elastic Deformation

The numerical integration for elastic deformation was achieved by dividing the full computational zone into (m) elements of non-uniform length, each subjected to a constant pressure. From equation (2.14) it can be seen that a strip of a unit pressure (P_u) applied over a width $(2S_j)$ on the surface of a semi-infinite plane will lead to a deformation coefficient (D_{ij}) at a distance (X_i) from the centre of the load region. The expression for the deformation coefficient (D_{ij}) is;

$$D_{ij} = \frac{2B}{\pi} P_u[(X_i - S_j) \ln |X_i - S_j| - (X_i + S_j) \ln |X_i + S_j|] + C$$

The total elastic deformation (V_i) at the location (X_i) due to all the contributions of the various rectangular zones of uniform pressure (P_j) was evaluated by the summation of every individual contribution, that is;

$$V_i = \frac{2B}{\pi} \sum_{j=1}^{m} D_{ij} P_j \qquad (4.8)$$

4.3.2 Pressure Distribution

Introducing reduced pressure (Q) of equation (4.3) into Reynolds equation (4.1) yields a reduced Reynolds equation which can be written in form;

$$\frac{d}{dX}\left(H^3 \frac{dQ}{dX}\right) = 12\,BU\left[\frac{dH}{dX} + B\,r(X)\right] \tag{4.9}$$

with boundary conditions,

$$\frac{dQ}{dX}(X_m) = Q(X_m) = 0, \quad Q(-\infty) = 0.$$

If the normal velocity ($\partial h/\partial t$) varies with (X), the reduced Reynolds equation (4.9) cannot be integrated analytically. Therefore, a finite difference approach was adopted for the solution of the reduced pressure (Q) from equation (4.9). The expansion of the differential operator on the left-hand side of equation (4.9) gives;

$$\frac{d^2Q}{dX^2} + \frac{3}{H}\frac{dQ}{dX}\frac{dH}{dX} = 12BU\,\frac{1}{H^3}\left[\frac{dH}{dX} + B\,r(X)\right] \tag{4.10}$$

Expanding $Q(X+\Delta X)$ in the vicinity of the point of (X_i) in Taylor series expansion, the expression for the value of (Q_{i+1}) by (Q_i) and its first and second derivatives is;

$$Q(X_{i+1}) = Q(X_i) + Q'(X_i)\,D_i - \frac{1}{2}\,Q''(X_i)\,D_i^2 \tag{4.11}$$

In the same way, the value of $Q(X-\Delta X)$ can be represented by;

$$Q(X_{i-1}) = Q(X_i) - Q'(X_i)\,D_{i-1} + \frac{1}{2}\,Q''(X_i)\,D_{i-1}^2 \tag{4.12}$$

From equations (4.11) and (4.12) the first and the second derivatives of the reduced pressure (Q) at the point of (X_i) are deduced. They are;

$$Q'(X_i) = D_c[(Q_{i+1} - Q_i)D_{i-1}^2 + (Q_i - Q_{i-1})D_i^2] \tag{4.13}$$

$$Q''(X_i) = 2D_c[(Q_{i+1} - Q_i)D_{i-1} - (Q_i - Q_{i-1})D_i] \tag{4.14}$$

where $D_i = X_{i+1} - X_i$

$D_{i-1} = X_i - X_{i-1}$

$$D_c = \frac{1.0}{D_{i-1}\, D_i\, (D_i + D_{i-1})}$$

Similarly, the first derivative of film thickness (H) at the point of (X_i) can be represented by;

$$\frac{dH}{dX} = D_c[(H_{i+1} - H_i)D_{i-1}^2 + (H_i - H_{i-1})D_i^2] \qquad (4.15)$$

Introducing equations (4.13), (4.14) and (4.15) into equation (4.10) gives a discrete form of the differential equation which is expressed by the following system of linear equations;

$$[C_{ij}]\ \{Q_j\} = \{B_i\} \qquad i, j = 1, 2, ..., m. \qquad (4.16)$$

Where $C_{ij} = 0$ if $j < i-1$ or $j > i+1$

$$C_{i,i-1} = D_i\,(2.0 - A_i\, D_i)$$

$$C_{i,i} = (D_{i-1} + D_i)\,[A_i\,(D_i - D_{i-1}) - 2.0]$$

$$C_{i,i+1} = D_{i-1}(2.0 + A_i\, D_{i-1})$$

$$A_i = 3.0\, D_c\, \frac{1}{H_i}\, \frac{dH}{dX}(X_i)$$

$$B_i = 12.0\, B\, U\, D_c\, \frac{1}{H_i^3}\, [\frac{dH}{dX}(X_i) + B\, r(X_i)]$$

The coefficient matrix $[C_{ij}]$ in the linear equation (4.16) is a tri-diagonal matrix, which can be solved by a Gaussian elimination approach. The number of the linear equations is dependent upon the cavitation position in the lubricant film. The cavitation point (X_m) was located by repeating the procedure for the solution of equation (4.16) until Reynolds' boundary condition was satisfied.

Having obtained the cavitation boundary (X_m), the reduced pressure (Q) was determined. Then the dimensionless pressure distribution can be calculated from the equation given below;

$$P(X) = \begin{cases} -\frac{1}{G} \ln[1 - GQ(X)] & \text{for } Q \le Q_1 \\ P_1 - \frac{1}{G_1} \ln[1 - G_1(Q(X) - Q_1)\, \exp(GP_1)] & \text{for } Q > Q_1 \end{cases} \qquad (4.17)$$

Consequently, the hydrodynamic load capacity (W_h) of the fluid pressure is found by integrating the pressure distribution between the limits of the extent of the oil film;

$$W_h = B \int_{-\infty}^{X_m} P(X)\, dX \tag{4.18}$$

4.3.3 Normal Velocity

From the present value of the film shape, (h), the change of the film shape during the next time step could be determined. The normal velocity which varies along the conjunction was estimated according to the Eulerian method. Thus;

$$\frac{\partial h}{\partial t}(x,\ t+\Delta t) \approx \frac{\Delta h}{\Delta t} = \frac{h(x,\ t+\Delta t) - h(x,\ t)}{\Delta t} \tag{4.19}$$

where $(\partial h/\partial t)$ represents the summation of the squeeze velocities arising from both normal motion of the rigid body and the elastic deformation. For a constant normal velocity solution, the normal velocity at the centre of the conjunction was adopted in a simple transient elastohydrodynamic analysis. This is;

$$\frac{\partial h}{\partial t}(0,\ t+\Delta t) = \frac{\partial h_c}{\partial t} \approx \frac{h(0,\ t+\Delta t) - h(0,\ t)}{\Delta t} \tag{4.20}$$

4.3.4 Solution Procedure

The well established method adopted to determine the cyclic variation of film thickness between a cam and follower was to evaluate the normal velocity and film shape with selected increments of cam angle, such that the cam and follower enjoyed vertical equilibrium throughout the engine cycle. This made it possible to march out a solution from any assumed starting condition and it was necessary to proceed beyond one complete cam working cycle in order to achieve a satisfactory measure of convergence. The criterion for the convergence was that the central film thickness should be within (0.1%) of its value on the previous cycle at same point.

In the present analysis the convergent solution at a given instant was obtained by the straight forward iterative procedure which is described by the process: hydrodynamic pressure --> elastic deformation --> film thickness --> hydrodynamic pressure. The converged pressure distribution and film shape were subsequently used as primary values for the next time

increment to evaluate the elastic deformation and normal velocity.

The elastic deformation arising from a known fluid pressure distribution was calculated from equation (4.8) at every point throughout the conjunction. New values of the film shape (H) and subsequently the normal velocity were estimated from equations (4.7) and (4.19) or (4.20). Consequently, a new pressure distribution was obtained by solving equations (4.16) and (4.17) with the currently estimated normal velocity. The criterion for the convergence of the pressure was that the sum of the absolute differences of the pressure between two iterative procedures should be within (1%). The requirement of the load equilibrium for the cam and follower were progressively satisfied within an iterative procedure. The criterion for convergence was that the difference of the the hydrodynamic load and the cam load should be less than (0.1%).

4.3.5 Flow Chart

The flow chart which is shown in figure (4.1) outlines the solution procedure adopted for the present analysis. There are four main loops within the flow chart. The first is the pressure loop which revises the pressure distribution obtained when the iterative procedure for the cavitation boundary (X_m) is convergent under a given central film thickness (H_c). The second is the load loop which produces a central film thickness corresponding to a specified cam load (W). The third is the elastic deformation loop, in which the pressure distribution at a given instant is determined. The final loop is the cam angle increment loop in which the cam moves to the next position with a time increment (Δt). The primary value of the central film thickness (H_c) for the next time step is estimated by a parabolic extrapolation of three central film thicknesses which had been determined in the previous three time steps.

4.4 Results

The general analysis outlined in this chapter has been applied to the four power polynomial cam which has the same lift characteristic as that detailed in Chapter (3). Some modifications were made to the cam parameters by Bedewi et al (1985) to obtain convergent results. Important data relating to the arrangement and operating conditions is given below:

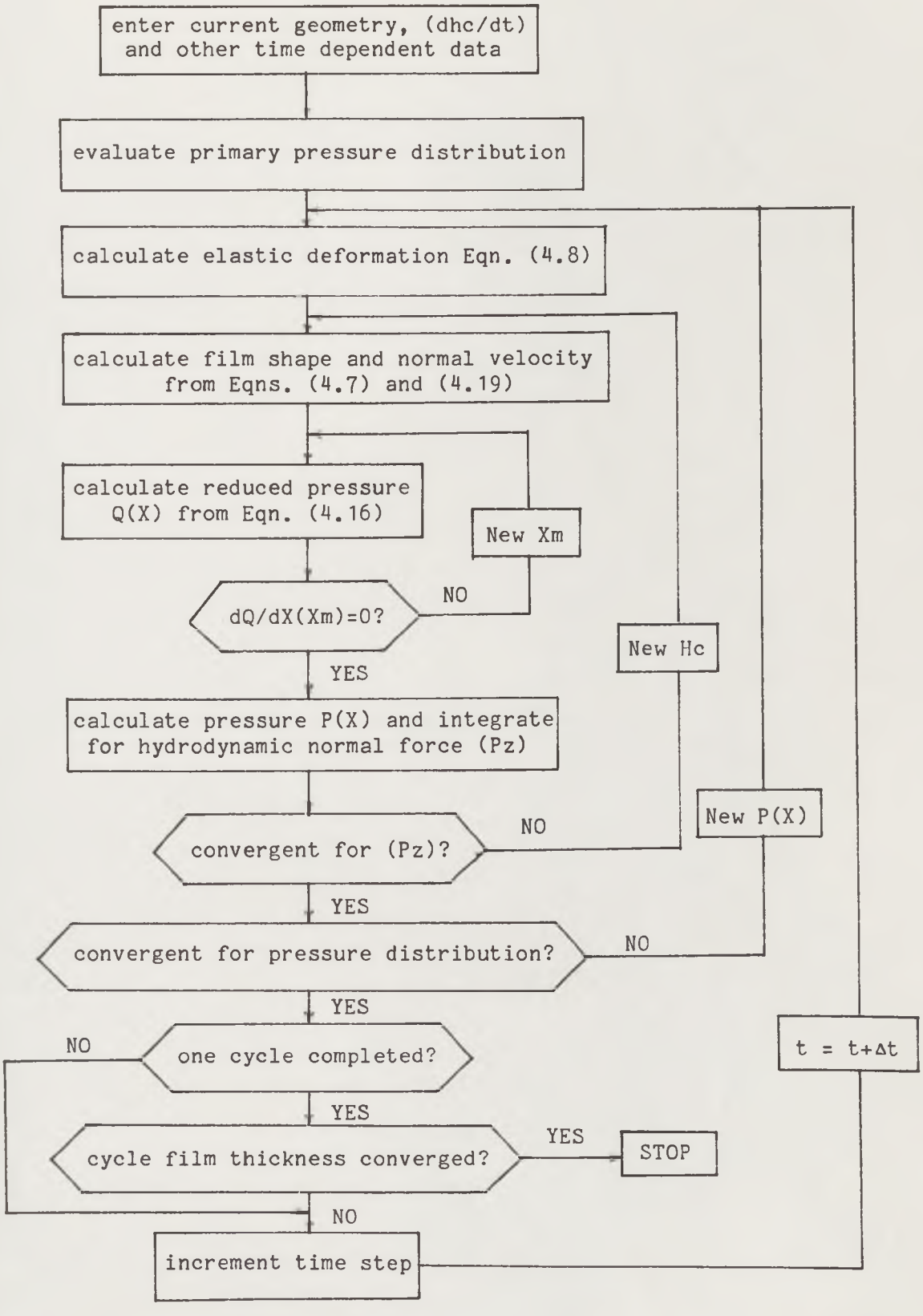

Figure (4.1) Flow chart of the straight forward iterative procedure for the transient elastohydrodynamic lubrication analysis of the cam and follower.

Cam action angle	60°
Base circle radius	25.0 mm
Maximum lift	9.4 mm
Cam width	20.0 mm
Spring stiffness	38.5 KN/m
Load at nose	240 N
Cam rotational frequency	50 Hz
Equivalent elastic constant of both surfaces (E')	2.3×10^{11} Pa
Lubricant viscosity (η_o)	0.01 Pas
Viscosity-pressure coefficient (α)	2.058×10^{-8} Pa^{-1}

The cyclic variations of the load parameter (W), speed parameter (U) and radius of cam curvature are presented in Figure (4.2) as a function of cam angle. In order to quantify the effects of surface elastic deformation and local squeeze velocity on the cyclic variations of the minimum film thickness and the pressure distributions four different analyses were undertaken. They were: (1) a transient rigid-isoviscous solution; (2) a transient rigid-piezoviscous solution; (3) a simple transient elastohydrodynamic solution with the assumption of constant normal velocity of ($\partial h_c/\partial t$) along the conjunction and (4) a full transient elastohydrodynamic solution by allowing the normal velocity to vary along the conjunction. Results are presented in Figures (4.3) to (4.7).

4.5 Discussion

4.5.1 Cyclic Variations of the Minimum Film Thickness

The cyclic variations of the minimum film thickness predicted by the four analytical procedures which are based upon the assumption that the cam and follower are always provided with a copious supply of lubricant, are shown in Figure (4.3). The film thickness variations of Figure (4.3) show the well known features, namely;

(1) Two portions of the cycle where substantial thicknesses of lubricant film are generated. These correspond to the rising and falling flanks of the cam where the entraining velocity of the lubricant into the contact and the contact effective radius of curvature are large.

(2) Two regions of extremely small film thickness at times when the entraining velocity of lubricant into the contact drops to zero for an instant (at cam angles of (−37.0°) and (37.0°)). On the basis of quasi-static analysis the minimum film thickness at these two points would be zero, however, here

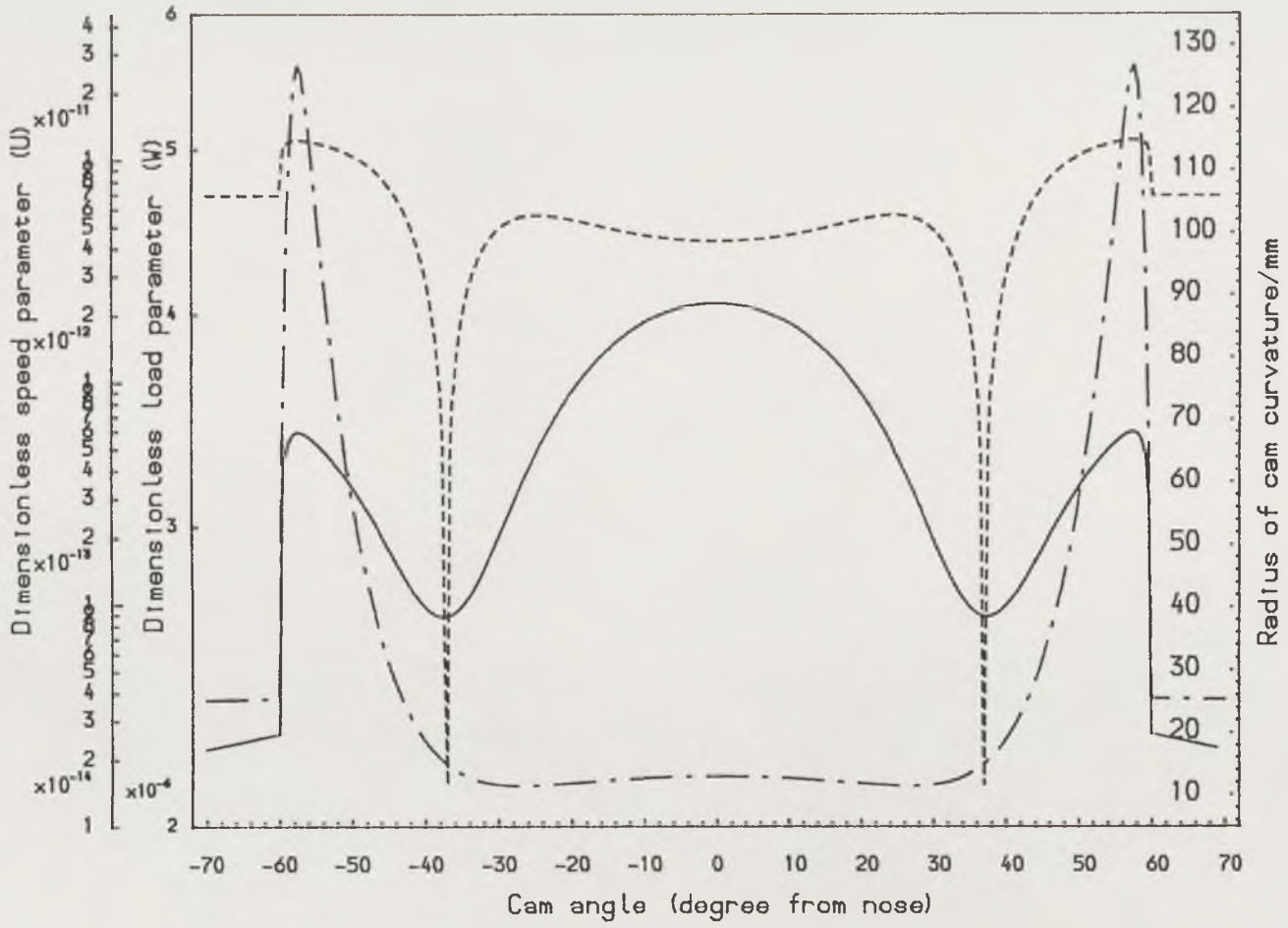

Figure (4.2) Cyclic variations of the load parameter, speed parameter and radius of cam curvature vas cam angle.

———— Dimensionless load parameter,

------- Dimensionless speed parameter,

—— · —— Radius of cam curvature.

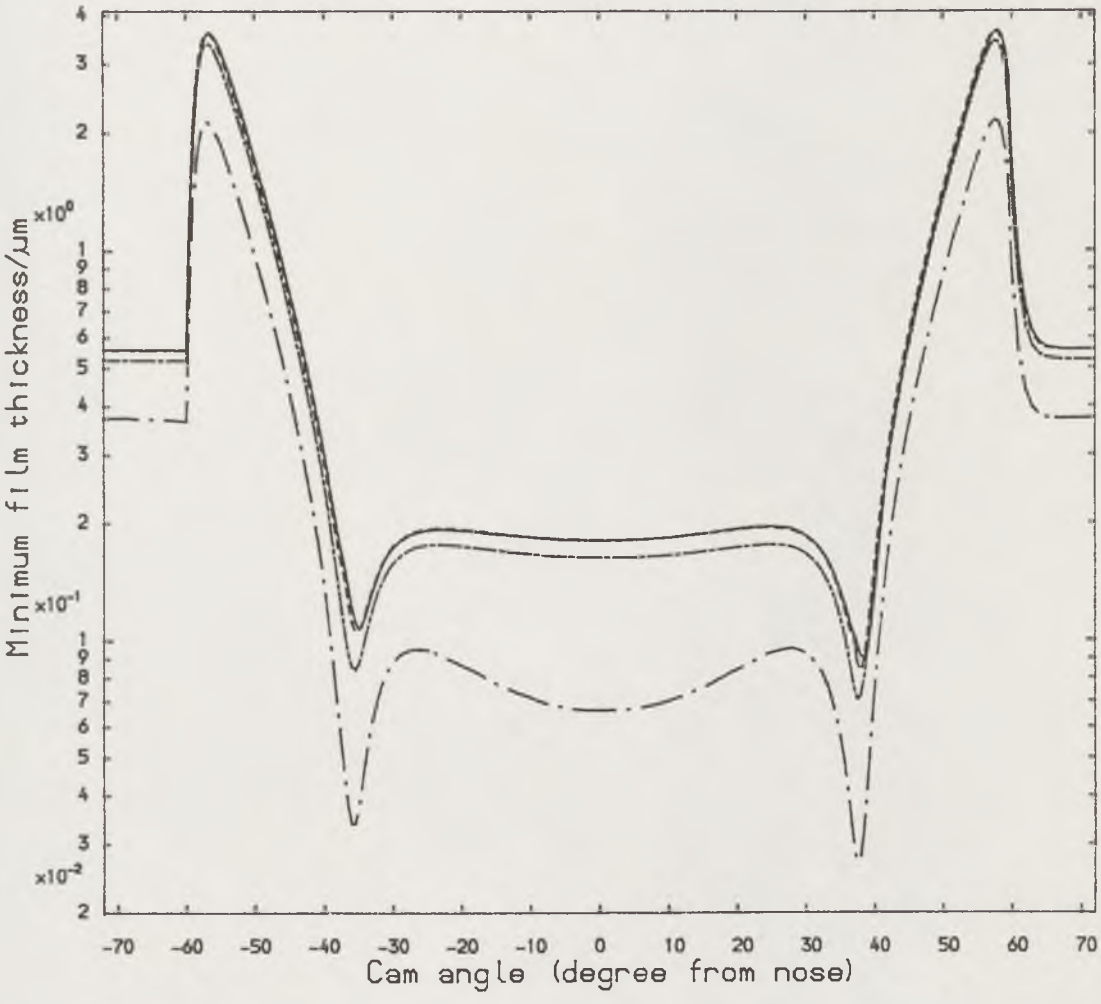

Figure (4.3) Cyclic variations of the minimum film thickness vs. cam angle predicted by four analytical procedures.

———— EHL solution (dh/dt) varies with x

-------- EHL solution (dho/ht) is constant along x

—·—·— Rigid-piezoviscous solution

——·——·— Rigid-isoviscous solution

the squeeze film analyses which have been undertaken reveal the protective action of squeeze film lubrication. The most interesting finding is that for all solutions depicted the film thickness on the rising flank, as the nose of the cam moves onto the follower, is greater than that as the nose leaves the falling flank. This is in agreement with the results according to the rough, rigid surface analysis detailed in Chapter (3) but contrary to the elastohydrodynamic analysis presented in the paper of Bedewi et al (1985). It is apparent that the lubrication conditions at both points of zero entraining velocity are dominated by the squeeze film action. Since the variations in the film thickness in the vicinity of the point of zero entraining velocity on the falling side of the cam are smaller than that on the rising side, which results in smaller squeeze velocities being generated, it seems to be more acceptable that the cycle minimum separation between the cam and the follower takes place in the region where the cam nose is leaving the falling flank. Furthermore, the experimental evidences detailed in Chapters (8) and (9), which confirms the finding from the present analysis, showed that the wear tracks found on the surface of the follower corresponded to the points during the cam cycle where the film thickness predicted by the lubrication theory were small. Two deeper marks corresponded to the points during the cycle where the cam and follower first make contact and where the entraining velocity of the lubricant into the contact drops to zero as the cam nose leaves the falling flank. The shallower marks corresponded to the position where the entraining velocity of the lubricant into the contact drops to zero on the rising flank and the point where the cam and follower separate. The reason why the opposite conclusion was reached by Bedewi et al may be due to the lack of consideration of a full cyclic prediction of the film thickness in their analysis.

(3) A period in the vicinity of contact of the cam nose where the minimum film thickness is small and fairly constant, corresponding to a region where the entraining velocity and cam radius are small and vary only slowly.

4.5.2 Local Squeeze Velocity Effects on Cyclic Variations of the Minimum Film Thickness

It can be seen in Figure (4.3) that the cyclic variations of the minimum film thickness predicted by the full transient elastohydrodynamic analysis lag the variations predicted by the rigid-piezoviscous solution. This implies that the local squeeze velocity produces an increased damping effect on the cyclic variation of the minimum film thickness. Furthermore, the squeeze film action plays a more important role in two regions of extremely small film thickness at times when the entraining velocity of lubricant into the

contact drops to zero for an instant. The variation of the minimum film thickness in the vicinity of zero entraining velocity as the cam nose is leaving the falling flank is presented in Figure (4.4). The minimum separation between the cam and follower and its position predicted by the four analytical procedures are summarized in Table (4.1).

The customary isoviscous analytical procedure throughout the cam cycle yields the lowest, long dotted, curve in Figure (4.4). The minimum film thickness predicted for this case occurs about (0.5°) behind the point of zero entraining velocity (at cam angle (37.0°)), and has a value of (0.0270 μm).

The influence of pressure upon viscosity has a significant effect upon film thickness predictions, even when the cam and follower are treated as rigid solids, as indicated by the short dotted line in Figure (4.4). The predicted minimum film thickness is increased by a factor about (2.6) to (0.0706 μm) which occurs at the same position as that from the rigid-isoviscous solution.

The predicted film thickness by a simple transient elastohydrodynamic analysis in which a constant normal velocity along the conjunction is assumed and the lubricant viscosity is allowed to vary with the pressure, is shown in Figure (4.4) in the form of the short-dashed line. This approximation yields a predicted minimum film thickness of (0.0832 μm), which is slightly greater than three times the value predicted in the rigid-isoviscous condition and occurs at the cam angle of (1°) behind the zero entraining velocity point.

In a full transient elastohydrodynamic lubrication analysis, in which normal velocity effects associated with both rigid body motion and local elastic deformations are taken into account and the lubricant viscosity is permited to vary with pressure, the predicted minimum film thickness is further increased to (0.0897 μm) as shown by the solid line in Figure (4.4). The minimum film thickness now occurs (1.5°) after the zero entraining velocity point. It is obvious that the combined effects of pressure upon lubricant viscosity, elastic deformation and local squeeze velocity contribute to a (3.6) fold increase in the prediction of this critical quantity. The gap between the short dotted curve and the solid curve is a measure of the beneficial effects of surface elastic deformation and local squeeze velocity action.

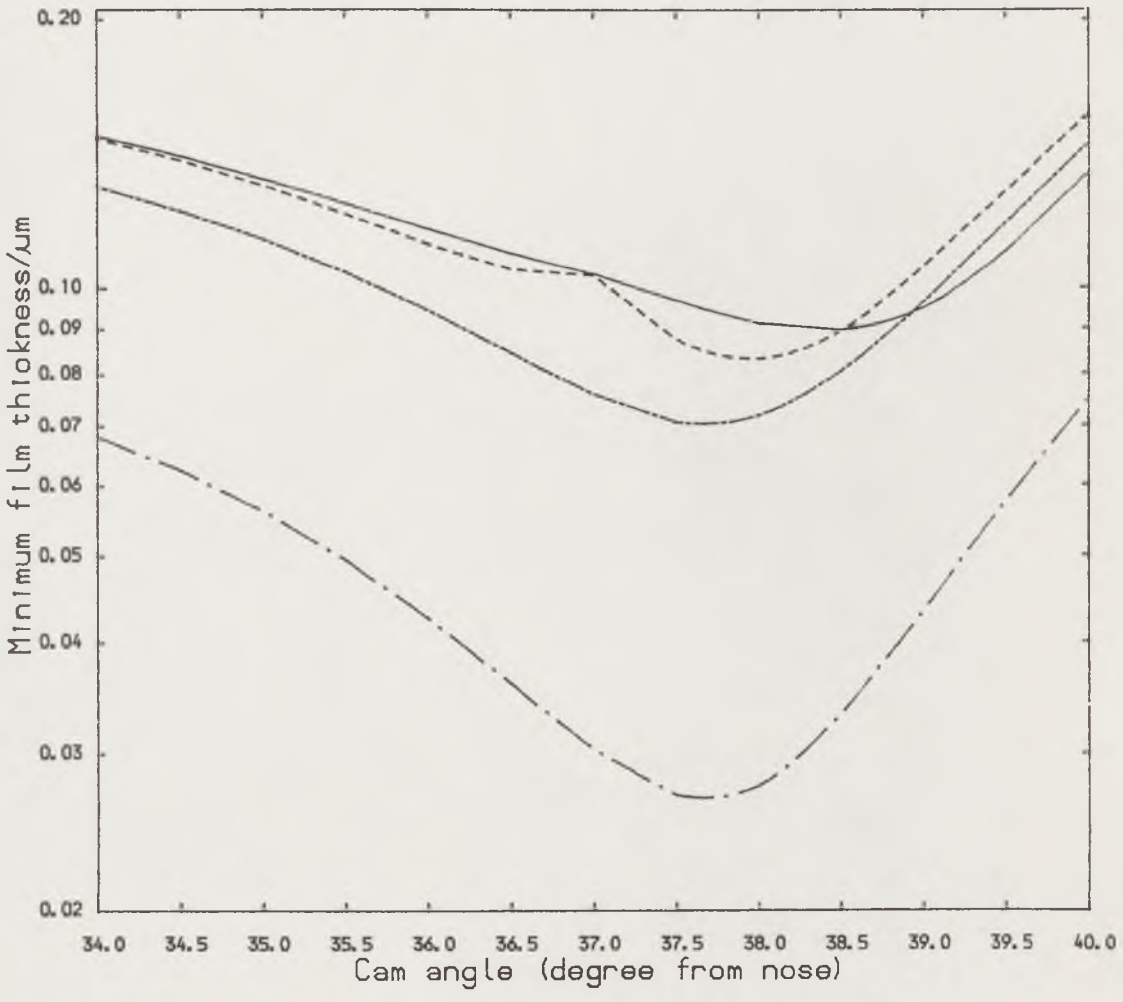

Figure (4.4) Comparison of variations of the minimum film thickness in the vicinity of the point of zero entraining velocity as the cam nose is leaving the follower.

———— EHL solution (dh/dt) varies with X,

- - - - - - - EHL solution (dho/dt) is constant along X,

—·—·—·— Rigid-piezoviscous solution,

—·—·— Rigid-isoviscous solution.

Table (4.1) The minimum separation between cam and follower and its position predicted by the four analytical procedures (on the cam falling flank side)

Analytical Procedures							minimum separation	
solid		normal	velocity	lubricant		h_{min}	cam angle	
rigid	elastc	const	varib	iso	v-p	(μm)	
*		*		*		0.0270	37.5°
*		*			*	0.0706	37.5°
	*	*			*	0.0832	38.0°
	*		*		*	0.0897	38.5°

Table (4.2) The minimum separation between cam and follower and its position predicted by the four analytical procedures (on the cam rising flank side)

Analytical Procedures							minimum separation	
solid		normal	velocity	lubricant		h_{min}	cam angle	
rigid	elastc	const	varib	iso	v-p	(μm)	
*		*		*		0.0339	-36.0°
*		*			*	0.0842	-35.5°
	*	*			*	0.1057	-35.5°
	*		*		*	0.1074	-35.0°

Table (4.3) The minimum film thickness on cam nose predicted by the four analytical procedures

Analytical Procedures							minimum separation	
solid		normal	velocity	lubricant		h_{min}	cam angle	
rigid	elastc	const	varib	iso	v-p	(μm)	
*		*		*		0.0663	0.0°
*		*			*	0.1621	0.0°
	*	*			*	0.1796	0.0°
	*		*		*	0.1795	0.0°

Similarly, Figure (4.5) shows the variation of the minimum film thickness in the region of zero entraining velocity on the rising flank side of the cam (at cam angle (−37.0°)). A close study reveals that similar situations exist to those described above, but the position where the minimum quantity occurs lags more from the zero entraining velocity point with phase lags of (1.0°), (1.5°), (1.5°) and (2.0°) respectively. The predicted minimum film thickness and its location based upon the four analytical procedures are summarized in Table (4.2). A significant variation in predicted minimum film thickness is shown for the four different approaches with viscous damping acting to reduce the effects of the variations of load, speed and geometry giving rise to enhanced film thicknesses. A further increase in predicted film thickness occurs when elastic effects are taken into consideration.

For the purpose of comparison, the minimum film thicknesses on the cam nose (at (0°) cam angle) predicted by the four analytical procedures are recorded in Table (4.3). The elastohydrodynamic analysis yields a minimum film thickness which is greater than (2.7) times that predicted by the transient rigid-isoviscous analysis. On the other hand, the comparison between the results of two elastohydrodynamic analyses shows that there is almost no difference. This is due to the slow variation of the entraining velocity and radius of cam curvature which leads to less significant variation of the squeeze film action existing at this instant.

4.5.3 Variations of Film Shape, Pressure Distribution and Normal Velocity in the Vicinity of Zero Entraining Velocity Points

The variations of the film shape, pressure distribution and normal velocity along the conjunction between the cam and follower in the vicinity of the two zero entraining velocity points are presented in Figures (4.6) and (4.7). The results predicted by the two elastohydrodynamic analytical procedures are plotted together. Figure (4.6) shows the variations of the film shape, normal velocity and pressure distribution with (0.5°) increments from a cam angle of (−38.0°) to (−34.5°) on the rising flank side of the cam. The variations of the film shape, pressure distribution and normal velocity between the cam angle of (36.0°) and (39.5°) on the falling flank side are presented in Figure (4.7).

These figures show that at the beginning of the cam moving toward the point of zero entraining velocity the film shape looks similar to its undeformed parabolic shape with the position of minimum film thickness shifted away from the centre of the conjunction towards the exit region (see

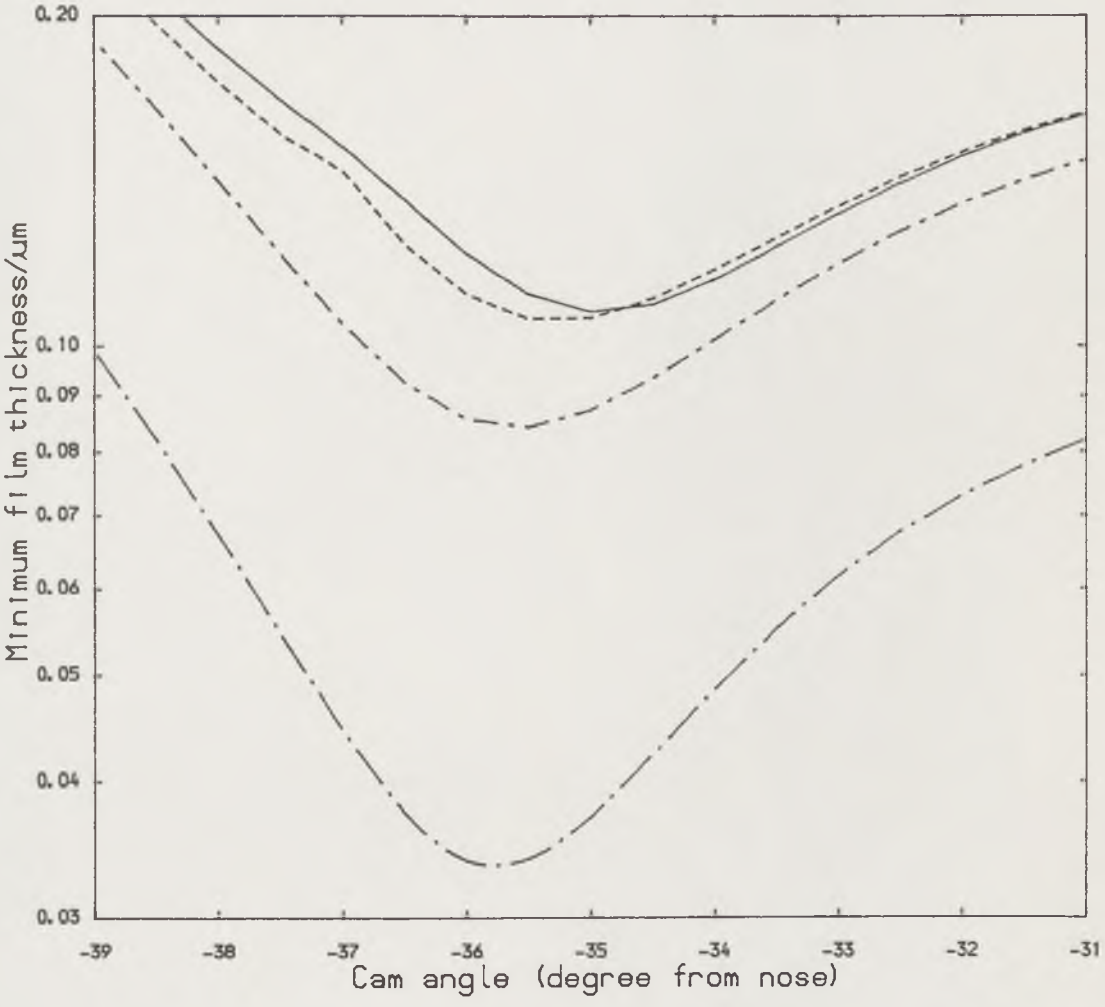

Figure (4.5) Comparison of variations of the minimum film thickness in the vicinity of the point of zero entraining velocity as the cam nose is approaching the follower.

———— EHL solution (dh/dt) varies with X,

- - - - - - - EHL solution (dho/dt) is constant along X,

—·—·— Rigid-piezoviscous solution,

——·—— Rigid-isoviscous solution,

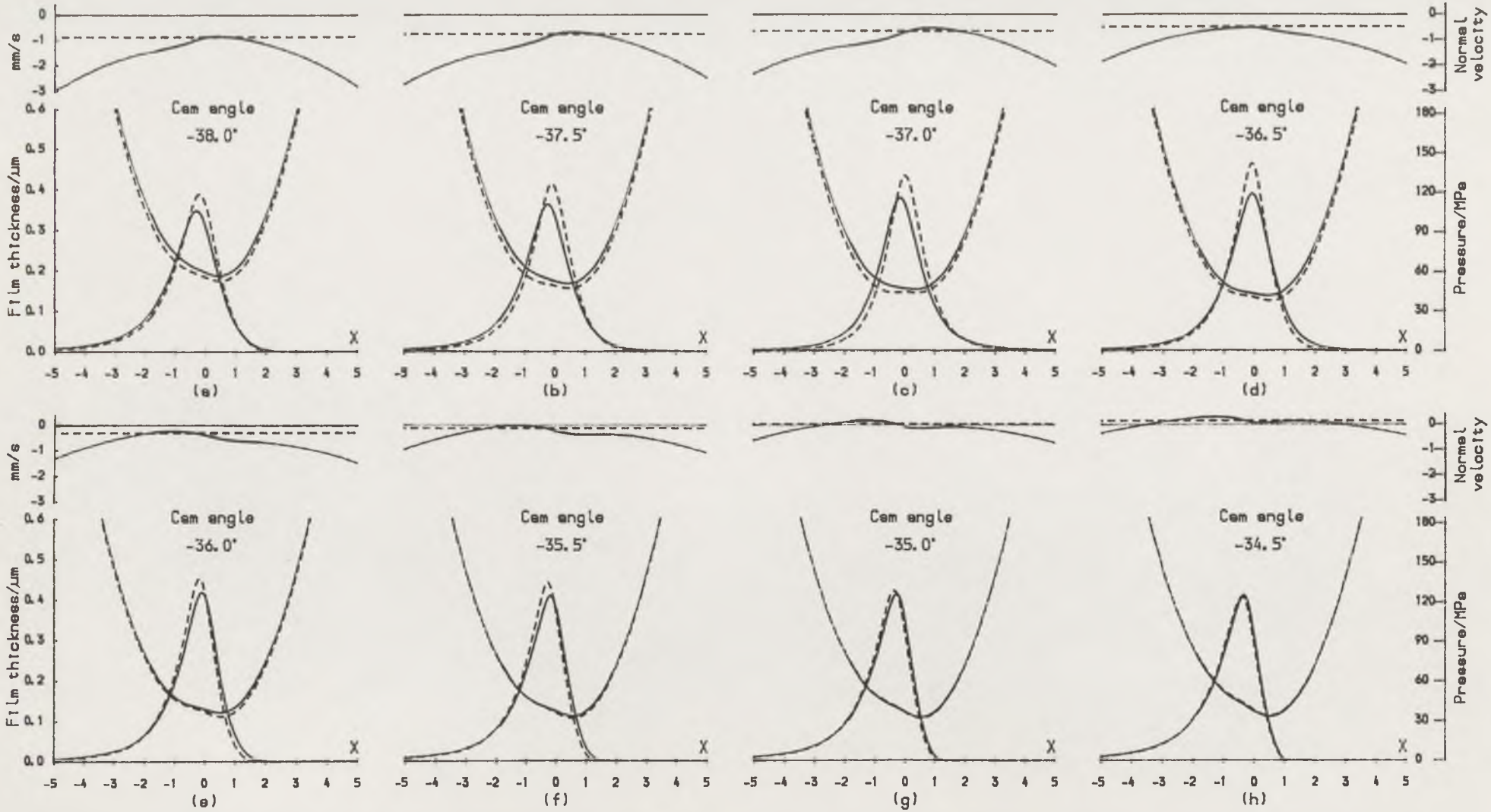

Figure (4.6) Variations of the film shape, pressure distribution and normal velocity in the vicinity of the point of zero entraining velocity as the cam nose is approaching the follower.
(——— Normal velocity varies with X, ----- Normal velocity (dho/dt) is constant along X.)

Figure (4.6 (a) and (b)) and Figure (4.7 (a)). As the cam moves closer to the zero entraining velocity point, the central region of the conjunction is gradually flattened by the increasing fluid pressure and consequently a dimple appears in the central region which is a typical phenomenon caused by strong squeeze film action (see Figure (4.6 (c))) and Figure (4.7 (c), (d) and (e)). A constriction appears as the cam travels beyond the zero entraining velocity point. This phenomenon appears more clearly in Figure (4.7) and is due to the increase of the entraining velocity. The comparison of the results of the two elastohydrodynamic analytical procedures shows that the influence of the variation of normal velocity along the conjunction has significant effects not only on the values of minimum film thickness but also on the film shape and pressure distribution. It is interesting to note that at the instant of zero entraining velocity, the simple transient elastohydrodynamic solution which is based upon the constant normal velocity assumption predicts a symmetrical pressure distribution and film shape with the maximum fluid pressure and a dimple appearing in the centre of the conjunction, while the variable normal velocity elastohydrodynamic analysis gives an asymmetrical pressure distribution and film shape in which a shallower dimple forms in the central region and a constriction appears in the exit region of the conjunction. From Figures (4.3) and (4.7 (c)) it can be seen that the film shape and the pressure distribution are substantially different, even though the two elastohydrodynamic analytical procedures predict the same minimum film thickness at this instant.

The variations of the normal velocity presented in Figures (4.6) and (4.7) show that the negative normal velocity which enhances the hydrodynamic effects is found in most of the instances as the cam nose moves onto the follower (see Figure (4.6)). However, the positive normal velocity which weakens the hydrodynamic effects dominates the instances as the cam nose leaves the follower (see Figure (4.7)). This explains the reason why the cyclic minimum film thickness should occur in the region where the cam nose leaves the falling follower but not on the rising side of the cam.

In case of the cam approaching the follower (negative normal velocity) elastohydrodynamic analysis based upon the assumption of variable normal velocity shows that the pressure curve and its peak shift more from the centre of the conjunction toward inlet than those predicted with the assumption of constant normal velocity, whilst, as the cam is separating from the follower (positive normal velocity) the reverse phenomena are found.

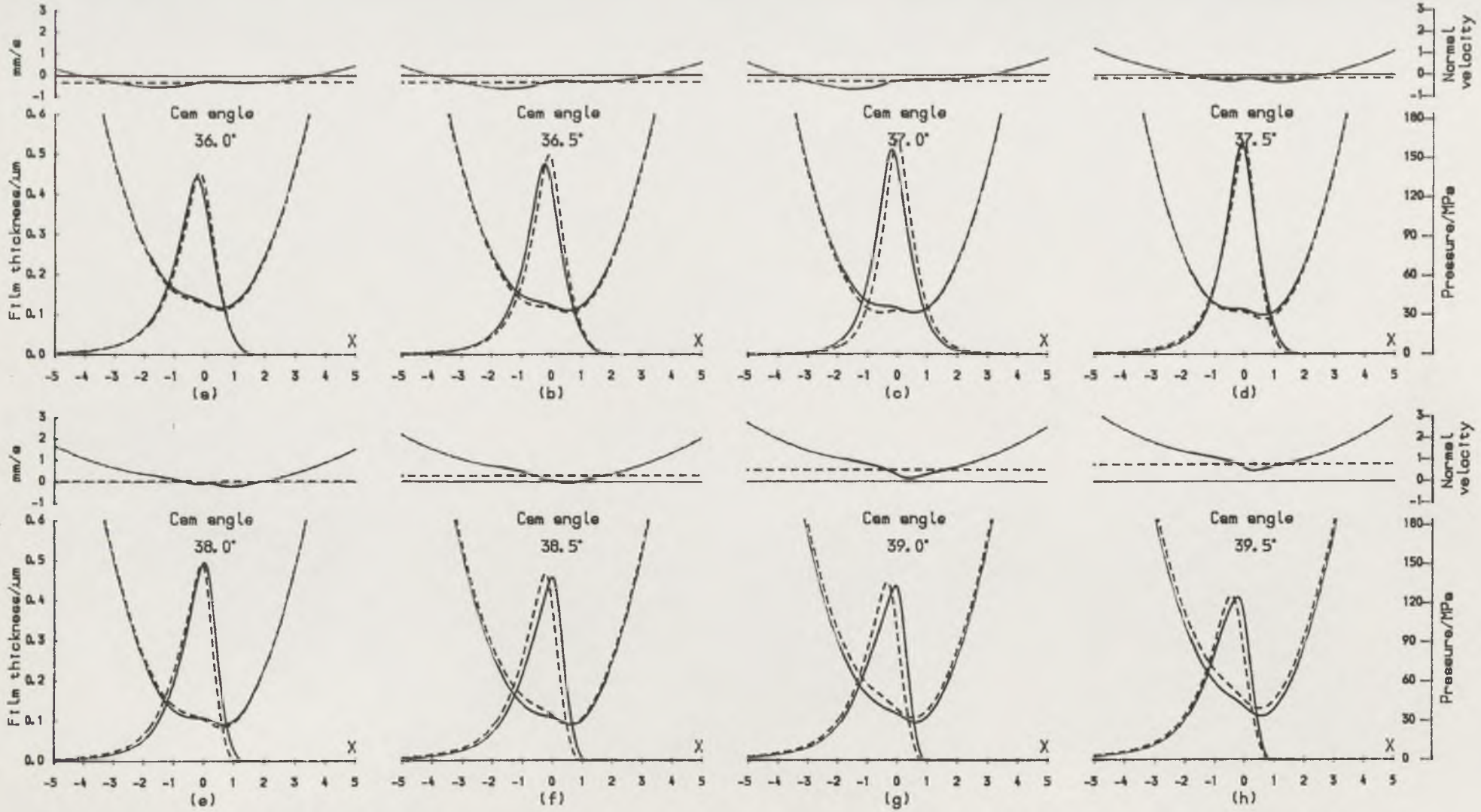

Figure (4.7) Variations of the film shape, pressure distribution and normal velocity in the vicinity of the point of zero entraining velocity as the cam nose is leaving the follower.
(——— Normal velocity varies with X, ----- Normal velocity (dho/dt) is constant along X.)

4.6 Conclusions

A full transient elastohydrodynamic lubrication analysis, allowing the normal velocity to vary throughout the conjunction, has been accomplished for a modified cam and flat faced follower arrangement. This is the first time that such an analytical procedure has been applied to the cam and follower arrangement. At the same time, for the purpose of comparison, a simple transient elastohydrodynamic analysis, a rigid-piezoviscous analysis and a rigid-isoviscous analysis have also been undertaken for the same cam and follower. The general conclusions which can be reached from the results of the analyses are as follows;

(1) The cyclic variations of the minimum film thickness predicted by the full transient elastohydrodynamic analytical procedure show the general features which include (a) two portions of the cycle where substantial thicknesses of lubricant film are generated, (b) two regions of extremely small film thickness in the vicinity of the point of zero entraining velocity and (c) relatively small but fairly constant minimum film thickness existing in cam nose region. These effects are similar to those predicted by rigid isoviscous analysis but reveal greater values of film thickness.

(2) With the full transient elastohydrodynamic analysis it has been demonstrated that the cycle minimum film thickness occurs in the region where the entraining velocity of lubricant into the contact drops to zero as the cam nose leaves the follower.

(3) The local squeeze velocity which relates to the elastic deformation of the surfaces provides an increased damping effect which contributes to the maintenance of the persistence of the cyclic minimum film thickness particularly in the two critical parts of the cam cycle where the entraining velocity drops to zero.

(4) The comparison of the results of the two elastohydrodynamic analytical procedures has shown that the influence of the variation of the normal velocity along the conjunction has significant effects not only on the value of the minimum film thickness but also on the film shape and hydrodynamic pressure distribution in the conjunction between the cam and follower.

CHAPTER 5

AN APPROXIMATE SOLUTION OF TRANSIENT ELASTO-HYDRODYNAMIC LINE CONTACT AND ITS APPLICATION TO THE MIXED LUBRICATION ANALYSIS OF A CAM AND FOLLOWER

5.1 Introduction

The discovery that the combined effects of elastic deformation and increased viscosity under pressure can result in a continuous oil film in a heavily loaded rolling and sliding contact has had an important influence upon the study of lubrication and wear since the 1960s. The complete solution of the theoretical problem requires a simultaneous solution to the equation governing the elastic deformation of the surface and hydrodynamic equation which is made non-linear by the dependence of viscosity upon pressure. Due to this nonlinearity, an analytical solution is not possible and most approaches use numerical procedures. Despite the apparent simplicity of the equations, this is not an easy task. The numerical methods developed so far are rather complex, operator dependent, and often at variance with each other in detail, especially in the case of moderate to heavy loadings and therefore not easy to repeat. For many years a considerable attention has been concentrated to pursue a numerical solution of steady state elastohydrodynamic line contact, while, comparatively speaking, very little attention has been directed to the influence of combined entraining and normal motion upon the elastohydrodynamic line contact problem.

An early attempt was made by Wada and Tsukijihara (1978) who presented a numerical solution to the elastohydrodynamic squeeze film problem of two rotating cylinders. The solution simultaneously satisfied the governing elastic and hydrodynamic equations for a fixed maximum pressure and exit film thickness. Reynolds equations for both Newtonian fluids and a Bingham solid lubricant were solved under fully flooded and starved conditions. The results showed that entrapment of the lubricant occurred in the central region of the conjunction as the approach velocity increased. Since the load parameter, speed parameter and ratio of normal velocity to entraining velocity adopted in their analyses were too far removed from those encountered in physical situations, it is quite difficult to apply these findings to practical use.

Under more realistic conditions, Bedewi et al (1985) explored the general features of an elastohydrodynamic line contact subjected to both normal and entraining velocity. The time histories of both central and minimum film thickness under constant and sinusoidal normal loading were considered. The problem here was the substantial computer time required for a full

elastohydrodynamic type solution which makes it difficult to apply such an analysis for design purposes.

By using a straight forward iterative procedure, Wu and Yan (1986) accomplished a full numerical solution to the elastohydrodynamic line contact in combined entraining and normal motion. This revealed that under the conditions of combined rolling and squeeze motion a dimple formed in the central region and a constriction appeared in the exit region. The depth of the dimple depended upon both entraining and approaching velocity, while in combined motions of entraining and separating the central region became flatter than that under steady state conditions. When the squeeze velocity decreased, the position of maximum pressure moved towards the exit and a pressure spike appeared. The parameters adopted in their analyses were similar to those corresponding to a polymer lubricated by a mineral oil or a metal lubricated by a fluid of low pressure-viscosity index. Here the problem encountered again was the difficulty of obtaining convergent results at heavy loads or high material parameters. Therefore, a reasonable simplified method for estimating a transient elastohydrodynamic line contact has been required for many years.

The earliest simple concept in the analysis of steady state elastohydrodynamic line contact came from the work of Grubin (1949): that in order to carry a very high load, the pressure must be high, and so the viscosity, by virtue of Barus pressure-viscosity relationship must be enormous. According to satisfying Reynolds equation;

$$\frac{dp}{dx} = 12\,\eta\,u\,\left(\frac{h - h_0}{h^3}\right)$$

the film thickness must be almost equal to (h_0), and so be almost constant over an appreciable distance. Thus if we take the surfaces to have the deformed shape of an unlubricated contact, as given by Hertz's theory, but moved apart by a fixed displacement (h_0), we shall get a good approximation to the actual conditions in a lubricated contact. Based upon the above assumptions Grubin calculated the film thickness. The values obtained were much greater than the classical ones, but agreed reasonably well with numerical results which have subsequently appeared. However, because of the geometrical symmetry of this model, it is unable to reproduce unsymmetrical effects such as the pressure spike and oil film constriction in the exit region which are the characteristic features of the computer

based numerical elastohydrodynamic model. Aware of the fact that a steep pressure spike occurred in the exit region of contact, Grubin used the picture of a rigid stamp with a segment cut away to illustrate his argument for arriving at this conclusion, but he never developed this idea of a modified stamp into a quantitative model for the outlet condition in elastohydrodynamic line contact.

In fact Greenwood (1972) showed that these features can be generated analytically by simply moving the parallel section of the contact to an off-centre position. A pressure distribution was needed to cancel the additional term in the film thickness equation caused by the off-central position. After deducing this elastic pressure distribution, he obtained the film shape outside the flattened region. The central film thickness was evaluated by the Grubin formula. Hydrodynamic effects in the inlet and exit regions were neglected.

A few years later, in an attempt to improve on some of the weaknesses of Grubin model and at the same time to retain much of the simplicity of this model, Christensen (1979), following Grubin's idea gave a simplified model for the solution of elastohydrodynamic line contact. The model, although a significant step in the direction of providing a semi-analytical approximate workable model of the elastohydrodynamic line contact, suffered from two major shortcomings. Firstly, like the Grubin model, the inlet to the contact based upon the assumption of ignoring the pressure of the lubricant was poorly modelled. Secondly, the load associated with the pressure tails in the inlet and exit, and the local deformations caused by these tails were not considered in the model. At first sight, this method seems to be different from Greenwood's, but mathematically these two methods are the same and produce similar results.

By assuming the end of inlet region is at the position where the ratio of pressure flow to shear flow is less than one percent, Prakash and Christensen (1981) overcame the shortcomings mentioned above by connecting the inlet region and exit region in the iterative procedure for the offset value of (e), so that a semi-analytical approximate method for the steady-state elastohydrodynamic line contact was completed. Due to Grubin's assumptions and the equation adopted for calculating the value of (e) being inappropriate for extreme conditions this method can only produce reasonably approximate results under moderate load conditions, but failed to

offer satisfactory approximate results at light loads and high speeds or at extremely heavy loads and low speeds.

The applicability of this model was further extended by Tonder and Christensen (1981) to include near hydrodynamic cases with or without viscosity-pressure variations. Although convergent results were obtained under extreme elastohydrodynamic conditions, the authors suggested that as the program would not be convergent in the near-hydrodynamic field, the results of extremely high load elastohydrodynamic condition might be coincidental. Consequently, the results published in their paper were all known elastohydrodynamic cases.

Furthermore the influence of surface roughness and its orientation on partial elastohydrodynamic lubrication of rollers was investigated by Prakash and Czichos (1983) who introduced average flow factors developed by Patir and Cheng (1978) into this approximate model.

To overcome the difficulties involved in the numerical analysis of the transient elastohydrodynamic line contact several attempts have been made to achieve some kinds of approximate evaluations. Perhaps the most rigorous treatment of transient elastohydrodynamic lubrication analysis to date has been presented by Vichard (1971). A Grubin type assumption was made for film shape and pressure distribution. The dynamic variations in load, entraining velocity and surface curvatures were included in the analysis.

Holland (1978) deduced a formula whereby the minimum film thickness in a transient situation including the distortion of the surfaces was estimated by superposition of an expression for the rolling term (Dowson and Higginson (1966)) and an expression for the squeeze term (Herrebrugh (1970)). The sum of the load capacities of the two terms was equivalent to the load acting on the cylinders. The proportion of the load capacity shared by each term was assumed to be the same as that under lubricated rigid contact condition. The formula was then applied to a cam and follower analysis in which the separation effect was neglected. Although the work presented by Holland gave a better insight into the lubrication of a cam and follower than any previous steady state solutions, some of the basic assumptions behind the analysis were incorrect. The final solution for the change in film thickness cannot be derived from a simple summation of the separate squeeze and entraining actions. Work by Bedewi et al (1985) (see Chapter

(2)) suggested that the cyclic variation in film thickness is considerably less than that predicted by Holland's formula.

On the other hand, the Grubin type assumption was still adopted by some authors to evaluate the transient elastohydrodynamic lubrication problem. Wang and Cheng (1981) incorporated Vichard's analysis into a model for the lubrication analysis of an involute spur gear, in which dynamic loading and thermal effect as well as the flash temperature were considered. Even though the work of Wang and Cheng is probably the most complete analysis of gear lubrication to date, considerable research is still required to verify their findings.

Lin and Medley (1984) performed an analysis which considered the lubrication of involute spur gears under isothermal conditions. The calculation of transient elastohydrodynamic line contact was performed by using the method of Vichard (1971) with an additional term to account for the variation in surface curvature in the inlet region of the contact at each instant throughout the meshing cycle. This geometrical modification resulted in a variable entraining velocity in the inlet region, which in turn leads to the term (du/dx) being retained in Reynolds' equation. The proposed modification of the geometry showed that under certain circumstance a significant influence upon the film thickness could be expected.

The most suitable application of the Grubin type assumption may be to the solution for a 'soft' elastohydrodynamic line contact problem. Medley and Dowson (1984) developed a simplified method by introducing a plane inclined surface slider bearing model based upon the notional length of Herzian contact zone. This approach was applied to the analysis of the lubrication of compliant layer surfaces as part of a study of a human ankle joint which was subjected to cyclic time-varying loads and entraining velocities. A resonable prediction of the variation of the film thickness during the walking cycle was achieved.

To surmount the weakness of losing the constriction in the exit region due to the adoption of Grubin assumption, an approximate technique has been developed in this chapter for estimating the minimum film thickness of the transient elastohydrodynamic line contact, in combined entraining and normal motion conditions. The reliability of the approximate technique has been verified by comparing its results to those predicted by the full

numerical analysis under the same transient conditions. Subsequently, the mixed lubrication model developed by Patir and Cheng (1978) is introduced into this approximate technique which, in turn, is applied to predict the cyclic variations of the minimum film thickness between a cam and follower. The investigations have been concentrated on the influence of the surface roughness upon the cyclic variations of the minimum film thickness and the lubrication conditions between the cam and follower.

5.2 Theoretical Basis of the Approximate Technique

As described in the last section, in order to evaluate the tribological performances of heavily loaded lubricated contacts, such as those encountered in gears and cams and followers, an approximate technique which can provide a convenient approach to estimate the minimum film thickness is required. As the solution procedure of the present approximate technique for rough cylinders is similar to that for the smooth ones, for simplification, the introduction given in this section mainly follows the procedure for the solution of smooth cylinders. The solution process of the approximate technique by taking the surface roughness effects into account is also briefly described. Unless otherwise specified, the notation and dimensionless groups adopted in this chapter are the same as those listed in the Nomenclature and Chapter (4).

5.2.1 Basic Assumptions

The full transient elastohydrodynamic lubrication analysis of the cam and follower presented in Chapter (4) revealed an unsymmetrical pressure distribution and film shape at the instant of zero entraining velocity. A shallower dimple formed in the central region of the conjunction and a constriction appeared in the exit region. This implied that the effect of the variation of the normal velocity along the conjunction was equivalent to adding an entraining velocity effect to a pure squeeze motion having constant normal velocity along the conjunction. In addition, the full numerical analysis to the transient elastohydrodynamic lubrication of line contact performed by Wu and Yan (1986) showed that in case of combined motion of entrainment and separation the central region of the conjunction became flatter than that encountered with entraining motion alone. Consequently, it is supposed that the elastic deformation of the two cylinders in combined entraining and normal motion is dominated by hydrodynamic pressures arising from entraining effects. In other words, the elastic

deformation of the cylinders in a non-steady state lubricated contact is assumed to be of the same form as that in a steady state lubricated contact in which there is a constriction in the exit region and a constant separation between the two cylinders in the central region. The film shapes predicted by the full transient elastohydrodynamic lubrication analysis showed that no matter what the normal velocity was, there was always a constriction in the exit region of the conjunction (see Chapter (4)). Thus the main feature of the elastohydrodynamic line contact is retained in the present approximate model. Although the dimple in the central region of the contact, which appears only in conditions of high approaching and low entraining velocity, cannot be generated by the model, it might be expected that the influence of this omission upon the values of the minimum film thickness can be neglected.

5.2.2 Generating the Elastic Deformed Shape of Smooth Cylinders

Based upon the main assumption which has been made above, the simplified model developed by Prakash and Christensen (1980) for the solution of the steady state elastohydrodynamic line contact problem has been adopted to generate the geometric shape of the conjunction between the two cylinders in combined entraining and normal motion. Since the method adopted by the authors for estimating the offset value (e) was unable to give a convergent result under extremely highly loaded conditions, some modifications have been made to the solution procedure in the present approximate technique.

The geometry of the model is shown in Figure (5.1a). It consists of a rigid flat stamp modified by cutting a segment of one end which is to represent the exit of the elastohydrodynamic contact. The stamp is now considered to be pressed into a cylindrical block of elastic material of equivalent elastic constant (E') and radius (R), with a load (w_i). For the purpose of analysis, this block of material is assumed to be semi-infinite. The resulting stress and deformation fields are calculated. The stress and deformation in the centre of the contact region are assumed not to be influenced by the pressure of the lubricant which is to be found in an elastohydrodynamic contact.

The equation for a (parabolic approximation) cylinder with the centre placed at a distance (l_1) from the origin of x-coordinate in Figure (5.1a) is;

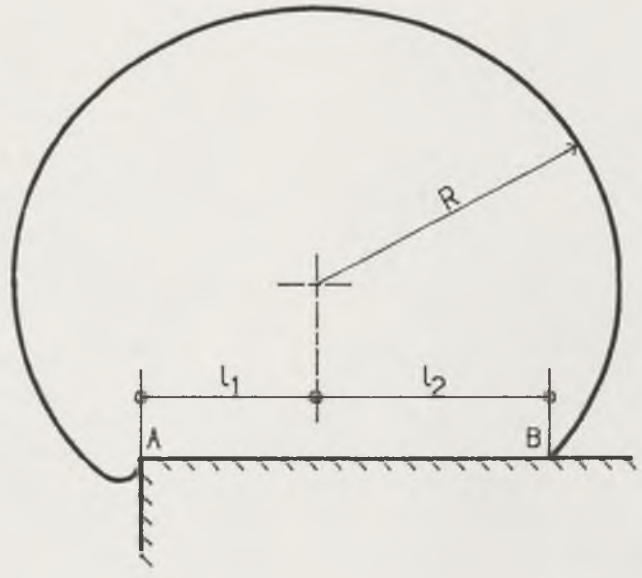

Figure (5.1a) Surface pressure generating stamp.

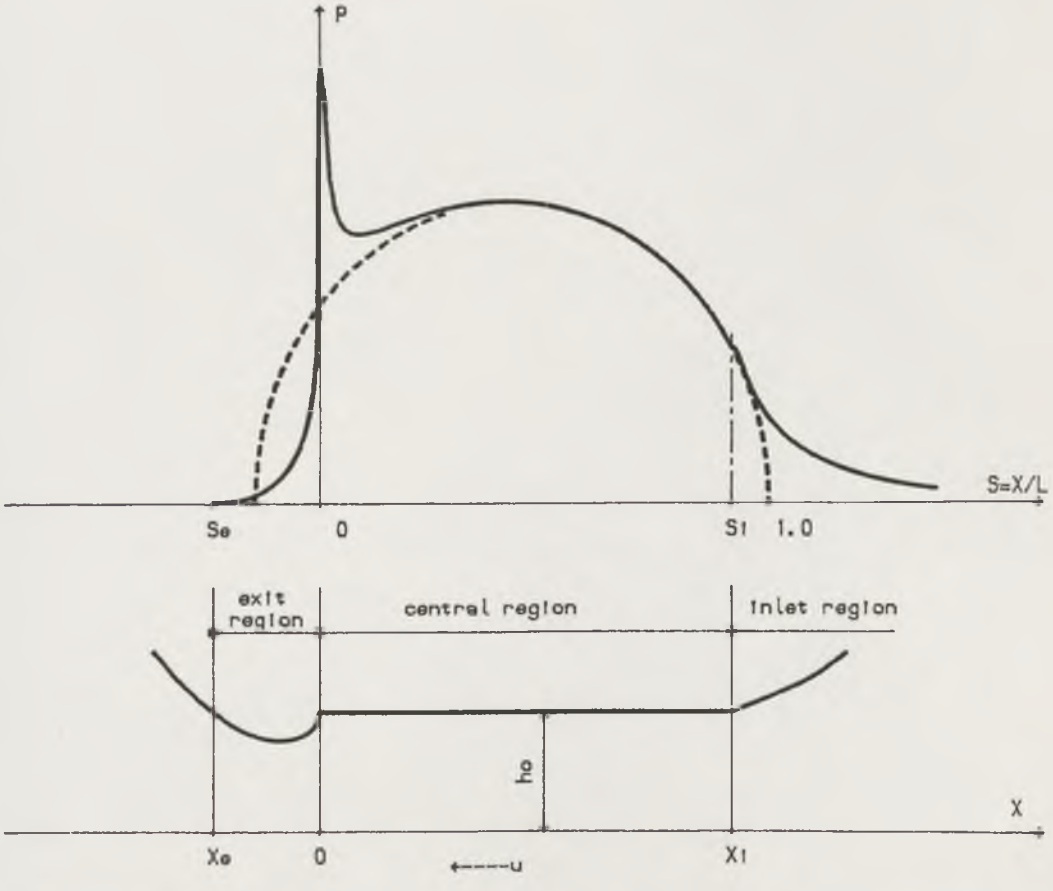

Figure (5.1b) A schematic of inlet, exit and central regions in an elastohydrodynamic line contact.

$$V_1(s) = \frac{L}{2R}\left[(0.5 - e)^2 - 2(0.5 - e)s + s^2\right] \qquad (5.1)$$

Where offset value (e) is defined as;

$$l_1 = (0.5 - e)\,L \qquad (5.2)$$

The quantity (e) is a measure of how much (l_1) is shorter than half of the total contact length (L). (l_1) is the coordinate of the cylinder centre. (L) is the coordinate of the other boundary of the contact and equals to the sum of (l_1) and (l_2). By making the total contact length (L) correspond to unity and letting

$x = L\,s$ and $z = L\,t$

if (t) is greater than zero and less than unity, we have

$x = z$ and $s = t$

If the loading is created by pressing a stamp of the form shown in Figure (5.1a) into an elastic cylindrical block and assuming the contact is generated over the arc from (A) to (B), the surface pressure distribution in the central region can be expressed in the form;

$$\alpha p(t) = y(t) = \frac{GL}{4R}\sqrt{t(1-t)}\left(1 + \frac{e}{t}\right) \qquad \text{for } 0 < t < t_i \qquad (5.3)$$

The elastic load per unit length is given by the integral of the surface pressure. Thus;

$$\alpha w_i = \int_0^L \alpha p(x)\,dx = L\int_0^L y(t)\,dt = \frac{\pi G L^2}{32R}(1 + 4e) \qquad (5.4)$$

and we have $\left(\frac{L}{R}\right)^2 = \frac{32\,W_i}{\pi(1+4e)}$, where $W_i = \frac{w_i}{E'R}$.

The surface displacement corresponding to the surface pressure given by equation (5.3) in the central region is;

$$V(s) = \frac{2L}{GR}\int_0^1 \sqrt{t\,(1-t)}\;\left(1 + \frac{c}{t}\right)\ln(s-t)^2\,dt + C$$

Thus the separation between a cylindrical surface and the deformed surface outside the contact region can be written as;

$$H(s) = V_1(s) - V(s) + C$$

Considering the constant as (H_o) and non-dimensionalizing the separation with (R) gives the expression for the film thickness;

In the inlet region (s > 1);

$$H(s) = \left(\frac{L}{R}\right)^2 \left[\frac{2s-1-4e}{4}\sqrt{s(s-1)} - \frac{1}{8}\ln[2s-1+2\sqrt{s(s-1)}] - e\ln(\sqrt{s}-\sqrt{s-1})\right] + H_o \qquad (5.5)$$

In the exit region (s < 0);

$$H(s) = \left(\frac{L}{R}\right)^2 \left[\frac{1-2s+4e}{4}\sqrt{s(s-1)} - \frac{1}{8}\ln[1-2s+2\sqrt{s(s-1)}] - e\ln(\sqrt{-s}+\sqrt{1-s})\right] + H_o \qquad (5.6)$$

In the central region ($0 \leq s \leq 1$);

$$H(s) = H_o$$

Figure (5.1b) presents a schematic diagram for the various regions. It can be seen that the lubricated region is divided into three parts: inlet region, central region and exit region. At first solutions are performed in each region separately, and then are connected together by an iterative procedure for convergent values of (H_o) and (e). The iterative procedure for generating the deformed shape of cylinders is outlined in the flow chart of Figure (5.2) which shows that there are four loops which are: inlet loop, exit loop, inlet and exit iterative loop and elastic load loop.

The first loop is the inlet loop. As the lubricant flow is almost entirely determined by the shear flow component in the central region, so that the point (s_i) at which the ratio of the pressure flow to the shear flow is less than one percent is chosen as the end of the inlet region, which means;

$$\frac{h_o^2}{12\eta u}\frac{dp}{dx} = \left(\frac{h_o}{R}\right)^2 \frac{e^{(-\alpha p)}}{12UG(L/R)}\frac{dy}{dt} < 0.01 \qquad (5.7)$$

The value of (s_i) is always less than or equal to unity. In the inlet region, viscosity effects are as important as elastic effects, therefore Reynolds' equation and the elastic deformation equation should be considered simultaneously. The Reynolds' equation for no side leakage is;

$$\frac{dp}{dx} = -12\,\eta\,u\,\frac{h-h_o}{h^3}$$

the boundary conditions on the pressure are;

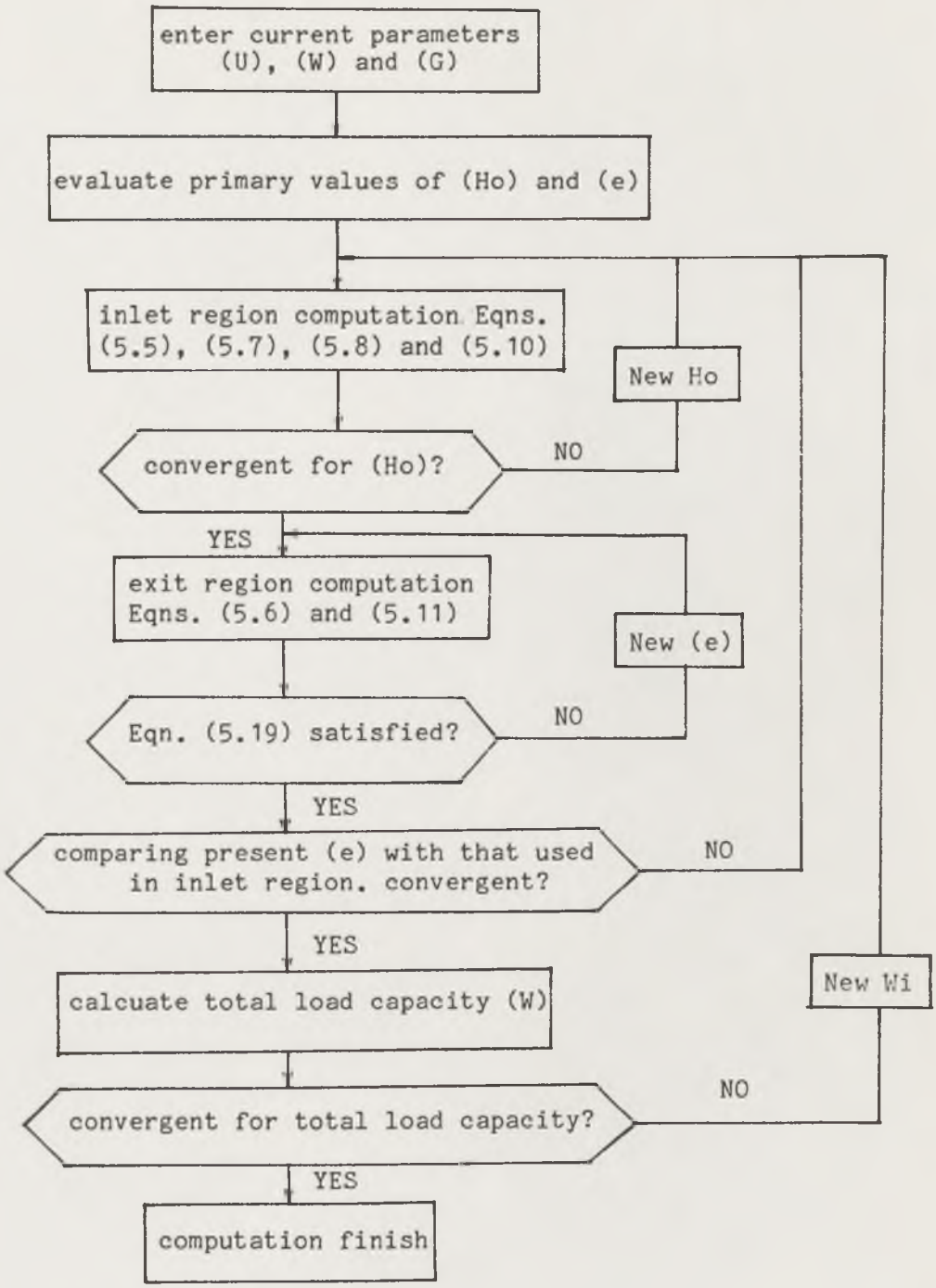

Figure(5.2) Flow chart of the approximate approach for generating the elastically deformed shape of the two cylinders.

$$p(\infty) = 0 \quad \text{and} \quad p(s_i) = p_i$$

Non-dimensionalizing the equation, integrating and by taking the boundary conditions into account give the hydrodynamic pressure distribution in the inlet region as;

$$\alpha p(s) = -\ln\left(1 - I\,\frac{\int_s^\infty \frac{H - H_o}{H^3}\,ds}{\int_{si}^\infty \frac{H - H_o}{H^3}\,ds}\right) \qquad \text{for } s \geq s_i \qquad (5.8)$$

$$\text{where } I = 1 - \exp(-\alpha p(s_i)) = 12GU\left(\frac{L}{R}\right)\int_{si}^\infty \frac{H - H_o}{H^3}\,ds \qquad (5.9)$$

As a first approximation, (H) is assumed to be evaluated from equation (5.5). The primary value of (e) is estimated by an empirical formula and the initial value of (H_o) is given by the Grubin formula. The additional deformation in the inlet region caused by hydrodynamic pressures are determined from the elasticity equation;

$$V(s) = -\frac{2L}{GR}\int_{si}^\infty p(t)\,\ln(s - t)^2\,ds + C \qquad (5.10)$$

These additional deformations in the inlet region are added to the first approximate film thicknesses. Subsequently, the new values of film thicknesses are used to work out a new central film thickness (H_o) from equation (5.9) and corresponding hydrodynamic pressure distributions from equation (5.8). The iterative procedure outlined above is repeated until the discrepancy between the two subsequent iterative values of (H_o) is within a tolerance of (0.5%).

The second loop is the exit loop. At the outlet end of the loaded region, hydrodynamics must again exert the major influence and reduce the pressure from a very high value down to zero. Following a similar procedure to that used in the inlet region, and considering the pressure boundary conditions;

$$p(s_e) = 0 \qquad \text{and} \qquad p(0) = \infty$$

As (p(0)) is the spike pressure the term ($e^{-\alpha p(0)}$) can be neglected in the analysis, consequently the hydrodynamic pressure distribution in the exit region is given by;

$$\alpha p(s) = -\ln\left(1 - I\,\frac{\int_{s}^{se}\frac{H-H_o}{H^3}\,ds}{\int_{o}^{se}\frac{H-H_o}{H^3}\,ds}\right) \qquad \text{for } s \le s_i \qquad (5.11)$$

$$\text{where } I = 12\,G\,U\left(\frac{L}{R}\right)\int_{o}^{se}\frac{H-H_o}{H^3}\,ds \qquad (5.12)$$

Again, as a first approximation, (H) is assumed to be given by equation (5.6), thus the initial pressure distribution in the exit region can be evaluated by equation (5.11). The additional deformation caused by the hydrodynamic pressure in the exit region is considered in the same way as that employed in the inlet region. The value of (e) adopted in the present analysis is a primary value which has been used for the analysis in the inlet region. If (e) is the solution of the problem, the following equation, which is deduced from equations (5.9) and equation (5.12), will be satisfied.

$$12\,G\,U\left(\frac{L}{R}\right)\left[\int_{se}^{o}\frac{H-H_o}{H^3}\,ds - \int_{si}^{\infty}\frac{H-H_o}{H^3}\,ds\right] = 0 \qquad (5.13)$$

If this equation is not satisfied, a new value of (e) is to be chosen. In the present analysis the new value of (e) is estimated by a bisection method and then the calculation in the exit region is repeated until equation (5.13) is valid. Here (s_e), the end of the exit region, depends upon the value of (e) and has to be recalculated every time. It should be pointed out that the approach adopted by Prakash and Christensen (1981) for calculating a new value of (e) failed to produce a convergent result at high load. This was because the equation used by the authors was quite sensitive to the value of oil film thickness (see equation (22) of the papaer of Prakash and Christensen (1981)). At extremely high load a very small variation in the oil film thickness in the exit region would result in a substantial change of the predicted value of (e) which was used as a new value in the next iterative loop in the inlet region. As a direct consequence of this change the value of (e) was hardly convergent under high loading conditions. On the contrary, in the present analysis the fluctuation of (e) was eliminated by the bisection method and the balance of equation (5.13) is dependent upon the integrations in both the inlet and outlet regions. Thus in cases of extremely high load the influence of small film thicknesses in the exit region will have little effect on the convergence of the value of (e). This modification

has led a successful prediction of the minimum film thickness at the condition with the load parameter (W) increased up to (1.0E-2), speed parameter (U) decreased down to (1.0E-14) and material parameter (G) risen up to (5000).

The third loop is the inlet and exit iterative loop. The value of (H_o) obtained in the inlet region is an approximate one, because it is based upon an approximate offset value of (e). The same is true for (e) which is determined in the exit region. To improve upon these values, the calculation in the inlet loop is repeated with a new value of (e) which is obtained in the exit loop to estimate new value of (H_o). This value is then used for producing a new approximation to (e) in the exit loop again. This outer iteration is repeated until no appreciable change occurs in the values of (H_o) and (e).

The final loop is the elastic load loop. The elastic load (W_i) in equation (5.4) is the load carried by the surface pressures in the central region, but not the total hydrodynamic load capacity. As a consequence of this, the bisection method was employed in this iterative procedure to work out a proper value of (W_i) with which the sum of hydrodynamic load capacities produced in the three regions is equal to the applied load.

5.2.3 Generating the Elastic Deformed Shape of Rough Cylinders

The main assumptions and the general procedure for generating deformed shapes of rough cylinders are similar to those for smooth surfaces. For simplification, the introductions given in this section are concentrated on presenting the different equations in each iterative loop.

By taking the surface roughness effects into account, the hydrodynamic pressure distributions in the inlet region is;

$$\alpha\bar{p}(s) = -\ln\left(1 - I\,\frac{\int_{s}^{\infty}\frac{\bar{H}_t-\bar{H}_{ot}}{\phi_x H^3}\,ds}{\int_{si}^{\infty}\frac{\bar{H}_t-\bar{H}_{ot}}{\phi_x H^3}\,ds}\right) \qquad \text{for } s \geq s_i \qquad (5.14)$$

$$\text{where } I = 1 - \exp(-\alpha\bar{p}(s_i)) = 12GU\left(\frac{L}{R}\right)\int_{si}^{\infty}\frac{\bar{H}_t-\bar{H}_{ot}}{\phi_x H^3}\,ds \qquad (5.15)$$

The additional deformation in the inlet region now caused not only by hydrodynamic pressures but also by asperity contact pressures (p_c) arising from the asperity interaction and is estimated from;

$$V(s) = -\frac{2L}{GR}\int_{si}^{\infty}[\bar{p}(t) + \bar{p}_c(t)]\ \ln(s - t)^2\, dt + C \qquad (5.16)$$

The hydrodynamic pressure distribution in the exit region is predicted by the following equations;

$$\alpha\bar{p}(s) = -\ln\left\{1 - I\frac{\int_{s}^{se}\frac{\bar{H}_t - \bar{H}_{ot}}{\phi_x H^3}\,ds}{\int_{o}^{se}\frac{\bar{H}_t - \bar{H}_{ot}}{\phi_x H^3}\,ds}\right\} \quad \text{for } s < o \qquad (5.17)$$

$$\text{where } I = 12\,GU\left(\frac{L}{R}\right)\int_{0}^{se}\frac{\bar{H}_t - \bar{H}_{ot}}{\phi_x H^3}\,ds = 1 \qquad (5.18)$$

For rough surfaces the offset value of (e) is the solution to the problem when the following equation is satisfied.

$$12\,G\,U\left(\frac{L}{R}\right)\left[\int_{se}^{o}\frac{\bar{H}_t - \bar{H}_{ot}}{\phi_x H^3}\,ds - \int_{si}^{\infty}\frac{\bar{H}_t - \bar{H}_{ot}}{\phi_x H^3}\,ds\right] = 0 \qquad (5.19)$$

For rough surfaces the determination of the elastic load (W_i) incorporates the effects of both hydrodynamic load and the asperity load, the latter being calculated by equation (2.25).

5.2.4 Pressure–Viscosity Relationship and Reduced Pressure

The pressure-viscosity relationship and reduced pressure adopted in the present analysis are the same as those detailed in Chapter (4), which are given by equations (4.2) and (4.3).

5.2.5 Hydrodynamic Equations

Reynolds' equation for fully flooded lubrication of two smooth cylinders in combined entraining and normal motion has been given in equation (2.12). The normal velocity term ($\partial h/\partial t$) of the cylinders is assumed to be constant throughout the conjunction region. By introducing the dimensionless groups into Reynolds' equation (2.12) and considering the

coordinate system shown in Figure (5.1b), a dimensionless Reynolds' equation is written in the form;

$$\frac{d}{dX}\left(\frac{H^3}{\bar{\eta}}\frac{dP}{dX}\right) = -12\,U\frac{L}{R}\left[\frac{dH}{dX} - \frac{L}{R}r\right] \tag{5.20}$$

with boundary conditions

$$P(\infty) = 0, \quad \frac{dP}{dX}(X_m) = P(X_m) = 0.$$

The one dimensional form of the average Reynolds equation, given by equation (2.19), was adopted to evaluate average hydrodynamic behaviour between two rough cylinders. In the present coordinate system the equation takes the form of;

$$\frac{d}{dx}\left(\phi_x\frac{\bar{h}^3}{12\eta}\frac{d\bar{p}}{dx}\right) = -\frac{(u_1+u_2)}{2}\frac{d\bar{h}_t}{dx} - \frac{(u_2-u_1)}{2}\sigma\frac{d\phi_s}{dx} + \frac{\partial\bar{h}_t}{\partial t} \tag{5.21}$$

The boundary conditions on pressure are;

$$\frac{d\bar{p}}{dx}(X_m) = \bar{p}(X_m) = 0, \qquad \bar{p}(\infty) = 0.$$

where $\dfrac{\partial\bar{h}_t}{\partial t} = \dfrac{\partial h_o}{\partial t}\int_{-h}^{\infty} f(s)\,ds = \dfrac{\partial h_o}{\partial t}K_t$

and (f(s)) is the polynomial density function. The dimensionless form of the equation and boundary conditions are;

$$\frac{d}{dX}\left(\phi_x\frac{H^3}{\bar{\eta}}\frac{d\bar{P}}{dX}\right) = -12\,U\frac{L}{R}\left[\frac{d\bar{H}_t}{dX} - \frac{u_s}{u}\frac{\sigma}{R}\frac{d\phi_s}{dX} - r\frac{L}{R}K_t\right] \tag{5.22}$$

$$\frac{d\bar{P}}{dX}(X_m) = \bar{P}(X_m) = 0, \quad \bar{P}(\infty) = 0.$$

where $u_s = \dfrac{u_1 - u_2}{2}$ and $u = \dfrac{u_1 + u_2}{2}$

5.2.6 Asperity Interactions

The asperity interaction model adopted in the present analysis is the

same as that used in Chapter (3), which was outlined in Chapter (2).

5.3 Analytical Procedure

5.3.1 Hydrodynamic Pressure Distribution

Introducing the reduced pressure (Q), of equation (4.7), into the dimensionless Reynolds' equation (5.20) for smooth surfaces yields a Reynolds' equation for piezo-viscous solutions. As the normal velocity is assumed to be constant along the conjunction of two cylinders in the present analysis, the reduced pressure can be obtained by integrating this equation twice and by taking into account the boundary conditions. Thus;

$$Q(X) = -12U\frac{L}{R}\left[\int_{X_m}^{X}\frac{H-H_m}{H^3}\,dX - r\frac{L}{R}\int_{X_m}^{X}\frac{X-X_m}{H^3}\,dX\right] \qquad (5.23)$$

where (H_m) is the film thickness at the point of (X_m) which is the cavitation boundary of the oil film. Having obtained the reduced pressure, the hydrodynamic pressure can be calculated from equation (4.17). Consequently, the hydrodynamic load (W_h) of the fluid pressure is found by integrating the pressure distribution between the limits of the extent of the oil film;

$$W_h = \frac{L}{R}\int_{X_m}^{\infty} P(X)\,dX \qquad (5.24)$$

Similarly, for rough surfaces the average reduced pressure can be expressed in the form;

$$\bar{Q}(X) = -12\,U\frac{L}{R}\left[\int_{X_m}^{X}\frac{\bar{H}_t-\bar{H}_t(X_m)}{\phi_x H^3}\,dX - \frac{\sigma u_s}{R u}\int_{X_m}^{X}\frac{\phi_s-\phi_s(X_m)}{\phi_x H^3}\,dX\right.$$

$$\left. - r\left(\frac{L}{R}\right)\int_{X_m}^{X}\frac{X K_t(X) - X_m K_t(X_m)}{\phi_x H^3}\,dX\right] \qquad (5.25)$$

The hydrodynamic force is now given by;

$$W_h = \frac{L}{R}\int_{X_m}^{\infty}\bar{P}(X)\,dX \qquad (5.26)$$

where $(\bar{P}(X))$ is the average hydrodynamic pressure.

5.3.2 The Solution for A Transient Elastohydrodynamic Line Contact

Since the elastic deformed shape of two boundary surfaces have been produced by the approximate approach which has been detailed in sections (5.2.2) and (5.2.3), the solution procedure to the transient elastohydrodynamic lubrication of a line contact is similar to that for a transient rigid solution. The problem here is to determine a central film thickness (H_c), under which the hydrodynamic force generated between the two lubricated cylinders in combined entraining and normal motion equals the cam load (P_z). The film thicknesses between the two cylinders is now given by;

$$H(X) = H_s(X) - H_{so} + H_c \tag{5.27}$$

where ($H_s(X)$) is the film thicknesses and (H_{so}) is the central film thickness predicted under the steady state condition by the approximate approach respectively. For rough cylinders, the nominal film thickness is represented by;

$$\bar{H}(X) = \bar{H}_s(X) - \bar{H}_{so} + \bar{H}_c \tag{5.28}$$

The load applied to rough cylinders now has two components namely the hydrodynamic force (W_h) and the asperity force (W_a). Thus;

$$W = W_h + W_a \tag{5.29}$$

5.3.3 Predicting the Cyclic Variation of Minimum Film Thicknesses of the Cam and Follower

The general analysis of the approximate technique outlined above for the solution of a transient elastohydrodynamic line contact has been applied to the mixed lubrication analysis of a cam and follower. The approach used to determine the cyclic variation of film thickness between the cam and follower is to establish the normal velocity and film shape at selected increments of cam angle, such that the cam and follower enjoy vertical equilibrium throughout the cycle.

The solution procedure to the lubrication analysis of the cam and follower is composed of three loops as shown in Figure (5.3). They are the deformation loop, the load equilibrium loop and the cam angle increment loop. In the first loop, the elastic deformation loop, the elastically deformed shape of the boundary surfaces is produced by using the approximate approach (see sections (5.2.2) and (5.2.3)). The second loop is the load equilibrium loop in which the equilibrium between the applied load and the hydrodynamic force (and asperity load) is progressively reached in the

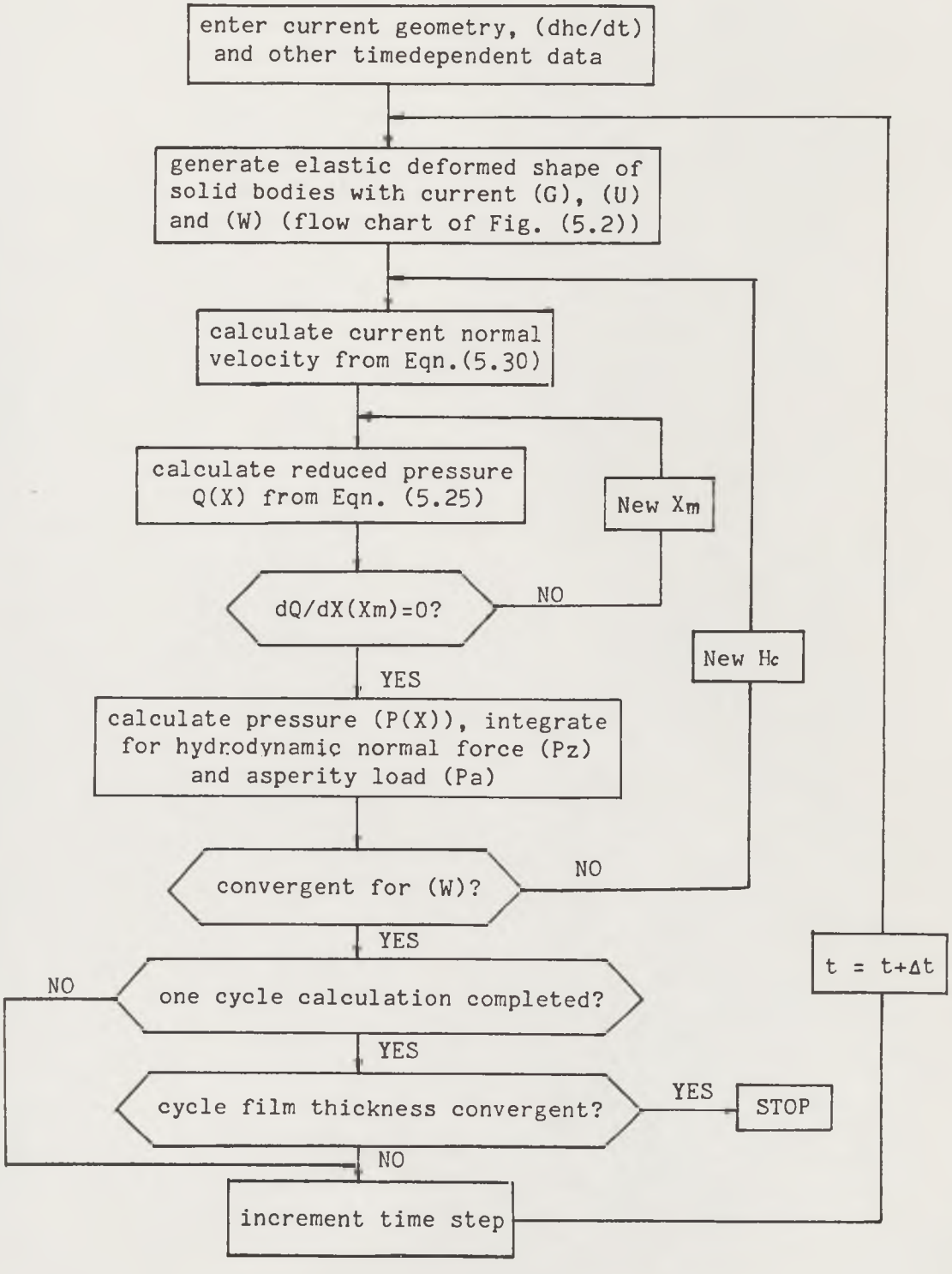

Figure (5.3) Flow chart of the mixed lubrication analysis of the cam and follower with the application of the approximate technique.

iteration for a proper value of the central film thickness. At the same time, the normal velocity which is assumed to be constant throughout the conjunction is revaluated for each iteration from the equation given below;

$$\frac{\partial h}{\partial t} \approx \frac{\Delta h_c}{\Delta t} = \frac{h_c(t + \Delta t) - h_c(t)}{\Delta t} \qquad (5.30)$$

The final loop is the cam angle increment loop in which the cam moves to the next position with a time increment of (Δt). It is quite clear that for this procedure it may be necessary to proceed beyond one complete cam cycle to achieve a satisfactory measure of convergence. The criterion for convergence was that the central film thickness should be within (0.1%) of its value on the previous cycle at the same point.

5.4 Results

In order to verify the accuracy of the approximate technique for the solution to a transient elastohydrodynamic line contact, comparisons have been made of the values of minimum film thicknesses evaluated by the approximate technique with those calculated by the full numerical analysis. The results are tabulated in Tables (5.1) to (5.6).

The approximate technique was then applied to the mixed lubrication analysis of a cam and follower. The results presented in this chapter relate to the same cam and follower arrangement as that detailed in section (3.4). The same operating condition and values as the reference case were chosen for the present analysis. In addition, the parameters of critical pressure (p_1), pressure-viscosity coefficient (α) and ratio of the coefficients (β/α) were taken to be (0.4 GPa), (2.058×10^{-8} Pa^{-1}) and (0.17) respectively in the present analysis.

The influence of variable composite surface roughness height, distribution of roughness between surfaces, lubricant viscosity and camshaft rotational frequency were investigated. Only isotropic surfaces were considered due to the limitation of the asperity interaction model adopted. Results are presented in Figures (5.4) to (5.11). Cam angle is taken as the abscissa variable and nominal minimum film thickness, film parameter, load carried by the asperities and the percentage that this represented of the total load are plotted.

5.5 Discussion

A series of comparisons have been made on the minimum film thicknesses estimated by the approximate solution to the transient elastohydrodynamic line contact with those predicted by the full numerical analysis, which are currently available from the learned society literature, to examine to the accuracy of the approximate technique. The operating conditions were kept exactly the same as those given in the publications.

The data in Tables (5.1) to (5.4) were taken from the four cases given by Bedewi (1985) who investigated the time-histories of both central and minimum film thickness between two rolling cylinders involving both entraining and squeeze motion and subjected to a constant loading. The squeeze velocity, minimum and central film thicknesses were presented at eight instants during the approach. At each instant the squeeze velocity remained the same as that from Bedewi's analysis to calculate a minimum film thickness with the present technique. Subsequently the predicted minimum film thickness was compared to the one given by Bedewi. A total of thirty-two data pairs are summarized in the tables. From the data of the tables it can be seen that the approximate technique can give good approximations to the minimum film thicknesses with the differences for all cases being less than (6%) except for one data pair in Table (5.3) being of about (7%).

Further comparisons were made with the results given by Wu and Yan (1986) who studied the general features of two rolling cylinders involving approaching or separating normal motion. The minimum film thickness predicted by the approximate technique for fourteen cases in approaching motion are listed in Table (5.5) and eleven cases in separating motion are recorded in Table (5.6). The comparison of the results shows a slightly greater difference between these results, but it is still acceptable. Owing to the difficulties encountered in the numerical solutions the materials parameters adopted by the authors represented the operating condition of a polymer lubricated by a mineral oil. In such a case the best approximation to the deformed shape of the cylinders might be that produced by considering the Grubin assumption, the elastic deformation model adopted in the approximate technique for generating the deformed shape of the two cylinders was based upon Grubin type assumption with an off-centre position, which will produce the characteristic features of a heavily loaded

Table (5.1) Comparison of the minimum film thickness of the transient elastohydrodynamic line contact.
(Case 1. $W = 3.26\times10^{-6}$, $U = 8.93\times10^{-14}$, $G = 4733$)

$V\ (\times10^{-16})$	$v/u\ (\times10^{-2})$	H_{min} ($\times10^{-5}$) P	F	Difference (%)
-27.100	-3.0347100	1.2301	1.1770	+4.50
-2.7590	-0.3089590	0.4682	0.4615	+1.45
-1.3890	-0.1555430	0.3570	0.3547	+0.65
-0.6210	-0.0695409	0.2518	0.2473	+1.82
-0.4251	-0.0476036	0.2172	0.2161	+0.51
-0.2737	-0.0306495	0.1854	0.1867	-0.70
-0.1582	-0.0177156	0.1560	0.1563	-0.19
-0.0036	-0.0004052	0.1009	0.1022	-1.27

P: Present analysis, F: Full numerical analysis

Table (5.2) Comparison of the minimum film thickness of the transient elastohydrodynamic line contact.
(Case 2. $W = 3.26\times10^{-6}$, $U = 4.47\times10^{-13}$, $G = 4733$)

$V\ (\times10^{-15})$	$v/u\ (\times10^{-3})$	H_{min} P	($\times10^{-5}$) F	Difference (%)
-2.6430	-5.912750	1.1448	1.1450	-0.02
-0.7854	-1.757047	0.6879	0.6980	-1.45
-0.3573	-0.799329	0.5094	0.5298	-3.85
-0.2180	-0.487696	0.4372	0.4574	-4.42
-0.1464	-0.327517	0.3957	0.4133	-4.26
-0.01697	-0.037964	0.3112	0.3222	-3.41
-0.00388	-0.008682	0.3001	0.3120	-3.81
-0.00131	-0.002931	0.2993	0.3086	-3.01

P: present analysis, F: Full numerical analysis

Table (5.3) Comparison of the minimum film thickness of the transient elastohydrodynamic line contact.
(Case 3. $W = 2.17\times10^{-6}$, $U = 8.93\times10^{-14}$, $G = 4733$)

$V\ (\times10^{-15})$	$v/u\ (\times10^{-2})$	H_{min} P	$(\times10^{-5})$ F	Difference (%)
-3.0700	-3.437850	1.2929	1.1990	+7.83
-1.4720	-1.648380	0.9031	0.8599	+5.02
-0.2720	-0.304591	0.4226	0.4234	-0.19
-0.1039	-0.116349	0.2832	0.2898	-2.28
-0.04803	-0.053785	0.2054	0.2181	-5.82
-0.01595	-0.017861	0.1458	0.1542	-5.45
-0.00324	-0.003632	0.1140	0.1192	-0.36
-0.00013	-0.000149	0.1081	0.1099	-1.64

P: Present analysis, F: Full numerical analysis

Table (5.4) Comparison of the minimum film thickness of the transient elastohydrodynamic line contact.
(Case 4. $W = 6.52\times10^{-6}$, $U = 8.93\times10^{-13}$, $G = 4733$)

$V\ (\times10^{-15})$	$v/u\ (\times10^{-2})$	H_{min} P	$(\times10^{-5})$ F	Difference (%)
-17.3400	-1.941770	2.8601	2.8190	+1.46
-11.9200	-1.334830	2.4283	2.4090	+0.79
-5.7490	-0.643785	1.7727	1.7890	-0.89
-3.2070	-0.359127	1.3912	1.4250	-2.39
-1.3620	-0.152520	0.9947	1.0130	-1.80
-0.5923	-0.066327	0.7484	0.7430	+0.73
-0.2427	-0.027178	0.5908	0.5827	+2.39
-0.0031	-0.000344	0.4468	0.4500	-0.71

P: Present analysis, F: Full numerical analysis

Table (5.5) Comparison of the minimum film thickness of the transient elastohydrodynamic line contact for the case of approaching normal motion.

$W(\times10^{-5})$	$G(\times10^{3})$	$U(\times10^{-11})$	v/u $(\times10^{-3})$	$H_{min}(\times10^{-5})$ P	F	Difference (%)
1.0	2.0	0.20	-5.0	1.65	1.74	-5.2
1.0	1.5	0.50	-0.2	0.88	0.93	-5.4
1.5	2.0	0.50	-0.8	1.32	1.34	-1.5
1.5	1.5	0.20	-4.0	1.46	1.58	-7.6
1.5	1.2	2.00	-0.5	1.98	2.14	-7.5
1.5	1.0	1.00	-0.1	1.06	1.13	-6.2
2.0	2.0	1.00	-0.8	1.92	1.89	+1.6
2.0	1.5	2.00	-0.2	2.03	2.00	+1.5
2.0	1.2	0.20	-5.0	1.58	1.71	-7.6
2.0	1.0	0.50	-0.2	0.73	0.75	-2.7
2.5	1.5	1.00	-1.0	1.84	1.88	-2.1
2.5	1.2	0.50	-1.6	1.46	1.59	-8.2
2.5	2.0	2.00	-5.0	4.92	5.00	-1.6
2.5	2.0	2.00	-10.0	6.54	6.60	-0.9

P: Present analysis, F: Full numerical analysis

Table(5.6) Comparison of the minimum film thickness of the transient elastohydrodynamic line contact for the case of separating normal motion.

$W(\times10^{-5})$	$G(\times10^{3})$	$U(\times10^{-11})$	$v/u\ (\times10^{-3})$	$H_{min}(\times10^{-5})$ P	F	Difference (%)
1.5	1.2	2.00	0.5	1.44	1.41	+2.1
1.5	1.5	4.00	0.3	2.73	2.78	-1.8
1.5	2.0	3.00	0.4	2.59	2.45	+5.7
2.0	1.0	3.00	0.3	1.83	1.82	+0.5
2.0	1.5	5.00	0.4	3.10	3.00	+3.3
2.0	1.5	2.00	0.2	1.74	1.68	+3.6
2.0	2.0	4.00	0.2	3.32	3.06	+0.8
2.5	1.0	4.00	0.4	2.09	1.97	+6.1
2.5	1.5	3.00	0.2	2.27	2.06	+10.2
2.5	2.0	5.00	0.3	3.67	3.39	+8.3
2.5	2.5	10.00	1.0	5.98	5.53	+8.1

P: Present analysis, F: Full numerical analysis

elastohydrodynamic line contact. It is expected that the present technique will give a more reasonable approximation for the case of a steel lubricated by a mineral oil under heavy loading. Unfortunately few numerical solutions for the heavily loaded case are available for comparison on either quantitative or qualitative basis. The convergence of the present technique for the solution to these cases was quite stable, the CPU time required for the solution of each case listed in the tables never exceeded ten seconds on the Amdahl 570 computer of Leeds University.

Figure (5.4) demonstrates the cyclic variation of the minimum film thickness between the cam and follower for the reference case by the two different solution procedures. The solid line shows the result of the present approximate solution of the transient elastohydrodynamic line contact for rough surfaces having a composite surface roughness height of (0.2 μm), while the dotted line represents the results of a transient isoviscous solution with rigid smooth surfaces. The gap between the dotted line and the solid line reveals the significant influence upon the cam and follower lubrication produced by taking into consideration the effects of surface elastic deformation, surface roughness and increased viscosity under pressure. The film thickness variations of Figure (5.4) exhibit similar well known features which have been described in Chapters (3) and (4). In addition, the cycle nominal minimum separation between the cam and follower occurred in the vicinity of the point of zero entraining velocity as the cam nose leaves the falling flank, but the value of the separation is much greater than that predicted by the rigid solution. This new analysis shows an increase of approximately (17) times the rigid prediction, from (0.008 μm) to (0.135 μm). At another extreme point, the film thickness increases by a factor of about (15) from (0.01 μm) to (0.158 μm). The nominal minimum film thickness on the cam nose is (0.230 μm) which is (6.7) times the value of (0.034 μm) predicted by the rigid-isoviscous solution.

The effect upon nominal film thickness of the introduction of surface roughness into the analysis of film thickness is clearly evident from Figure (5.5). For the reference case, with a composite surface roughness height of (0.2 μm), the nominal minimum film thickness at the nose increases from (0.194 μm) to (0.230 μm) with respect to the smooth surface prediction whilst the increase approaches (0.271 μm) for a composite surface roughness height of (0.6 μm). The increased percentage of the nominal minimum film thickness arising from the increase of the composite surface roughness

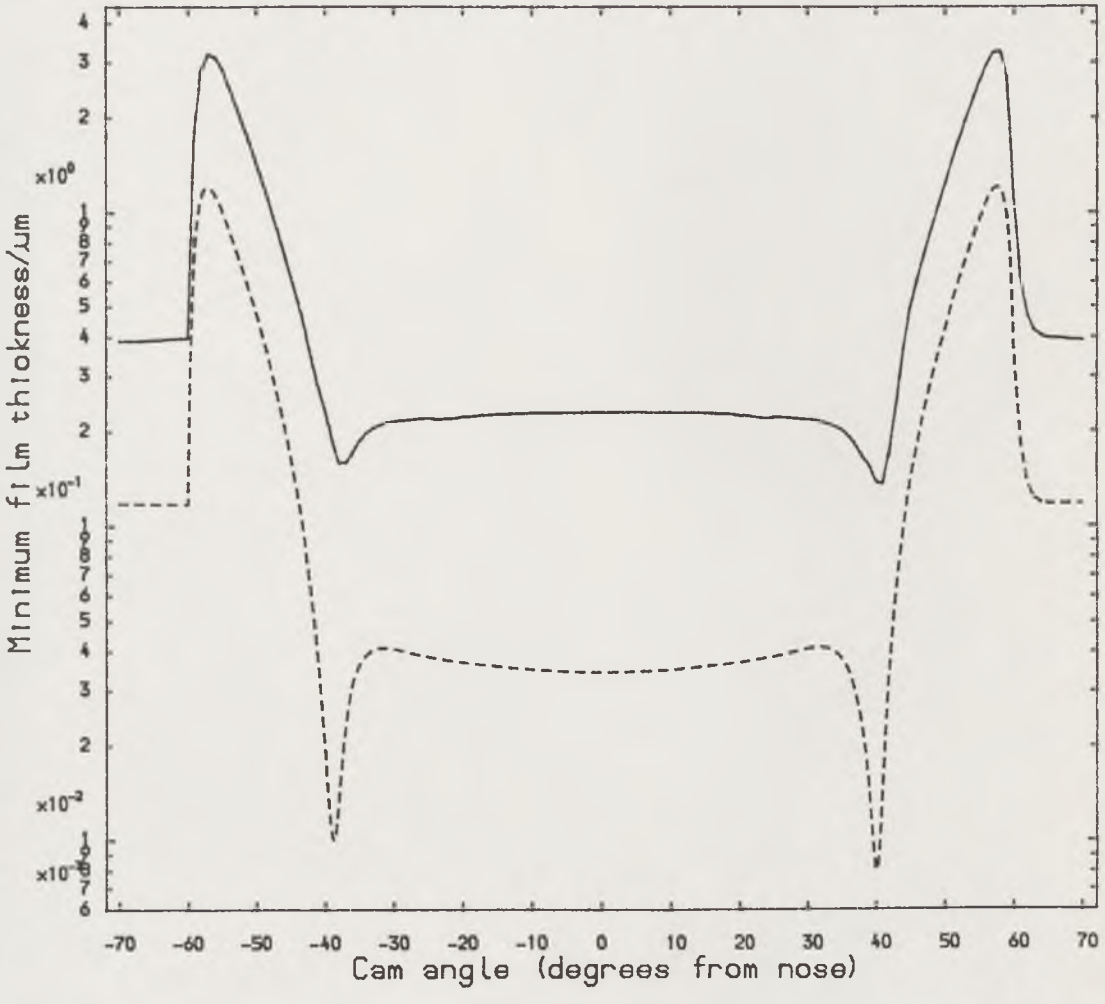

Figure (5.4) The cyclic variations of the minimum film thickness predicted by different solution procedures.

——— Transient EHL solution (rough surface 0.2μm)

-------- Transient rigid solution (smooth surface)

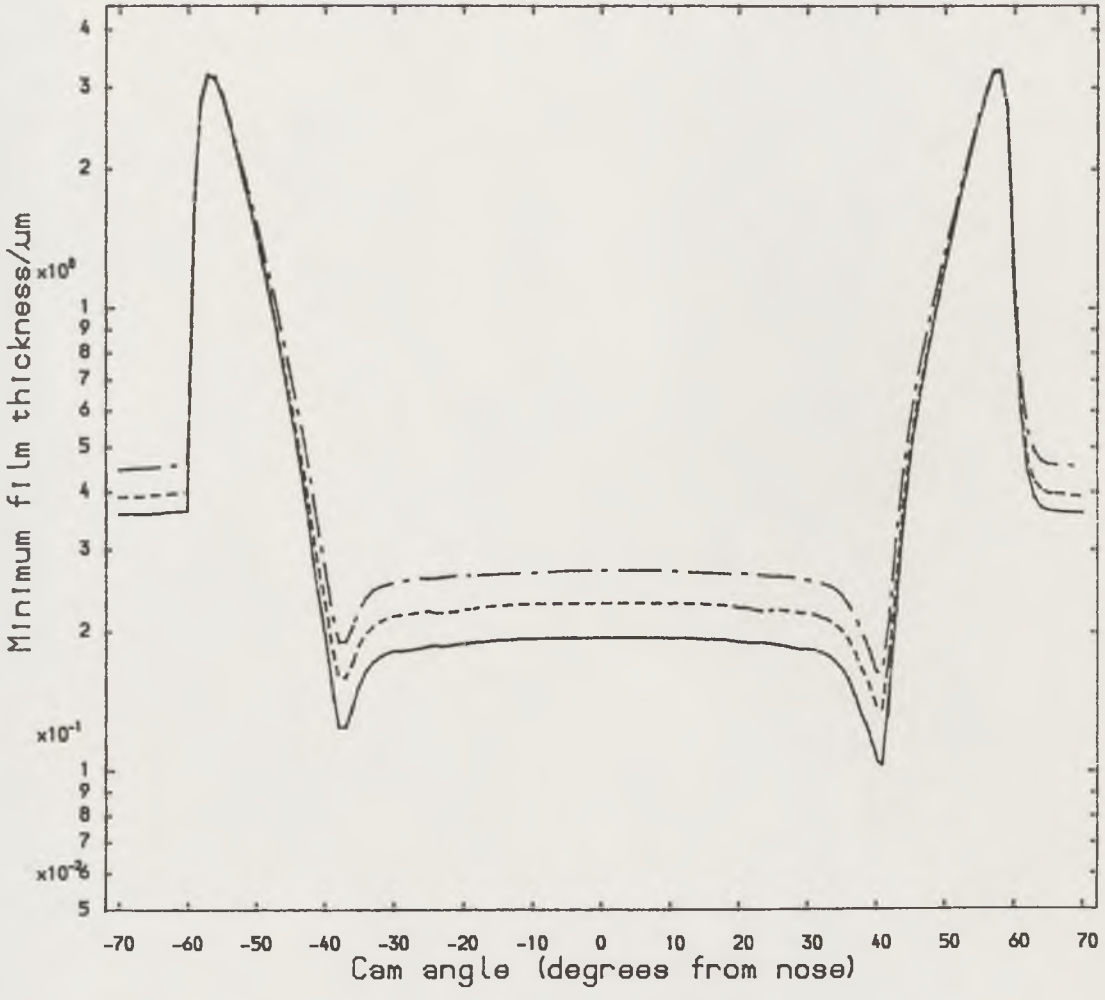

Figure (5.5) The effect of composite surface roughness height on minimum film thickness.

———— Smooth surface

-------- Composite surface roughness 0.2μm

—·—·— Composite surface roughness 0.6μm

height in the present analysis seems to be less than that relating to the rigid-isoviscous solution to rough surfaces (see Chapter (3)). This is because the values of the nominal minimum film thickness predicted by the present approximate transient elastohydrodynamic analysis are several times greater than those corresponding to the rigid solution. Indeed, in comparison to the smooth case the absolute increase of the nominal minimum film thickness on the nose estimated by the approximate technique for a composite surface roughness height of (0.2 μm) is about (0.040 μm), whilst the rigid-isoviscous solution only gives the increase of about (0.020 μm). As a result of the flattened region formed in the centre region of the elastohydrodynamic line contact it is expected that the influence of surface roughness upon the nominal film thickness in elastohydrodynamic analysis will be greater than that which occurs in the rigid solution. The effect of the surface roughness height upon the cyclic variation of the film parameter (λ) (the ratio of the nominal minimum film thickness to the composite surface roughness height, or (h_{min}/σ)) is presented in Figure (5.6). It is interesting to note that the film parameter now decreases from (1.15) to (0.45) on the cam nose with the increase in composite surface roughness from (0.2 μm) to (0.6 μm). On the whole, the increase of composite surface roughness height results in an increase of nominal film thickness and a decrease in the film parameter (λ).

The effect of the distribution of roughness between the cam and follower is detailed in Figure (5.7). The composite roughness height was kept fixed at (0.2 μm) for three different roughness distributions: same roughness on cam and follower (the reference case), smooth cam and rough follower and rough cam and smooth follower. Contrary to the tendency of the variation of the nominal minimum film thickness evaluated by the rigid solution (see Figure (3.6)), Figure (5.7) shows that the case of a smooth follower and rough cam would result in a higher nominal minimum film thickness in the nose region than that for equal roughness on the surfaces. With a smooth cam and rough follower the converse is true, the nominal minimum film thickness being less than that for the case of the same roughness on cam and follower. However, the trend of the influence of the distribution of surface roughness upon the nominal minimum film thickness is reversed on the two cam ramps. Furthermore, whilst the tendency for the cases of the same surface roughness on each surface and the smooth cam and rough follower combination leads to a cyclic nominal minimum separation in the vicinity of zero entrainment during separation, the smooth follower and

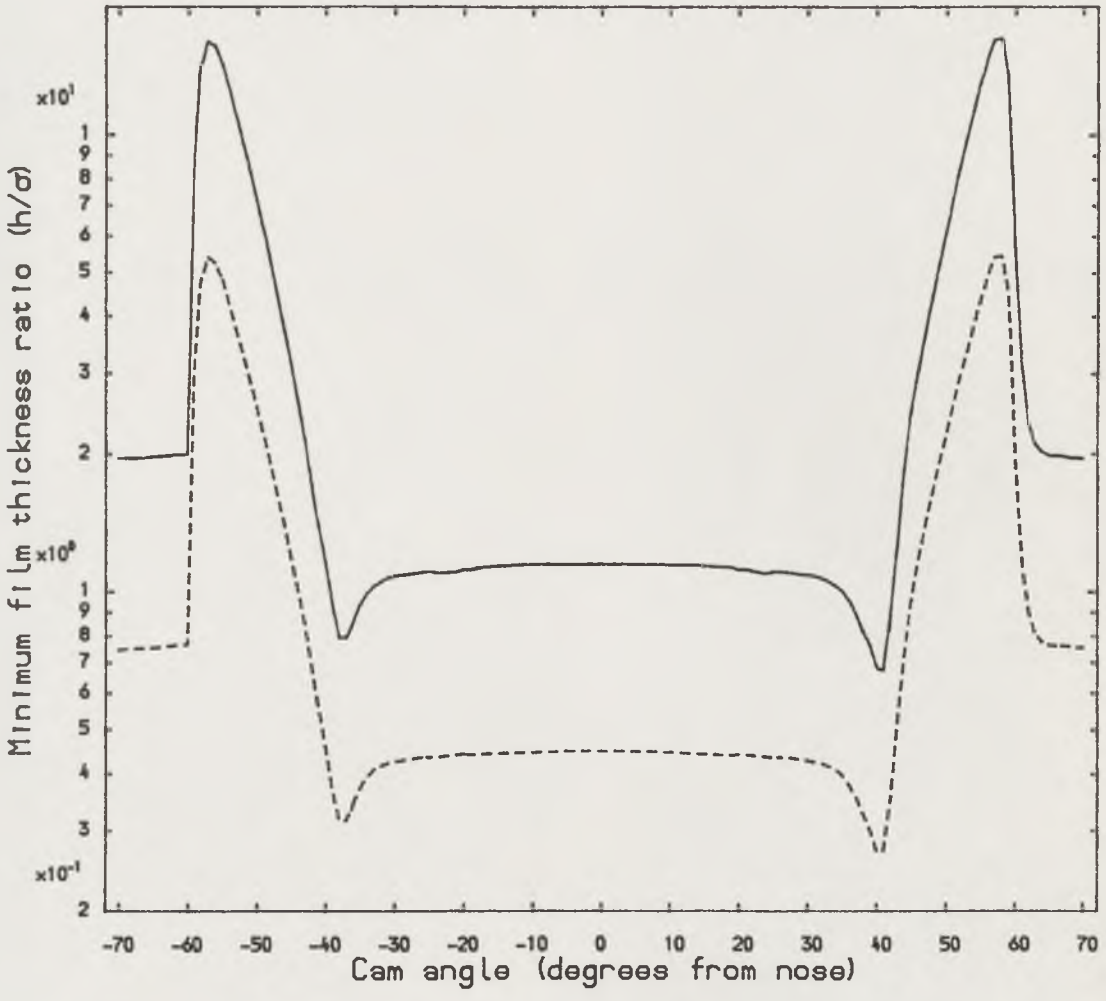

Figure (5.6) The effect of composite surface roughness height on minimum film thickness ratio.

———— Composite surface roughness 0.2μm

-------- Composite surface roughness 0.6μm

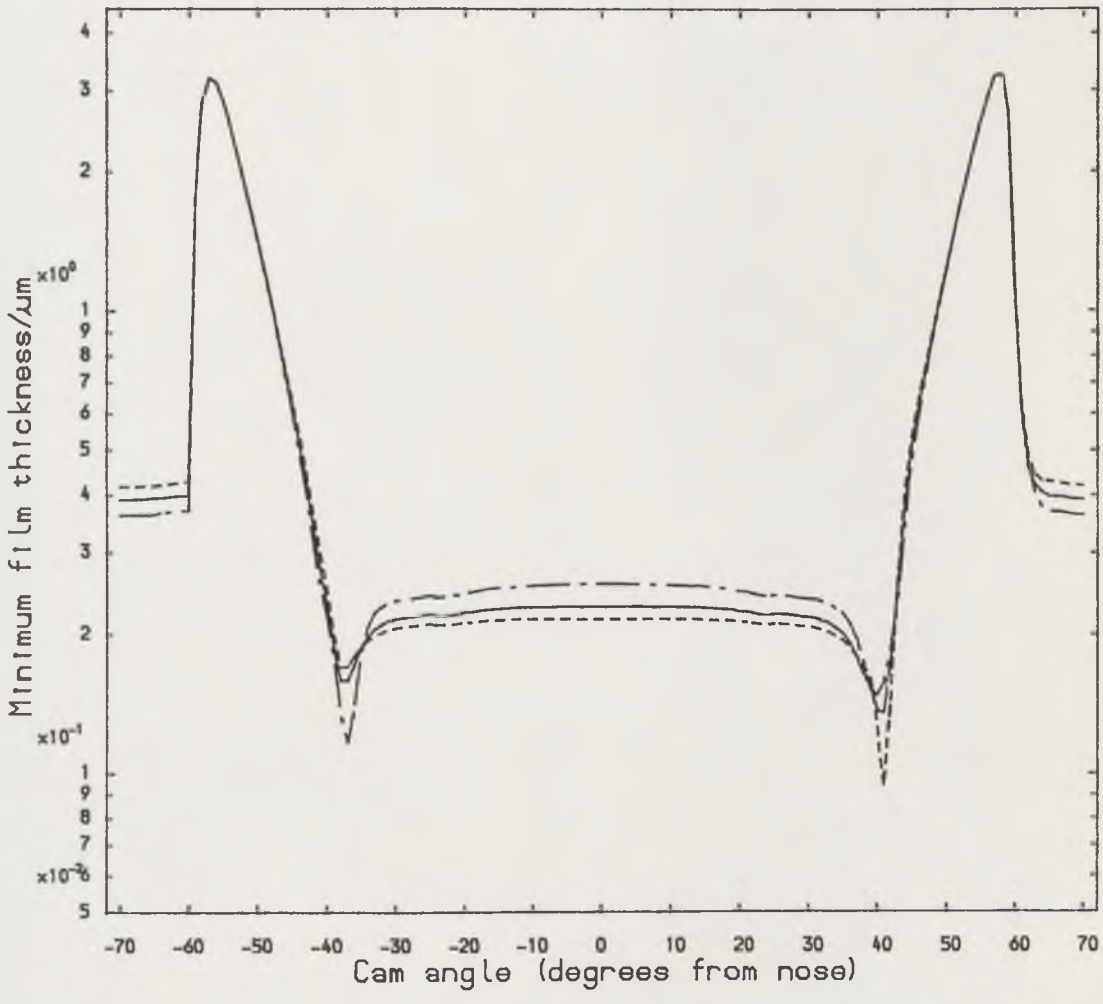

Figure (5.7) The effect of distribution of roughness between cam and follower surfaces on minimum film thickness.

———— Same roughness on cam and follower

--------- Smooth cam and rough follower 0.2μm

—·—·— Smooth follower and rough cam 0.2μm

rough cam case leads to a cyclic nominal minimum separation in the region of zero entrainment as the nose of the cam approaches the rising flank. As the film thickness ratio in these regions is about (0.5), which is the limitation of the numerical experiment upon which the mixed lubrication model is based (see Patir and Cheng (1978) and (1979)), these findings should be verified by the experimental evidence. A further study in Figure (5.8) demonstrates the cyclic variations of the nominal minimum film thickness ratio for different roughness distributions. This shows that the values of (λ) for the present cases are all greater than (0.5) which is found to be identical to the situation for a composite surface roughness height of (0.04 μm) (see Figure (3.7)). Thus, the opposite trends arising from rigid and elastohydrodynamic analyses for a fixed composite surface roughness height of (0.2 μm) can be explained in the same way as that discussed in Chapter (3) on the influence of the shear flow factor (ϕ_s) upon the nominal film thickness for the cases of different roughness distributions. Again, it is found that the change in the nominal minimum film thickness at the nose due to the variation in distribution of isotropic roughness investigated is not significant. The increase with a smooth follower and rough cam is about (12%), whilst the corresponding decrease with a smooth cam and rough follower is only about (5.9%).

A detailed study of the data relating to the film parameter (λ) of Figures (5.6) and (5.8) reveals an important fact that under certain circumstances the cam and follower, in most of its operating cycle, works under mixed or elastohydrodynamic lubrication conditions. It is known that the film parameter is associated with the lubrication regime in which the component is operating. These regimes normally include: boundary lubrication ($\lambda < 1$), mixed lubrication ($1 < \lambda < 3$), elastohydrodynamic lubrication ($3 < \lambda < 10$) and hydrodynamic lubrication ($\lambda > 10$). Taking the cam and follower arrangement adopted in the present analysis as an example and considering the clearance of (0.4 μm) between the cam and follower on base circle, the cam initiates contact with the follower at a cam angle of about ($-65°$) and completes at about ($65°$). Thus, the cam lift portion is about ($130°$). A consideration of the variation of film parameter for the reference case indicates that the percentages of various lubrication regimes, including boundary, mixed, elastohydrodynamic and hydrodynamic lubrication regime, to the cam lift portion are of (10.8%), (65.4%), (11.5%) and (12.3%) respectively. Figures (5.6) and (5.8) also show that mixed lubrication regime has a commanding influence over the cam nose region. Whilst boundary

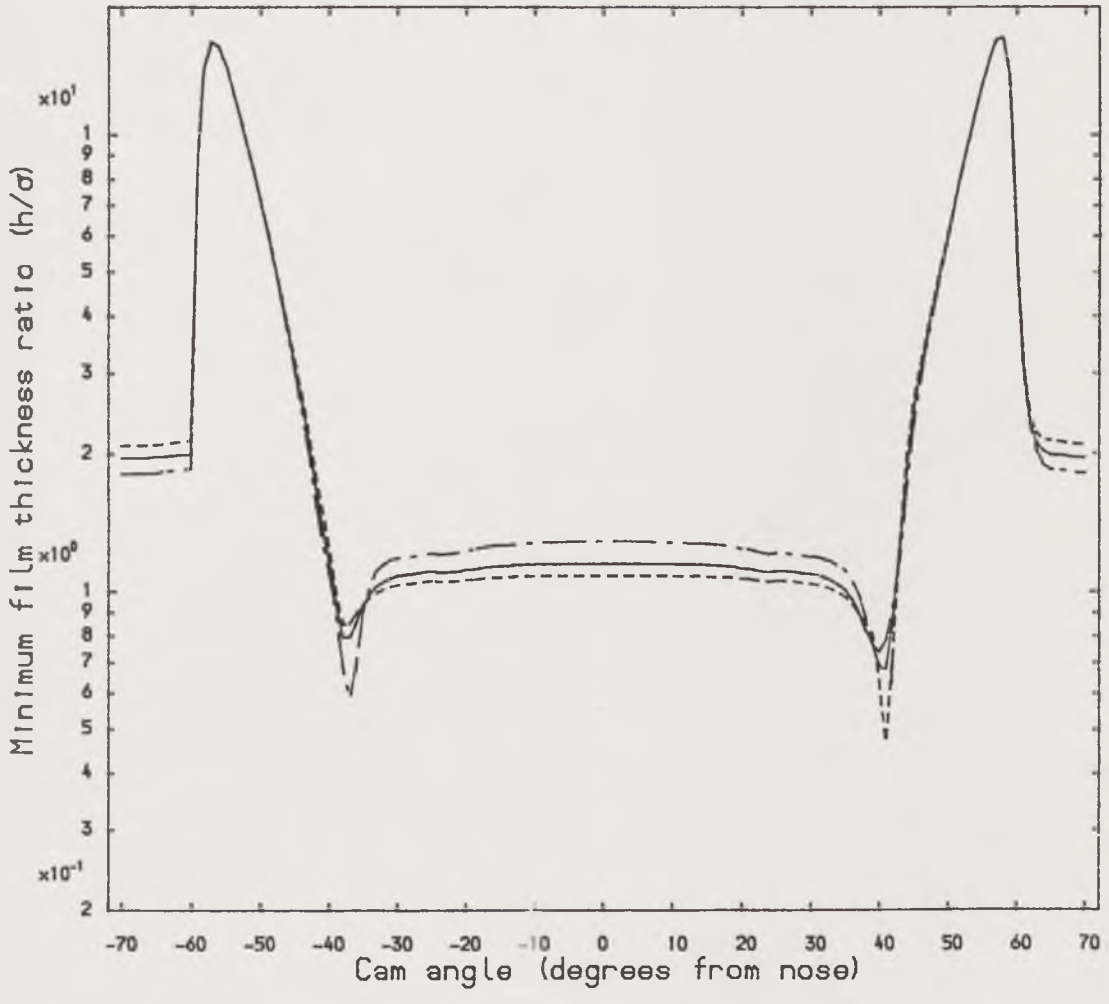

Figure (5.8) The effect of distribution of roughness between cam and follower surfaces on minimum film thickness ratio.

———— Same roughness on cam and follower

--------- Smooth cam and rough follower 0.2μm

——·——·— Smooth follower and rough cam 0.2μm

lubrication dominates the two extremely small film thickness regions in which the entraining velocity decreases to zero, the lubrication conditions in the cam flank regions are either elastohydrodynamic or hydrodynamic. Conventional wisdom suggests that the cam and follower contact suffers boundary lubrication with almost continuous surface contact during operational conditions. The present analysis, however, shows that the nature of the contact between the cam and follower may not be as severe as it is generally envisaged to be. Under certain circumstances the cam and follower still enjoy mixed and elastohydrodynamic lubrication for the greater part (say about (90%) in terms of the cam angle) of its lift portion.

The load carried by the asperities and the proportion that this represents of the total load is presented in Figure (5.9). Only the reference case and details for a composite surface roughness height of (0.6 μm) are presented. The total load at the nose is approximately (240 N) and that carried by the asperities is about (0.6 N) and (5.5 N) for the composite surface roughness heights of (0.2 μm) and (0.6 μm) respectively. It can be seen that the asperity load is only a small percentage of the total load. For the reference case, the asperity load is even smaller than those predicted by the rigid solution (see Figure (3.2)). This is a direct consequence of the increase in the nominal film thickness arising from taking the effects of surface elastic deformation and the variation of viscosity with pressure into consideration. For the two regions of extremly small film thickness, the percentage of the load carried by the asperities increased but still only represented about (1.5%) and (5%) of the total load for the composite roughness height of (0.2 μm) and (0.6 μm) respectively.

The effect of the variation of lubricant viscosity and cam shaft rotational frequency upon the nominal minimum film thickness during the cycle is presented in Figures (5.10) and (5.11) respectively. Apart from the applied variable presented in the figures, all other factors remain as for the reference case detailed in Chapter (3), with the composite surface roughness height taken as (0.2 μm). The results of these two figures are physically consistent. A five-fold increase in lubricant viscosity causes the nominal minimum film thickness at the nose to increase by a factor of about (2.7) whilst a reduction in cam rotational frequency from (50 Hz) to (16.7 Hz) is reflected in a drop in this film thickness from (0.29 μm) to (0.11 μm). It is evident that the influence of variation of the rotational frequency has greater effect upon the film thickness than that of viscosity, even though

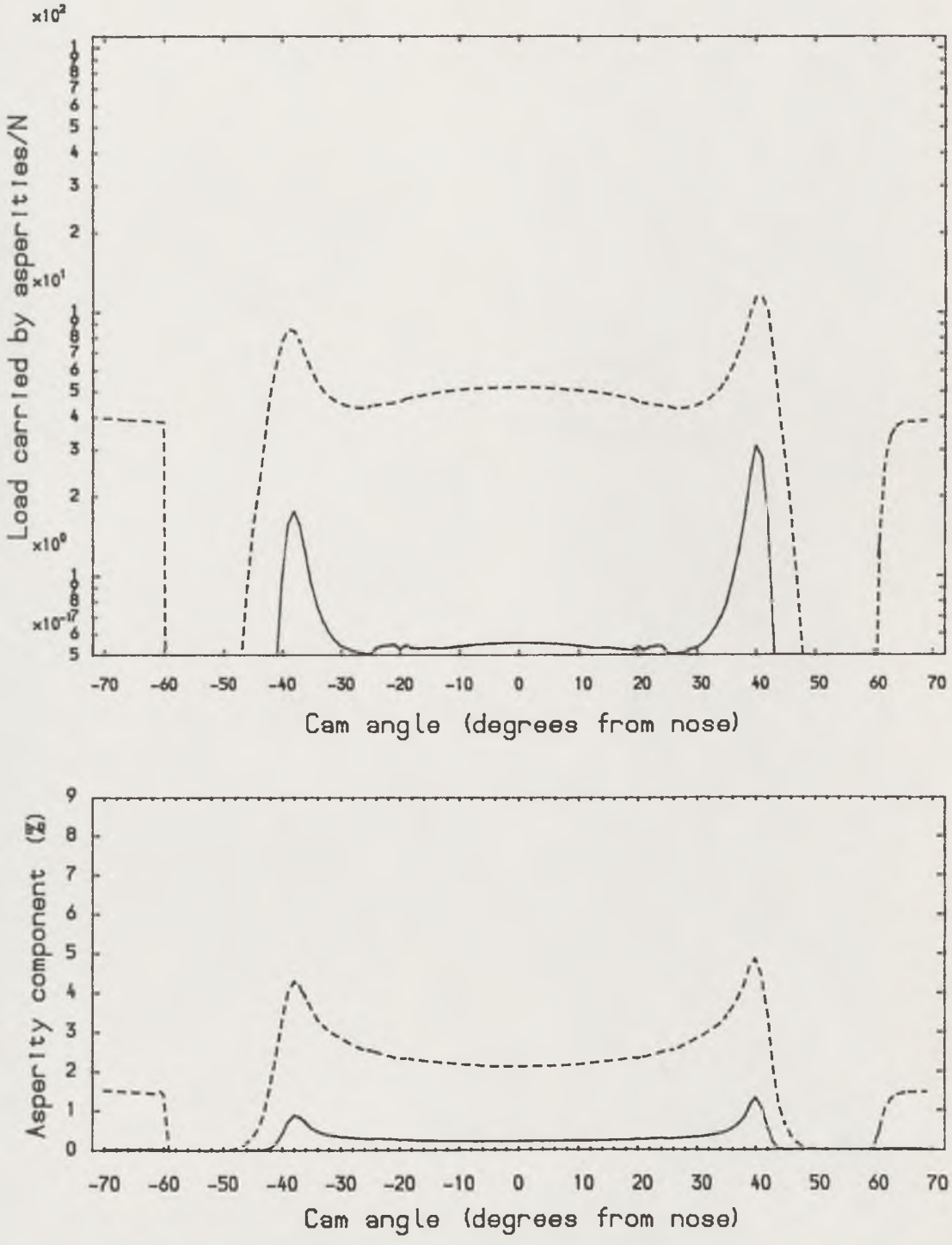

Figure (5.9) The effect of composite surface roughness height on load carried by the asperities and the percentages this represents of the total load.

———— Composite surface roughness 0.2μm

--------- Composite surface roughness 0.6μm

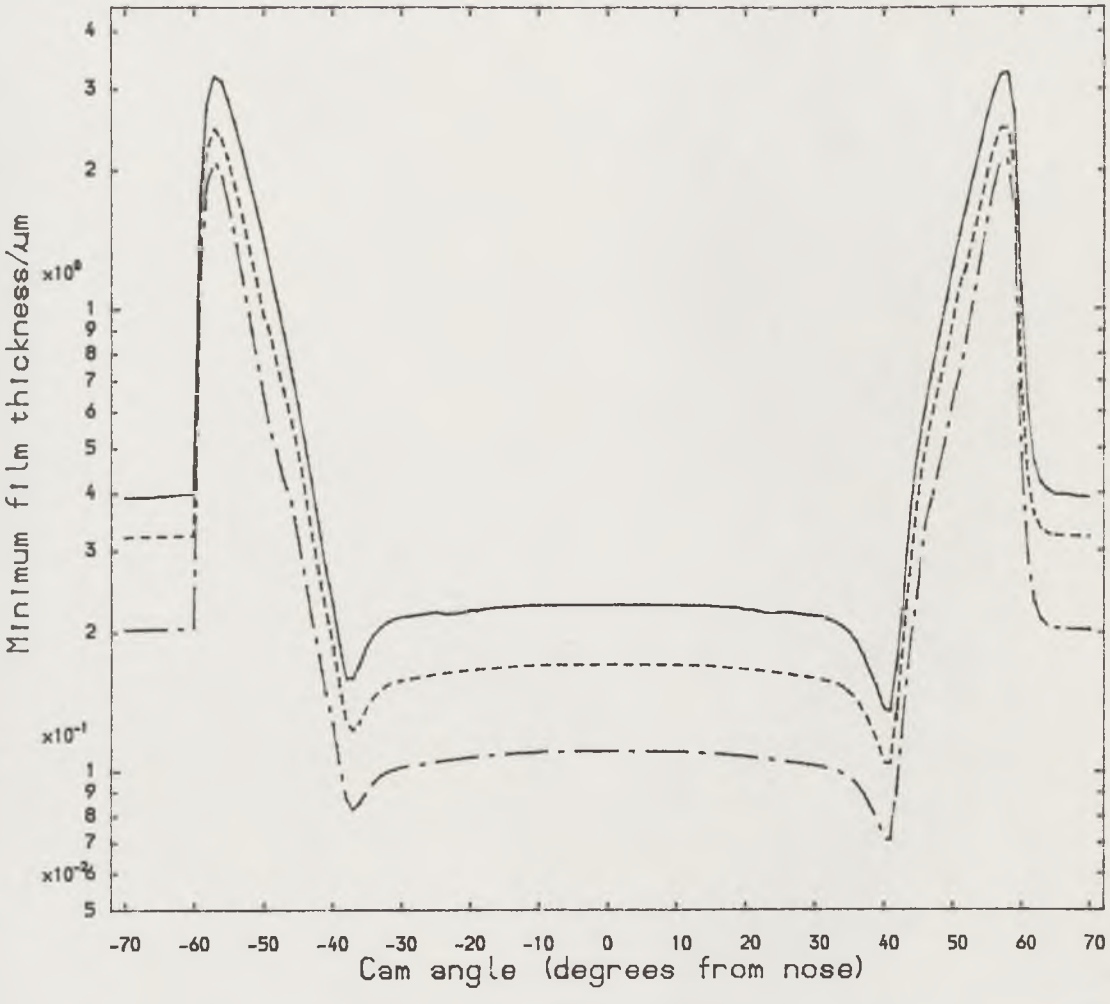

Figure (5.10) The effect of camshaft rotational speed on minimum oil film thickness.

———— Camshaft rotational speed 3000 r/min (50.0Hz)

--------- Camshaft rotational speed 2000 r/min (33.3Hz)

—·—·— Camshaft rotational speed 1000 r/min (16.7Hz)

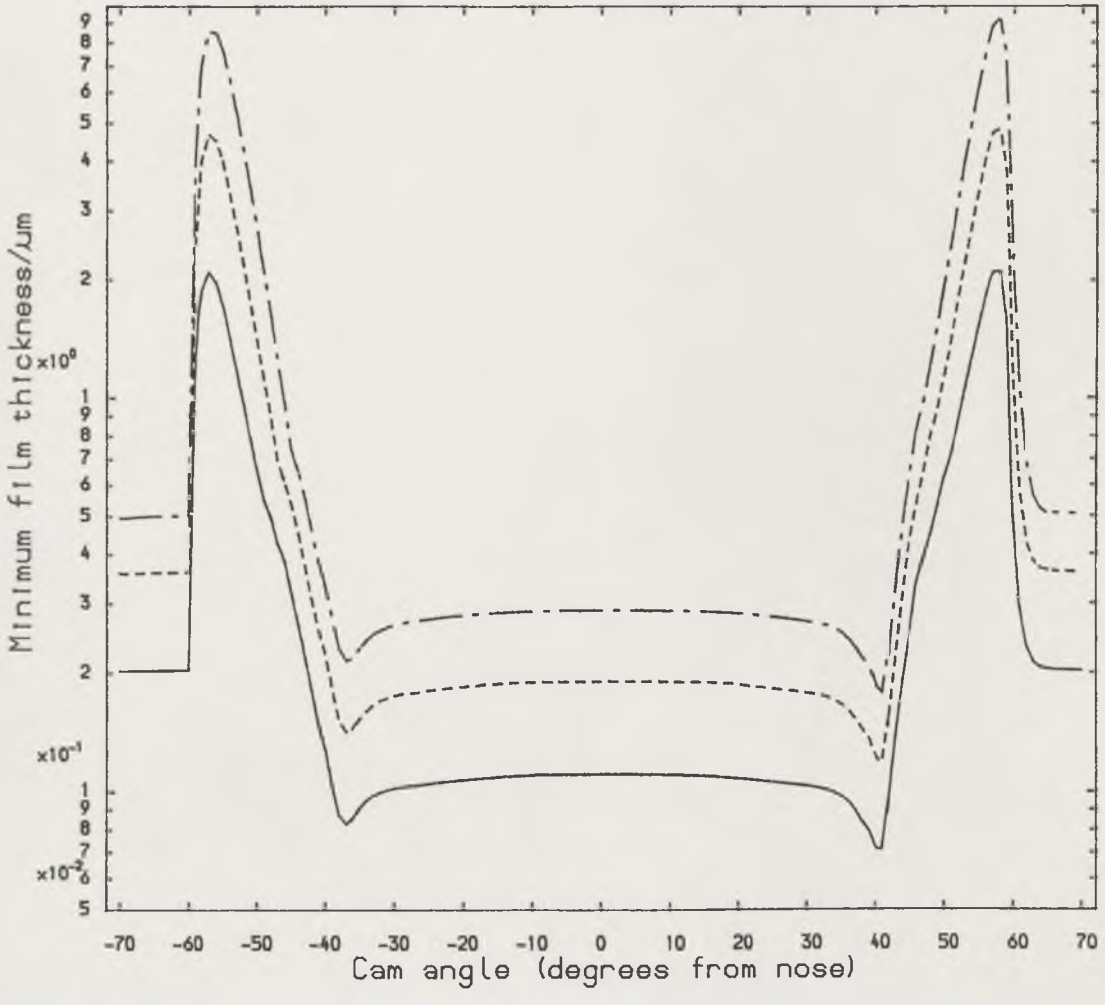

Figure (5.11) The effect of lubricant viscosity on minimum film thickness. (camshaft rotational speed 1000 r/min)

———— Lubricant viscosity 0.010 Pas.

--------- Lubricant viscosity 0.025 Pas.

—·—·— Lubricant viscosity 0.050 Pas.

the rotational speed and lubricant viscosity have the same influence upon the dimensionless speed parameter. Increasing the camshaft rotational frequency not only results in an increase in the entraining velocity but also leads to a decrease of the load acting on cam. Clearly, this dual action is of great benefit in promoting the formation of a lubricant film between the cam and follower.

5.6 Conclusions

An approximate technique for estimating the minimum film thickness of a transient elastohydrodynamic line contact associated with rough surfaces has been developed. The results of a series of comparisons to the minimum film thickness predicted by a full numerical analysis under the same operating conditions has shown that the technique can give good approximations to the minimum film thickness. This is the first published analysis of a transient elastohydrodynamic line contact with rough surfaces. The convergence of the solution is also quite stable and only required minimal computer time particularly for the case of heavy loading and low entraining velocity. This makes it possible for the approximate technique to be applied to the mixed lubrication analysis of machine elements such as gears, rolling bearings and cams and followers.

A further application of the approximate technique to the mixed lubrication analysis of the four-power polynomial cam and flat faced follower has yielded the following conclusions:

(1) The cyclic variation of the nominal minimum film thickness is greatly enhanced by including the effects of surface elastic deformation, surface roughness and the variation of lubricant viscosity with pressure. The general features of the cyclic variations of the nominal minimum film thickness between the cam and follower are similar to those predicted by the rigid-isoviscous solution for rough surfaces and the full numerical transient elastohydrodynamic solution for smooth surfaces.

(2) Surface roughness exerts a significant influence upon the lubrication performance of the cam and follower. The increasing of the composite surface roughness height causes an increase of the nominal minimum film thickness but a decrease in the film parameter.

(3) The effect of the distribution of surface roughness between the cam and follower upon the nominal minimum film thickness varies in different parts of the cam lift portion. Comparing the results with those for the case of the same roughness on cam and follower, in the cam nose region a smooth follower and rough cam generates a higher predicted film thickness, whilst a smooth cam and rough follower produces a lower film thickness. By contrast, on the cam ramps the effects are reversed.

(4) Contrary to the general finding that the cyclic minimum separation between the cam and follower occurs in the vicinity of the point of zero entraining velocity as the cam nose leaves the falling follower, for the case of a smooth follower and rough cam the minimum separation now appears on the rising flank of the cam. Although the situation predicted in the present mixed lubrication analysis can be explained reasonably by the change of direction of the entraining velocity and the influence of the shear flow factor upon the solution of the Reynolds' equation, this finding has yet to be confirmed by the experimental evidence.

(5) Under certain circumstances, such as the reference case adopted in the present analysis, the cam and follower works under mixed and elastohydrodynamic lubrication conditions for the greater part of its lift portion. This implies that the nature of the contact between the cam and follower is not as severe as it is generally envisaged to be.

PART II

AN EXPERIMENTAL STUDY OF THE TRIBOLOGY OF A CAM AND FOLLOWER

CHAPTER 6

THE DESCRIPTION OF THE EXPERIMENTAL APPARATUS

6.1 Introduction

A literature survey of the experimental research on the cam and follower presented in this chapter has illustrated that some findings from previous experiments should be verified under higher bulk temperature operating conditions. As it is necessary to control the bulk temperature in the present experiment and to reduce the parasitic power loss, many modifications have been made to the mechanical construction of the test apparatus. Detail descriptions of these modifications are given in this chapter. The remainder of the chapter deals with instrumentation for measuring temperature, torque and electrical resistivity between the cam and follower. A computer based data acquisition system and relevant software are also described.

In this chapter and subsequent ones the term camshaft rotational speed is used instead of camshaft rotational frequency and consequently the unit of revolution per minute (rpm) is adopted. This is thought to be more convenient for most engineers and is also consistent with the custom of learnt society literature.

6.2 Experimental Background and the Aim of the Experimental Study

6.2.1 A Literature Survey

In the early 1960s, Fairman and Duff-Barclay (1961) set up a test apparatus which has two identical test units, both of which house two cam and follower assemblies. According to experiments on commercial cams and followers, the authors put forward the interesting postulation that the pitting phenomenon on cams and followers involved not only a cyclic stressing of the surfaces beyond the fatigue strength but also a high flash temperature at the cam and follower interface which induced a reaction between the additives and components of the surface structure.

The 'spark discharge' method described by Machonochie and Cameron (1960) was also used to measure the oil film thickness. It is, however, important to note that the method and instrumentation adopted by the authors cannot give satisfactory quantitative results. Only a qualitative indication to the cyclic variations of the oil film thickness can be expected. The authors found that metallic contact was not greatly affected by a rise in

bulk oil temperature from (60°C) to (90°C), but was appreciably increased at (120°C). The durability test of a cam and follower with different metals and additives indicated that a straight oil was better than an additive oil if a steel cam and a chilled iron follower were used.

From 1962 to 1965 Andrew et al (1962), (1965) and Taylor et al (1963) published three reports in which they introduced the concept of median result for each test group into durability tests of the cam and follower to overcome the scatter of data for pitting failure. This concept was also adopted by some researchers to determine the scuffing failure load from each test group.

Bona and Ghilardi (1965) studied the influence of tappet rotation on scuffing and pitting failures. From the conclusion of Naylor and Dyson's study the authors set up a test apparatus having positive tappet rotation at a speed of (300 rpm). The results showed that the rotation of the tappet might increase the scuffing load by as much as (100%) when compared with a stationary tappet, and may also decrease the pitting resistance. However, some tests at MIRA showed that tappet rotation improved both scuffing and pitting performance. The reason why the difference occurs between the two tests needs further study.

The experimental work on cam and follower tribological studies in the 1960s was mainly concentrated on metallurgical properties (including material and surface treatment) and lubricant additives effects on pitting and scuffing failure. The general conclusions from those studies were summarized by Naylor (1967-68) as follows:

(1) In any particular system the maximum Hertz stress at the cam nose is of overriding importance but, depending on the design of the valve train, the safe maximum value may vary from (0.7 GPa) up to (1.1 GPa) (and in some instances even higher). The reasons why large differences should exist between different designs are not always clear.

(2) Metallurgical factors come high in order of importance. Chilled cast iron is cheap and is relatively free from failure by scuffing. It does, however, suffer from pitting and in this respect may be adversely affected by e.p. additives in the lubricant. Hardenable cast iron is relatively free from pitting and its tendency to fail by scuffing can be combated by the inclusion of e.p. additives in the lubricant. Hardenable steel components in combination with suitable e.p. lubricants are very effective but expensive.

(3) Surface treatment such as phosphating and oxidizing have been shown to improve the resistance to scuffing. Nitriding produces a surface which is highly resistant to pitting and which also provides some improvement in scuffing performance.

(4) Tappet rotation increases the load at which scuffing occurs but generally reduces resistance to pitting. In some test at MIRA, however, tappet rotation improved both scuffing and pitting performance.

(5) Extreme pressure additives of the zinc dialkyldithio-phosphate type increase the scuffing load, often very considerably, but may promote pitting, particularly if used at a high concentration.

In the same paper Naylor also reviewed studies on the friction behaviour of cams and followers. Finally, he pointed out that the mechanism of scuffing and friction behaviour in an elastohydrodynamic contact needed further study. The results of engine and laboratory tests of the type previously described are exceedingly difficult to generalize in any quantitative sense.

The wear mechanisms which are generally associated with the cam and follower are well documented and summarized by Barwell and Roylance (1978). The wear of cam mechanisms may be classified into three main types, namely pitting, scuffing and polishing wear. Pitting is both running time and stress-dependent. It occurs as a direct consequence of surface fatigue in which cracks propagate as a function of time under the action of repeated cyclic stressing. Scuffing arises in situations where some relative sliding exists in the absence of adequate fluid film lubrication, resulting in increased asperity contact. Polishing wear produces a smooth burnished appearance on the surface. It has been suggested that it may be an intermediate case between scuffing and pitting which is assisted by a chemical action involving the oil.

Vichard and Godet (1967-68) made a simultaneous measurement of load, friction and film thickness in a cam/tappet system on a test apparatus. The oil film thickness was measured by using dynamic capacitive measurements but the results obtained showed no valid correlation between theoretical and experimental results. The authors hoped to obtain more information on the viscosity at the contact by using a embedded thermocouple method for temperature determination in their next experiment. Unfortunately the results of the following experiments have not been published.

Ten years later Ninomiya et al (1978) observed the formation and break down of an oil film between a cam and tappet by using electrical conductivity methods on a TOYOTA 5R engine which was driven electrically. The oil film formation process during running-in or cold start was also observed by continuous observation of the voltage variation. This may have been the first time a computer-aided data processing system was used to analyse the instantaneous signals from the cam and tappet contact, but no significant result was obtained from the experiment.

Using the electrical capacitance method with the transducer mounted on the surface of the follower, Hamilton (1980) measured the oil film thickness between a cam and tappet. By moving the follower in the direction perpendicular to the camshaft, the oil film thickness around the surface of a three arc cam was measured. The observed maximum oil film thickness in the flank regions was about (8 μm). Due to asperity contact, the capacitance method failed in the cam nose region, where full film lubrication was not achieved. The oil pressure distribution across the cam was also measured, and the results were in good agreement with the results predicted by Martin's lubrication theory.

Coy and Dyson (1981) designed a test apparatus which could simulate the kinematics of the contact between a cam and finger follower in the vicinity of the zero entraining velocity position. It was found that the surfaces of the parts showed appreciable wear in the apparatus and that cams and followers from engines in field tests showed high correlation in a direction transverse to that of the motion, the peaks of one surface corresponding with the valleys of the other and vice versa. This high correlation of surface roughness was particularly in the cam nose and flank regions, and also implied that some regions which were often considered to suffer boundary lubrication were operating with mixed or elastohydrodynamic lubrication condition.

On a carefully prepared test apparatus Armstrong and Buuck (1981) performed a series of excellent experiments on valve gear energy consumption. The effects of speed, oil temperature, valve gear type and valve spring load on the torque required to drive the camshaft were studied. A rotary torque transducer was used which was directly coupled to the cam shaft. Variation of speed, temperature and load were subsequently

determined to have a major effect on valve gear energy consumption. Experimental results showed that the energy consumption within a valve gear was a complex interplay of many factors including an implied dependence on the presence and quality of oil film at the cam and follower interface.

In an attempt to establish a CEC standard scuffing test procedure, Chatterley (1981) carried out some test with two different oils RL/33 and RL/85, and investigated various operating conditions in the test machine with one of the oils. The results showed that oil temperature, sump temperature and volume of oil in the sump had a significant effect on the failure load, while the oil flow rate and the surface hardness of cam and follower specimens did not appear to have any particular influence on the results. The variation of the spraying oil temperature by (10°C) from (90°C) to (100°C) and then to (110°C) had an important effect on failure load, the higher the temperature the lower the failure load. This result was in agreement with the findings of Fairman and Duff-Barclay (1961).

Twenty 1980 Ford Fairmonts which were purchased from the factory in numerical sequence and equipped with (2.3) litre engines were employed by Harris and Zahalka (1983) for tests. The factory-fill crankcase oil was drained and the engines were flushed and recharged with test oil. Five different oils were evaluated with four cars assigned to each oil. The most interesting finding in their study showed that there were two phases of camshaft wear. For the oil in this test there was an initial break-in wear that occurred during the first (16,000 Km) followed by a second wear rate that was significantly lower. The higher wear rate was predominately dependent on engine break-in while the second phase was controlled by additive chemistry.

This conclusion was confirmed by Smalley and Gariglio (1982) who ran a laboratory test apparatus and presented the results of an investigation into the total wear process. A range of low alloy steel materials was either carburized or carbonitrided to produce a hard, wear resistant surface, and tested in a series of electrically driven car engine rigs. The electrical capacitance method was also used to measure the oil film thickness between the cam and tappet continuously. Three wear stages were detected: a high initial material loss where the phosphate layer was removed, a mild wear stage where a reduced wear rate existed and was characterized by the

presence of etched asperities still remaining from the phosphating treatment, and a final severe wear stage with a particularly high rate of weight loss and characterized by polishing wear. The results of oil film thickness measurement at the cam nose and flank suggested films of about (5 μm), which seem to be much greater than the theoretical results and implied full film lubrication existed on the cam nose and flank regions. This is contradictory to previous findings from theoretical and experimental studies.

To overcome the difficulties encountered in previous experiments for measuring the friction and temperature between the cam and follower conjunction, Bair et al (1986) designed a simulator which had a stationary follower and a camshaft which moved up and down. The follower was mounted on a triaxial strain gauge so that the normal force and the friction force could be monitored simultaneously, thus eliminating potential errors resulting from the uncertainties in the cam position or in the load as calculated from spring compression and inertia. The movement of the cam ensured the contacting point moved within a very small region, say less than (0.1 mm). A series of eight follower materials were investigated for frictional loss as a function of the speed. In addition the effects of lubricant temperature, the running-in process, follower rotation and follower spherical radius were studied. With one of a (Al_2O_3) followers, the surface temperature of the cam was measured at peak lift by employing an infra-red scanning system. Peak temperatures in excess of (300°C) were observed for some operating conditions. On the whole, this test apparatus has some conceptual advantages over the ones with a rotary torque transducer. Since the inertia or load acting on the cam has been changed due to the movement of the camshaft, this test apparatus is not suitable for evaluating overall friction torque arising from a practical engine valve train.

Other reports on the cam and follower experimental research in the recent literature have been given by van Helden et al (1985) and Sun and Rosenberg (1987) in which a conventional cam and follower contact was motored and friction was determined from data collected by a torque transducer attached to the camshaft.

A dramatic decrease of friction coefficients between the cam and follower from (0.12) to (0.05) in the cam flank regions was observed by van Helden et al (1985). This was in agreement with the theoretical predictions

from the non-steady elastohydrodynamic lubrication analysis. However, the conclusion put forward by Sun and Rosenberg (1987) based upon steady load experiments, using a round "cam", ruled out the possibility of elastohydrodynamic lubrication at the contact of the cam and follower. This conclusion seemed to be somewhat doubtful and was contrary to the general findings from the previous experimental work. As the entraining velocity in the vicinity of the contact point between the cam and follower was totally different from the situations existed in round "cam" conditions, the conclusion was not applicable to the practical cams and followers. In addition, the test equipment employed by Sun and Rosenberg (1987) suffered two major deficiencies: lack of temperature control and lack of experimental data processing to remove harmonics generated by drive system flexibility from the torque signal. The latter deficiency resulted in the superposition of an additional waveform on the friction versus cam angle curves, which could introduce considerable errors into the friction versus cam angle data.

In order to show the effects of surface roughness on the durability of the materials and the running-in process, Harrison (1985) initiated an experimental programme on a test apparatus. An electrical resistivity technique was adopted to estimate the film state with a high inertia voltmeter. The overall power losses of the valve train, with cams having different initial surface roughness, were measured by using a torque transducer. The experimental results showed that, whatever the initial surface roughnesses were, the composite surface roughness height would become about (0.2 μm) at the end of the running-in process. As a result, the average power losses for cams with different initial surface roughness showed no significant differences. The most interesting finding might be the very low percentage of the average voltage drop between the cam and follower conjunction, which was only about (4%). This implied the number of asperity contacts between the cam and follower was quite low. As the experimental bulk temperature was considerably lower than that in practical engines, this finding should be verified under conditions of bulk temperatures higher than (100°C). In addition, due to the cam action angle being only about one third of the whole cycle, the average votage drop and power loss would not be sensitive enough to the variations of operating conditions. Therefore the instantaneous torque and the instantaneous electrical resistivity should be investigated.

6.2.2 The Aim of the Present Experimental Programme

As part of a continuing effort to understand cam and follower tribological characteristics, the aim of the present experimental work was to investigate the tribological performance of the cam and follower at different bulk temperatures and different camshaft rotational speeds. The test apparatus has been equipped with thermostatic control facilities. It was to be run under practical environmental conditions with bulk temperatures higher than (100°C) to verify the previous findings. The qualitative estimations of the film state and lubrication conditions between the cam and follower were to be determined. The cyclic variations of the electrical resistivity measured between the cam and follower can be used for a qualitative comparison with the cyclic variations of the oil film thicknesses predicted by a non-steady state elastohydrodynamic analysis. The variables measured in the present experiment were:

(1) Average friction torque, power loss and speed
(2) Instantaneous torque required to drive the camshaft
(3) Average resistivity of the cam and follower conjunction
(4) Instantaneous resistivity versus cam angle
(5) Temperature on the cam nose, in the valve stem guide, of the sprayed lubricant and the bulk temperature in the main housing
(6) Camshaft position
and (7) Surface roughness, surface profile and material hardness of the cam and follower before and after test run.

6.3 The Modifications to The Apparatus

6.3.1 General Layout and Assembly

The general view of the apparatus is shown in Figure (6.1). A general assembly drawing of the apparatus is given in Figure (6.2) and a parts list is included. For the purpose of verifying the findings in Harrison's (1985) experimental research, the overall main construction of the camshaft system and valve/follower assembly remained unchanged. Considerable modifications were made to the lubricant spray system, slipring assembly and oil seal elements et cetera. The new functions added to the present test apparatus were bulk temperature control, lubricant spray temperature control and computer based ADC (analogue to digital convertor) data acquisition system with relevant softwares. A detailed introduction to these facilities is given in the following sections.

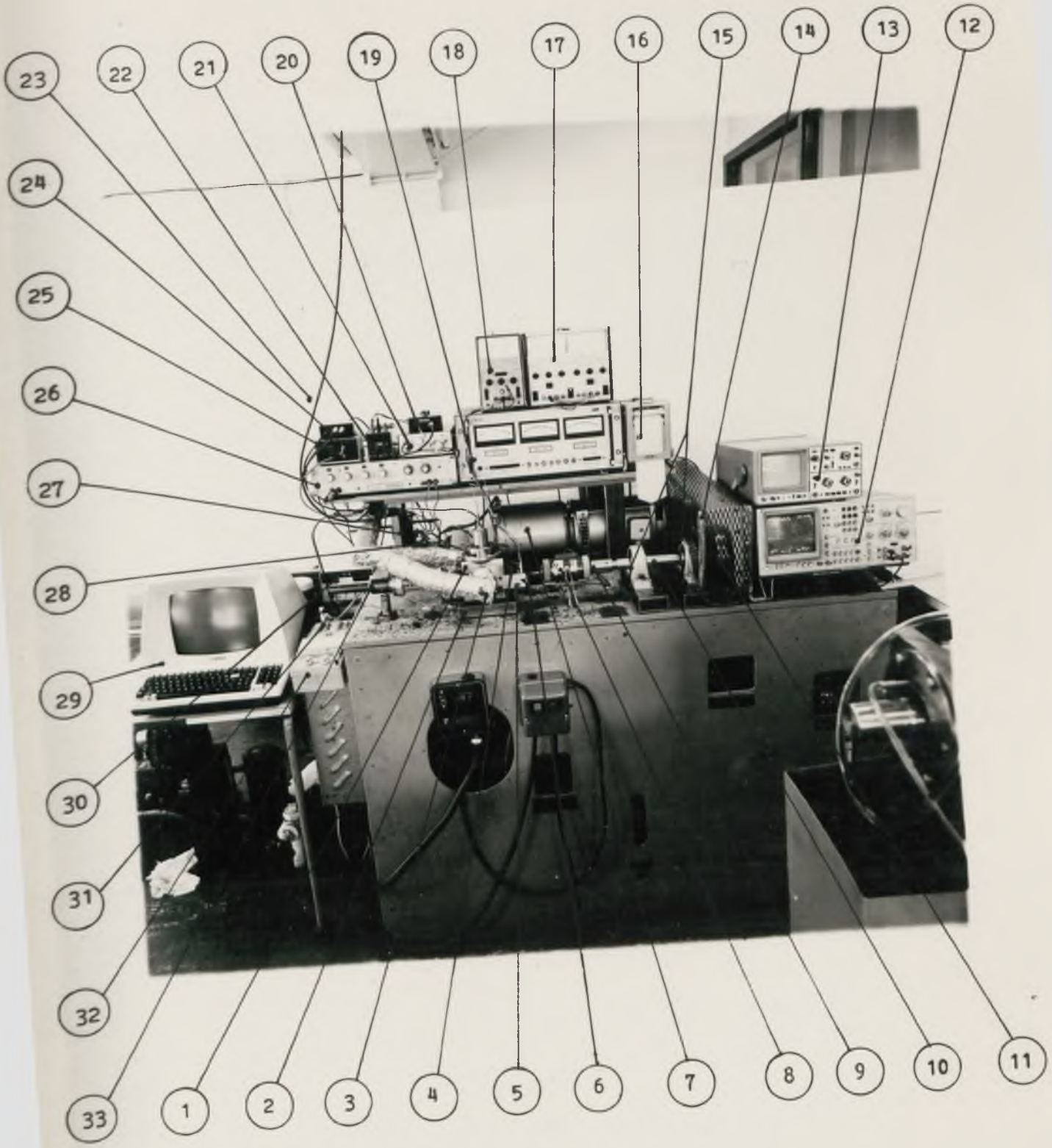

Figure (6.1) General view of the test apparatus.

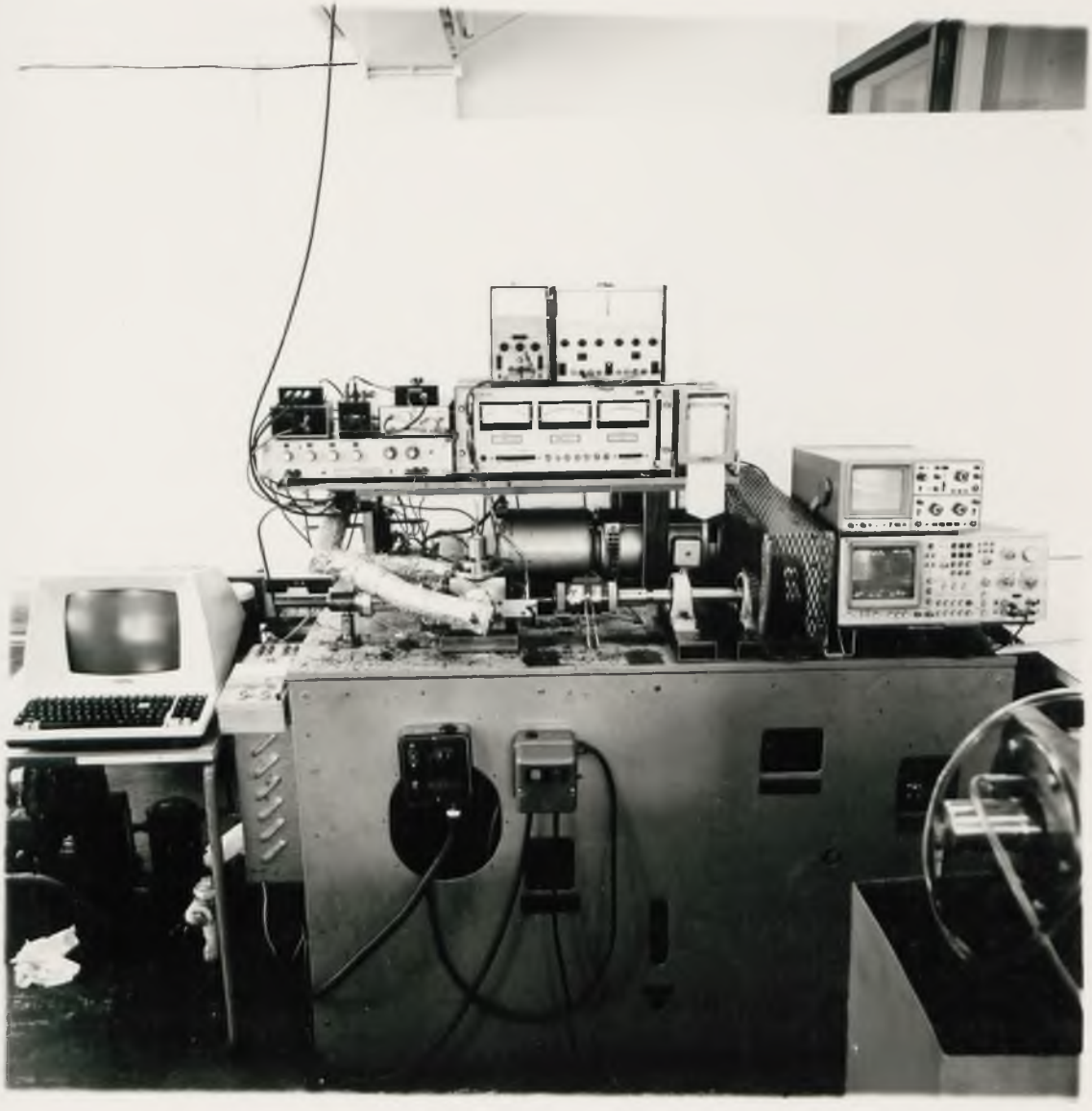

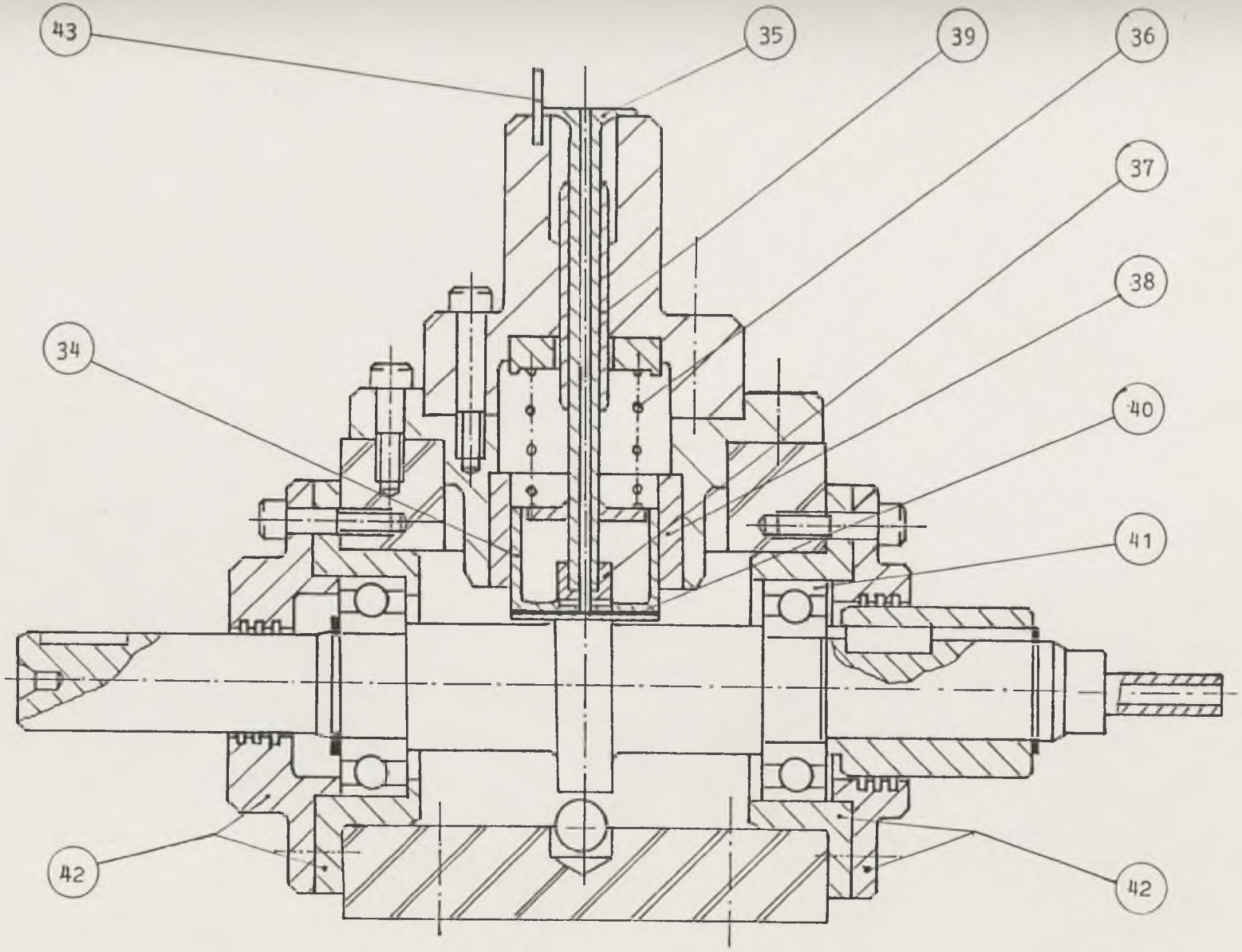

Figure (6.2) Details of the test apparatus.

APPARATUS PARTS LIST

[1] Main Housing

[2] Electric Heater

[3] T-Type Valve

[4] Trigger Disc

[5] Photo Cell

[6] Ebonite Connector

[7] TASC Unit and Motor

[8] Torque Transducer

[9] Keyed Connector (Steel)

[10] Mild Steel Main Shaft

[11] Flywheel (Driven Shaft)

[12] Spectrum Analyser

[13] Dual Trace Oscilloscope

[14] Vee-Belts

[15] Self-Aligning Bearings

[16] High Inertia Voltmeter

[17] Stabilized Power Supply

[18] Power Supply (Photo Cell)

[19] Indicator

[20] Resistivity Circuit

[21] Variable Gain Amplifier

[22] Millivolt Source

[23] Screen Cable

[24] Voltage Followers

[25] Amplifier

[26] Analogue Filter

[27] ADC Connecting Box

[28] Heater Controller

[29] Terminal

[30] Thermostat Circulator

[31] Selector Unit

[32] Electronic Thermometer

[33] Mercury Slipring

[34] Follower

[35] Valve

[36] Valve Spring

[37] Valve Cap

[38] Follower Guide

[39] Valve Guide

[40] Mica Biscuit

[41] Ball Bearing (Camshaft)

[42] Mica Mounts

[43] Guide Pin

[44] Nozzle Pipe

6.3.2 Mechanical Modifications to the Apparatus

In order to improve dynamic stability of the test apparatus and to reduce parasitic power losses arising from the camshaft system some modifications were made. A detailed description of these modifications is presented in this subsection.

A new flywheel [11] was mounted on the Vee-belt pulley at main shaft [10] driven end to reduce the fluctuations of the torque signal caused by the vibrations of the Vee-belts [14]. The flywheel was steel, (17.0 cm) in diameter and (2.9 cm) thick. To reduce the parasitic power losses arising from the oil seals, two lip-type oil seals were replaced by labyrinth-type seals cut on the mica mounts [42]. To prevent the valve [35] from rotating due to the friction force arising from the cam and follower conjunction, a half circle slot was cut on the valve head with a small guide pin [43] inserted in it.

Figure (6.3) shows the insulated wire for the resistivity circuit. Instead of soldering the wire on a bronze screw wedged behind the mica biscuit (Harrison (1985) Figure (7.4b)), it was welded directly onto the metal piece which is cemented onto the mica biscuit, so that the conductivity between the wire and the metal piece was greatly improved.

A four channel VIBRO mercury slipring [33] type (4-TMA/T) was adopted in the present test apparatus. The slipring was connected to the free end of the camshaft with a spring coupling. Two channels were used for the temperature measurement on the cam nose and one for the electrical resistivity measurement.

6.4 Lubricant Supply and Temperature Control

As the bulk temperature effects on the cam and follower tribological characteristics were to be investigated, a lubricant circulating system with thermostatic control and an electric heater were employed to obtain a controllable temperature environment in the main housing.

A HAAKE thermostat circulator [30] type (F3) supplied the lubricant to two nozzles located on each side of the cam and follower conjunction as shown in Figure (6.4). Each nozzle pipe [44] was connected to a (6 mm) inner-diameter copper lubricant supply pipe through a two way T-type valve [3]. The other outlets of the valve were used for measuring the oil flow

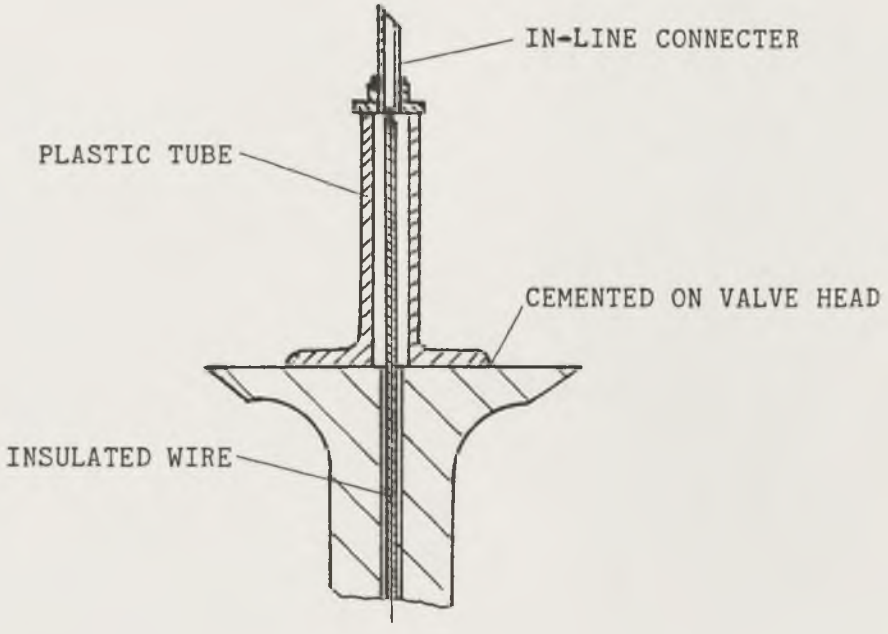

(a) Prevention of movement and breakage of the insulated wire

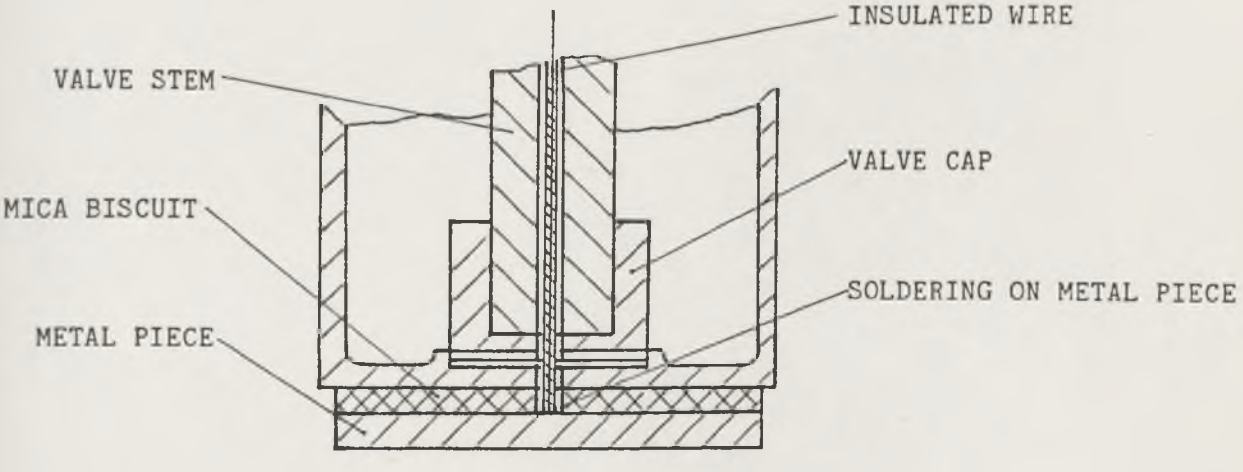

(b) Improving the connection between the metal piece and insulated wire

Figure (6.3) Details of the arrangement of the insulated wire

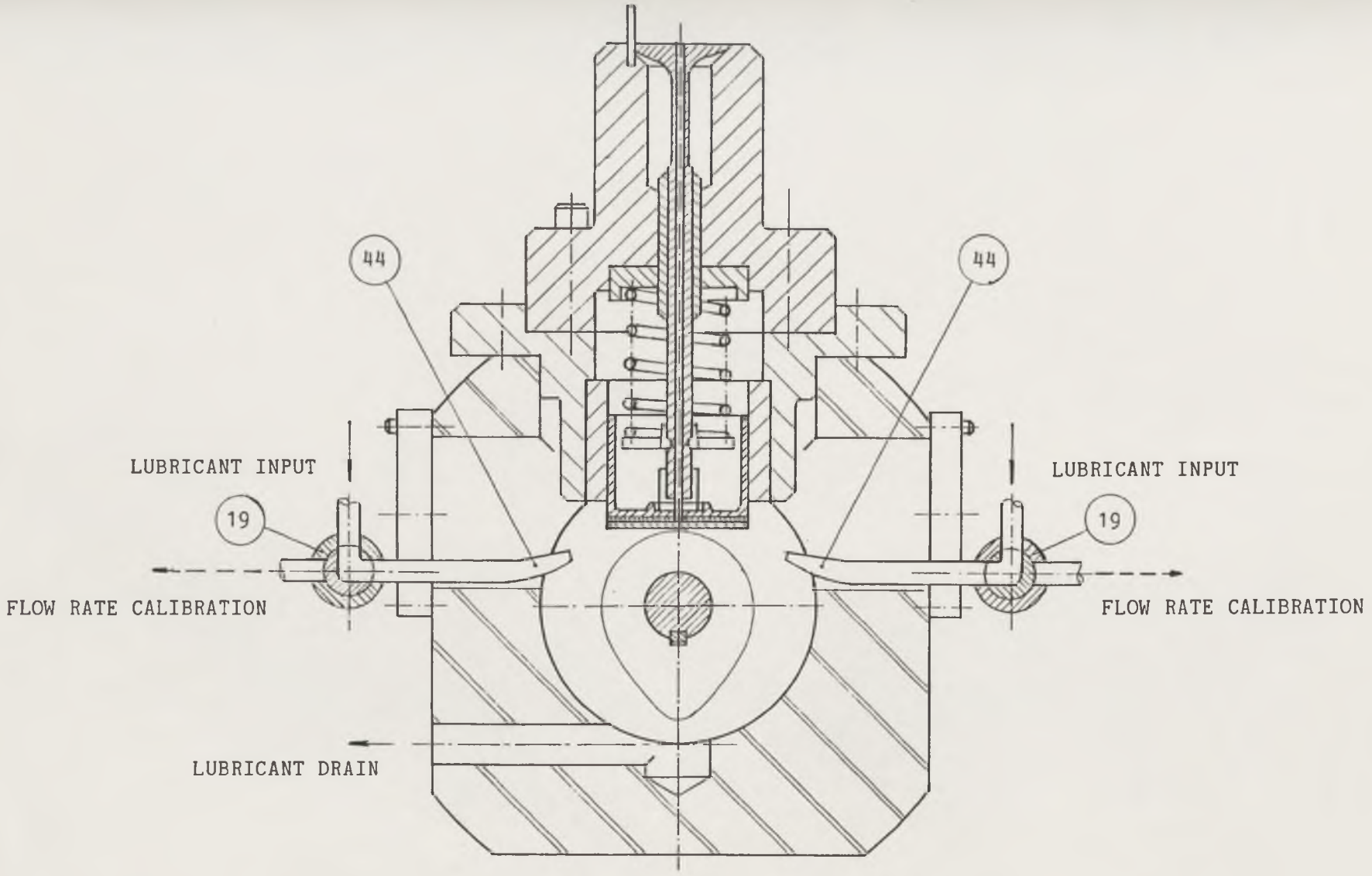

Figure (6.4) Showing the method of lubricating the cam and follower

rate. The temperature of the lubricant spray was monitored with two nickel/chromium thermocouples embedded on the tips of the nozzle pipes. A Comark electronic thermometer [32] type (1604-2) and a Comark selector unit [31] type (1694F) were used to display the temperature. The lubricant was drained through a hole at the bottom of the main housing and returned to the oil tank of the circulator. All the lubricant pipes were wrapped with thermal insulation to reduce heat dissipation.

The main housing [1] was heated by the electric heater [2] inserted beneath the main housing and thermally insulated from the test base with a mica piece. The sensor of the electricity heater controller [28] (a nickel/chromium thermocouple) was glued on the main housing surface. The cam and follower bulk temperature was monitored by two thermocouples cemented on the inside wall of the main housing in the vicinity of the camshaft support bearings. The trigger temperature of the heater controller was dependent upon the bulk temperature detected by the two thermocouples inside the main housing.

6.5 Instrumentation

The instrumentation adopted in the present experimental study was divided into five main parts:

(1) Torque, speed and power loss measurement
(2) Film state measurement by the resistivity technique
(3) Temperature measurement
(4) Optical camshaft position trigger
and (5) Computer based data acquisition system.

6.5.1 Torque, Speed and Power Loss Measurement

A line diagram of the apparatus used for the measurement of torque, speed and power loss is presented in Figure (6.5). The measurements were undertaken by two systems operating simultaneously. They were:

(a) Average torque and power loss measurement
(b) Instantaneous torque measurement.

6.5.1a) Average Torque and Power Loss

As shown in Figure (6.1), an EEL torque transducer [8] type (TT2.4.AD) was connected in line with the camshaft. As a load was applied on the cam, the shaft of the torque transducer twisted, resulting in variations of the

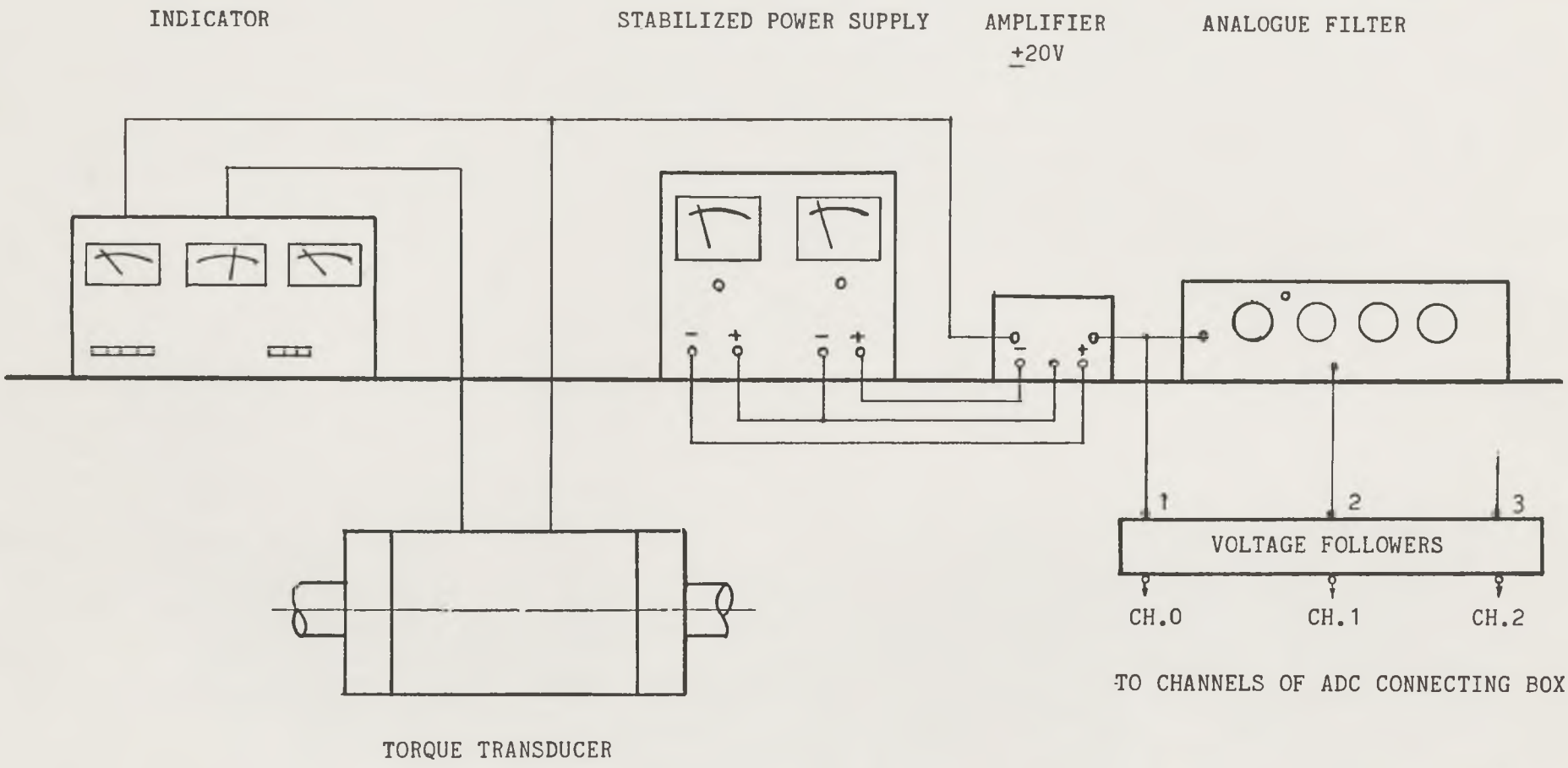

Figure (6.5) Line diagram of the apparatus used for torque, speed and power loss measurement

strain measured by the strain gauges cemented to the transducer shaft. The electrical signal was fed to an EEL indicator [19] type (TM30.3) which indicated the average torque. The rotational speed was obtained by a photo cell triggered by marks on the transducer shaft. The indicator converted the triggered signal into rotational speed. The power loss was estimated by electronically integrating the product of the torque and rotational signals. The average torque, power loss and rotational speed could be read simultaneously from the indicator [19].

6.5.1b)Instantaneous Torque Measurement

As the cam action angle was only about one third of the whole cycle, the sensitivities of average values to variations in operating conditions must be quite low. In addition, the cam and follower enjoyed various lubrication conditions in different cam portions resulting in dramatic changes of the friction coefficient during the operating cycle. For the precise estimation of the friction coefficient the instantaneous torque must be measured in the present experiment. The torque signal was magnified to a level which is high enough to prevent it from being interrupted by noise before it was sent to the VAX/8600 computer through a long screen cable [23]. The amplifier [25] was made by the Electronic Workshop of the Department of Mechanical Engineering. As the maximum input level of the ADC multiplexor was (10 V), the gain of the amplifier was set to be about (300).

The magnified signal was fed to the voltage followers [24] which has high input impedance and very low output impedance with the gain being (1.0) and then to the channel zero of the ADC multiplexor which converted analogue signals to digital data. In order to remove the harmonic components from the torque signal, caused by camshaft torsional vibrations, a ROCKLAND analogue filter [26] type (1020F) was used. The analogue signal output from the filter was sent to the channel one of the ADC multiplexor and also digitalized.

6.5.2 Film State Measurement

Because of difficulties encountered by previous workers when using various techniques to achieve a direct measurement of the film thickness between a cam and follower, it was thought that the electrical resistivity technique should be used to give a qualitative indication of the film state or cyclic variations of the film thickness between the cam and follower under different operating conditions. For the purpose of comparing the present

experimental results with the previous results (Harrison (1985)) a RECORD high inertia voltmeter [16] was retained in the present experiment for average resistivity measurement. As there was no meaningful results obtained from the contact counting measurement in the previous experiment (Harrison (1985)) this measurement was not performed. In order to measure the cyclic variations of the resistivity between a cam and follower conjunction the instantaneous resistivity signal (voltage across the contact of the cam and follower) was also recorded at the same moment. A line diagram of the apparatus for the measurement described above is shown in Figure (6.6).

For the resistivity measurement the camshaft and the end of the follower were electrically isolated from the other parts of the test apparatus. An insulated wire was soldered to the end of the follower, passing through the centre of the valve, and connected to one end of the resistivity circuit shown in Figure (6.7). The mercury slipring [33] coupled to the free end of the camshaft by a spring coupling allowed the connection to the resistivity circuit to be made.

The circuit for the resistivity measurement is shown in Figure (6.7). It was based on the circuit used by Harrison (1985). The variable resistor (R_3) represented the resistance of the oil film. A low impedance D.C. voltage was supplied from a TIME millivolt source [22] type (404S) to the input side of the resistivity circuit [20]. Resistor (R_1) was adjusted to give a voltage drop of (50mV) across (R_3) when the cam and follower were separated. This small voltage was deemed to be high enough to prevent the signal from being affected by noise. Thus the cyclic variations of the oil film thickness and asperity contact led to the variations of the resistivity between the cam and follower, hence the voltages across the resistor (R_3).

The voltage signals across the resistor (R_3) were enlarged by a variable gain amplifier [21] and then sent to the high inertia voltmeter which gives a continuous record of the average voltage drop across the contact. At the same moment the amplified voltage signal across the resistor (R_3) was fed to the channel two of the ADC multiplexor of the computer in which they were digitalized and stored. A detailed introduction to the data acquisition system employed in the present experiment will be given in the last section of this chapter.

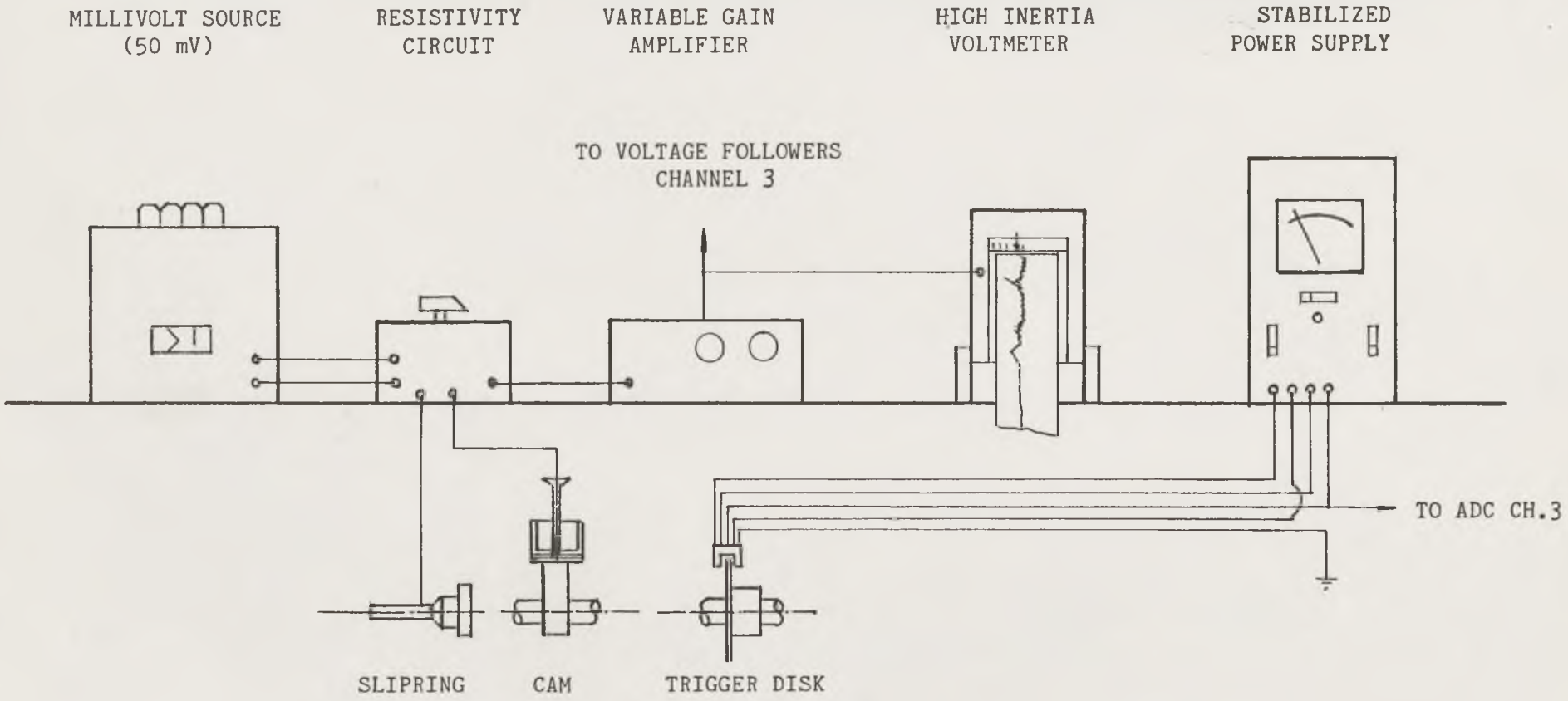

Figure (6.6) Line diagram of the apparatus used for the film state and cam position measurement

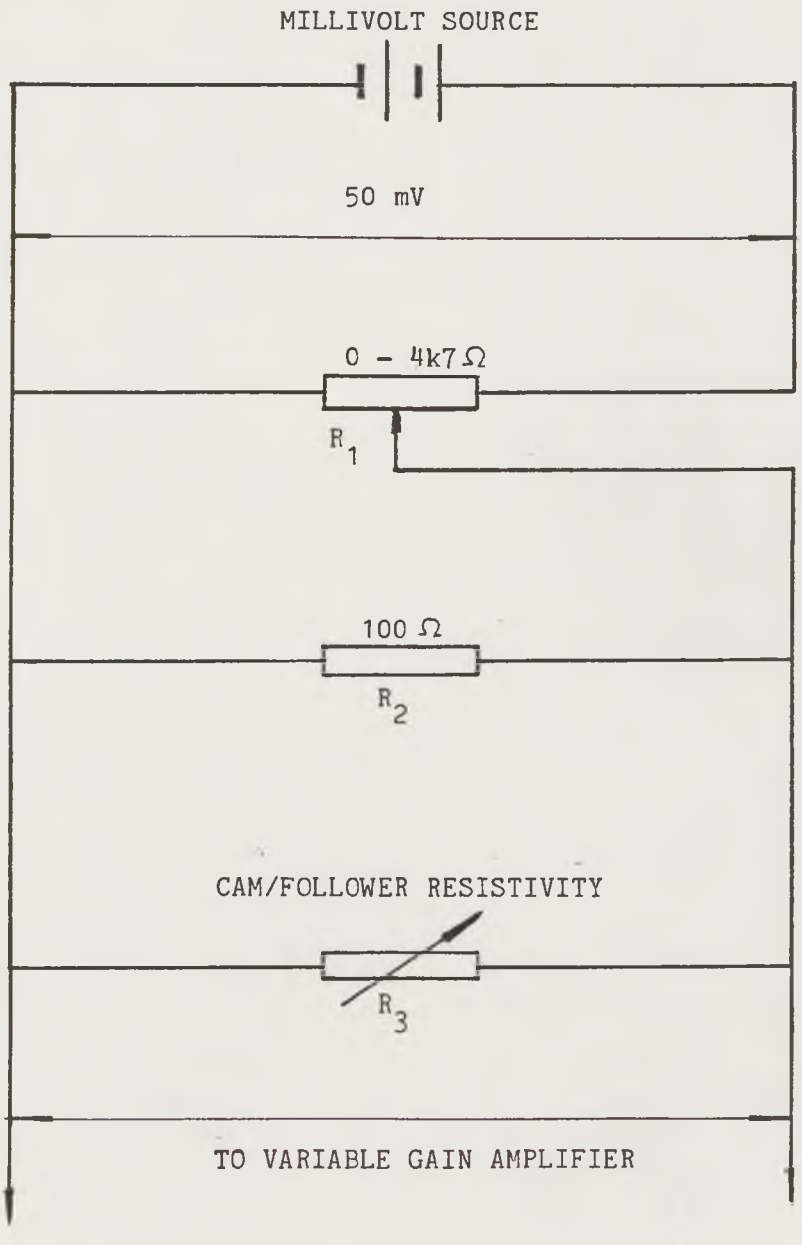

Figure (6.7) Circuit used for resistivity measurement

6.5.3 Temperature Measurement

All temperatures measured at given positions were performed with nickel/chromium thermocouples except for the oil sump temperature which was monitored by a semiconductor thermometer assembled in the circulator. In the present experiment the temperatures of the cam nose, valve stem guide and lubricant spray were investigated as well as the bulk temperature in the main housing.

For estimating the temperature just below the surface of the cam nose, a (0.8 mm) diameter inclined hole was drilled from one side of the cam to the centre plane of the cam about (1 mm) below the cam nose surface. The thermocouple inserted was connected to the mercury slipring through the hole in the centre of the camshaft. The thermocouple embedded in the valve stem guide was (1 mm) away from the inner surface of the value guide. The bulk temperature in the main housing was detected by two thermocouples cemented to the inside wall of the housing, about (10 mm) away from the camshaft support bearings. The temperature of the lubricant spray was monitored by two thermocouples which are stuck on the centre of the tips of the spray nozzle. An electronic thermometer and selector unit were adopted to display the value of the temperature detected by each thermocouple.

6.5.4 Camshaft Position

The camshaft position was determined by a pulse generated with a photo cell [5] which in turn was triggered by a disk [4] mounted on the ebonite connector [6]. The trigger was set at the base circle of the cam (90°) ahead of the point of the maximum cam lift. The impulse signal was fed to the channel three of the ADC multiplexor and converted into digital data stored in the same data file together with torque and resistivity signals. This enabled all digitalized signals to be correlated with the cam angle, so that comparisons could be made between experimental results and theoretical predictions. The photo cell was powered by a FARNELL power supply [18] type (L30B).

6.5.5 Data Acquisition System

A VAX/8600 computer based data acquisition system was adopted in the present experiments. The system consisted of two main parts, software and hardware.

The software, the routines in the ADC package provided a conventional

FORTRAN user interface to the Micro Consultants VHS analogue to digital converter on the VAX-11/780. The analogue to digital convertors were interfaced via a direct memory access interface (DR-11B) and allowed a maximum data sampling rate of (200 KHz) at fourteen bits. An input of (10 V) gave a value of (8192).

The hardware of the ADC system was provided with an eight channels multiplexer and channel zero to three were fitted with a parallel sample. This allowed the user to specify the start and finish channel. At specified intervals all the channels from 'start' to 'finish' were digitalised and the values were put into the memory of the computer. A terminal [29] connected to the VAX/8600 computer was equipped to run the FORTRAN program for the data collection operation. If it was desired the digitalised signals from each channel could be displayed on the screen immediately after the data collection run.

CHAPTER 7

CALIBRATIONS TO INSTRUMENTATION AND COMMISSIONING EXPERIMENTS

7.1 Introduction

A detailed introduction to the calibration of instrumentation for measuring the torque, electrical resistivity and temperature is given in this chapter. The results of the calibration have shown that the instrumentation adopted in the present test is reliable. The linearity and dynamic characteristics of the torque measurement system are good enough to allow the measurement of the instantaneous torque required to drive the camshaft.

Several hundred hours of auxiliary tests run with different camshaft rotational speeds indicated some dynamic characteristics of the camshaft system. Consequently the experimental rotational speeds were determined. In addition, the spring coupling on the mercury slipring was replaced by a piece of plastic tube to obtain more stable torque signals.

With a modified construction of the bucket follower assembly and the adoption of a new kind of adhesive, the test apparatus ran successfully under high bulk temperature conditions up to (120°C).

Commissioning tests with different bulk temperatures and different rotational speeds showed that results obtained with the test apparatus were consistent and repeatable. The preparation of experimental specimens, cams and followers, is also described in this chapter.

7.2 The Calibration of the Instrumentation

7.2.1 Calibrations for the Temperature Measurement

Six thermocouples were employed in the present test apparatus; two for indicating the bulk temperature in the main housing, two for monitoring the temperature of the inlet lubricant spray, one for the temperature on the cam nose and one for the temperature in the valve guide. Each thermocouple was connected to one channel of the selector. A Comark electronic thermometer was adopted to display the temperature.

Before the thermocouples were fixed in their positions, all of them were immersed in ice water in which the temperature was assumed to be zero degrees centigrade. The shift of the temperature measured by each thermocouple from zero degrees was less than (0.2°C). When the test

apparatus was static and in a thermally balanced condition, all thermocouples assembled in the apparatus should indicate the room temperature. Comparisons were made between the temperature measured by each thermocouple and the temperature indicated by a mercury thermometer. The maximum relative difference was less than (2%). Such calibrations were performed several times under different room temperatures. Similar results were obtained.

7.2.2 Calibration of the Electical Resistivity Measurement Equipment

The contact electrical resistivity between the cam and follower was measured by applying a (50 mV) voltage between the cam and the follower through the resistivity circuit presented in Figure (6.7). The gain of the variable gain amplifier was set to be (100), thus the maximum output voltage from the amplifier was (5 V). The applied voltage (50 mV) and the output voltage (5 V) of the amplifier were checked by a KEITHLEY TRMS digital avometer type (179A).

The calibration of the high inertia voltmeter was performed by applying zero and (5 V) D.C. signals to its input side. Some adjustments were made on the voltmeter until the marks on the recording paper indicated zero and (5 V) respectively.

7.2.3 Measuring the Lubricant Flow Rate

The lubricant flow rate was measured by turning two way T-type valves to their outlet channels. Instead of flowing into the main housing, the lubricant flowed into two volumetric cylinders. After two minutes the valves were turned back to their original positions. Under different bulk temperature the flow rate was kept almost the same by adjusting a valve fixed on the lubricant supply pipe, with the flow rate measured at the same time. The lubricant flow rate in the present experiments was about (3.4 cm^3/S). During the test run, the actual flow rate might be slightly greater than the one measured. This was owning to the suction effect of the circulator.

7.2.4 Measurement of the Camshaft Rotational Speed

Since the camshaft rotational speed displayed on the indicator was not accurate enough for the present test, a spectrum analyzer was adopted for indicating the speed. The rotational speed could be worked out from the basic frequency component existing in the frequency spectrum of the torque

signal.

In addition, the camshaft rotational speed could also be calculated from the impulse signal which is triggered once per camshaft revolution by the photo cell. The impulse signals were sampled and digitalized in the computer. The differences between the rotational speeds indicated by the spectrum analyzer and that calculated from digitalized impulse signals were less than (1%).

7.2.5 The Calibration of the Torque Measurement System

The torque measurement system was composed of the torque transducer, amplifier, voltage follower, screen cable and ADC multiplexer. As the maximum sampling rate of the ADC multiplexor was (200 KHz), the band width of the measurement system was mainly dependent upon the amplifier.

The static calibration of the amplifier was performed by applying known voltages from a millivolt source to the amplifier and recording the output voltages. A simple linear regression of the input and output voltage data pairs was performed. The results of the regression together with the data pairs are presented in Figure (7.1). As can be seen the correlation between the regression results and the calibrated data pairs was excellent. The linearity of the amplifier was also quite good in the whole of the calibrated region which covered the maximum and the minimum possible input voltages generated by the torque transducer under practical operating conditions. The gain of the amplifier was found to be of (300.79).

High frequency sine wave and square wave signals generated by a SINE SQUARE OSCILLATOR type (SS0603) were fed to the amplifier. Both input and output signals were monitored with a dual trace HAMEG 20MHZ oscilloscope [13] type (HM204). The comparison between the input and the output signals showed that the bandwidth of the amplifier was about (28 KHz), which is adequate for the present measurement. The phase shift of the output signal from the input signal was very small and could be neglected.

Further more, the torque measurement system was calibrated as one 'Black Box' to eliminate the influence arising from each element of the measurement system. By applying a known torque to the torque transducer, the output signals which are sampled by the ADC multiplexor were displayed on the screen of the terminal which is connected to the (VAX/8600)

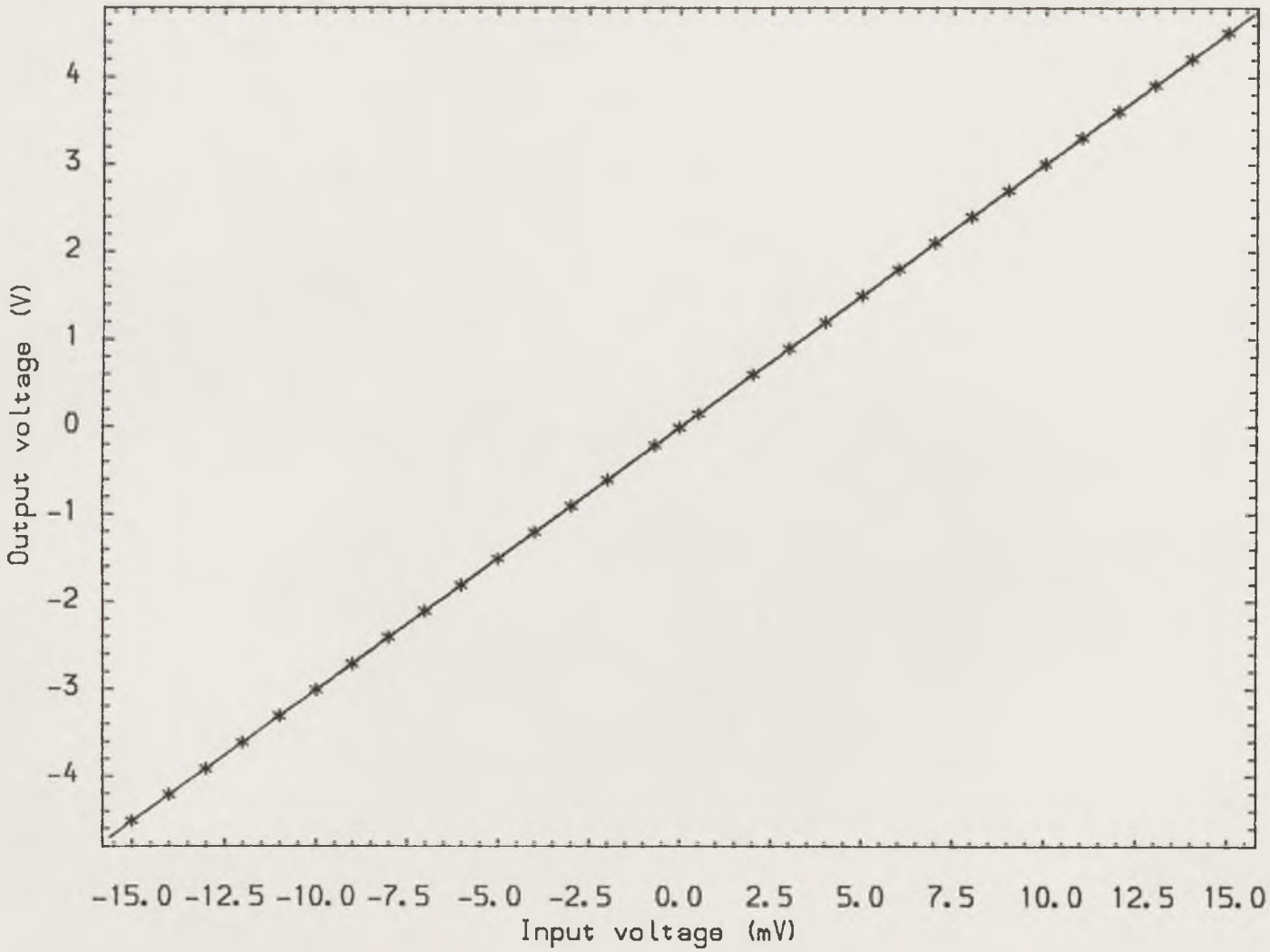

Figure (7.1) Calibration of the amplifier of the torque measurement system

computer. In the present calibration the sampling rate of the ADC multiplexer was (5 KHz). In each sampling operation (32764) data points were collected and stored in the computer, then the average value of these data points was evaluated. For each applied torque such sampling and averaging operations were repeated five times. Finally, the output voltage of the torque measurement system corresponding to the applied torque to the transducer was calculated by averaging the five averaged values of the sampling operations. The torque loaded on the transducer was increased with (0.245 N-m), (0.49 N-m) and (1.23 N-m) increments from (−10 N-m) to (+10 N-m) in twenty-six steps and then decreased from (+10 N-m) to (−10 N-m) step by step. The smaller the torque applied to the torque transducer the smaller was the increment adopted. A simple linear regression with twenty-six pairs of applied torques and output voltages was carried out. A straight line of the form;

$$T = 2.92803\ V - 2.3127 \quad \text{(N-m)} \qquad (7.1)$$

with data points (V_1,T_1), (V_2,T_2), ... (V_{26},T_{26}) was obtained. The mean square of deviation about the regression was about (0.00004 N-m). The results calculated using equation (7.1) are presented in Figure (7.2) together with the twenty-six calibrated data pairs. Figure (7.2) shows that the linearity of the torque measurement system was also excellent. Such calibrations were repeated several times and similar results were obtained.

7.3 Commissioning Experiments

As so many modifications had been made to the test apparatus, it was necessary to assess its performance capability for the operating conditions envisaged. The auxiliary experiments described in this section were to estimate the dynamic characteristics of the camshaft system rotating with different speeds and to verify the reliability of the test apparatus running under high bulk temperature conditions. At the same time the software developed for the data sampling and processing was also to be tested.

Four pairs of cam and follower specimens were used in the auxiliary experiments. Three of them failed (under different bulk temperature conditions) due to the failure of the conjunction between the metal piece and the mica biscuit cemented onto the bucket follower. With improved thermal conductivity between the metal piece and the bucket follower and by employing a new kind of adhesive, the last auxiliary test ran successfully

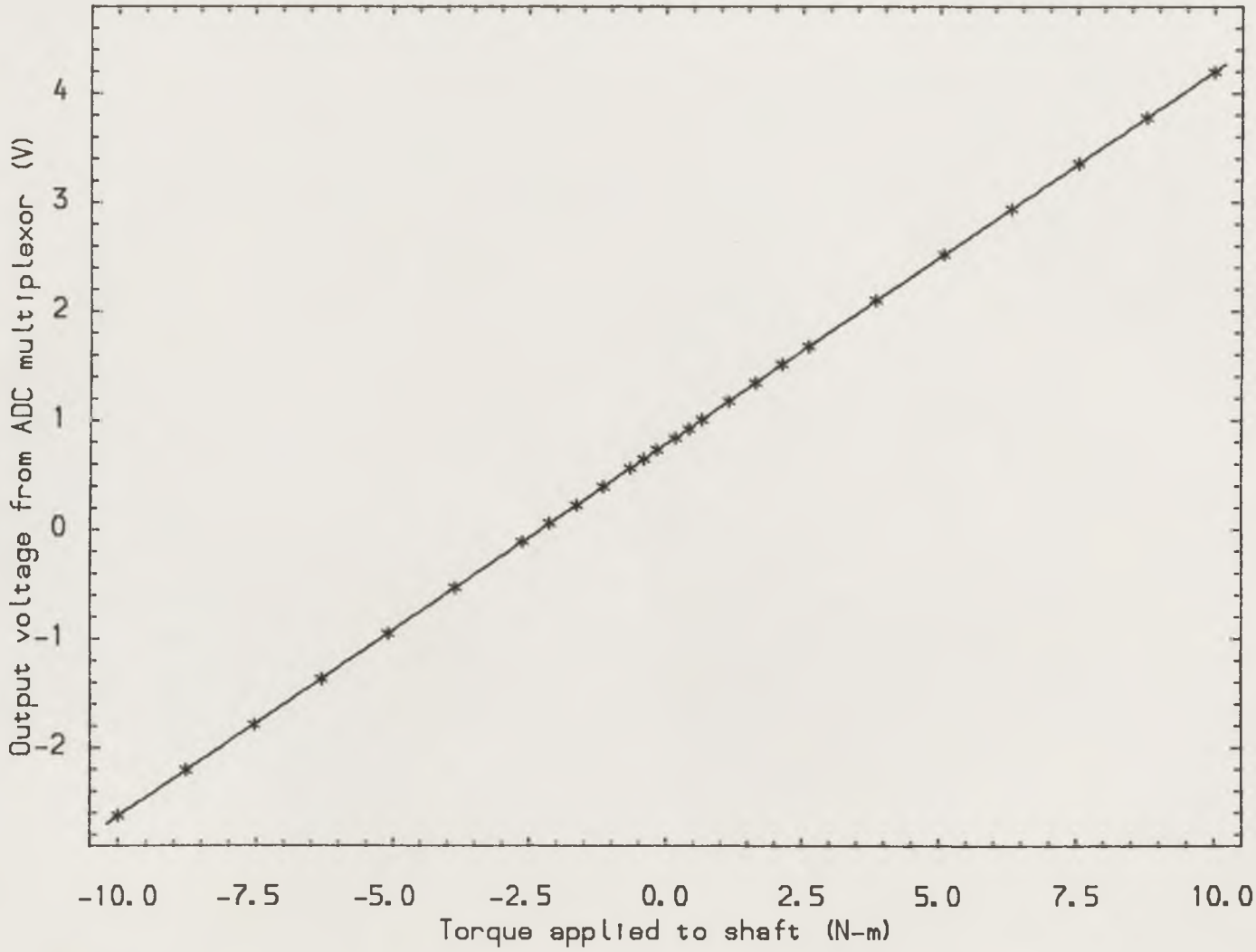

Figure (7.2) Calibration of the torque measurement system

for more than two hundred hours under different bulk temperatures varied by (15°C) from (50°C) to (120°C), and under different rotational speeds increased from (440 rpm) to (2200 rpm). Most of the results presented in this section were obtained from the last auxiliary test run.

7.3.1 Auxiliary Tests at Different Camshaft Rotational Speeds

7.3.1a) The Main Frequency of Torsional Vibration of Camshaft System

The original torque signal presented in Figure (7.3a) looked quite different from the one predicted by the theoretical analysis. It seemed that a high frequency signal was superimposed on the expected torque signal. This phenomenon was reported by Harrison (1985), but he did not explain where the source of the high frequency signal.

It was known that the torque with the follower on the cam base circle was only caused by the frictional force arising from the camshaft supporting bearings and remained at the same value over the whole base circle region. The characteristic features of the torque signal measured in this region looked quite similar to those of a damped free vibration. Thus it was supposed that the high frequency signal might come from the torsional vibration of the camshaft system itself.

Frequency spectrum analyses of the torque signals under different camshaft rotational speeds revealed that there was always an amplitude peak appearing in the region of frequency between (155 Hz) and (175 Hz). At certain camshaft rotational speeds, the amplitude of the peak would be much higher than that of other higher order frequency components. A typical frequency spectrum of the torque signal at the camshaft rotational speed of (1200 rpm), or rotational frequency of (20 Hz), is presented in Figure (7.3b). The frequency at which the high peak appeared was (160 Hz). This phenomena implied that at certain speeds, the main rotational frequency and its higher order frequency components would excite severe torsional vibrations at a frequency close to the natural torsional frequency of the camshaft system. The value of the natural frequency of the camshaft system was somewhere between (155 Hz) and (175 Hz).

Furthermore, an impact test performed on the cam nose confirmed the conjecture mentioned above. The response signal as measured by the torque transducer is presented in Figure (7.4a) which indicates a typical damped

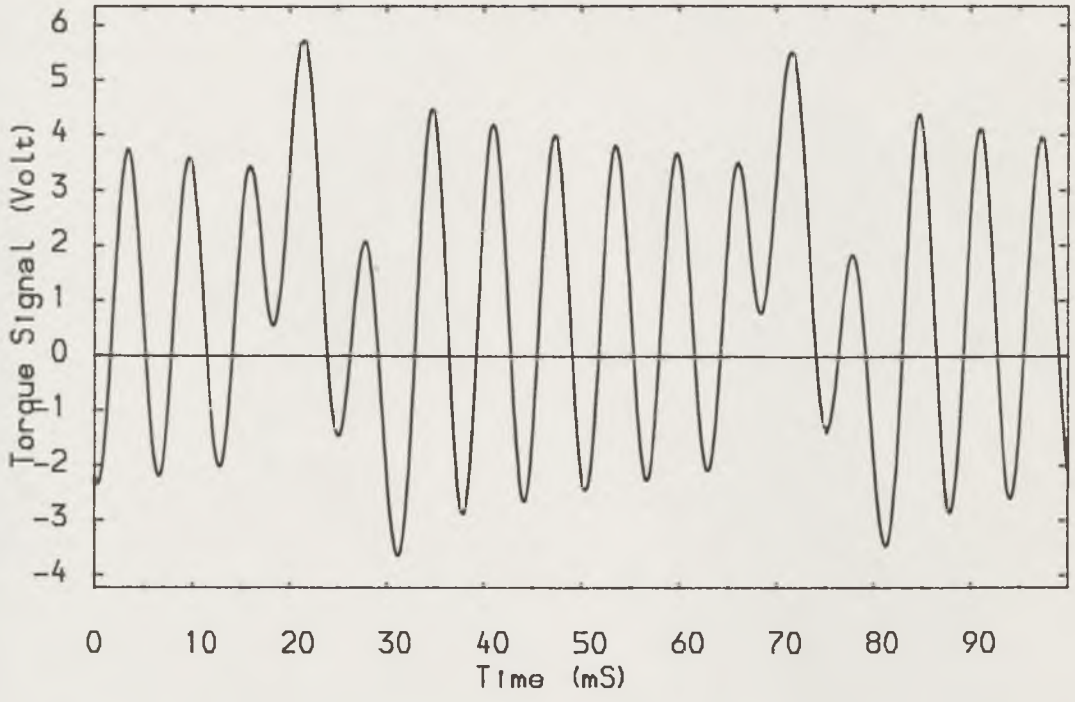

Figure (7.3a) Original torque signal with 1200rpm camshaft rotational speed and (120°C) bulk temperature

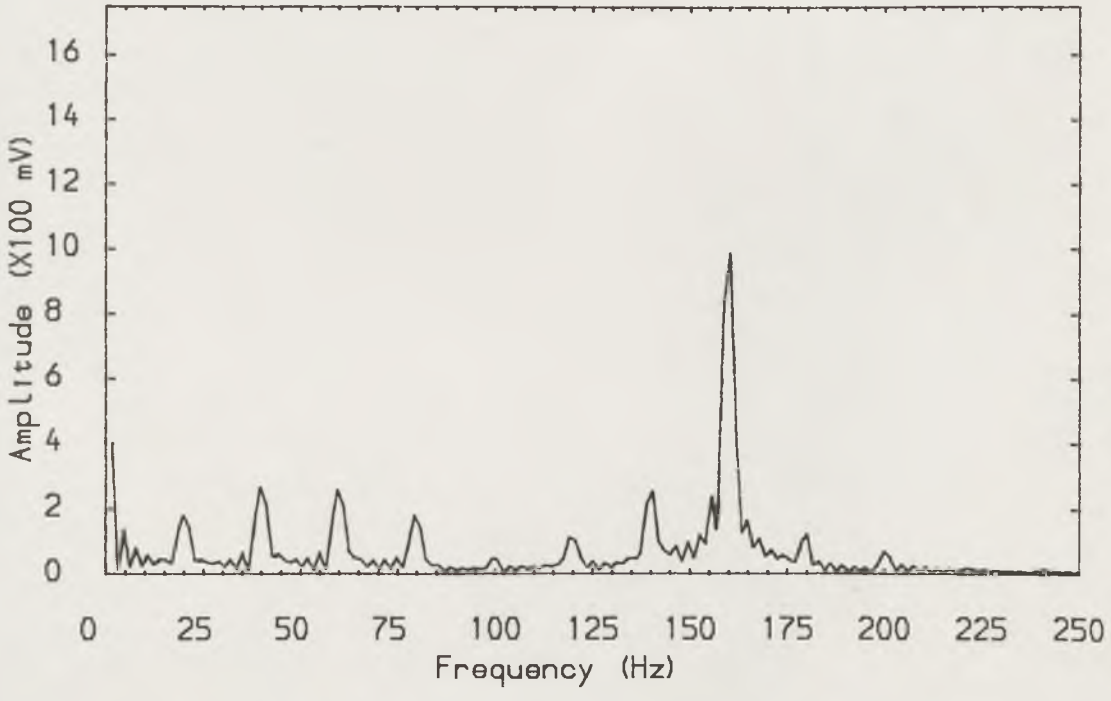

Figure (7.3b) Frequency spectrum of the torque signal shown above

free vibration. The frequency spectrum of the signal is shown in Figure (7.4b). It can be seen that the main energy of the vibration was concentrated in a narrow frequency band between (155 Hz) and (175 Hz) with a peak occuring at a frequency of (165 Hz).

It was also found that the spring coupling of the mercury slipring connected to the free end of the camshaft excited a low frequency torsional vibration of the camshaft system. Reducing the stiffness of the spring coupling by replacing the spring with a piece of plastic tube eliminated this low frequency vibration. As a result the torque signal looked more stable than before.

7.3.1b) The Determination of the Camshaft Rotational Speed

As described above, under certain camshaft rotational speeds severe torsional vibrations would be induced by the rotational frequency and its higher order frequency components. In order to reduce the influence of such vibrations on the torque signal, the camshaft should rotate with the frequency whose higher order frequency components are furthest away from the frequency of (165 Hz).

Since the rotational speed was one of the experimental variables, a series of auxiliary tests at different speeds was carried out. The frequency spectrums of the torque signals showed that if the camshaft ran with speeds of (440 rpm), (650 rpm), (1030 rpm), (1240 rpm), (1470 rpm), (1820 rpm) and (2070 rpm), the amplitudes of the torsional vibrations would be much lower than those occurring at other speeds around the values listed above. The torque signals and their frequency spectrums at these speeds are recorded in Figure (7.5).

7.3.2 Auxiliary Tests at Different Bulk Temperatures

The test apparatus was run at different bulk temperatures to make sure that the apparatus could work normally with high bulk temperature conditions. Under natural conditions, without heating the lubricant in the thermostat circulator, the test apparatus reached thermal balance after running for about ten hours. The bulk temperature in the main housing and the lubricant spray temperature were about (50°C). This was the lowest experimental bulk temperature at which the test apparatus could run.

Running the test apparatus at high bulk temperatures up to (120°C) led

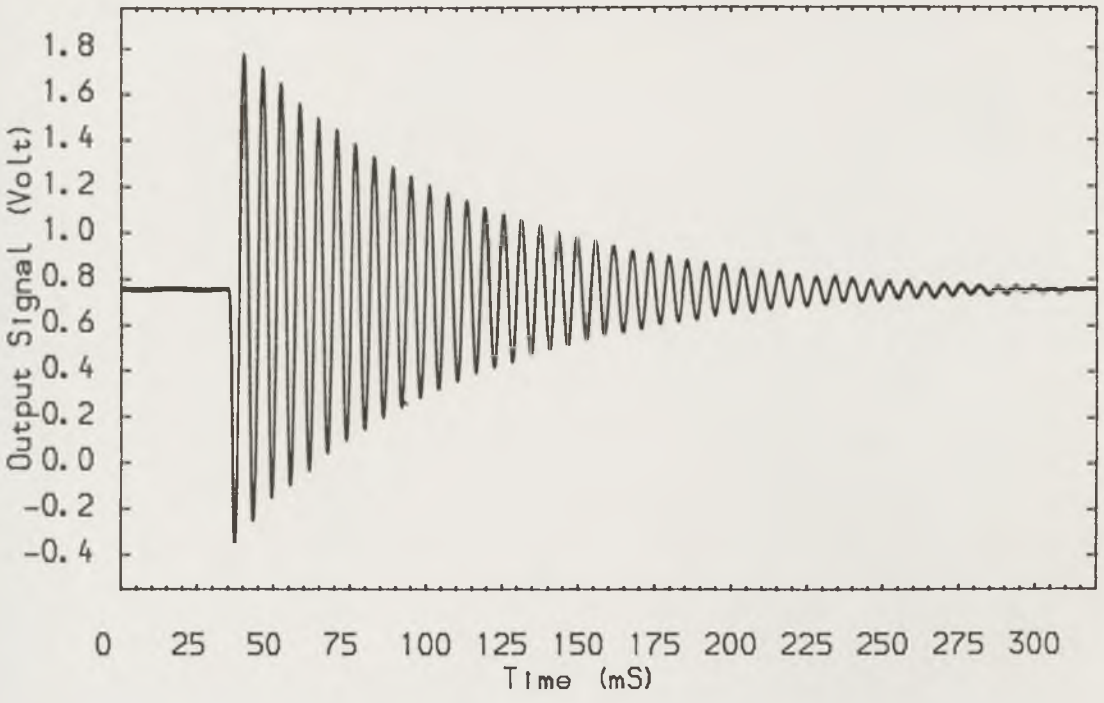

Figure (7.4a) Output signal of the torque transducer from the impact test.

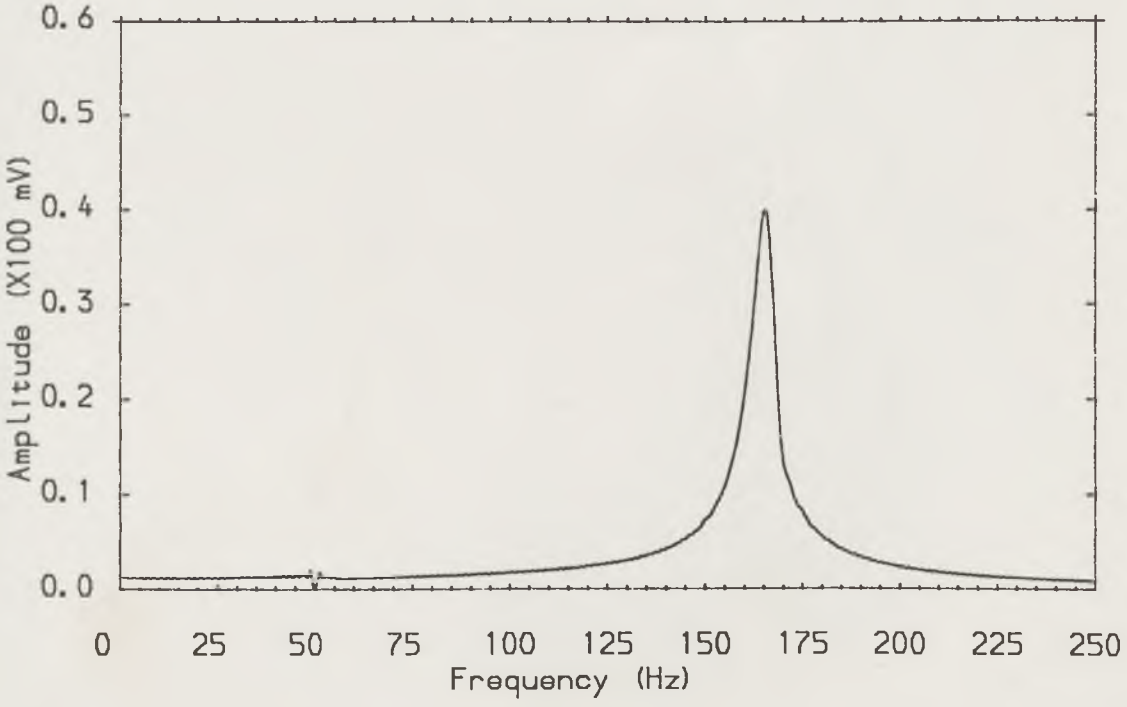

Figure (7.4b) Frequency spectrum of the output signal shown above

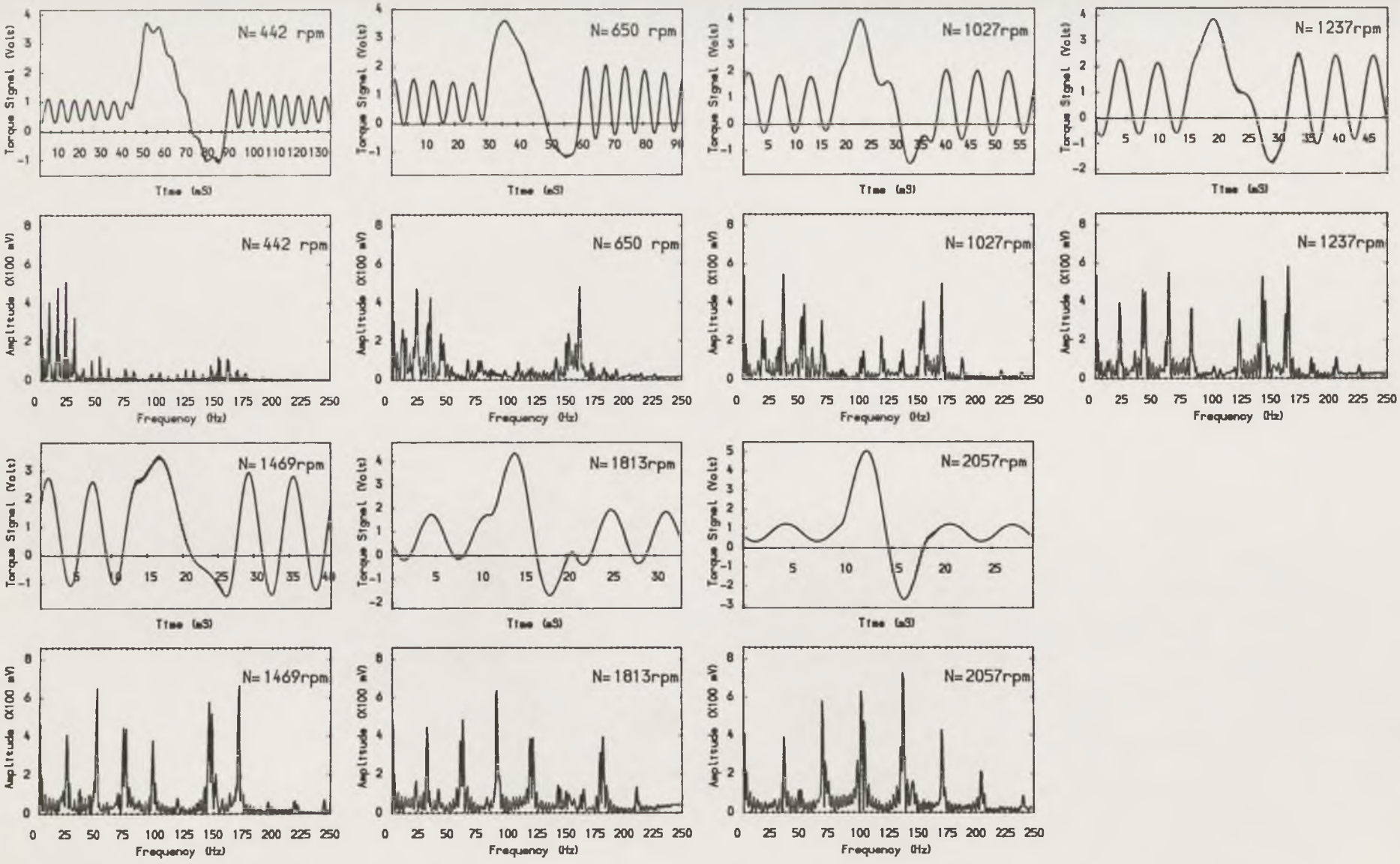

Figure (7.5) Torque signal and frequency spectrum with different camshaft rotational speeds with (105°C) bulk temperature.

to the failure of the adhesive which is used to cement the metal piece and the mica biscuit onto the bucket follower. A PERMBOND ESP110 adhesive was adopted as an alternative. Since the adhesive itself was a good thermal conductor, some modifications were made to the mica biscuit to improve the thermal conductivity between the metal piece and the bucket follower, which in turn will result in a decrease in the temperature that the adhesive has to tolerate. In order to do so the thickness of the mica biscuit was reduced from (0.8 mm) to (0.35 mm) and thirty (2 mm) diameter holes were drilled on it. As a result of these modifications the test apparatus ran successfully with (120°C) bulk temperature conditions.

At high bulk temperature conditions, some heat will be conducted from the camshaft to the torque transducer shaft and consequently the temperature in the transducer will rise. If the temperature exceeds the tolerant operating temperature of the transducer severe errors may occur in the measured torque signal. In order to investigate the bulk temperature effects on the torque transducer two twenty-four hour long duration tests were undertaken, one at a low bulk temperature of (50°C) and another at a high bulk temperature of (120°C). At the end of each test the static output voltages from the torque transducer was sampled and stored in the computer. Average values of the sampled data from each test run were almost the same. This meant that the variations of the bulk temperature in the main housing had little effect on the output voltage of the torque transducer. This was due to the ebonite coupling which is inserted between the camshaft and the torque transducer shaft working as a good thermal insulator.

7.4 The Preparation of Experimental Specimens

Eight pairs of cam and follower specimens were prepared for the experimental studies. Eight cams which were made from EN8D (080A42) steel, induction hardened, ground and phosphated were chosen arbitrarily from twenty cams ordered from ZEPHYR CAMS LTD. Sixteen commercial bucket followers manufactured from chilled cast iron were used for making eight bucket follower specimens. In order to maintain the same surface characteristics on the specimens as those on commercial ones, eight (3 mm) thickness circle metal piece were cut from eight bucket followers. The other bucket followers were shortened by (3.5 mm) in length. An insulated wire was soldered onto the metal piece which was then stuck onto the mica biscuit

which was in turn cemented onto the shortened bucket follower. Subsequently, the eight specimens were put into an oven and cured at a temperature of (150°C) for two hours. Finally, the bottom surface of each bucket follower was ground slightly on a grinding machine to make the bottom surface perpendicular to the follower skirt surface. Since the specimens were machined and processed in the same way and at the same time the specimens could be expected to be similar.

7.5 Lubricant Temperature-Viscosity Relationship

To investigate the thermal effect on the tribological performance of the cam and follower it was necessary to known the temperature-viscosity characteristics of the lubricant. This was determined using a suspended level viscometer in which the time for a specified amount of lubricant to pass through a certain distance was checked. The kinematic viscosity was calculated by multipling this time by the constant of the viscometer used for the test. The variation of the dynamic viscosities of the lubricant with temperature are shown in Figure (7.6). The solid line was an exponential curve fit to six data pairs measured at the temperatures of (30.0°C), (50.0°C), (72.5°C), (90.5°C), (105.0°C) and (122.0°C) respectively. The lubricant used in the present experimental study was TEXACO 10W/30 as specified by the Ford Motor Company Ltd.

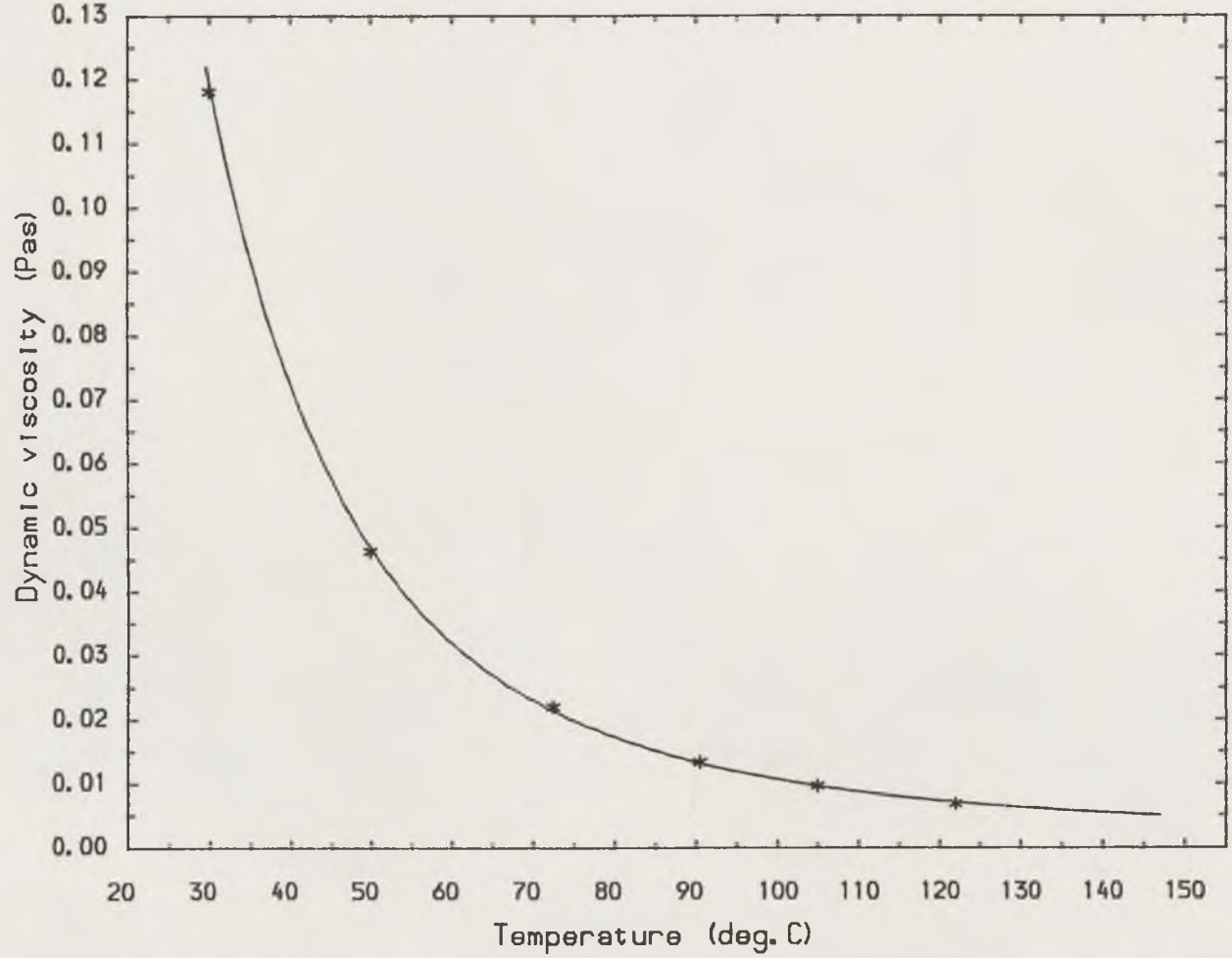

Figure (7.6) Temperature-viscosity characteristics of the lubricant (TEXACO 10W/30).

CHAPTER 8

EXPERIMENTAL RESULTS AND DISCUSSION

8.1 Introduction

A comprehensive experimental programme has been carried out to investigate the tribological performance of a polynomial cam and non-rotating flat faced follower. The apparatus and instrumentation as described in the previous chapters were used to record the running-in process and normal operation of the cam and follower at different bulk temperatures and camshaft rotational speeds. In order to investigate the thermal effects on the tribological performance of the cam and follower several (100 hour) duration tests were undertaken at (1240 rpm) rotational speed with bulk temperatures of (50°C), (75°C), (90°C), (105°C) and (120°C) respectively. In addition the effects of the camshaft rotational speed on the tribological performance of the valve train were also investigated; the apparatus was run at speeds of (440 rpm), (650 rpm), (1030 rpm), (1240 rpm), (1470 rpm), (1820 rpm) and (2070 rpm) at (105°C) bulk temperature. Several parameters including the instantaneous torque, average friction torque, power loss, instantaneous electrical resistivity, average voltage drop, surface roughness, material hardness and the temperatures on the cam nose and in the valve stem guide were measured for each test. The results obtained from these tests are reported in this chapter. The details of the experimental data processing with dynamic analysis of the camshaft system and the adoption of a digital filter are also given in this chapter. Since the instantaneous friction torque in the cam lift portion of the cycle is closely related to the geometric torque which can only be predicted from a theoretical analysis, the detailed introduction to the experimental results for the instantaneous friction torque acting on camshaft will be given in the next chapter.

8.2 Test Procedure

8.2.1 Tests at Different Bulk Temperatures

Five tests were performed at different bulk temperatures to investigate the effect of bulk temperature on the tribological performance of the cam and follower. The apparatus was rebuilt prior to each test using a new cam and follower pair. A clearance of (0.4 mm) between the cam and follower on the cam base circle was carefully set. To prevent edge loading the contact of the cam and follower was inspected by painting the follower surface with engineering blue and turning the camshaft by hand for one or two revolutions to make the cam contact with the follower. If the contact

produced by the surfaces which erased the engineering blue showed edge loading, the follower was re-ground until the contact mark covered the full cam width. Before starting each test all the instruments were re-calibrated to within (1%) of their nominal values. All the electrical equipment including the heater and thermostat circulator were switched on two hours before starting each test to warm up the apparatus and instruments.

The (100 hour) test duration was divided into two steps, (1) (10 hour) running-in procedure and (2) (90 hour) normal test procedure. After the running-in procedure the apparatus was shut down overnight and the lubricant was drained. Subsequently, oil pipes were cleaned with compressed air and the sump of the thermostat circulator was flushed with INHIBISOL solvent. Finally the circulator sump was re-charged with fresh oil. The apparatus was then re-started the next morning and run for (90 hours) continually.

The experimental data were recorded as a function of time. As the data changed dramatically in the first five hours of both the running-in procedure and the normal test procedure, the intervals of data recording in these periods were smaller than those adopted in other periods. During each normal test the data were recorded every (5 hours) in the day time and (10 hours) in the evening.

8.2.2 Tests at Different Camshaft Rotational Speeds

As described in Chapter (7) the camshaft rotational speeds selected for the speed test were (440 rpm), (650 rpm), (1030 rpm), (1240 rpm), (1470 rpm), (1820 rpm) and (2070 rpm) to minimize the influence of the harmonic components on the torque signals due to the torsional vibration of the torque transducer. One pair of cam and follower specimen was used in the speed test. The normal speed test was initiated with a stabilizing sequence in which the apparatus was run at various speeds and bulk temperatures from (50°C) up to (120°C) for (100 hours). The normal speed test was then followed by a (24 hour) warm-up sequence during which the apparatus was run at a speed of (1240 rpm) and (105°C) bulk temperature, the temperature at which the normal speed test was to run. The following sequence describes the data recording procedure which consisted of two test loops, an increasing speed loop and a decreasing speed loop. At the beginning of the increasing speed loop the camshaft rotational speed was reduced to the lowest test speed of (440 rpm) and run for half an hour. Subsequently the torque signal,

electrical resistivity and cam position trigger signal were sampled through the four channels of the ADC multiplexer of a VAX8600 computer. After the sampling operation the camshaft rotational speed was increased to the next test speed of (650 rpm), run again for half an hour and followed by a sampling operation. This procedure was repeated several times with the rotational speed increased step by step until finishing the sampling operation at the highest test speed of (2070 rpm). After that, the decreasing speed loop was started with the camshaft rotational speed remaining constant for another half an hour before the sampling operation. This procedure was repeated with the speed being decreased step by step down to the lowest test speed of (440 rpm). This completed the speed test procedure. Such speed test loops were performed several times; the differences of the average friction torques between each test loop at each of the test speeds was always less than (5%).

8.2.3 Data Sampling Operation

The data sampling operation was made up of three sequences which are the sampling sequence, displaying sequence and storing sequence. In the present tests the torque signal, the torque signal after an analogue lowpass filter, the electrical resistivity and the cam position trigger signal were sampled through the four parallel channels (numbered (0) to (3)) of the ADC multiplexer. The data sampling operation was performed by running the data acquisition program. The total number of channels, data points sampled by each channel and sampling interval between two data points of each channel can be set as desired. In all tests to be described in this chapter, the total data points were (32764) (or (8191) points for each channel) and the sampling interval was (40 μS) which is equivalent to a sampling frequency of (25 KHz), except for the speed test at (440 rpm) camshaft rotational speed in which an (80 μS) sampling interval was employed. In order to minimize the influence of the random factors the sampled signal for each channel included at least three cam running cycles. The digital signal collected from each channel could then be displayed on the screen. Before being stored in the computer the sampling sequence and display sequence could easily be repeated to make sure that all the signals were in order. A typical example of the signals sampled from each channel is shown in Figure (8.1) as a function of time in units of milliseconds.

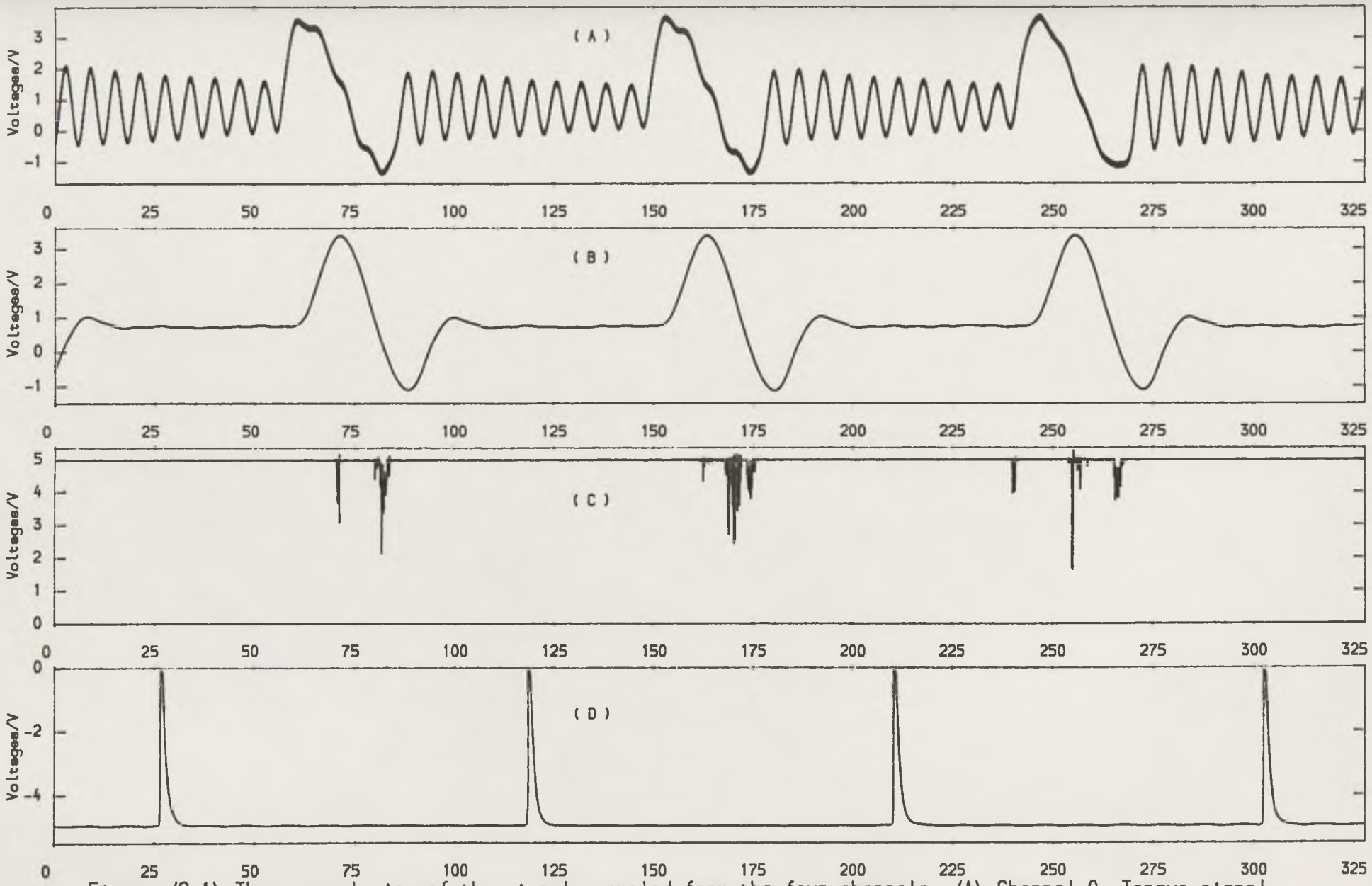

Figure (8.1) The general view of the signals sampled from the four channels. (A) Channel 0: Torque signal, (B) Channel 1: Torque signal after an analogue filter, (C) Channel 2: Voltage across the contact and (D) Channel 3: Cam position trigger impulse (Test speed (650 rpm) at a (105°C) bulk temperature).

8.3 Data Processing

8.3.1 Instantaneous Torque Acting on Camshaft

As can be seen from Figure (8.1) the signal from the torque transducer looks quite different from that anticipated. This is due to the mechanical oscillation of the transducer shaft caused by its low torsional rigidity. Since the torsional rigidity of the camshaft and coupling were much greater than that of the transducer shaft, the torsional vibration of the camshaft system including the torque transducer can be modelled by a rigid disk connected to one end of the transducer shaft which is treated as a torsional spring. Thus the cyclic instantaneous torque acting on the camshaft could be considered as an external torque applied to the camshaft system exciting a one-degree forced damped vibration of the transducer shaft. In fact, the output signal from the transducer was the vibration signal responding to this external cyclic torque. The external cyclic torque was mainly composed of three parts, (1) a geometric torque which is caused by the force of the valve spring and inertia forces applying a load to the cam with an eccentricity to the centre of the camshaft, (2) a friction torque arising from the interfaces of the cam/follower and the follower/guide and (3) a friction torque which is the contribution of the camshaft and transducer shaft support bearings. The angular displacement (θ) of the transducer shaft can be expressed by the well known second-order ordinary differential equation given below;

$$J\ddot{\theta}(t) + c\dot{\theta}(t) + k\,\theta(t) = T(t) \qquad (8.1)$$

where (J) is the moment of inertia of the camshaft system, (c) is the damping coefficient which relates to, for instance, the viscous force in the supporting bearings, (k) is the torsional stiffness of the transducer shaft and (T) is the instantaneous torque acting on the camshaft. As the torque (T_o) measured by the transducer can be represented by the following relationship;

$$T_o(t) = k\,\theta(t) \qquad (8.2)$$

Equation (8.1) can be expressed in terms of (T_o) as;

$$\ddot{T}_o(t) + \frac{c}{J}\dot{T}_o(t) + \frac{k}{J}T_o(t) = \frac{k}{J}T(t). \qquad (8.3)$$

Assuming $2a = \frac{c}{J}$ and $\omega_o^2 = \frac{k}{J}$, we have

$$\ddot{T}_o + 2a\dot{T}_o + \omega_o^2 T_o = \omega_o^2 T \qquad (8.4)$$

where (ω_o) is the natural frequency of the transducer shaft and (a) is the logarithmic damping coefficient of the camshaft system.

On the left-hand side of equation (8.4), (T_o) was measured by the torque transducer and $(\ddot{T}_o)$ and $(\dot{T}_o)$ could be obtained by numerical differentiation of (T_o) which are similar to those expressions given by equations (4.13) and (4.14). Thus if the parameters (a) and (ω_o) were known the instantaneous torque (or external cyclic torque) acting on the camshaft could then be worked out from equation (8.4). Further studies on the torque signal on the cam base circle showed that this torque was only caused by the friction of the supporting bearings and remained constant around the whole of the cam base circle. So that, on the cam base circle equation (8.1) takes the form;

$$J\ddot{\theta}(t) + c\dot{\theta}(t) + k\theta(t) = 0 \qquad (8.5)$$

This is a typical free damped vibration problem. The classical solution to this equation is given by;

$$\theta(t) = A\, e^{-at} \sin(\omega_n t + \varphi) \qquad (8.6)$$

where $\omega_n^2 = \omega_o^2 - a^2$

From the spectral analysis of the torque signal on the cam base circle the value of (ω_n) could be obtained. At first it seemed that there was a little difficulty in obtaining the value of (a). As a matter of fact, from equation (8.6) it was found that the peak values of the periodic signal were given by the relationship;

$$A_i = A \exp(-at_i) \qquad (8.7)$$

A regression analysis to the data pairs (A_i, t_i) gave the value of (a). As the parameter (a) is a speed dependent variable it was more reasonable to estimate it from the torque signal on the cam base circle than to evaluate it from an impact test under static conditions. Knowing all the parameters in equation (8.4) the instantaneous torque acting on the camshaft could be expressed in a discrete form;

$$T_i = \frac{1}{d^2 \omega_o^2}\left[(1 - 2ad)\, T_{oi-1} + (\omega_o^2 d^2 - 2)\, T_{oi} + (1 + 2ad)\, T_{oi+1}\right] \qquad (8.8)$$

where (d) was the interval between two subsequent data points and was equal to $(t_i - t_{i-1})$.

8.3.2 Average Friction Torque

The average friction torque in the cam lift portion gave a good indication of the condition of the lubrication of the valve train and of the state of the running-in process. The clearance of (0.4 mm) on the cam base circle ensured that the average value of the torque signal on the cam base circle represented the sum of the zero output shift of the amplifier and the ADC multiplexor and the friction torque arising from the supporting bearings under gravitational load and this consequently was assumed to be constant. Besides this average torque, the instantaneous torque in the cam lift portion was composed of three further components: the geometric torque, the friction torque arising from the interfaces of the cam/follower and the follower/guide and the friction torque caused by the camshaft supporting bearings under dynamic load. Because of the symmetry of the cam profile, valve spring load and inertia force about the cam maximum lift position, the contribution of the geometric torque to the average friction torque over the cam lift period was zero. It followed that the difference between the average value of the instantaneous torque signal in the cam lift cycle and the average value of the torque signal on the cam base circle represented the average friction torque in the cam lift portion.

The problem was how to determine the cam lift portion of the cycle. As it was impossible to keep the clearance on the cam base circle to exactly (0.4 mm) for each test, the cam lift portion for each test would be slightly different. The electical resistivity signal recorded at the begining of each test associated with the cam position trigger signal which is sampled simultaneously with the torque signal, made it possible to work out the points at which the cam initiated and completed contact with the follower.

8.3.3 Average Voltage Drop

The average voltage drop across the contact was defined as the difference between the nominal applied voltage between the cam and follower and the average value of the instantaneous contact voltage in the cam lift portion. In fact, the voltage drop was caused by asperity contact or the low resistance of the thin lubricant film. The voltage varied between (0) and (50 mV) for contact and no contact respectively. Thus the average voltage drop and the instantaneous contact voltage could be taken as a qualitative measure of the film state and the degree of asperity contact. In the present test the average contact voltage was recorded by a RECORD high inertia voltmeter continually during the whole test period. At the same time,

the instantaneous voltage across the contact was also sampled by the computer simultaneously with the torque signal and cam angle trigger signal at a given data recording time. The average voltage drop was estimated from these signals in the same way as the average friction torque.

8.3.4 The Elimination of High Frequency Noise

Figure (8.1) shows high frequency noise signals superimposed on the main torque signal. These high frequency noises came from the electronic instrumentation adopted in the present test and the environmental noise which is inducted into the long cable between the ADC connection box and the VAX8600 computer. Unfortunately, it was impossible to eliminate this noise from the measurement system. Moreover, the existence of this noise made it totally impossible to work out the instantaneous torque from equation (8.8). The small fluctuations in the torque signals caused by the noise dramatically changed the value of $(\ddot{T}_o)$ and $(\dot{T}_o)$, the numerical differentiations of the torque signal. A logical solution to this problem was the adoption of a lowpass filter.

As an analogue filter caused severe phase changes of the original signal (see Figure (8.1b)), which was quite difficult to correct, it was decided that a digital filter should be used. The phase change was cancelled by passing the data through the digital filter twice, once in the usual way, and a second time with the data points arranged in reverse order. This operation could never be realized in the real time process (for example in analogue signal process) but could easily be achieved on a digital computer.

An eighth-order Butterworth lowpass digital filter was designed and programmed in FORTRAN on a Amdhal computer. The details for designing a digital filter have been given by Beauchamp and Yuen (1973) and Valkenburg (1982). The cutoff frequency of the lowpass filter for smoothing torque signals was (400 Hz) which is considered to be low enough to eliminate high frequency noise and high enough to preserve the higher order frequency components of the torque signal. A listing of the computer program is given in Appendix (A2).

8.4 Experimental Results

8.4.1 Tests at Different Bulk Temperatures

Five pairs of cam and follower specimen were used for the tests at (1240

rpm) camshaft rotational speed at bulk temperatures of (50°C), (75°C), (90°C), (105°C) and (120°C) respectively. The corresponding cams for these tests were numbered (A), (D), (E), (H) and (J) while the followers were marked (B), (D), (E), (3) and (4). The sequence of the numbers of cams and followers listed above corresponded to the listed sequence of the bulk temperatures at which each pair of cam and follower specimens was tested. A detailed introduction to the results of these experiments is given in this section including surface characteristics of the cam and follower, friction torque, electrical resistivity and temperatures at the cam nose and in the valve stem guide.

8.4.1a)Surface Characteristics

Follower

The general view of the wear tracks on the follower surfaces after each test are shown in Figure (8.2a). Full contact along the cam width was achieved for each specimen which demonstrated the accuracy of the alignment between the cam and follower, except that slight edge loading was found on follower (3) tested at (105°C) bulk temperature. Generally the wear which occurred on the follower was polishing wear which formed a smooth surface. The follower (B) tested at room temperature was only slightly polished by the two ridges on each side of the cam formed in the machining process. The original surface texture produced in the grinding process was still clearly visible on the follower (B). The appearances of the wear tracks on followers (D), (E) and (3) were quite similar. Although the grinding marks could still be observed on the wear tracks, the wear on these followers looked more severe than that on follower (B). The most severe wear was found on follower (4), where machining grooves were totally worn away and a highly burnished surface was found with longitudinal wear traces. In spite of this, highly polished wear scars also appeared at the two extreme ends of the wear track on each follower, at which the entraining velocity dropped to zero. Also, two shiny grooves were found in the middle of the wear track. One wider groove occurred at the position at which the cam completed contact with the follower whilst a narrower groove corresponded to the position where the cam initially made contact with the follower.

It was interesting to note that severe scoring scars were found on the follower skirt sides which were perpendicular to the cam sliding direction

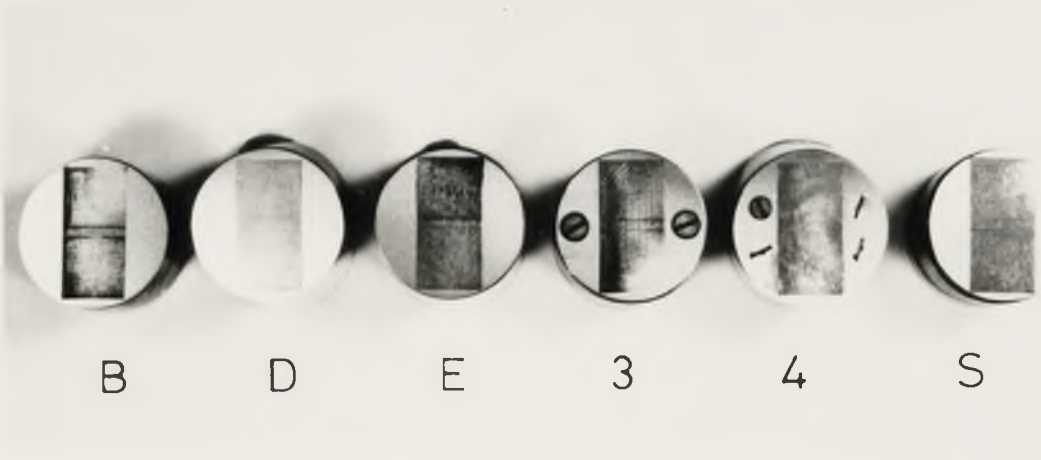

(a)

(b)

(c)

Figure (8.2) General view of the bucket followers

as shown in Figure (8.2b) whilst (see Figure (8.2c)) on the other sides which were parallel to the cam direction of motion very few wear scars were observed. These findings revealed an important fact that the follower tilted as it moved up and down in the follower guide.

Surface characteristics of each follower were recorded both before and after each test, including;

(1) Surface roughness value (Rq) in both longitudinal and transverse directions corresponding to the cam sliding direction,
(2) Surface profile in the centre of the wear track in both directions,
and (3) The hardness of the material.

The surface roughness value (Rq) was measured with a TAYLOR-HOBSON Talysurf machine in both longitudinal and transverse directions. The surface roughness values in both directions were taken from the average value of three parallel traverses with a (5 mm) interval between each longitudinal traverse and a (10 mm) interval for the transverse direction. The surface roughness values for each test are summarized in Table (8.1). It can be seen that the roughness values in the transverse direction are all greater than those in the longitudinal direction except for follower (B). In general, at the end of each test all the surface roughness values were reduced.

At the same time Talysurf profiles were taken in the central regions of the follower in the two directions prior to and subsequent to each test. Generally, the sharp peaks of asperities were flattened in both directions due to the running-in of the cam and follower surfaces.

It was supposed that the material hardness was the same everywhere on the follower surface before each test. Thus the Vickers Pyramid Number of hardness (Hv) was measured at four points out of the contact region of the cam and follower with a ZWICK low load hardness tester. The test load adopted in the present test was (5 Kg). The material hardness after each test was measured at fifteen points within the wear track of the follower surface. The average values of the hardness at these points both before and after each test are summarized in Table (8.2). From this table it can be seen that the material hardness of the follower surfaces increased after each test. The hardness after the tests at different bulk temperatures showed a decreasing

Table (8.1) Cam and follower surface roughness values (Rq) before and after each test at different bulk temperatures. (μm)

CAM					FOLLOWER				
No.	Before Test		After Test		No.	Before Test		After Test	
	L	T	L	T		L	T	L	T
A	0.107	0.230	0.092	0.137	B	0.350	0.170	0.262	0.077
D	0.176	0.251	0.088	0.241	D	0.227	0.294	0.142	0.185
E	0.160	0.363	0.088	0.226	E	0.222	0.296	0.146	0.244
H	0.274	0.442	0.108	0.322	3	0.311	0.384	0.218	0.318
J	0.132	0.247	0.172	0.224	4	0.158	0.280	0.088	0.243

KEY: L : Longitudinal direction, T : Transverse direction.

Table (8.2) Vicker hardness of cam and follower surface before and after each test at different bulk temperatures. (Hv)

CAM			FOLLOWER		
No.	Before Test	After Test	No.	Before Test	After Test
A	730	720	B	671	672
D	730	680	D	687	703
E	748	678	E	659	672
H	739	658	3	681	672
J	701	639	4	627	662

trend with increased bulk temperature.

Cam

Generally the wear which occurred on the cam was limited to the nose area. The appearance looked polished to the naked eye. Again it was found that the most severe wear occurred on the cam (J) which was tested at (120°C) bulk temperature. On the two cam flanks there was almost no evidence of a wear track. Two polished tracks were found on the two flanks where the cam initiated and completed contact with the follower. The widths of the tracks were different and corresponded to the two grooves found in the middle of the follower surface.

The surface roughness values of the cams were measured both before and after each test in several portions of the cam profile. In the transverse direction measurements were performed on the cam nose, base circle and at three points on the cam flanks. The average of these values are presented in Table (8.1). In the longitudinal direction the surface roughness values were only taken on the cam nose and base circle due to the limitation of the TAYLOR-HOBSON Rotary Talysurf machine. Since there was no contact between the cam and follower on the cam base circle, the average value of these measurements on the cam nose was taken as the longitudinal surface roughness value of the cam and also recorded in Table (8.1). From Table (8.1) it can be seen that all of the surface roughness values in the transverse direction are greater than those in the longitudinal direction both before and after each test. This is similar to the situation on the follower surface described above. After each test the values of the surface roughness in both directions reduced due to the running-in of the cam and follower surfaces, except that the surface roughness value in the longitudinal direction increased on cam (J). This was consistent with inspection by the naked eye.

As the cam surface was induction hardened it could be assumed that the material hardness on the cam surface was the same everywhere. To preserve the surface of the cam lift portion prior to each test the material hardness was only measured at several points on the cam base circle. The test load adopted in the present hardness tests was (5 Kg) which is the same as that used for the follower. After each test the material hardness was examined at three points on the cam nose. The average values are also summarized in Table (8.2) together with the hardness number measured before each test.

Similar to the situation found on follower surface after each test the material hardness decreased as the bulk temperature increased. Contrary to the finding on the follower, a reduction of the hardness on each cam nose at the end of test was found.

8.4.1b) Friction Torque

The friction forces arising from the valve train, including the cam/follower interface, bucket follower/guide interface and supporting bearings, is an important parameter in evaluating the tribological performance of the valve train. In the present test the friction force was determined by measuring the instantaneous torque acting on the camshaft. As has been discussed in the previous section, the average value of the instantaneous torque in the cam lift portion represented the average friction torque caused by these friction forces.

The variation of the average friction torque during the running-in procedure is presented in Figure (8.3) as a function of running time. Generally the average friction torque decreased progressively in the whole running-in process. Since a new cam and follower pair was used in each test while the supporting bearings remained the same, the reduction of the average friction torque in this period represented the running-in of the cam/follower and follower/guide interfaces. At the end of the running-in procedure the average friction torque still showed a decreasing trend which implied that the running-in process of the valve train may not have finished. In spite of this, a general tendency of increasing friction torque due to increasing bulk temperature was found.

The average friction torque in each normal test procedure is plotted against running time in Figure (8.4). In the first (30 hours) running of the normal test procedure the average torque further decreased to a value around which the friction torque fluctuated during the following (60 hours) of test run. The fluctuation of the friction torque in this latter period was within (5%). It was also found that the increase of the bulk temperature resulted in an increase in the friction torque. A relatively greater fluctuation of the friction torque at the low bulk temperature of (50°C) was attributable to the variation of the room temperature and consequently the variation of the oil temperature in the sump of the circulator. The thermostat control was not switched on in this test.

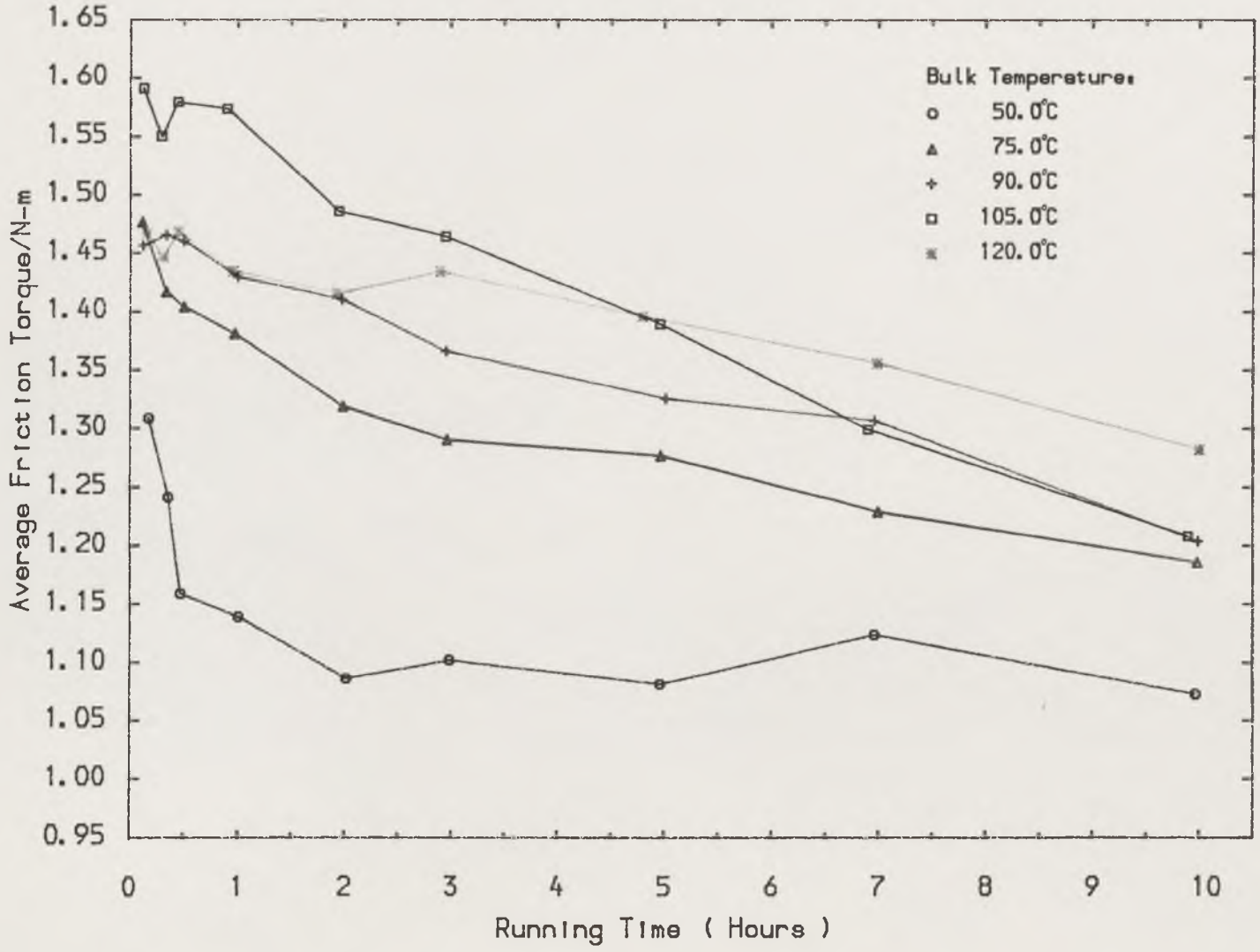

Figure (8.3) The variation of the average friction torque during the running-in procedure.

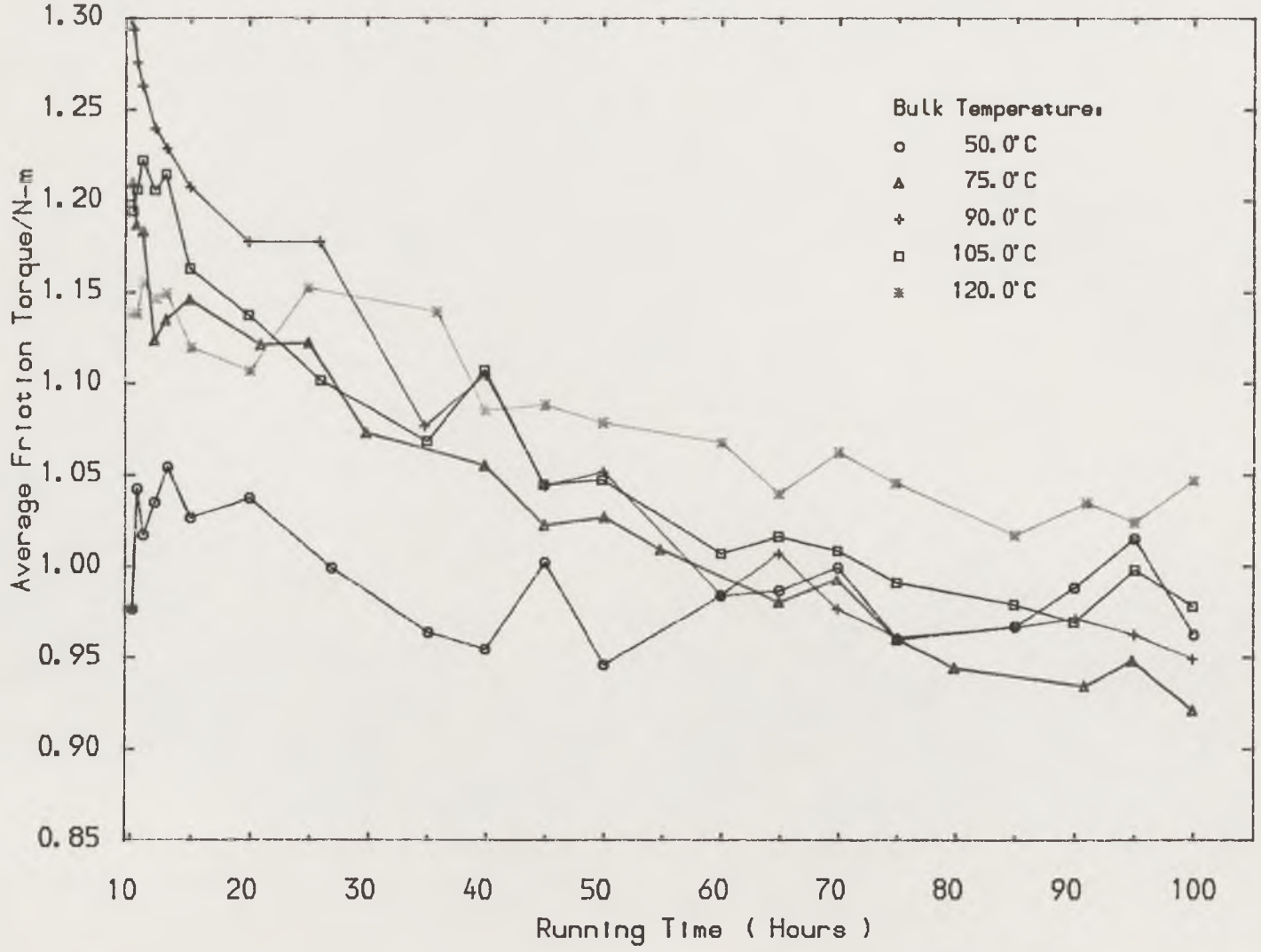

Figure (8.4) The variation of the average friction torque during the normal test procedure.

In order to investigate the variation of the friction torque arising from the different parts of the valve train in the running-in test procedure the instantaneous torques sampled at the beginning and the end of each running-in procedure are presented in Figure (8.5) as a function of the cam angle from the nose. Similarly the instantaneous torques sampled at (13 hours), (50 hours) and at the end of each normal test procedure are presented in Figure (8.6).

8.4.1c) Electrical Resistivity

In the present tests the electrical resistivity across the contact of the cam and follower was inspected by measuring the corresponding voltage drop. Thus in this and subsequent sections the results are presented in terms of voltage drops or, in a more straightforward way, as the voltage across the contact.

The variation of the average voltage across the contact was monitored with the RECORD voltmeter continually for (100 hour) duration. At the beginning of the running-in procedure the average voltage drop across the contact showed a general downward trend with time (or an upward trend of the average voltage). The rates of change of the voltage drop were different at different bulk temperatures. It was found that the higher the bulk temperature at which the test was performed the higher the rate of decrease of the voltage drop. For instance, the duration for the percentage contact to drop from its very high initial value down to approximately (5%) was (185 minutes), (145 minutes), (85 minutes) and (65 minutes) for the test at bulk temperature of (75°C), (90°C), (105°C) and (120°C) respectively. It was also noticed that a moderate increase of percentage of contact occurred after its initial drop and lasted for several minutes in each test, except for the test at (50°C) bulk temperature. This increase occurred in the tests at (352 minutes), (395 minutes), (280 minutes) and (142 minutes) running corresponding to the test temperatures of (75°C), (90°C), (105°C) and (120°C) respectively.

In the normal test procedure the voltage across the contact between the cam and follower reached a stable value at about (10 minutes) to (15 minutes) after restarting the apparatus and then remained at a low level with some irregular small peaks occurring occasionally in the whole test process. These small peaks were caused by the fluctuation of the camshaft rotational speed and the inlet oil temperature. Further studies of the

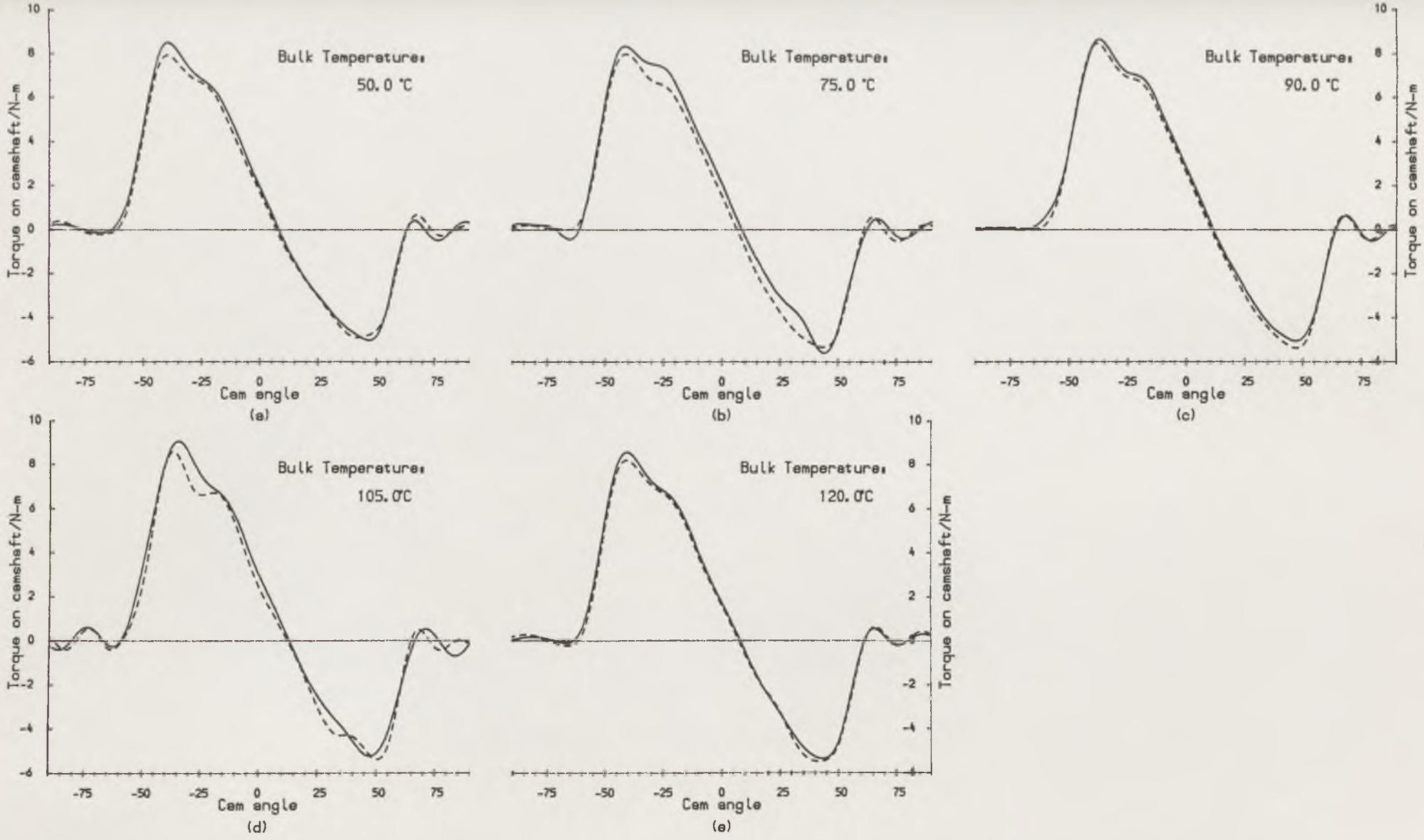

Figure (8.5) Comparison of the instantaneous torque acting on the camshaft at the beginning and the end of the running-in procedure to show the running-in effects on the friction torque.
(——— Torque at (10 minutes) running time, ----- Torque at the end of the running-in procedure.)

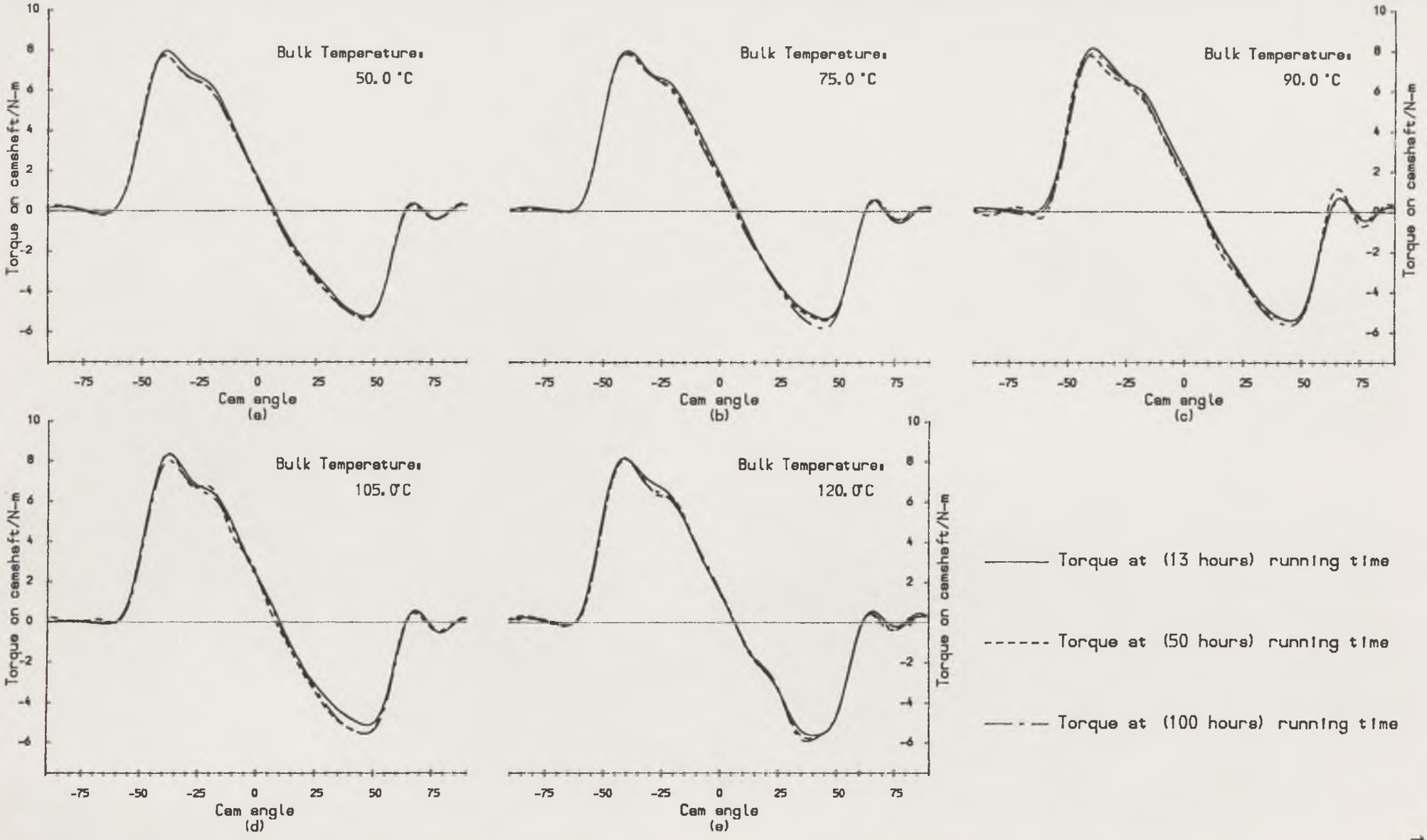

Figure (8.6) Comparison of the instantaneous torque acting on the camshaft at the beginning, (2 hours) running time and the end of the normal test procedure.

experimental results revealed that the electrical resistivity across the contact was quite sensitive to these fluctuations. A comparison between these records of the average voltage drop showed that the results obtained in the (75°C) test were not only the lowest but also the most stable, whilst the results from the test at room temperature condition ((50°C) bulk temperature without thermostatic control) gave the highest and the most fluctuating curve. These phenomena can be seen more obviously from the average voltage drops presented in Figure (8.7). The figure shows the variation of the average voltage drop in the running-in procedure for each test. It is clear that the increase in the bulk temperature results in an increase in the rate of decrease of the average voltage drop. For example, at (120 minutes) running time the percentages of the average voltage drop in the cam lift period corresponding to the tests at (50°C), (75°C), (90°C), (105°C) and (120°C) bulk temperatures are (19.1%), (8.3%), (8.2%), (1.9%) and (0.3%) respectively. Figure (8.8) shows the variation of the voltage drop against running time in each normal test procedure. The first data point of each test plotted in this Figure was worked out from the data sampled by the computer (10 minutes) after initiating each normal test procedure. A substantial decrease of the voltage drop is found in Figure (8.8). This is similar to the results recorded by the voltmeter. After that the average percentage drop remained at a very low value for each test although it fluctuated from time to time. The maximum value of the percentage drop in the normal test procedure was only about (3.2%) which occurred at (20 hours) running time in the test at (120°C) bulk temperature. Similar to the findings from the results recorded by the voltmeter, in the whole normal test procedure of each test the lowest curve represented the voltage drop in the (75°C) bulk temperature test while the highest curve showed the results from the test at room temperature. A slightly high voltage drop was found in the normal test procedure at (90°C) bulk temperature. It was thought to be related to a tendency for the follower to rotate slightly. This can be inspected from the wear track on the surface of follower (E) (see Figure (8.2a)). This slight rotation was caused by the existence of a clearance between the slot of the follower and the valve cap. The slight rotation of the follower provided a new surface for running-in and consequently yielded more asperity contact.

Furthermore, in order to investigate the lubrication condition in the whole cam lift portion of the cycle instantaneous voltages across the contact which are sampled at the beginning, (2 hour) running time and the end of

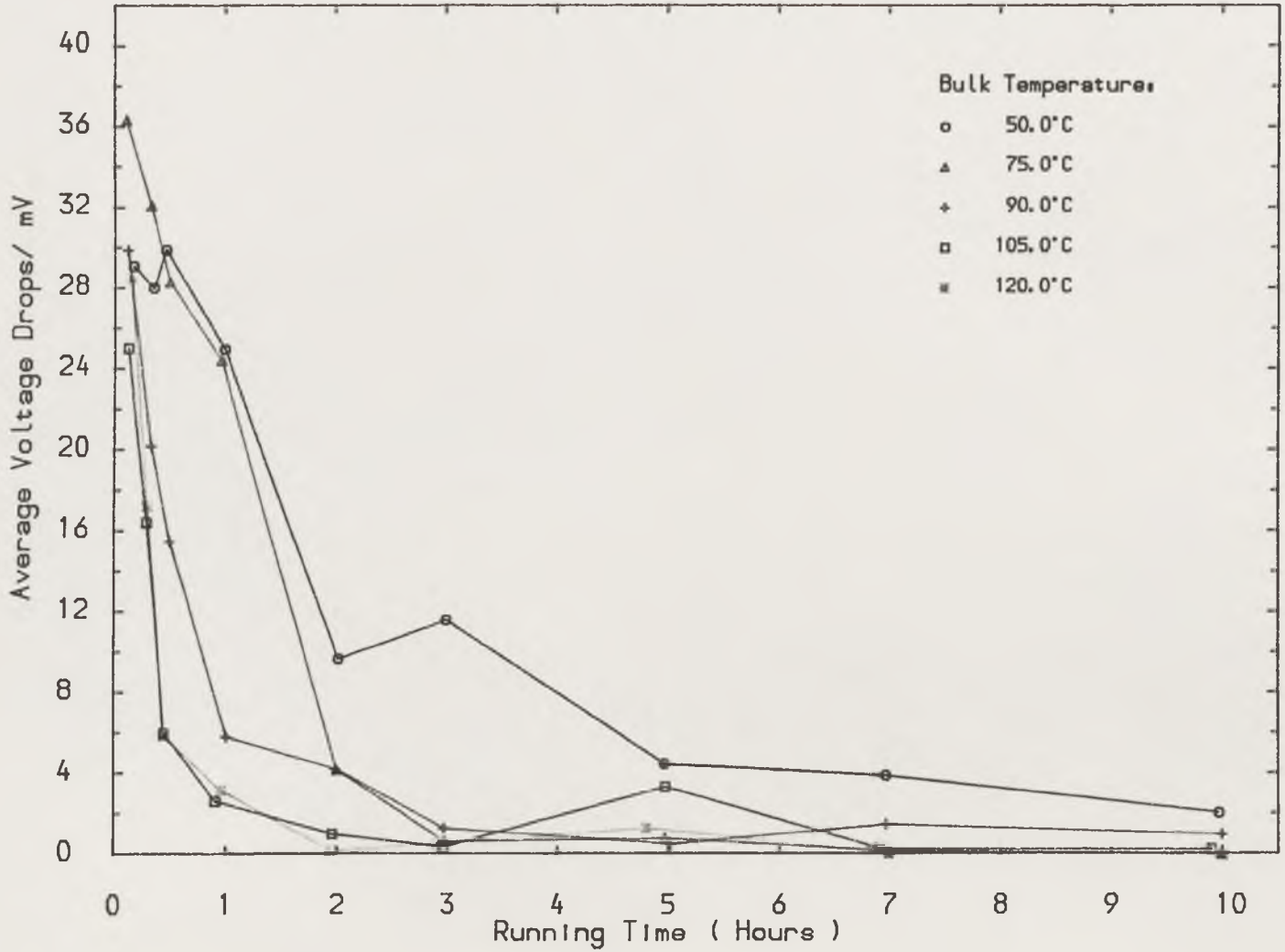

Figure (8.7) The variation of the average voltage drops during the running-in procedure.

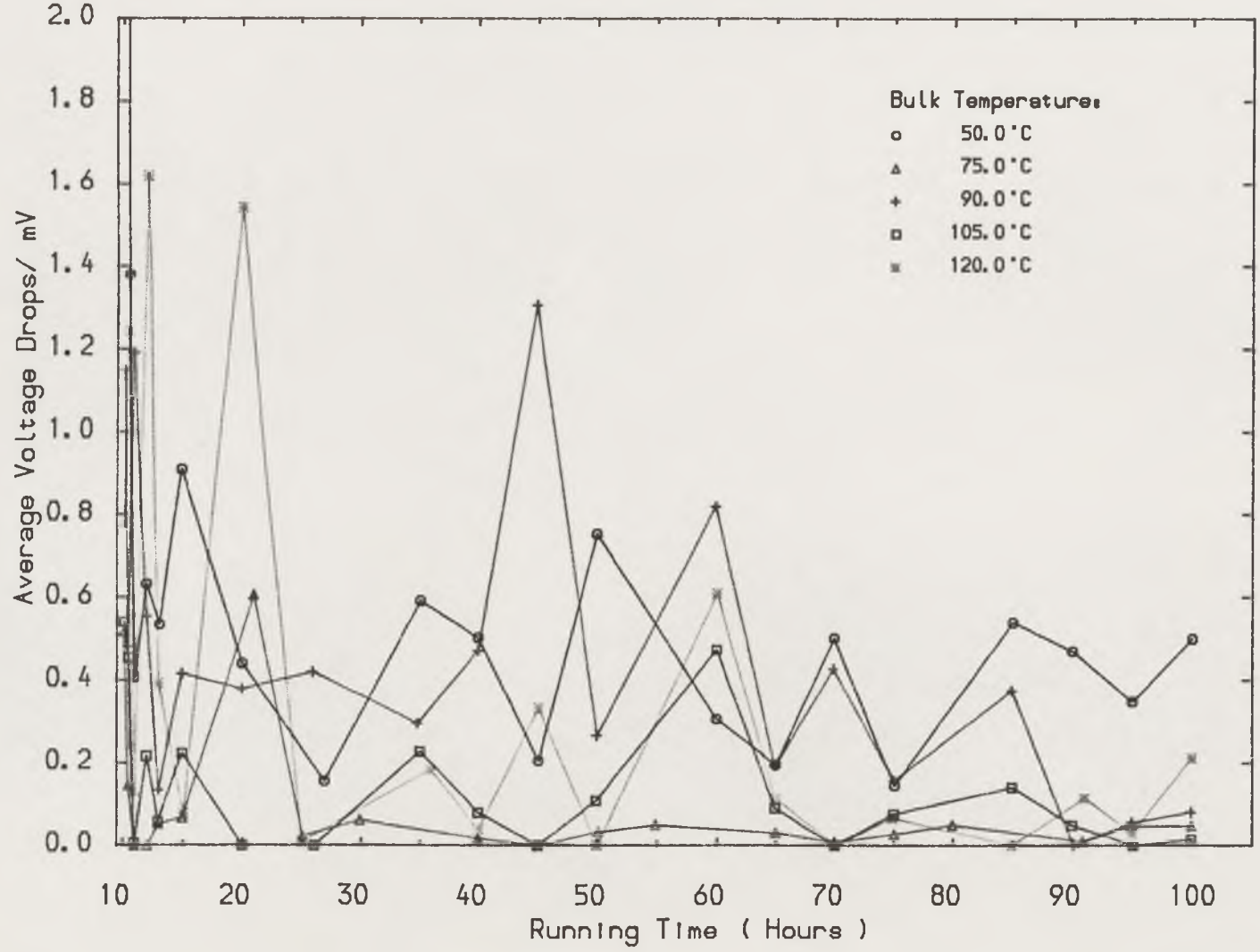

Figure (8.8) The variation of the average voltage drops during the normal test procedure.

the running-in procedure are presented in Figure (8.9) as a function of cam angle. The results which were sampled at the beginning, (60 hour) running time and the end of each normal test procedure are shown in Figure (8.10). A higher value of the instantaneous voltage signal represented a thicker film and less asperity contact, while a lower value implied a thinner film with more asperity contact. In order to show the general features of the electrical resistivity across the contact between the cam and follower a lowpass digital filter was adopted to eliminate the sharp peaks caused by the asperity contact. The cutoff frequency was (1.5 KHz). The phase shift was cancelled by transfering the data through the filter twice as described before. A detailed discussion of these results will be given later.

8.4.1d)Temperatures on the Cam Nose and in the Valve Stem Guide

It is known that the temperature of the cam nose is an important variable in evaluating the operating conditions of the cam and follower. The temperature rise on the cam nose is a parameter which can be used for estimating the energy dissipation at the cam and follower conjunction. Thus the temperature rise on the cam nose can be used as an indication of the magnitude of the friction force and associated power loss arising from the conjunction. The temperature variation on the cam nose during the running-in procedure of each test is presented in Figure (8.11) as a function of running time. Likewise, the results in each normal test procedure are presented in Figure (8.12). At the beginning of the running-in procedure the temperature increased progressively and after several hours running it decreased due to the improvement of the accommodation between the two surfaces of the cam and follower. The only exception was that in the test carried out at room temperature an upward trend existed in the whole running-in procedure. This was because of the apparatus starting at a room temperature of about (20°C). The energy dissipated from the valve train not only had to heat the lubricant but also had to warm the apparatus and consequently there was a slow increase in the temperature of the cam nose. As a result of these influences the apparatus took much longer to reach its thermal balance condition at approximately (50°C) bulk temperature. So, it could be suggested that the fluctuation of the room temperature caused the variation of the temperature of the cam nose. The results measured in this normal test procedure also showed the same tendency. On the other hand, the tests at higher thermostatically controlled bulk temperatures indicated that the temperature variation of the cam nose was very small and almost independent of the variation of the room temperature. In general the

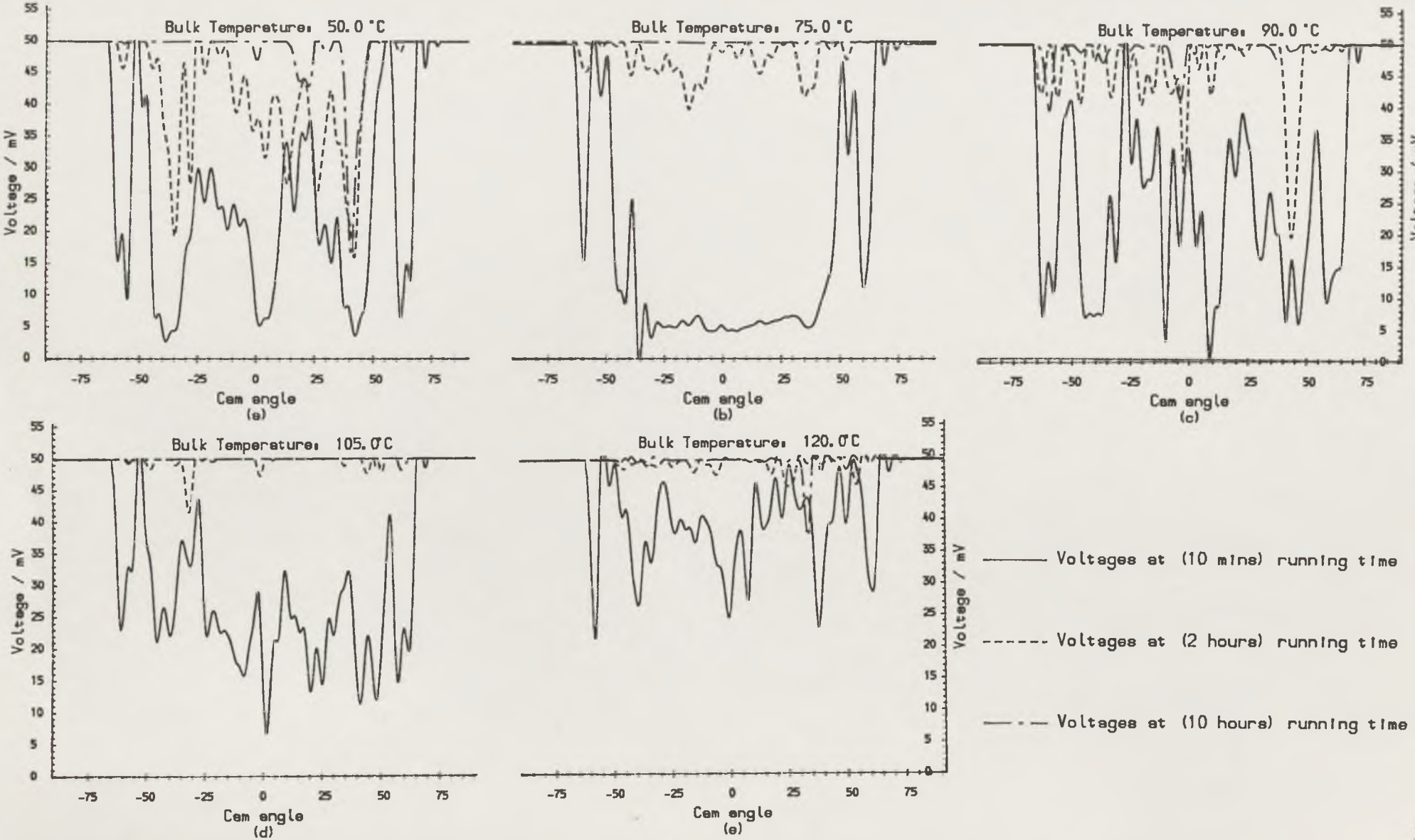

Figure (8.9) The variation of instantaneous voltages between the cam and follower at the beginning, (2 hours) running and the end of the running-in procedure.

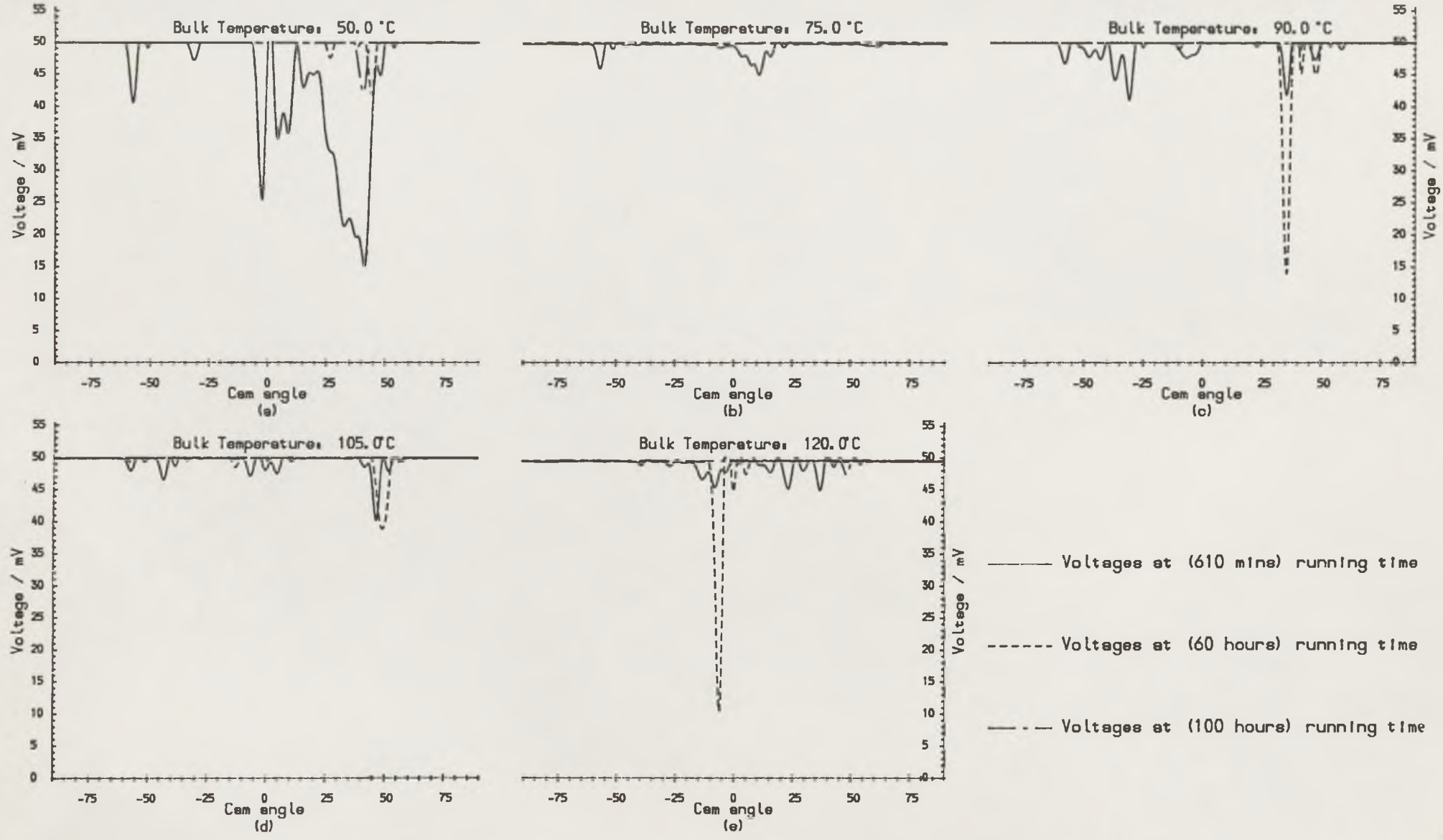

Figure (8.10) The variation of instantaneous voltages between the cam and follower at the beginning, (60 hours) running and the end of the normal test procedure.

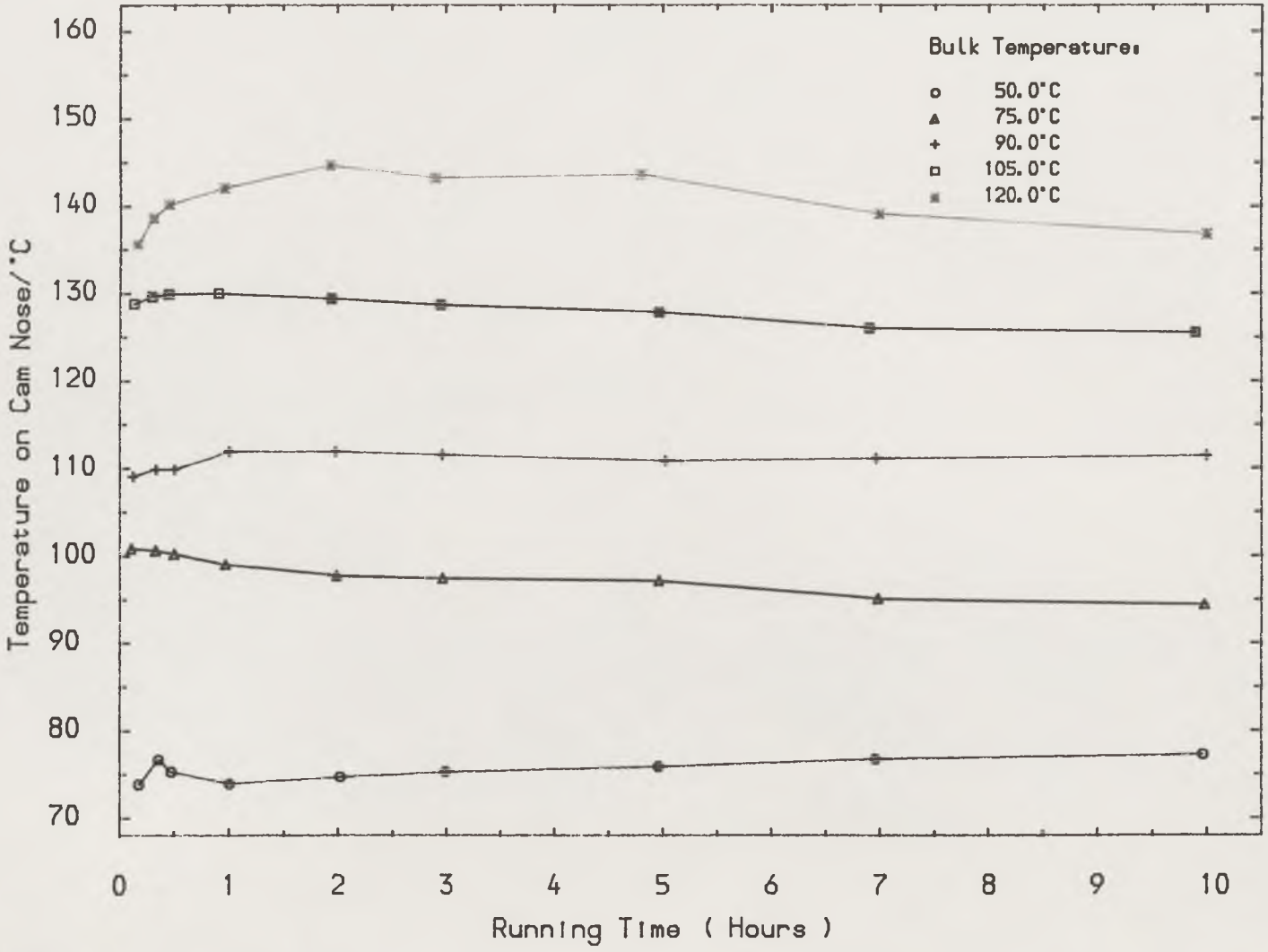

Figure (8.11) The variation of the temperature on the cam nose during the running-in procedure.

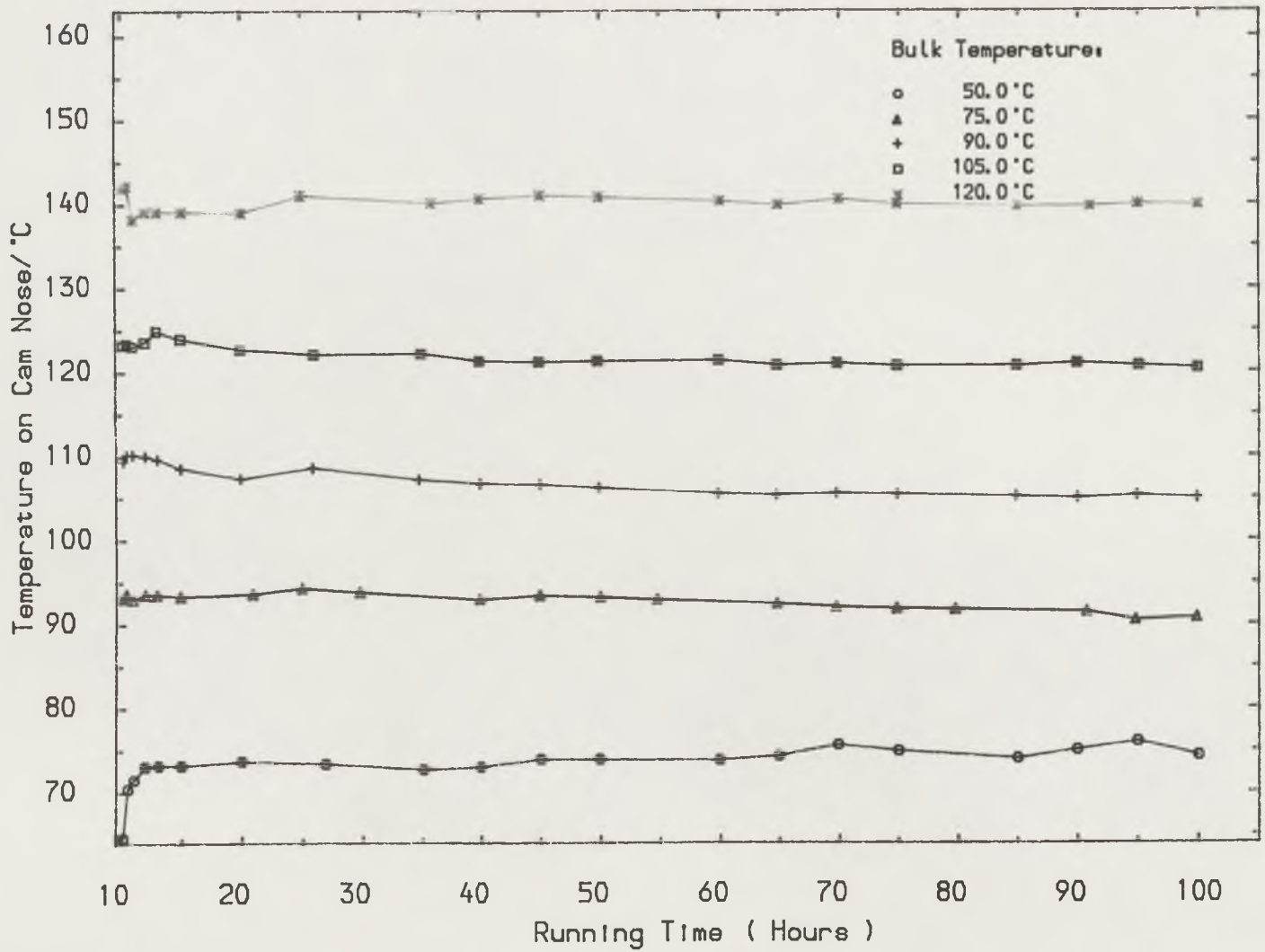

Figure (8.12) The variation of the temperature on the cam nose during the normal test procedure.

temperature of the cam nose increased as the bulk temperature was increased.

An effect which was noticed during each of the tests occurred when the inlet oil temperature was increased by several degrees. The average voltage drop was seen to increase considerably. If the temperature remained at this level the value of the average voltage drop would return to a low value several minutes later. Increasing the inlet oil temperature by (3°C) in the (120°C) bulk temperature test resulted in an (24%) increase in the percentage contact during the cam lift period. It is suggested that this phenomenon might be connected to the disintegration of the surface films. An increase in the inlet oil temperature led to a decrease of the lubricant viscosity and consequently a decrease of the nominal oil film thickness between the cam and follower. The sudden decrease of the film thickness might cause some extent disintegration of the surface films. In addition, due to the counterformal contact between the cam and follower the reduction of the nominal film thickness resulted in more asperities coming into contact. As a direct consequence of these variations the percentage of contact increased considerably. Further running of the two surfaces of the cam and follower caused the reformation of the surface film and the accommodation of the fresh surfaces under these new conditions brought the percentage of contact back to a normal value. A close correlation between the average voltage drop and the temperature rise of the cam nose was found particularly at high bulk temperatures, for instance at the (105°C) and (120°C) conditions. The variations of the temperature rise on the cam nose during the running-in procedure and the normal test procedure are presented in Figures (8.13) and (8.14) respectively. The temperature rise of the cam nose was defined as the difference between the temperature of the cam nose and the bulk temperature in the main housing. Since the nominal film thicknesses between the cam and follower under high bulk temperature conditions were extremely small, a small variation of the film thickness would lead to a dramatic change of the contact characteristics between opposing surfaces, including chemical and physical changes. On the contrary, in the case of a lower bulk temperature, the film thickness was thicker than those at higher temperatures and thus less sensitive to the fluctuation of the inlet oil temperature. A similar close correlation between the average friction torques which were shown in Figures (8.3) and (8.4) and the temperature rise of the cam nose was also found. The steep decrease in the temperature rise at the beginning of each normal test procedure

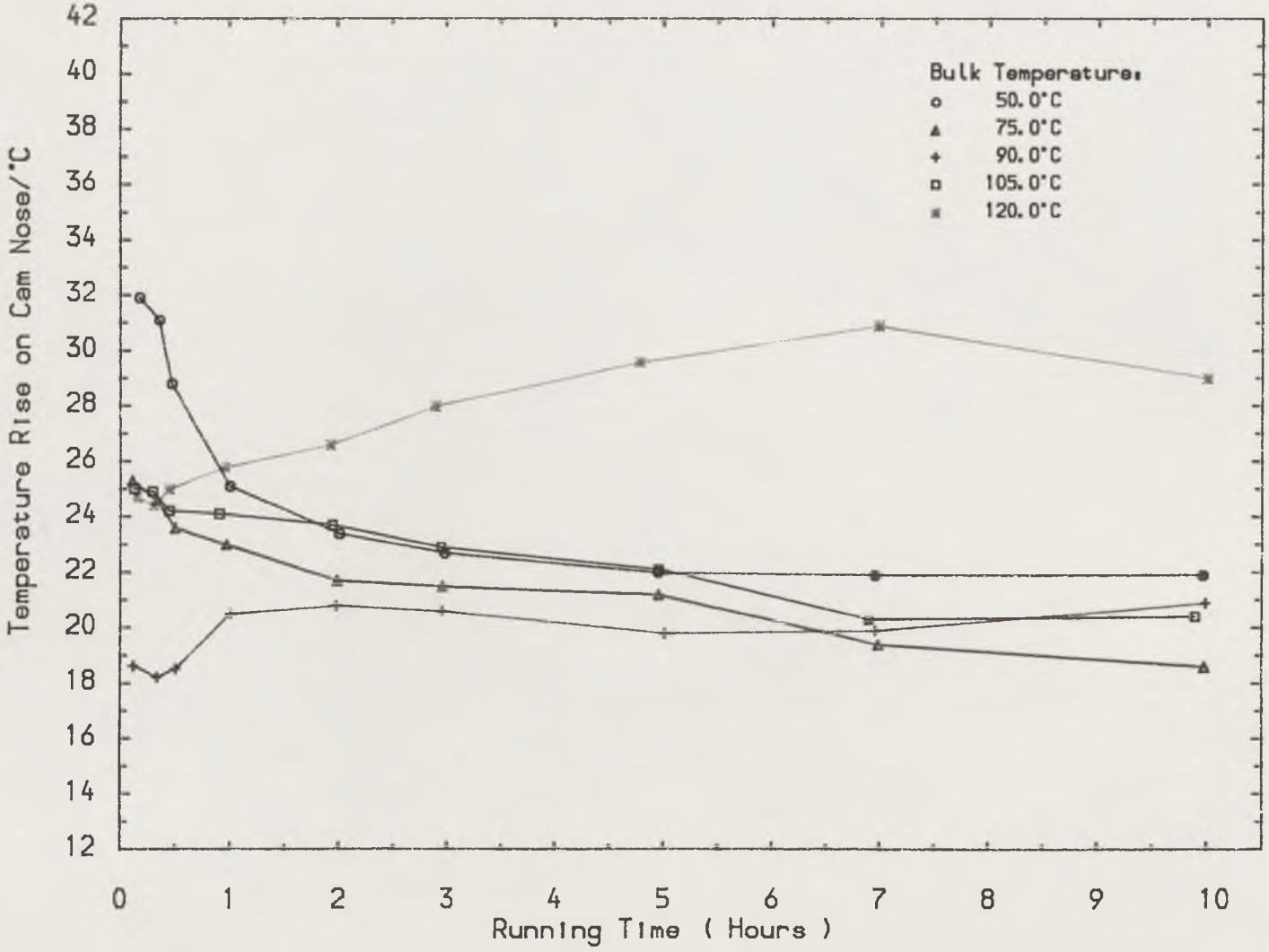

Figure (8.13) The variation of temperature rise on the cam nose during the running-in procedure

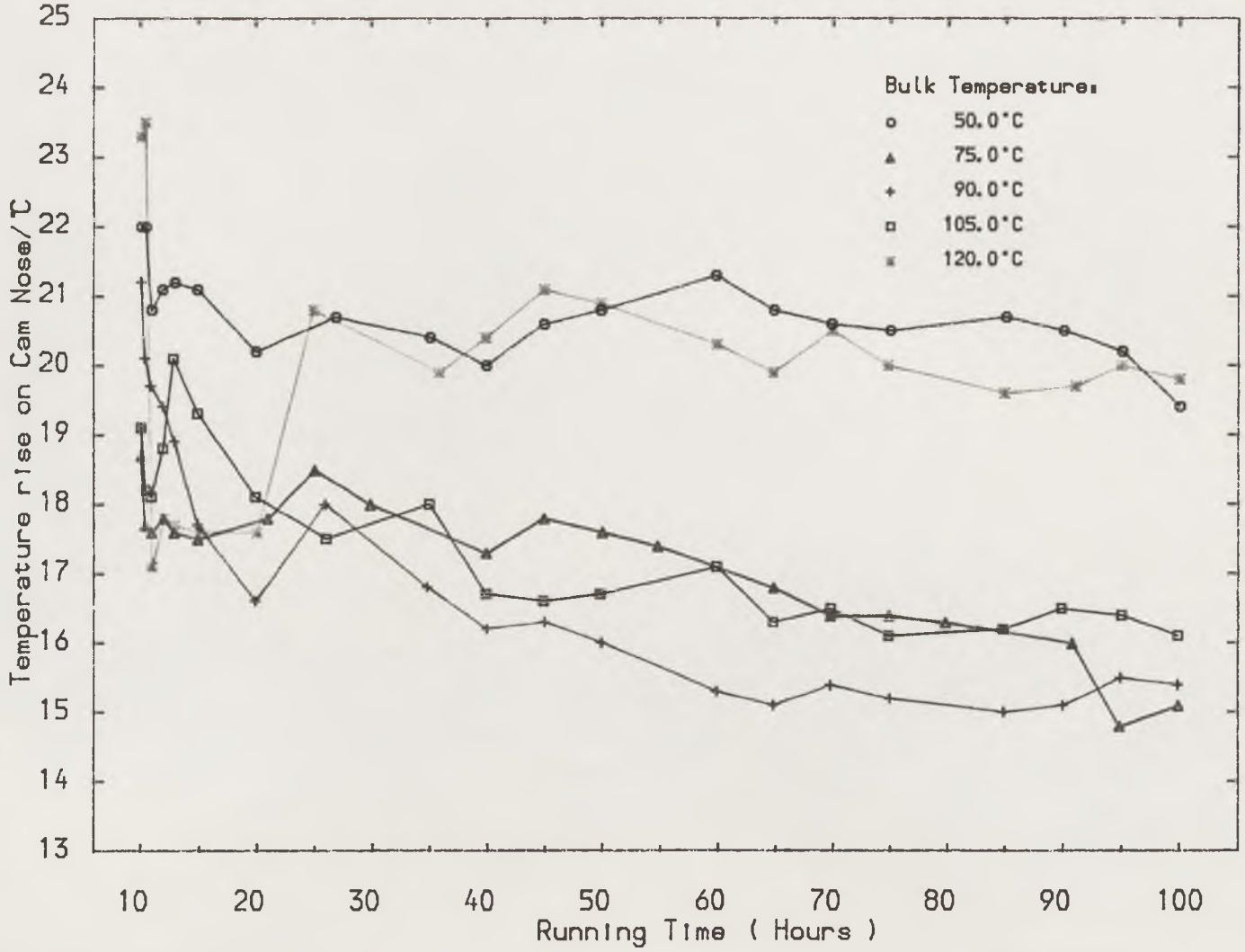

Figure (8.14) The variation of temprature rise on the cam nose during the normal test procedure.

indicated the quick rise of the bulk temperature. After the running-in of the cam and follower surfaces both the temperatures and the temperature rises of the cam nose in all normal test procedures were lower than those in the running-in procedures.

As has been described in the previous section the temperature in the valve stem guide was also measured in both running-in and normal test procedures of each test. The results are presented in Figures (8.15) and (8.16) respectively. In general the trend of the variation of the temperature in the valve stem guide was quite similar to that of the cam nose except that the values of the temperature were much lower than those of the cam nose. The figures show that the temperature in the valve stem guide increased from an initial value to a maximum one and then decreased very slowly with small fluctuations. Again it was found that the valve stem guide temperature for the test run at room temperature increased progressively until the end of the test and fluctuated with the variation of the room temperature. Due to the high thermal inertia of the valve stem guide it took longer (about (5 hours)) for the temperature to reach its highest value, whilst it only took about (2 hours) for the temperature of the cam nose to reach its highest values.

8.4.2 Tests at Different Camshaft Rotational Speeds

One pair of cam and follower specimens was used for the speed test at (105°C) bulk temperature with nominal speeds of (440 rpm), (650 rpm), (1030 rpm), (1240 rpm), (1470 rpm), (1820 rpm) and (2070 rpm). Both specimens of the cam and the follower were marked with the letter (S). The follower tested is shown in Figure (8.2a). Detailed introductions to the experimental results for the average friction torque, power loss, instantaneous torque, electrical resistivity across the contact and the temperatures on the cam nose and in the valve stem guide are given in this section.

8.4.2a) Average Friction Torque and Power Loss

The average friction torques and associated power losses measured in both the increasing and decreasing speed loop are presented in Figure (8.17) as a function of the camshaft rotational speed. The instantaneous torques acting on the camshaft at different speeds are presented in Figure (8.18) as a function of cam angle. These are important parameters for estimating the tribological performance of the cam and follower.

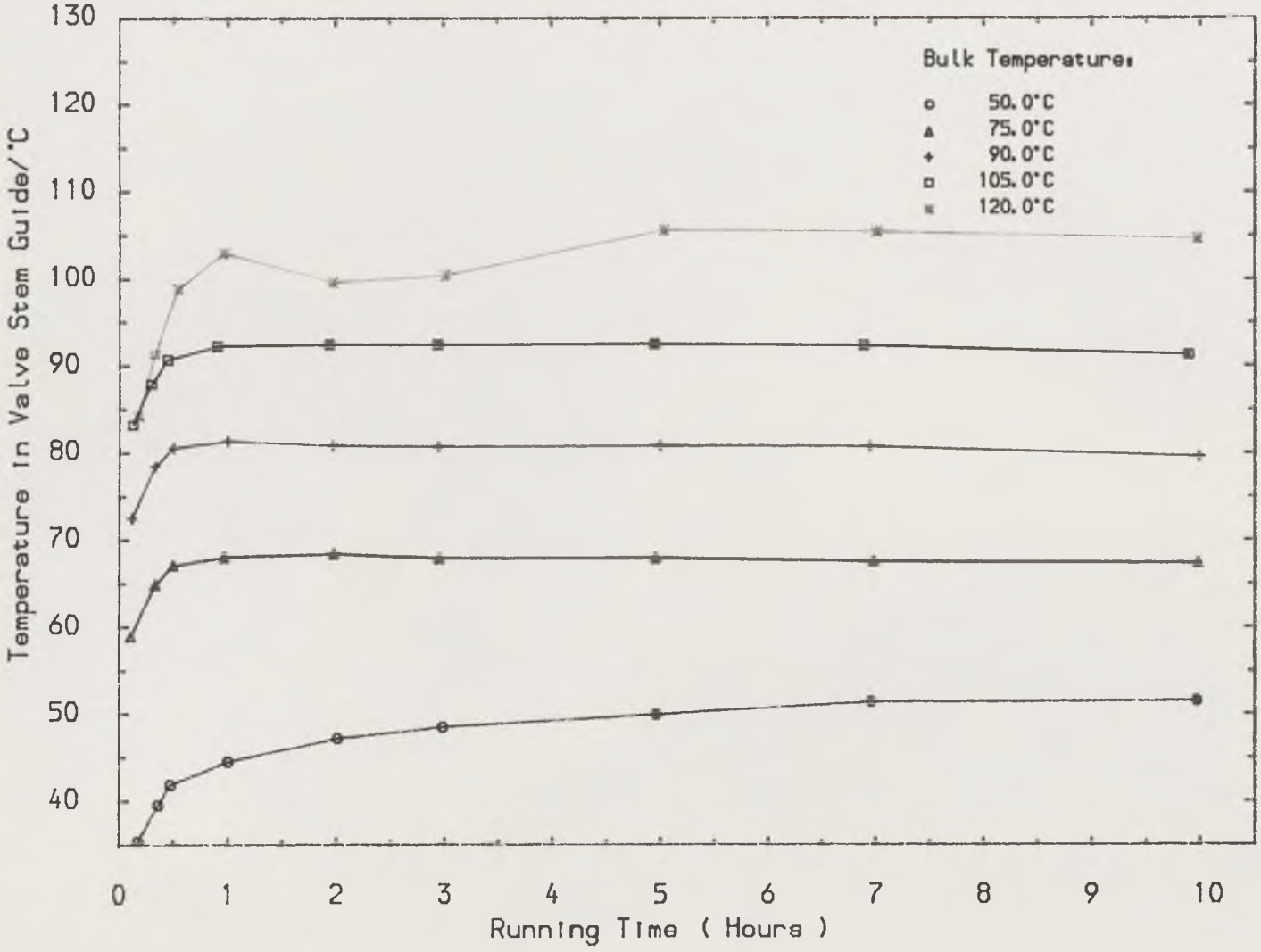

Figure (8.15) The variation of temperature in the valve stem guide during the running-in procedure.

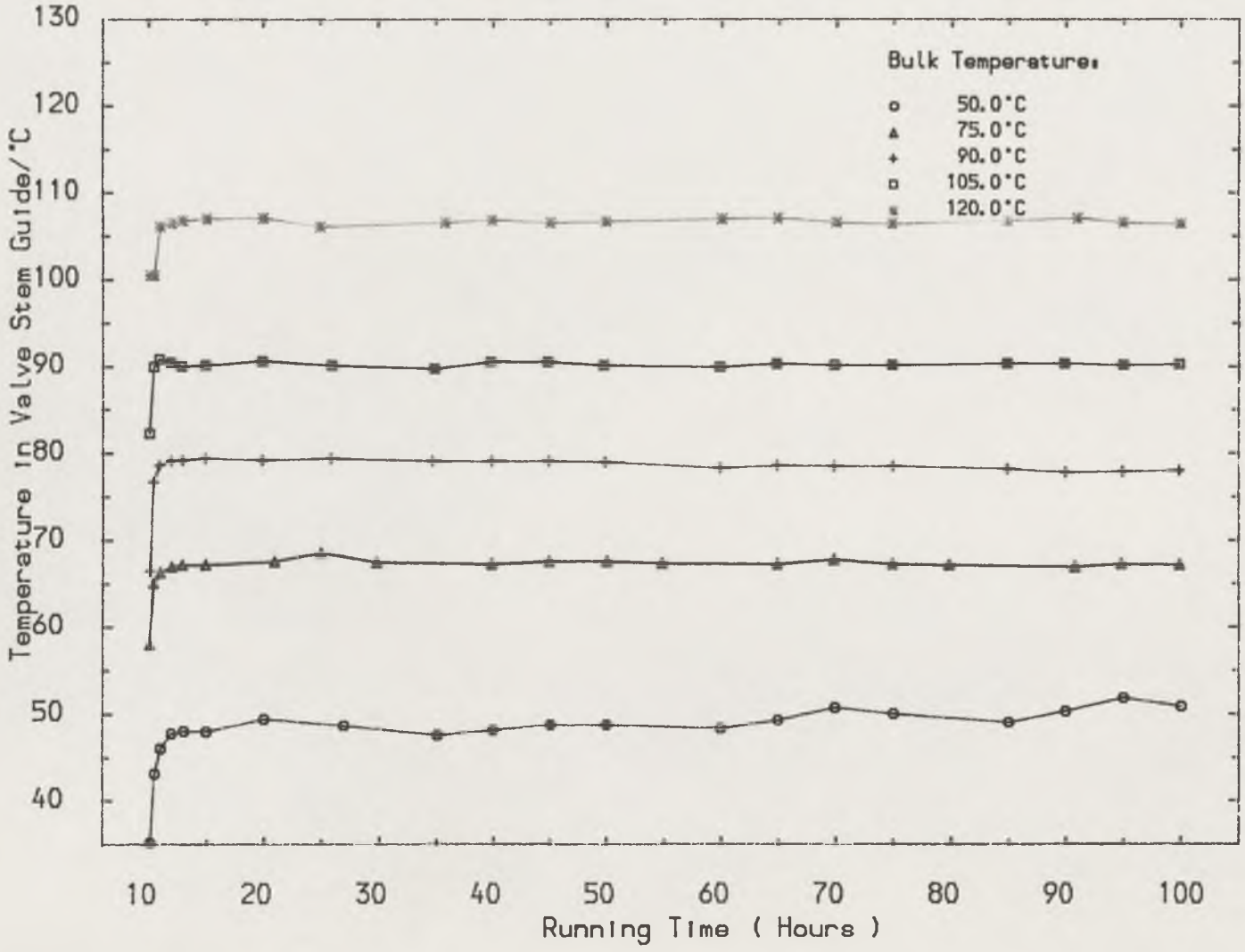

Figure (8.16) The variation of temprature in the valve stem guide during the normal test procedure.

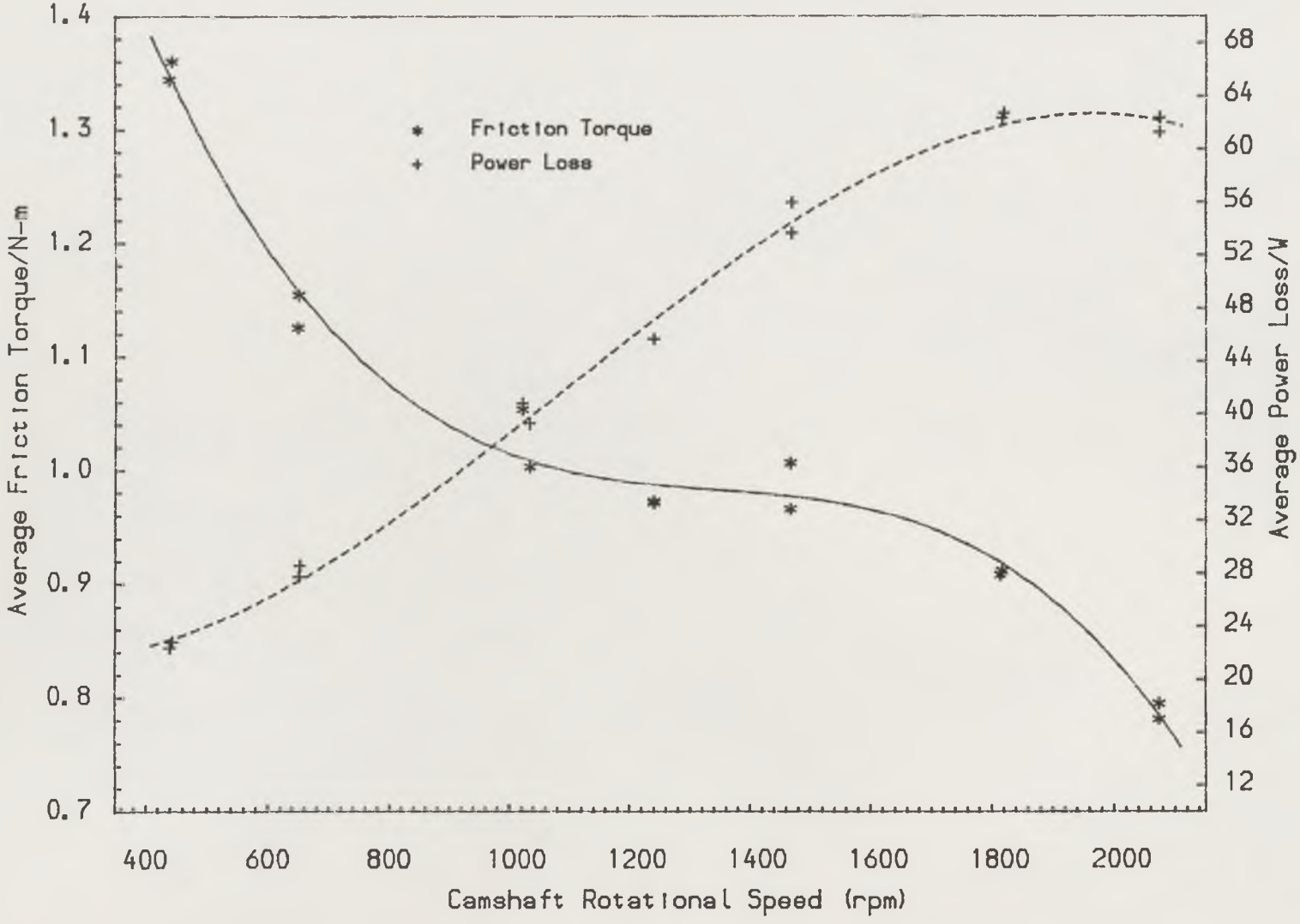

Figure (8.17) The variation of the average friction torque and power loss at different camshaft rotational speeds.

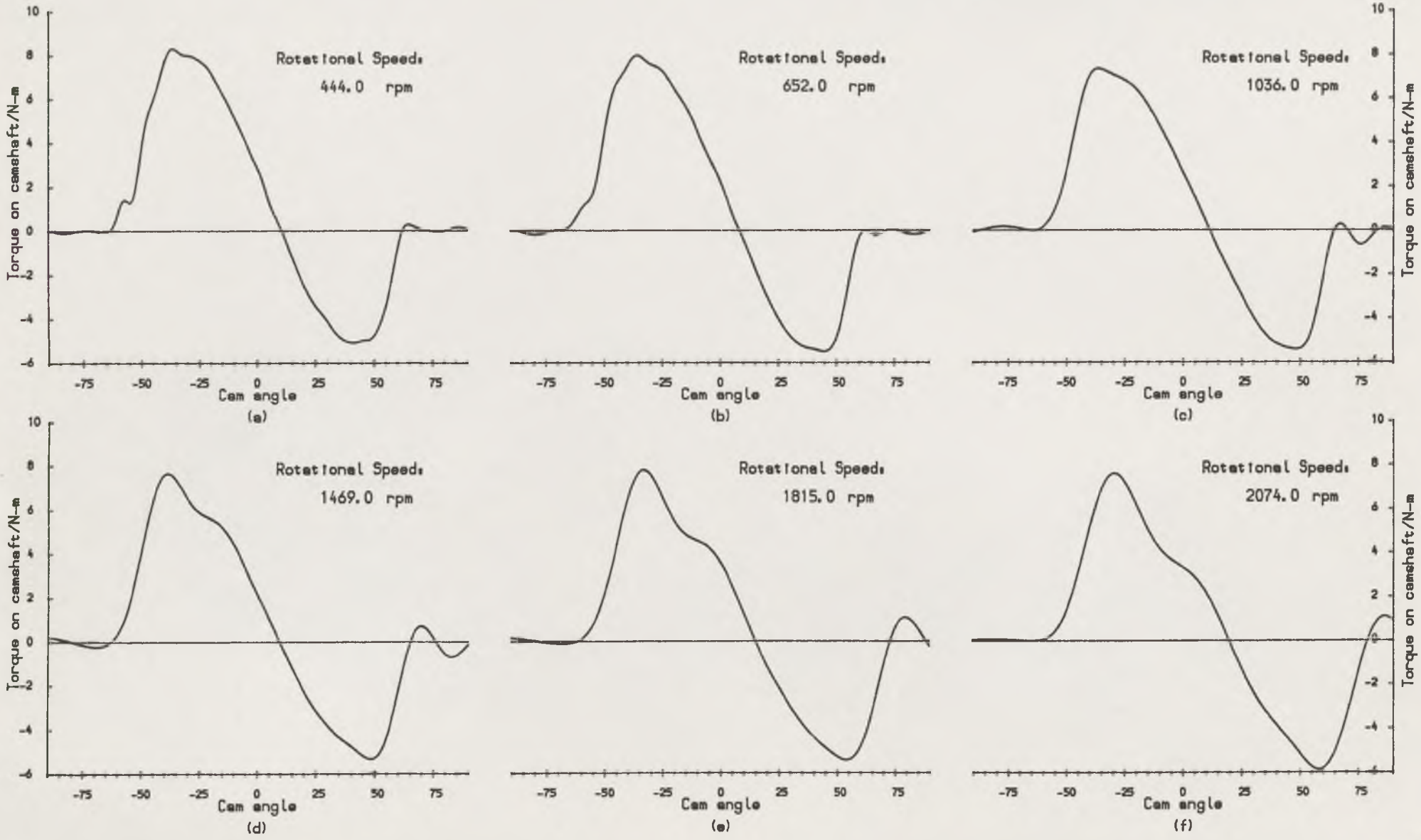

Figure (8.18) Comparison of the instantaneous torque acting on the camshaft at different rotational speeds.

8.4.2b) Electrical Resistivity

The average voltage drop across the contact of the cam and follower was recorded during the whole period of the speed test. Again it was found that the average voltage drop across the contact was seen to increase substantially whenever the speed was increased or decreased in both the speed increasing and decreasing loops. If the speed then remained at the subsequent test speed it was noted that the average voltage drop across the contact took several minutes to return to its normal value. It has been suggested that the change of the speed alters the dynamics of the valve train and the load acting on the cam. Thus the variation of the oil film thickness changed the correlation of the two surfaces of the cam and follower which in turn led to more asperity contact.

Furthermore, for the purpose of comparison, the instantaneous voltage across the contact sampled at the end of the speed tests at (440 rpm) and (2070 rpm) are presented in Figure (8.19). The figure shows that the higher the camshaft rotational speed the lower the voltage drop across the contact. This indicated that the lubrication condition was improved, or in other words, the asperity contact decreased as the speed increased. This was in concordance with the findings from the experimental results for the average friction torque at different rotational speeds (see Figure (8.17)).

8.4.2c)Temperatures on the Cam Nose and in the Valve Stem Guide

The temperatures on the cam nose and in the valve stem guide were recorded just before each sampling operation at different speeds. The results are presented in Figure (8.20) as a function of camshaft rotational speed. The solid line demonstrates variation of the temperature on the cam nose while the broken line shows the temperature in the valve stem guide. It can be seen from these figures that both the temperatures on the cam nose and in the valve stem guide increase with an increase of the camshaft rotational speed. The increase of the rotational speed resulted in an increase in the power loss (see Figure (8.17)) and consequently an increase in the heat being generated in the valve train. Likewise, an increase of the camshaft rotational speed also caused an increase of the temperature rise on the cam nose. An increase of the camshaft speed from (440 rpm) to (2070 rpm) caused the temperature rise on the cam nose to increase from (7.2°C) to (11.6°C).

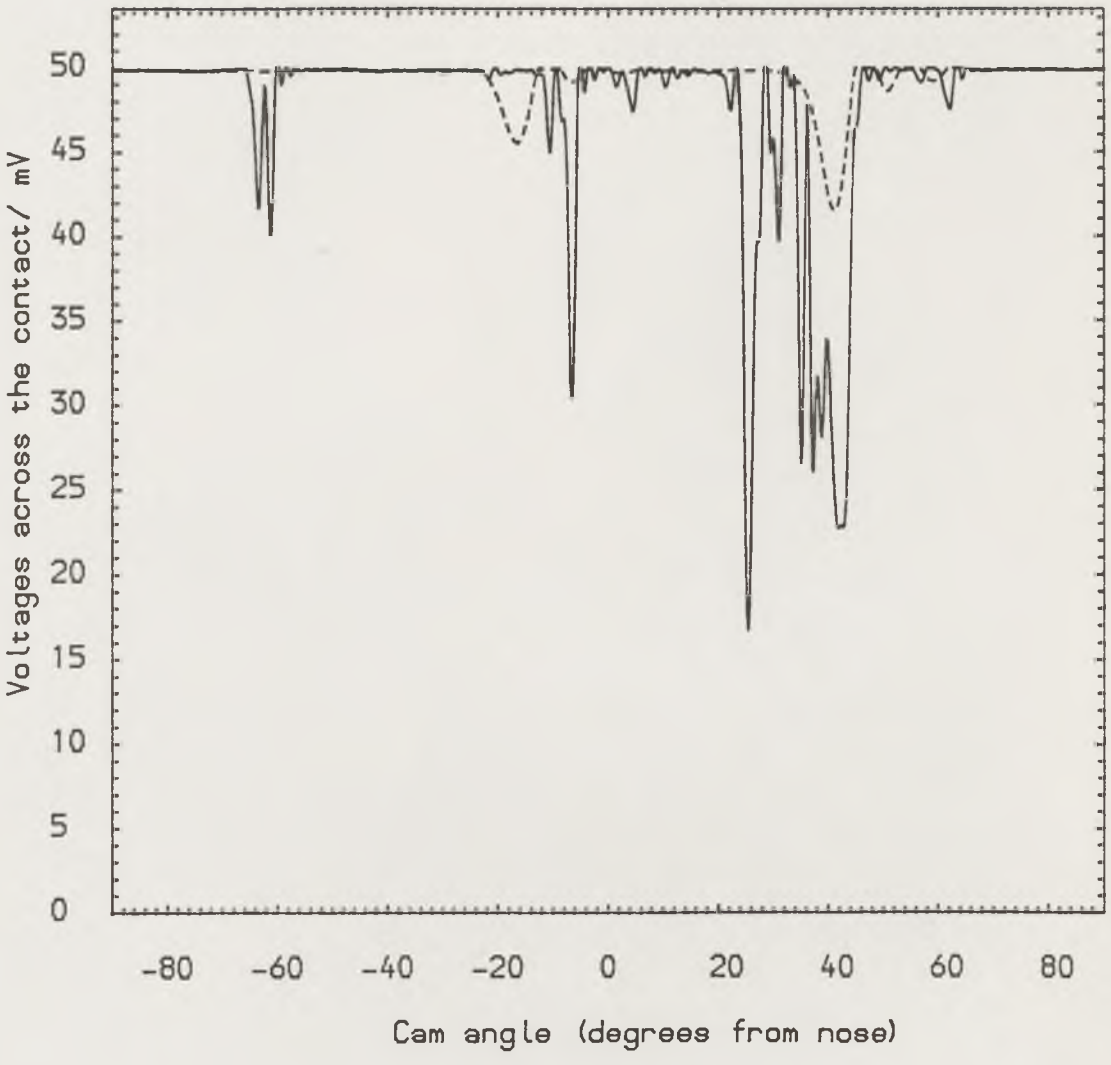

Figure (8.19) The comparison of the voltages across the contact at different camshaft rotational speeds.

——— Camshaft speed 440 rpm

------ Camshaft speed 2074 rpm

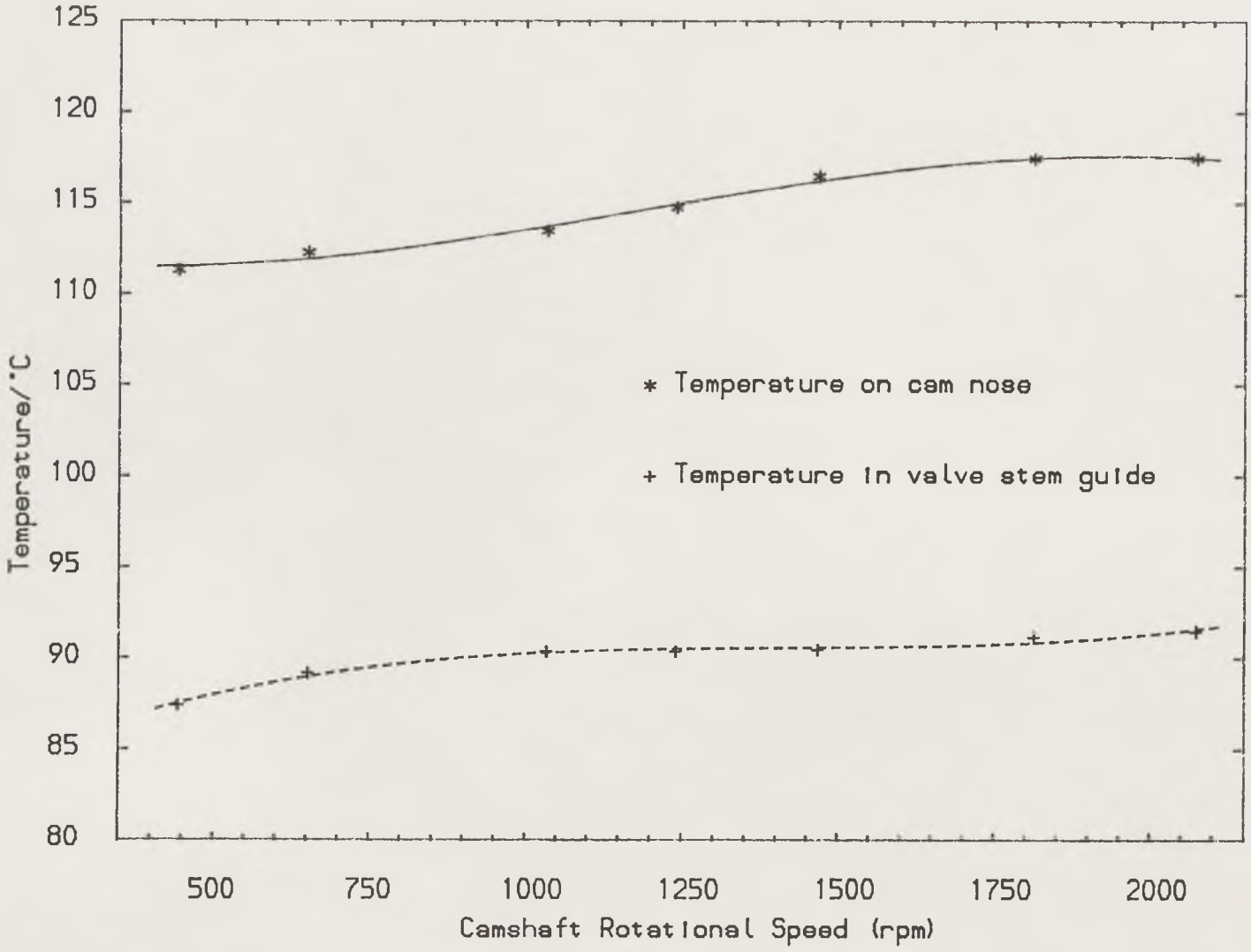

Figure (8.20) The variation of temperatures on the cam nose and in the valve stem guide at different camshaft rotational speeds.

8.5 Discussion of the Experimental Results

8.5.1 Thermal Effects on Surface Characteristics

For all tests at different bulk temperatures the appearance of the wear tracks on the cam and follower showed polishing wear which produced a smooth burnished appearance on the surface. It has been suggested that it may be an intermediate case between scuffing and pitting which is assisted by a chemical action involving the oil. The naked eye inspection had shown that the most severe wear might occur on both the cam and follower run at the (120°C) bulk temperature whilst the mildest wear was found on the specimens tested at room temperature. Generally the asperities were worn smoother by the running-in process with all surface roughness values in both directions decreased. But in the case of the test at (120°C) bulk temperature the longitudinal roughness increased from (0.132 μm) to (0.172 μm) after (100 hours) running (see Table (8.1)). This indicated that dramatic changes had occurred on the cam nose at the highest test temperature. The comparison of the material hardness measured before and after each test (see Table (8.2)) proved to be interesting. The initial hardness of the cam varied between (701 Hv) to (748 Hv) in a random sequence and (627 Hv) to (683 Hv) on the follower surfaces. But at the end of each test the hardness values showed a decreasing trend with an increase of the test temperature. This is consistent with the results reported by the British Technical Council of the Motor and Petroleum Industries (1972). Thus the most severe wear is expected to occur on the cam and follower in the test at (120°C) bulk temperature. Figure (8.21) shows the Talysurf traces across the wear track (perpendicular to the cam sliding direction) on each follower surface. It can be seen that the deepest wear track did occur on the follower tested at the highest bulk temperature (see Figure (8.21) on specimen (4)).

Another interesting phenomenon was that at the end of each test the hardness of the follower increased while on the cam nose it decreased. The increase of the final hardness on the chilled cast iron follower surfaces was due to surface plastic deformation and the formation of martensite. The hardness of martensite is about (700 Hv). The decrease of the hardness on the steel cam nose was thought to be mainly caused by the high temperature within the conjunction of the cam and follower. The variation of the hardness on both cam and follower after the test at room temperature was slight. This shows that the bulk temperature had a remarkable influence on the material hardness of the cam and follower and consequently on the wear

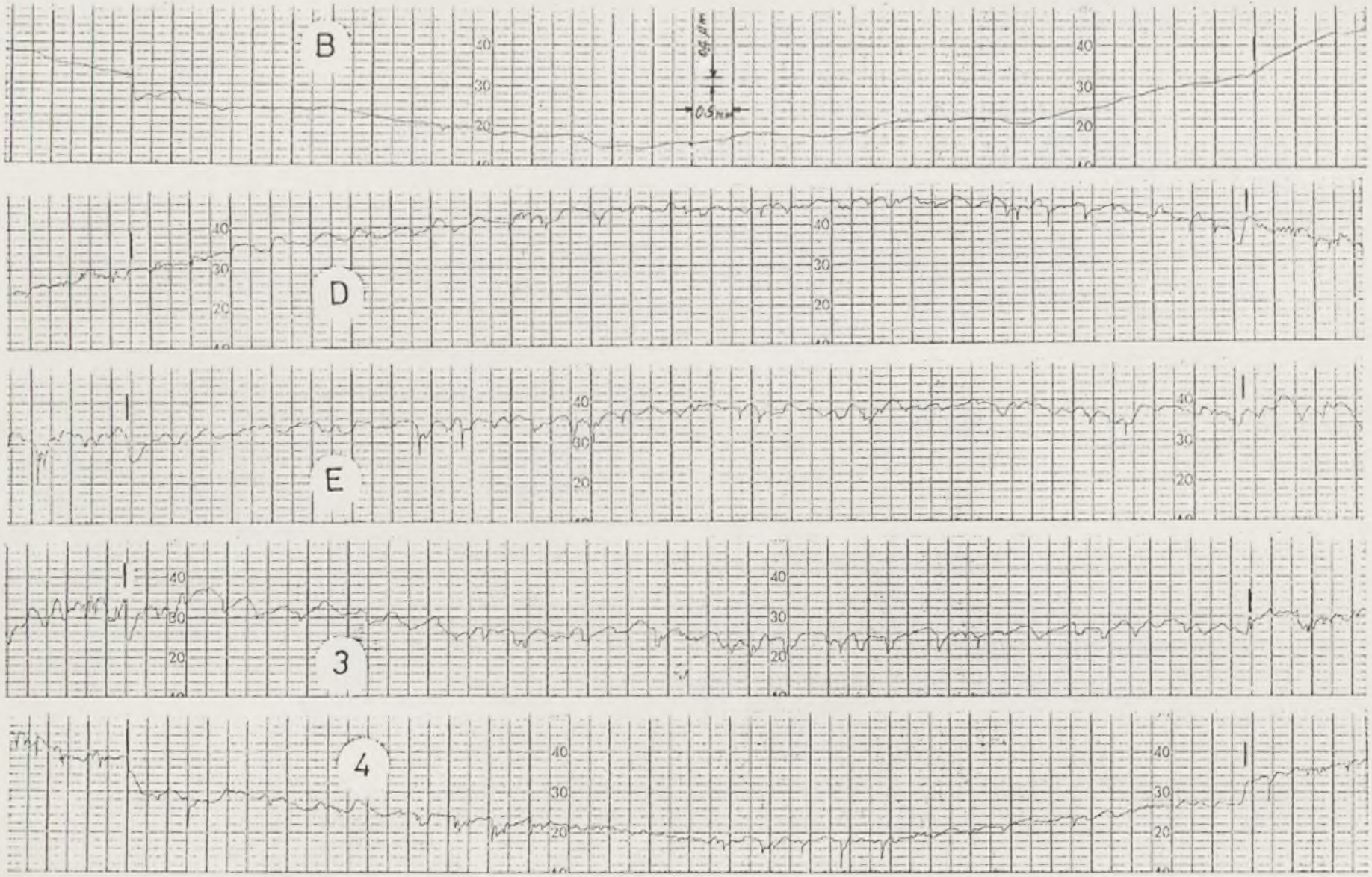

Figure (8.21) The final surface profiles cross the wear scar on the surface of the follower tested at different bulk temperatures.

characteristics. Generally speaking, the test at room temperature showed the mildest wear on the cam and follower surfaces. Increasing the bulk temperature from (75°C) to (105°C) had a mild influence on the surface characteristics of the cam and follower but the further increase of the temperature to (120°C) showed an important effect on the final surface characteristics. It is interesting to note that Fairman and Duff-Barclay (1961) reported that metallic contact was not greatly affected by a rise in bulk oil temperature from (60°C) to (90°C), but was appreciably increased at (120°C).

8.5.2 Thermal Effects on the Electrical Resistivity

Increasing the bulk temperature brought about an increase in the rate of decrease of the average voltage drop across the contact at the beginning of the running-in procedure. This phenomenon, it was felt, was mainly associated with the influence of the temperature on the surface plastic deformation, material hardness, adhesive wear and the reaction rate of the chemical additives in the lubricant. As discussed above, increasing bulk temperature led to a decrease of the material hardness which made it easier for asperities to deform plastically. A higher bulk temperature would also promote adhesive wear which in turn would reduce the number of asperity peaks which penetrated the oil film forming bridges between the two contacting surfaces. In addition, since the reaction rate of the chemical additives was dependent upon the temperature, at high temperatures the formation of the chemical film on the contacting surfaces was accelerated. All these variations arising from increasing the bulk temperature resulted in accelerating the reduction of the surface roughness and the formation of the surface film and consequently a considerable increase in the electrical resistivity across the contact. The higher the bulk temperature the stronger the influence of these factors.

The second peak of the average voltage drop that appeared on the recorded trace of the voltmeter was thought to be related to the formation and reformation of the surface film. A hard and brittle layer formed on the specimen surfaces during the grinding process. This layer was worn away on the asperity tips at the beginning of the running-in procedure but still remained in the valleys between asperities. The plastic deformation and thermal expansion of the asperities made the space which was available for this remaining machining layer become smaller and smaller as the running-in of the two surfaces proceeded. In addition the repeated elastic deformation of the subsurface material caused fatigue of the layer. The

combined effects of these factors finally led to the separation of this layer from the cam and follower surfaces. The disintegration of the layer not only provided some fresh surface for running-in but also made some of the chemical and physical films formed since the beginning of the test break. As a result, more asperities came into contact again and consequently the electrical resistivity decreased dramatically. As the surface roughness had been reduced to some extent in the previous running-in process and some chemical film had been deposited on the cam and follower surfaces the voltage drop at this moment looked lower than those that occurred at the beginning of each test. The times required for the average voltage drops to return to their normal value were also shorter than the initial ones.

8.5.3 The Running-In of the Valve Train

A continuous tendency of the average friction torque to decline was found not only in the running-in procedure but also in the normal test procedure as shown in Figures (8.3) and (8.4). A further study on the variation of the instantaneous torques in the cam lift period (see Figures (8.5) and (8.6)) revealed some important facts. Figure (8.5) shows the variation of the instantaneous torque at the beginning and the end of the running-in procedure. The gap between the solid line and the broken line reflected the reduction of the friction torque due to the running-in of the valve train. It can be seen that at the end of each running-in procedure the friction torque declined in the cam lift portion. The dramatic reduction of the friction torques was mainly found in the two regions between the cam angles of (−60°) to (−25°) and (+25°) to (+60°). The theoretical analysis on the lubrication of the cam and follower which is given in the previous chapters showed that small film thicknesses were found in these two regions. In addition, the severe scoring of the follower skirt surfaces indicated that the friction force caused by the follower and its guide could no longer be neglected. A theoretical analysis (see Chapter (9)) of the friction arising from the tilted follower moving in the follower guide predicted that about (30%) of the friction torque on the camshaft came from this friction and reached its peak value in these two regions as well (see Figure (9.4)). Thus it was evident that the considerable reduction of the friction torque in these two regions was the contribution not only from the running-in of the cam and follower but also from the improvement of the lubrication condition between the follower and its guide. Since the surface of the follower skirt was severely scored (see Figure (8.2b)) at the beginning of the running-in procedure it was obvious that the running-in

of these two surfaces must have been longer than that for the cam and follower, and sometimes it was almost impossible due to the repeated scoring. The small fluctuations of the average friction torque which were found even after (40 hours) running time were thought to be caused by the repeated scoring of the surface of the follower skirt. A further comparison was made on the instantaneous torques at the beginning, (50 hours) running and the end of normal test procedures (see Figure (8.6)). Although the torques still showed some reductions in these two regions after (50 hours) running, the extent of these reductions were much smaller than those in the running-in procedure. The difference between the broken line which reflects the decrease of the friction torque from (50 hours) running to the end of each test was almost undetectable.

The instantaneous voltages across the contact during the running-in procedure of each test at different bulk temperatures have been presented in Figure (8.9) plotted against cam angle. The figure shows that the voltage across the contact drops substantially in five regions. This is particularly obvious at the beginning of each test. The first and last drops corresponded to the position at which the cam initiated and completed the contact with the follower respectively. The middle drop appeared on the cam nose while the other two drops took place in the two regions between the cam angles of (−25°) to (−50°) and (+25°) to (+50°) within which extremely small fluid films existed due to the small entraining velocity. It is interesting that these two regions were coincident with the regions in which the friction torque decreased substantially during the running-in procedure. High voltages across the contact on the cam flanks were also observed. This suggested that the surfaces of the cam and follower in these regions were well separated by a lubricant film. At the end of each running-in procedure the combined effects of the elastohydrodynamic and some kinds of chemical films on the surfaces brought the voltages across the contact almost back to the applied voltage (50 mV), which indicated the substantial increase of the electrical resistivity between the two surfaces. Further comparisons between each test at different bulk temperatures again showed that the increase of the electrical resistivity was closely related to the increase of the bulk temperature. This is associated with the reaction rate of the chemical additives in the lubricant. In normal test procedures the voltage across the contact was usually high in most of the cam lift portion except in the two regions mentioned above and on the cam nose in which small voltage drops were still visible (see Figure (8.10)).

8.5.4 Effects of Elastohydrodynamic Lubrication

A sensitivity of the electrical resistivity across the contact of the cam and follower to the fluctuations of both camshaft rotational speed and inlet oil temperature was found in the present tests. The detailed discussion of this phenomenon in the previous section revealed the important fact that the elastohydrodynamic effect still played an important role in separating the cam and follower surfaces. Even the formation of the surface (or boundary) film on the contacting surface was dependent upon this effect to some extent. These findings confirm the conjecture of Bell (1978) that at high temperatures the elastohydrodynamic film has an important effect on the coefficient of friction in the contact and presumably also on the severity of conditions in areas of boundary lubrication. This is a typical mixed lubrication situation in which the separation of the two surfaces not only depends upon the elastohydrodynamic film but also relates to the asperity contact condition which in turn is associated with the existence of the surface films. Thus it can be said that the lubrication condition in the cam and follower conjunction depends upon both the elastohydrodynamic film and surface films including the physical and chemical reactions on the surfaces as well as the changes of the asperities.

8.5.5 Thermal Effects on the Average Friction Torque and Power Loss of the Valve Train

As has been discussed above the running-in of the valve train took more than (10 hours). Thus in order to investigate the bulk temperature effect on the average friction torque of the valve train, which is presented as a function of running time in Figure (8.4), was time averaged in the running period from (40 hours) to the end of each test. The results are presented in Figure (8.22) as a function of the bulk temperature. The power loss associated with these time averaged friction torques is also shown in the same figure. The curves show an upward trend of the average friction torque and power loss with an increase of the bulk temperature. It is well known that an increase of the bulk temperature leads to a decrease of the lubricant viscosity and consequently a decrease of the oil film thickness which in turn causes an increase of the shear rate between the two surfaces. The increase of the shear rate tends to increase the friction between the two surfaces but this positive effect on increasing the friction is limited to a certain extent because the lubricant viscosity decreases at the same time. On the other hand the reduction of the nominal film thickness makes more asperities come into contact which increases the friction as

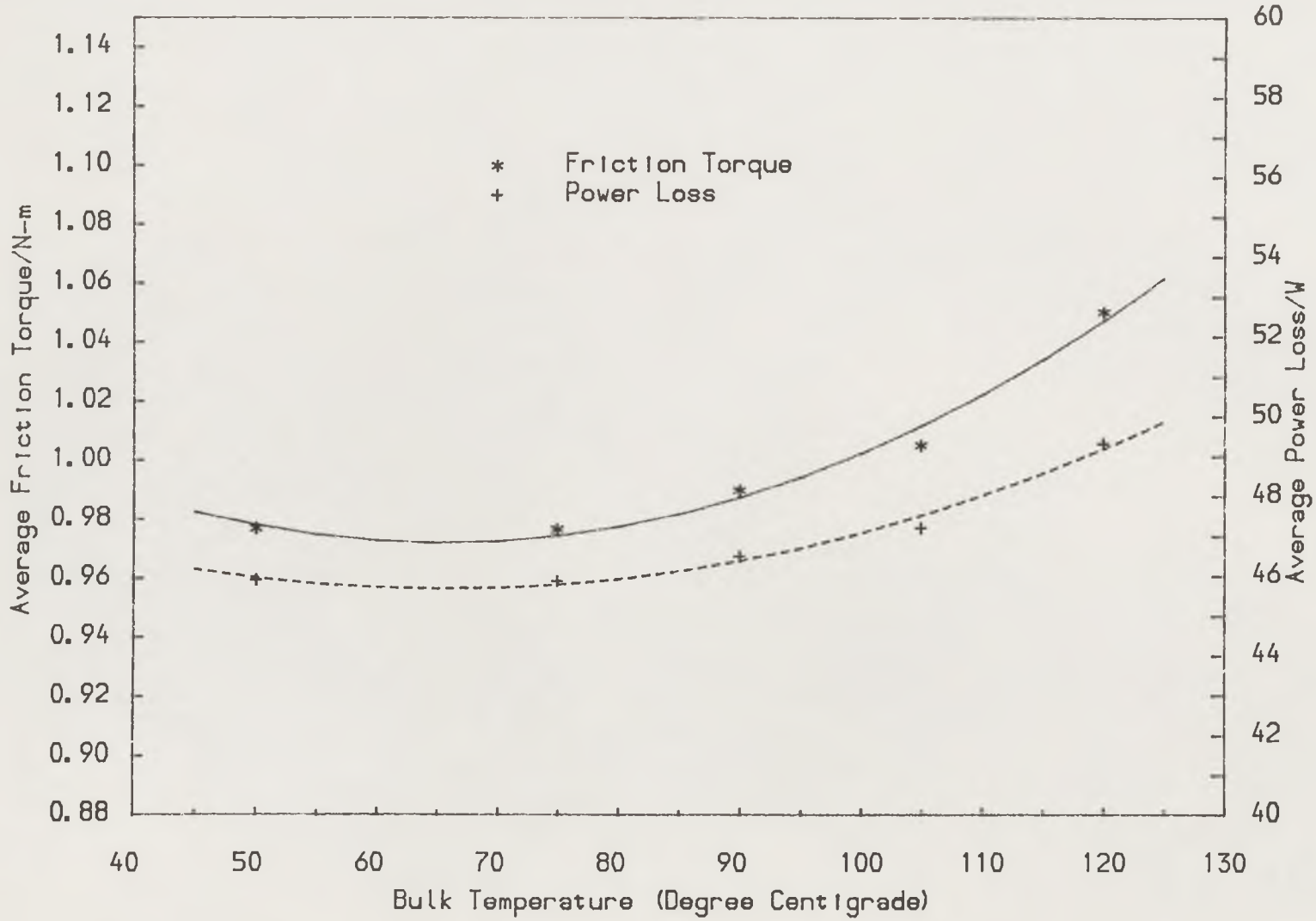

Figure (8.22) The variation of the average friction torque and power loss at different bulk temperatures.

well. However, the increase of the bulk temperature is beneficial to the formation of the chemical film on the contacting surfaces. Beside these factors, as has been concluded in Chapter (3), the friction force is also influenced by the composite surface roughness height. Considering that the friction torque is associated with so many complicated factors which in turn influence each other it is quite possible that under certain circumstances the increase of the bulk temperature will have little effect on increasing the friction torque and sometimes the reverse effect may be expected. Although Figure (8.22) shows a generally increasing trend of the friction torque due to the influence of increasing the bulk temperature, this influence is generally minor. The increase of the bulk temperature from (50°C) to (120°C) only results in a (7%) increase in the average friction torque from (0.98 N-m) to (1.05 N-m).

8.5.6 Speed Effects on the Average Friction Torque and Power Loss of the Valve Train

The effect of the camshaft rotational speed on the average friction torque and associated power loss has been shown in Figure (8.17). Generally there was a downward trend of the average friction torque as the camshaft speed increased. By contrast, the variation of the power loss showed an upward trend as the speed increased from (440 rpm) to (1820 rpm) but a further increase of the camshaft rotational speed from (1820 rpm) to (2070 rpm) resulting in a slight decline. As discussed in Chapter (5) the increase of the camshaft speed not only resulted in an increase in the entraining velocity but also led to a reduction of the load in the cam nose region. This dual action was of great benefit in promoting the formation of an elastohydrodynamic film between the cam and follower. The instantaneous torques acting on the camshaft at different rotational speeds are presented in Figure (8.18) as a function of cam angle. The figure shows that increasing the camshaft speed leads to an increase in the torque on the cam flanks and a decrease on the cam nose. This was a direct consequence of the changes of the load on the cam due to the variation of the speed. The reduction of the load on the cam nose region resulted in an improvement of the lubrication in this region and consequently a reduction of the friction force. Whilst on the cam flanks the cam and follower enjoyed full film lubrication due to the high entraining velocity and large equivalent radius of cam curvature, the increase of the load had less effect on the lubrication condition as well as the friction force. Therefore, the increase of the camshaft rotational speed resulted in a decrease of the average friction torque. An approximate five fold increase of the speed from (440 rpm) to (2070 rpm) resulted in a (42%)

decrease of the average friction torque from (1.36 N-m) down to (0.79 N-m). Interestingly, the increase of the camshaft speed from (1820 rpm) to (2070 rpm) led to a (12%) decrease of average friction torque. The considerable reduction in the friction torque is thought to be due to the appreciable improvement of the lubrication condition, not only limited to the cam/follower interface, but also the follower/guide interface. Consequently, instead of increasing the power loss decreased slightly. In the same way the cam nose temperatures in these two cases showed a similar trend (see Figure (8.20)). Because of the limitation of the present test this phenomenon should be verified at higher speeds.

8.6 Conclusions

A careful and comprehensive experimental programme consisting of a series of tests at different bulk temperatures and camshaft rotational speeds has been undertaken to investigate the tribological performance of a polynomial cam and non-rotating flat faced follower. Several important variables including the friction torque, power loss, electrical resistivity across the contact of the cam and follower and temperatures at the cam nose and in the valve stem guide have been monitored in each test. Some sophisticated techniques for data acquisition and data processing including a ADC data sampling system, a spectrum analyser and a digital filter have been adopted in the present tests. The wear characteristics have been examined by measuring the surface roughness values, surface profile and material hardness of the cam and follower prior to and subsequent to each test. The main conclusions which can be drawn from the experimental results are summarized below;

(1) The bulk temperature shows a mild effect on the wear characteristics of the cam and follower as it is increased from (75°C) to (105°C). However, the wear characteristics are considerablely affected by further increasing the bulk temperature from (105°C) to (120°C).

(2) The lubrication condition of the cam and follower in the present tests is found to be determined by both elastohydrodynamic lubrication and surface films. The sensitivity of the electrical resistivity to the small fluctuations of the inlet oil temperature and camshaft rotational speed shows that the elastohydrodynamic effect still plays an important role in separating the cam and follower surfaces. Moreover, the formation of the

surface film is also dependent upon this effect to some extent.

(3) According to the observation of the variation of the electrical resistivity across the contact of the cam and follower and the substantial reduction of the friction torque in the two zero entraining velocity regions, it can be said that in terms of lubrication conditions and wear characteristics three critical points are found. These are the two zero entraining velocity regions and the cam nose.

(4) The tests at different bulk temperatures show that increasing the bulk temperature results in an increase in both the friction torque and power loss of the valve train, but this increase is not considerable.

(5) It is evident that the increase of the camshaft rotational speed led to a decrease of the average friction torque and an increase of the power loss. Under certain circumstances a further increase in camshaft rotational speed resulted in a slight decrease in the power loss.

(6) The existence of the severe scoring scar and its distribution on the surface of the follower skirt revealed two important facts; firstly the follower tilts when it moves up and down in the follower guide and, secondly, the lubrication condition between the follower and its guide is much worse than that anticipated previously. Therefore, it is suggested that boundary lubrication predominates at the follower/guide interface. The friction force arising from this interface must be considered.

PART III

COMPARISION OF THEORETICAL AND EXPERIMENTAL RESULTS

CHAPTER 9

COMPARISON OF THEORETICAL AND EXPERIMENTAL RESULTS

9.1 Introduction

A theoretical model for predicting the oil film thickness in a transient elastohydrodynamic line contact associated with rough surfaces has been developed and detailed in Chapter (5). A further application of this model to the mixed lubrication analysis of the four-power polynomial cam and non-rotating flat faced follower has yielded some interesting results. In this chapter the film thicknesses predicted by this model are related to the voltage drop across the conjunction between the cam and follower as well as the talysurf traces of the wear track on the surface of the follower.

As has been described in Chapter (8), the existence of the severe scoring scars and their distribution on the follower skirt has revealed two significant facts: firstly, the follower tilts when it moves up and down in the follower guide and, secondly, boundary lubrication predominates in the follower/guide interface. Unfortunately, in previous theoretical analyses dealing with the power loss of the valve train the friction force arising from this interface was always neglected or underestimated. A friction model of the valve train based upon experimental findings is developed in this chapter. The model takes account of the tilting of the follower and the consequent friction force.

The measurement of instantaneous friction torque as a function of the cam angle has proved to be extremely difficult (Sun and Rosenberg (1987)), particularly at high camshaft rotational speeds due to the torsional vibration of the transducer shaft. According to the current learned society literature the highest speed at which reliable experimental results can be obtained is limited to about (1000 rpm). By adopting a series of advanced techniques for data acquisition and data processing, the friction torque was successfully presented in terms of the cam angle with camshaft rotational speeds exceeding (2000 rpm). This is indeed an important achievement in the present experimental study and consequently makes it possible to study the tribological performance of the cam and follower in great detail.

The accomplishment of the comprehensive experimental programme detailed in Chapter (8) has provided a vast amount of reliable data. This enables the validity of the theoretical model for predicting the tribological performance of the cam and follower to be examined. In addition, a brief discussion on the percentage of the friction torque arising from the

cam/follower, follower/guide and support bearings of the valve train respectively is given in this chapter.

9.2 Theoretical Model

The theoretical model detailed in this section was adopted for estimating the oil film thickness across the cam and follower and the friction force arising from various parts of the valve train. The results predicted by the present model are also discussed briefly in this section.

9.2.1 Predicting the Film Thickness between the Cam and Follower

The lubrication analysis of transient elastohydrodynamic line contacts associated with rough surfaces detailed in Chapter (5) was adopted for predicting the nominal oil film thicknesses between the cam and follower.

9.2.2 Friction Force of the Valve Train

The friction model developed in this chapter deals with the friction force arising from three tribological pairs of the valve train including the cam/follower interface, follower/guide interface and support bearings. The friction caused by the conjunction of the valve stem and its guide was neglected.

9.2.2a) Cam and Follower Interface

The total friction force acting on the cam surface involves three components due to (a) the mean viscous shear flow, (b) the interface component associated with the local pressure on asperities and (c) the force associated with boundary lubrication arising from the asperity interactions. These three components were evaluated from equations (3.5), (3.6) and (3.12) respectively. If the total predicted interface frictional stress on the cam exceeded the boundary film shear strength given by equation (3.10), the latter was adopted in computing the friction force. The rate of change of shear stress with pressure of the boundary film was assumed to be (0.08). In addition, as discussed in Chapter (3), the mixed lubrication model of Patir and Cheng (1978) was only valid when the film thickness ratio (λ) was greater than (0.5). Thus, in cases where the film thickness ratio was less than (0.6) it was assumed that the boundary film was sheared. The friction coefficient was given a limiting value of (0.08). Instead of assuming an isoviscous behavior, the lubricant viscosity was considered to be a pressure dependent variable and was estimated by equation (2.16).

9.2.2b) Follower and Guide Interface

A general view of the configuration of the tilted follower contacting with its guide and the cam and associated forces is shown in Figure (9.1). The static balance of these forces yields an expression for the friction force arising from the interface of the follower and guide and is given below;

$$F_{f1} = \mu \frac{e}{l} \left(1 + \mu \mu_2 \frac{c}{e} \right) P_z \qquad (9.1)$$

$$F_{f2} = \mu \frac{e}{l} \left(1 + \mu \mu_2 \frac{c}{e} - \mu_2 \right) P_z \qquad (9.2)$$

$$P_z = \frac{W}{1 - 2\mu \frac{e}{l} - 2\mu_2 \mu^2 \frac{c}{l} + \mu \mu_2} \qquad (9.3)$$

Where (W) is the load which arises from the valve spring and the inertia of the valve train including the valve, bucket follower and valve spring and is estimated from equation (2.10). The effects of the valve train friction force on the acceleration of the moving parts was neglected. As concluded in Chapter (8), a boundary lubrication model was employed for estimating the friction force caused by the conjunction of the follower and its guide. The friction coefficient (μ) for the follower/guide interface was assumed to be (0.08) in the present analysis. For the sake of simplicity, in the present analysis the friction force (F_2) due to the cam/follower interface was assumed to be equal to the product of the cam load (P_z) and a friction coefficient (μ_2). Since the friction coefficient (μ_2) of the cam and follower conjunction was of the same or even smaller order of magnitude as that of the follower/guide interface, from equations (9.1) to (9.3) it could be seen that the influence of the cam/follower friction force on the value of (F_{f1}) and (F_{f2}) was so small that it could be neglected. Thus, equations (9.1) to (9.3) can be simplified as;

$$F_f = F_{f1} = F_{f2} = \mu \frac{e}{l} P_z \qquad (9.4)$$

and

$$P_z = \frac{W}{1 - 2\mu \frac{e}{l}} \qquad (9.5)$$

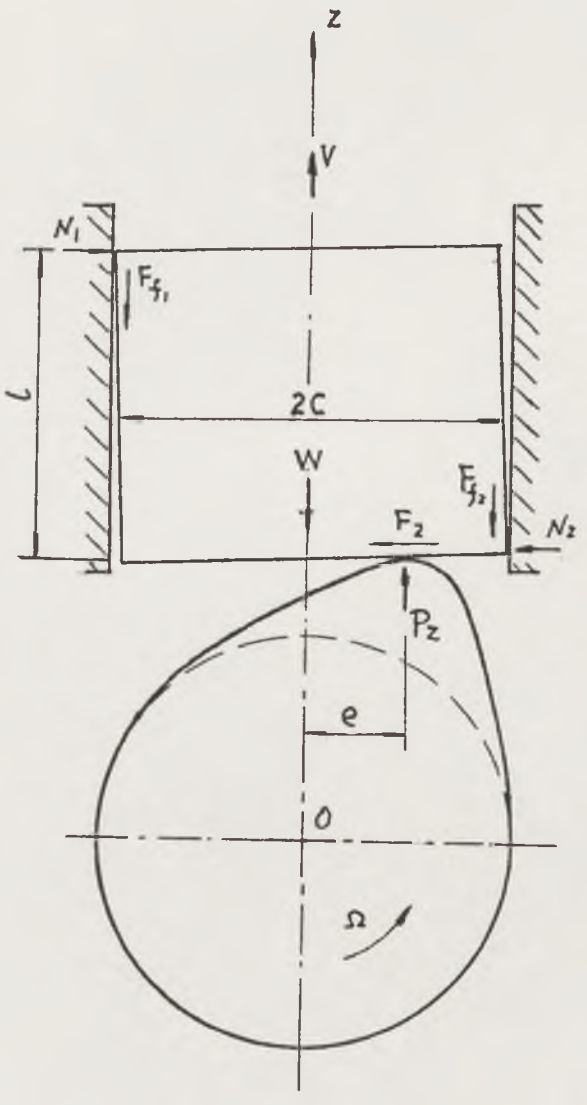

Figure (9.1) A general view of the follower/guide interface and associate force.

9.2.2c) Support Bearings

The friction torque associated with the support bearings was evaluated using the method described in the S.K.F. bearing catalogue. This included the effects of several factors including the bearing load, speed of rotation and the viscosity of the lubricant. In the present analysis it takes the form;

$$T_b = 0.0009 \left(\frac{P_z}{2 \times 6950}\right)^{0.05} \frac{P_z}{2} \times 38.5 + 10^{-7} \times (\eta\, n)^{2/3} \times 38.5^3 \quad \text{(N-mm)} \qquad (9.6)$$

Where (η) is the kinematic viscosity of the lubricant dependent upon the bulk temperature, (n) is the camshaft rotational speed in (rpm) and (P_z) is the cam load in (N) given by equation (9.5).

9.2.2d) Geometric Torque

In order to work out the instantaneous friction torque from the global camshaft torque measured by the transducer connected to the camshaft, the geometric torque must be subtracted. As it was almost impossible to measure the geometric torque and the total camshaft torque simultaneously by using existing techniques, this torque was predicted theoretically. The geometric torque is defined as the torque caused by the valve spring force and the valve train inertia which load the cam with an scrub radius (eccentricity (e)). This torque was calculated by;

$$T_g = e\,W \qquad (9.7)$$

9.2.2e) Instantaneous Friction Torque and Friction Coefficient

Knowing the geometric torque, the instantaneous friction torque was calculated by subtracting this torque from the measured global instantaneous torque acting on the camshaft. It was evident that this friction torque represented the total friction torque arising from the three tribological pairs of the valve train namely the cam/follower interface, follower/guide interface and support bearings. As has been mentioned in Chapter (8) the friction torque caused by the static load on the bearings has been eliminated by subtracting the torque signal averaged on the cam base circle from the global torque signal.

The instantaneous friction torque was converted into a friction force acting on the cam at a given cam angle by dividing this torque with an equivalent radius which is equal to the sum of the radius of the base circle

and the cam lift. The friction coefficient at a given cam angle was readily calculated from the quotient of the friction and the cam load (P_z). Unless otherwise specified, the friction coefficient mentioned here and in subsequent sections represents the overall friction coefficient of the valve train.

9.2.3 Brief Discussion of Theoretical Results

The effects of the camshaft rotational speed on the cam load, entraining velocity, sliding velocity and the friction torque on the camshaft due to the friction in the follower/guide interface are briefly discussed in this subsection.

The cam load at different speeds is shown in Figure (9.2) as a function of cam angle. The figure showed that the cam load was not symmetrical about the cam nose due to taking into account the fiction force of the follower/guide interface. Consequently the load on the cam rising flank was greater than that on the falling flank. Increasing the speed caused an increase in the load on the cam flanks and a decrease in load on the cam nose.

Figure (9.3) shows the variation of the entraining and sliding velocity at different camshaft rotational speeds. It was obvious that increasing the camshaft speed led to an increase in both entraining and sliding velocity. The maximum sliding velocity occurred on the cam nose. As the sliding velocity was proportional to the camshaft rotational speed the increase of the speed from (440 rpm) to (2070 rpm) resulted in an increase in the sliding velocity by a factor of (4.7).

The friction force arising from the follower/guide interface is presented in terms of the friction torque in Figure (9.4) as a function of cam angle. The sudden increase of the cam load and its eccentricity caused a steep increase of the friction torque until it reached the maximum value on the cam rising flank. As the contact point of the cam and follower moved towards the centre of the follower the eccentricity decreased to zero and consequently the friction torque due to the friction of the follower/guide interface fell to zero. On the falling side of the cam profile the reverse situation was found but the value was smaller than that on the rising side. As the eccentricity of the cam load was independent of the camshaft rotational speed the friction of the follower/guide was only dependent upon the cam

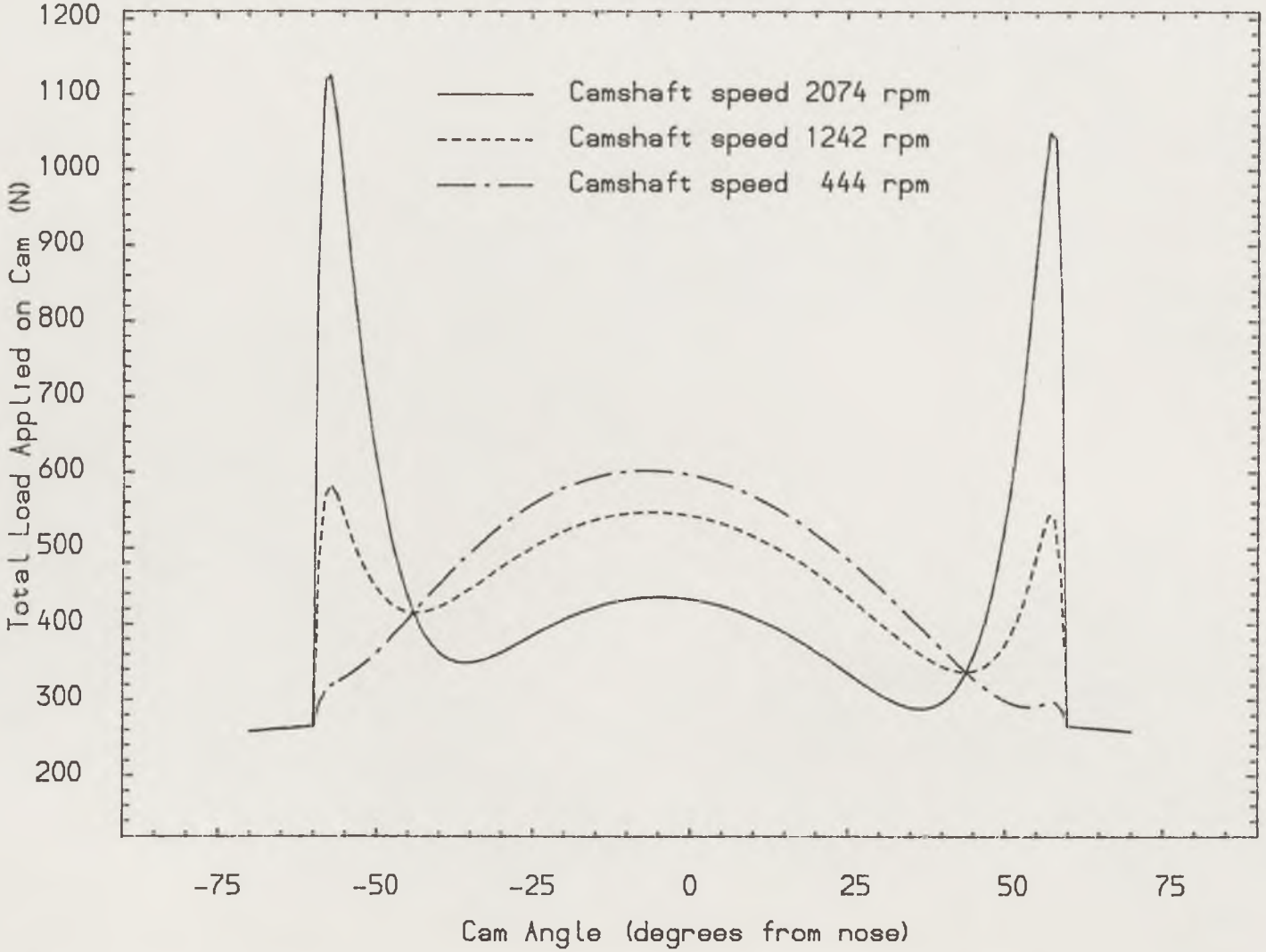

Figure (9.2) The variation of the load on cam at different camshaft rotational speeds.

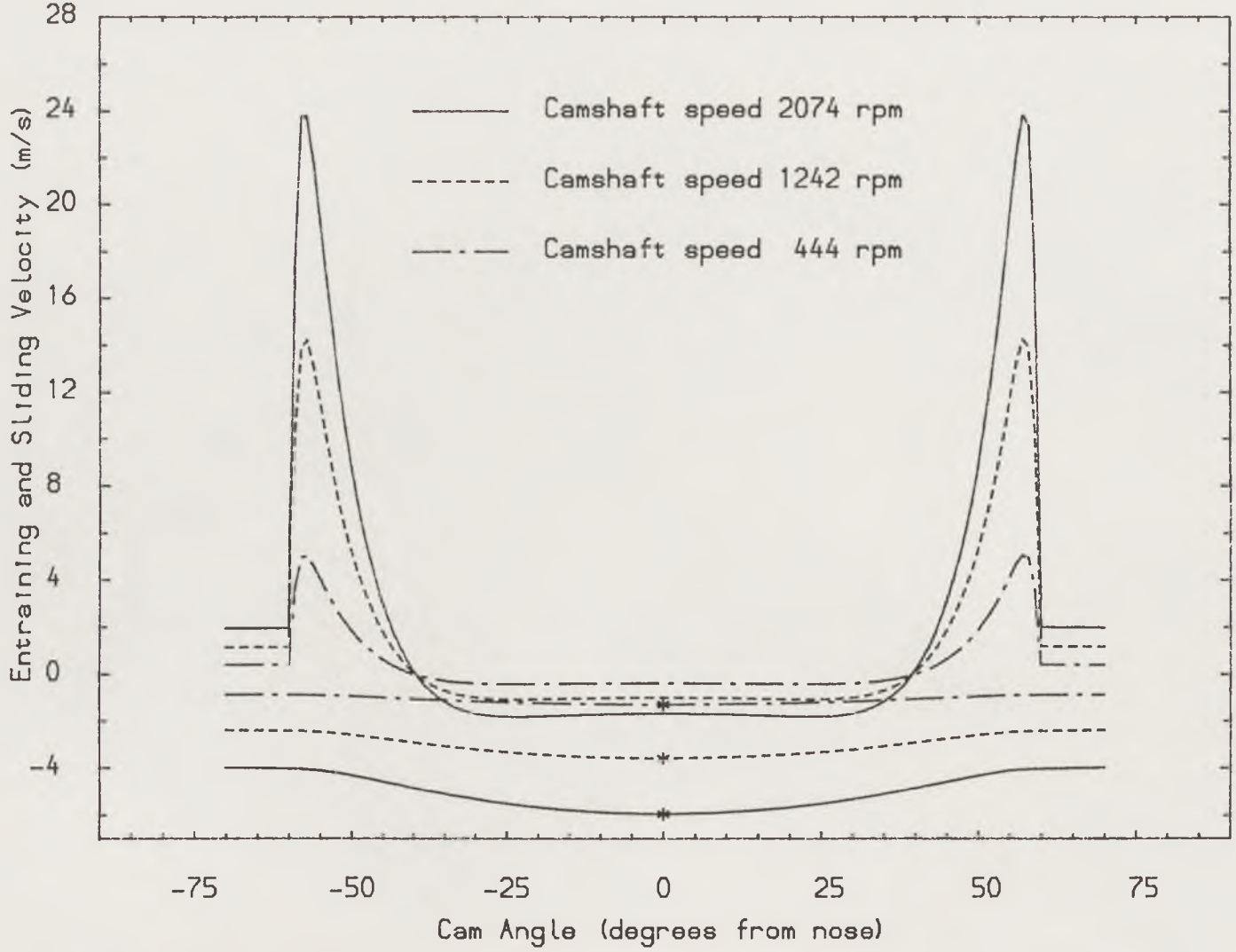

Figure (9.3) The variation of entraining and sliding (*) velocity at different camshaft speeds.

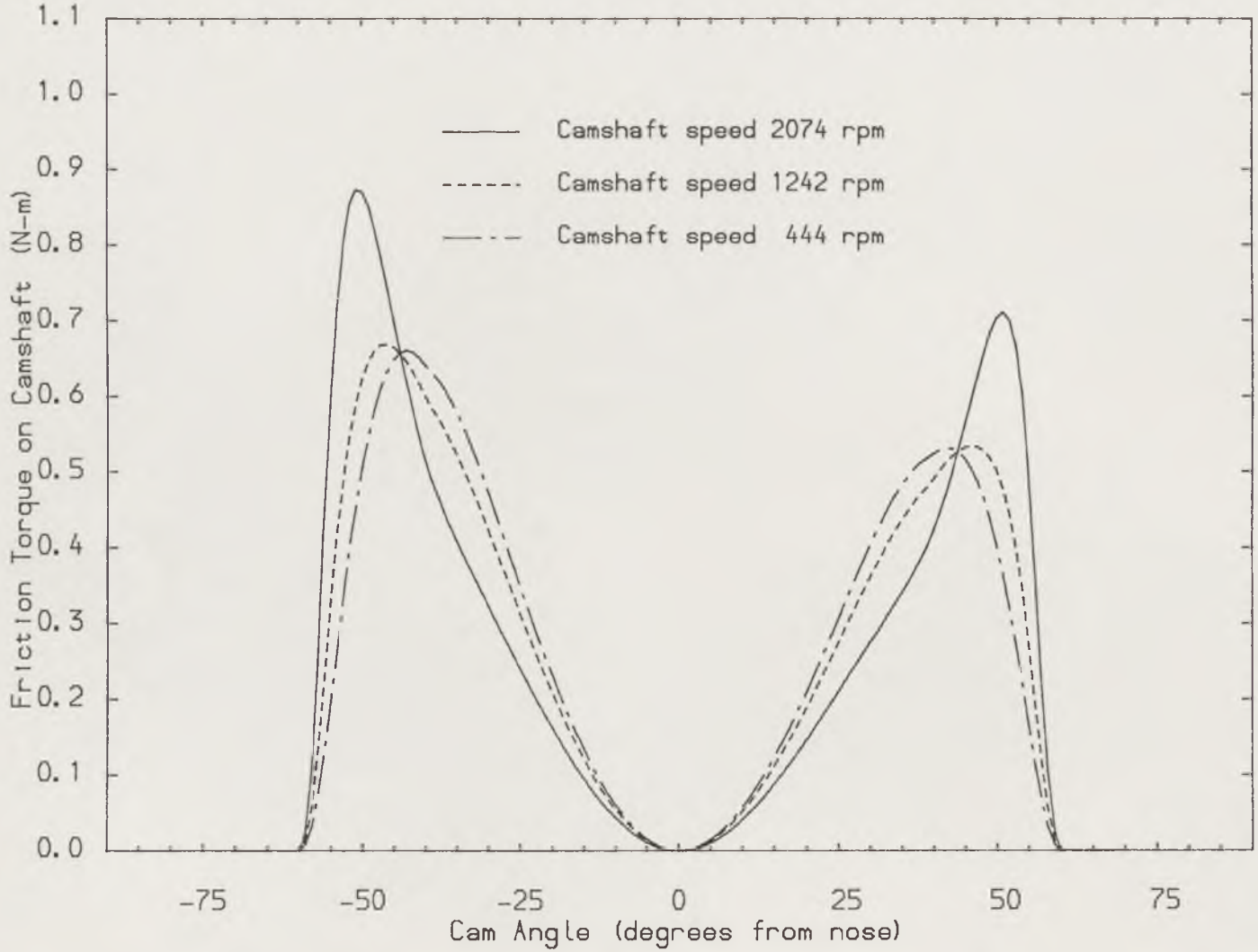

Figure (9.4) The variation of the friction torque arising from the follower/guide interface at different camshaft rotational speeds.

load if the friction coefficient (μ) of the follower/guide interface was assumed to be constant at any speed. Thus the influence of the speed on this friction torque was the same as that on the cam load. To summarize, it can be said that the friction torque caused by the friction of the follower/guide interface had a significant influence on values of the instantaneous friction torque measured on the two cam flanks and parts of the cam nose (between cam angles of (−60°) to (−25°) and (25°) to (60°)).

The theoretical model developed in this chapter was further applied to evaluating the friction torque arising from the three tribological pairs of the valve train. The average total friction torque in the cam lift portion is shown in Figure (9.7) as a function of the camshaft rotational speed. The broken line shows a least square curve fit to the theoretical results. It demonstrates a declining trend with the increase of the speed. The percentages of the contribution of each pair to the total friction torque of the valve train were also estimated. Increasing the camshaft rotational speed from (440 rpm) to (2070 rpm) led to a decrease in the contribution of the cam/follower interface to the total friction torque from (71.7%) down to (62.5%) but an increase in the percentage from the follower/guide interface from (27.7%) up to (36.1%). In fact the average friction torque caused by the follower/guide friction remained almost the same at any camshaft speed. The increase in the percentage of the contribution to the total friction torque was due to the decrease of the total friction torque as the speed increased. According to the present model the friction torque arising from the support bearings was only about one percent of the total.

9.3 Further Discussion of Experimental Results

A theoretical model has been developed to estimate the geometric torque applied to the camshaft. Subsequently, the instantaneous friction torque of the valve train was evaluated from the measured overall torque acting on the camshaft. A detailed discussion on these friction torques and friction coefficients as well as some additional conclusions which can be obtained from the further discussion are given in this section.

9.3.1 Instantaneous Friction Torque of the Valve Train

The friction torque at different camshaft rotational speeds is presented as a function of cam angle between (−65°) and (65°) in the top frames of Figure (9.5) from (a) to (g). The detailed features of the friction

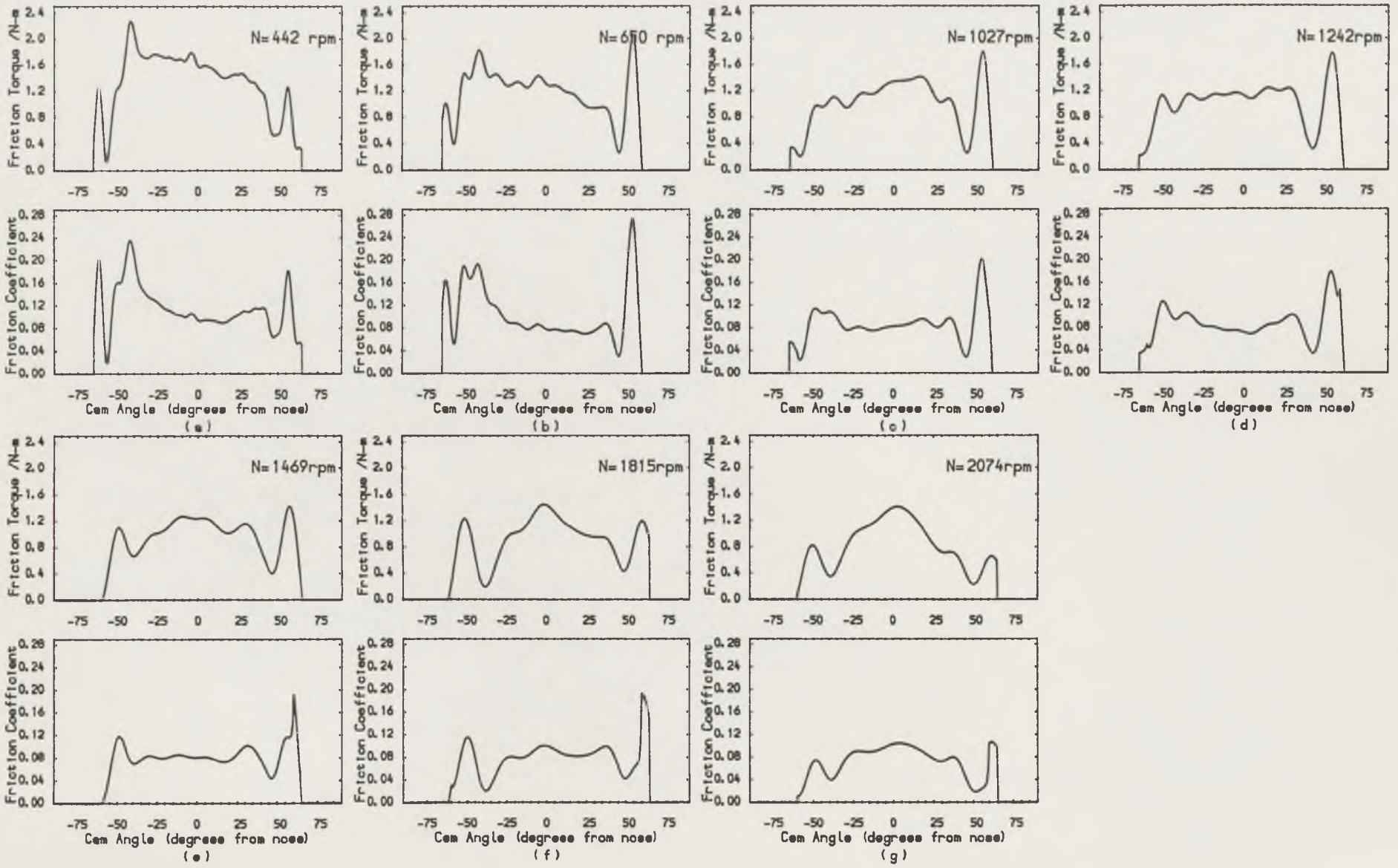

Figure (9.5) The variation of friction torques and friction coefficients in the cam lift cycle at different camshaft rotational speeds with (105 C) bulk temperature.

torque of the valve train were readily evaluated from these figures; these features were usually masked by the averaging process.

Generally, the curves of the fiction torque showed five peaks in the cam lift portion. The first and the last peak corresponded to the sudden increase and decrease of the load on the cam as the cam initiated and completed contact with the follower on the cam ramps. From Figure (9.4) it was known that the friction torque arising from the friction of the follower/guide interface also made some contributions to these two peaks, particularly in the case of higher camshaft rotational speeds. The detailed discussion of these two peaks relating to the dynamic characteristics of the valve train are beyond the scope of the present study. The following discussion therefore concentrates on the features within the cam flanks and nose regions.

There was generally an increase of the friction torque in the vicinity of the zero entraining velocity point on the cam falling side in each case shown in this figure. Another peak occurring on the opposite side of cam was not quite as evident except at low test speeds where a higher peak than that visible on the cam falling side was found (see Figure (9.5) (a), (b) and (c)). In addition, a peak was observed in the middle of the curves, which corresponds to the cam nose. This phenomenon was very typical at low test speeds as shown in (a) and (b) of Figure (9.5).

Interestingly, increasing the camshaft speed caused the friction torque to decrease on each side of the cam nose, but the reduction of the friction torque on the nose was not as considerable as in other regions. From Figure (9.5) (a) and (b) it can be seen that at low test speeds the friction torque decreased progressively from the highest peak value in the vicinity of the point of zero entraining velocity on the cam rising side to a lower value on the cam falling side with a small peak appearing on the cam nose. A substantial decrease of the friction torque on the cam rising side due to the increase of the camshaft rotational speed resulted in a relatively smooth curve with two small peaks occurring in the two zero entraining velocity regions. A further increase of the speed led to a dramatic decrease of the friction torque on each side of the cam nose with the maximum torque appearing on the cam nose.

9.3.2 Instantaneous Friction Coefficient of the Valve Train

The coefficient of friction is an important parameter in estimating the lubrication conditions at the cam/follower interface. The friction coefficients of the valve train at different camshaft rotational speeds are presented in Figure (9.5) along with friction torques. It can be seen that for each test speed the variation of the friction coefficient in the cam lift portion was quite similar to the trend of variation of friction torque. It was interesting to note that in case of low test speeds besides the two peaks occurring on the cam ramps and parts of the cam flanks, two peaks of the friction coefficient were found in the zero entraining velocity regions, the values of both peaks being greater than that on the cam nose. This reflected agreement of the experimental findings with the theoretical predictions that extremely small film thicknesses, more asperity contact and high friction force occurred in these two regions. Furthermore, the substantial decrease of the friction coefficient down to (0.015) on the cam flanks indicted that elastohydrodynamic lubrication existed here due to the large entraining velocity and effective radius of curvature. Encouragingly, the lubrication analysis predicted the same trend (see Chapter (5)).

In the case of the lowest test speed of (440 rpm) the highest friction coefficient of the valve train was (0.24) which was found on the cam rising flank. This value corresponded to a friction coefficient (0.12) of the cam/follower interface. Here the friction forces arising from the follower/guide interface and support bearings were predicted by theoretical models which have been detailed in sections (9.2.2b) and (9.2.2c). This implied that boundary lubrication occurred in this region, whilst the sharp decrease of the friction coefficient of the cam/follower interface down to about (0.07) and the subsequent increase to (0.10) on the cam nose indicated the transition of the lubrication regimes from boundary to severe mixed lubrication conditions due to the increase of the entraining velocity in the cam nose region. Likewise, the test at (650 rpm) camshaft rotational speed showed a similar trend but with smaller values of valve train friction coefficient which varied between (0.20) and approximately (0.08). For high test speeds this transition could no longer be detected. This was because most parts of the cam lift portion were operating under mixed or elastohydrodynamic lubrication conditions. The maximum range of the friction coefficient of the valve train in the cam lift portion was dependent upon the camshaft rotational speed. In the case of the lowest test speed the friction coefficient of the valve train varied between (0.24) and (0.06),

whilst the test at the highest speed revealed that the variation of the friction coefficient was within the range of (0.10) to (0.015).

On the whole a general decreasing trend of the friction coefficient with increasing camshaft speed was found. But the reduction of the friction coefficient on the cam nose was not as pronounced as that in other regions of the cam lift portion. The friction coefficient on the cam nose remained at an almost constant value of about (0.08) as the speed was increased from (650 rpm) to (1470 rpm). Further increasing the camshaft speed to (1820 rpm) and then (2070 rpm) showed an increase in the friction coefficient on the cam nose up to (0.09) and then (0.10) respectively. A similar situation was also found in the friction torque as shown in traces (f) and (g) of Figure (9.5). As discussed in section (9.2) increasing camshaft rotational speed resulted in a decrease in the cam load and an increase in the sliding speed in the cam nose region. Consequently, an increase in the friction coefficient in this region as the speed increased can be predicted. On the other hand, the increase of the friction coefficient may also be due to the lack of a simultaneous measurement of the cam load. It should be kept in mind that the previous theoretical predictions on the oil film thicknesses and friction forces and even the friction coefficient presented in this chapter were all related to the cam load which is predicted by the theoretical model in which the dynamics of the valve spring were not taken into consideration. Beard and Hempson (1962) pointed out that the vibration of the spring had no effects on the average value of load in the whole cam cycle but did have significant influence on the instantaneous values of the cam load. A further interpretation for the dynamic effects of the valve spring will be given in the discussion section.

9.3.3 Average Friction Coefficient of the Valve Train

The average friction coefficient for the valve train in the cam lift portion is presented in Figure (9.6) as a function of the camshaft rotational speed. The figure showed a decreasing trend as the camshaft speed was increased. The increase of the camshaft rotational speed from (440 rpm) up to (2070 rpm) resulted in a decrease in the average friction coefficient from (0.12) down to (0.07). Considering the contributions of the friction force arising from the follower/guide interface and support bearings the average friction coefficient of the cam/follower conjuction must be lower than these values. Indeed, subtracting the friction forces arising from the follower/guide interface and support bearings from the overall friction of

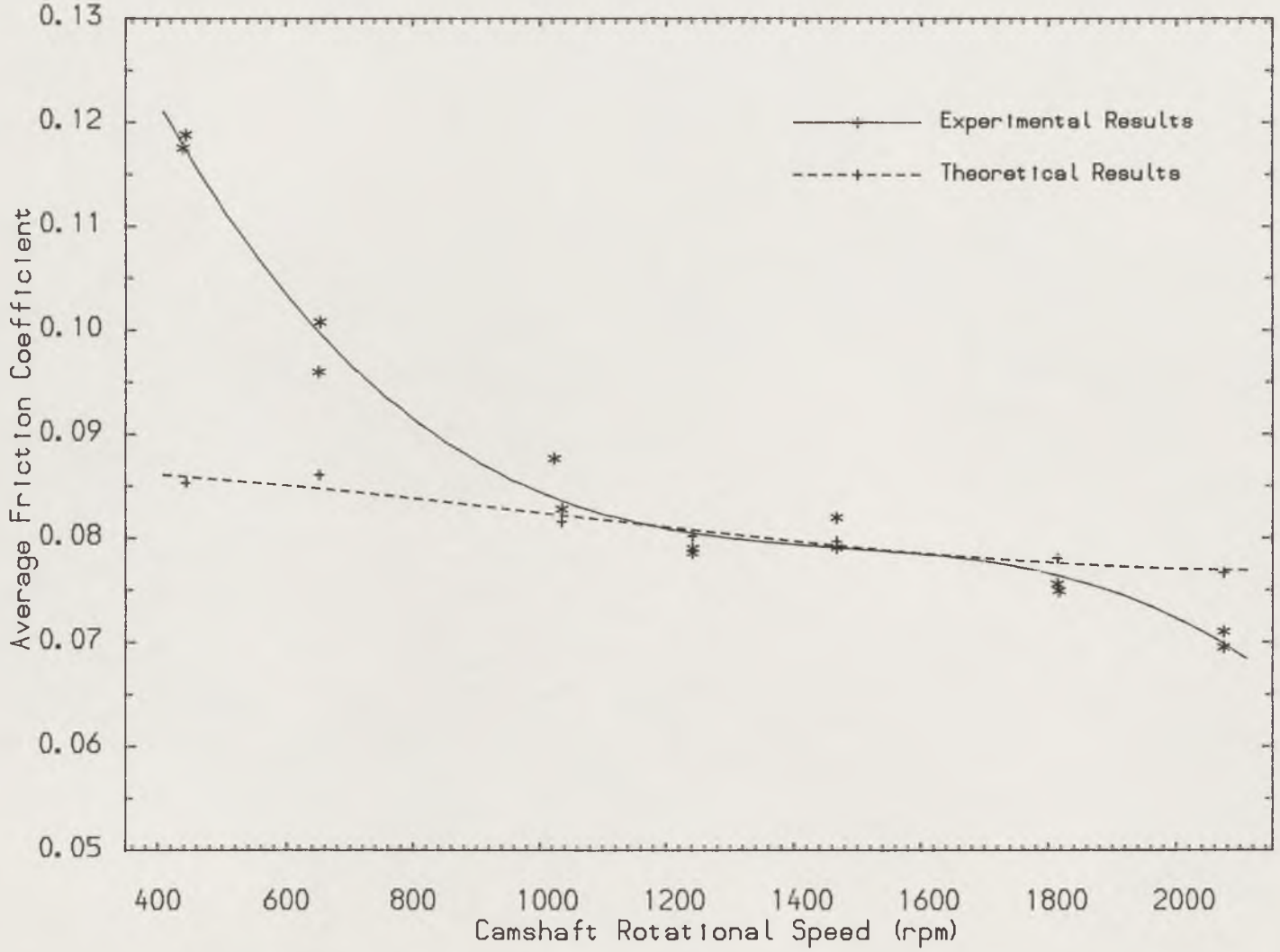

Figure (9.6) The variation of the average friction coefficients at different camshaft rotational speeds.

the valve train revealed that the average friction coefficient of the cam/follower interface decreased from (0.09) down to (0.04) as the speed increased from (440 rpm) up to (2070 rpm).

9.3.4 Concluding Remarks

Based upon a theoretical model for predicting the load and associated geometric torque by taking into account the friction force arising from the follower/guide interface and camshaft support bearings, the friction torque and the friction coefficient of the valve train have been presented in terms of the cam angle. This is the first time that three peaks of the friction coefficient have been detected, these being associated with the two zero entraining velocity regions and the cam nose respectively. This is consistent with both theoretical predictions and experimental findings which indicated that extremely small film thickness and more asperity contact occurred in these regions. Moreover, the occurrence of small friction coefficients on the flanks further confirmed that full elastohydrodynamic lubrication condition was achieved in these areas.

The maximum range of the friction coefficient of the valve train in the cam lift portion was found to be (0.015) to (0.24) with the test speed varied between (440 rpm) to (2070 rpm) at a bulk temperature of (105°C). This revealed an important fact: at low speed the cam and follower conjunction predominately suffered boundary lubrication, while at higher speeds the lubrication condition transferred to the mixed or the full elastohydrodynamic lubrication regime. The direct consequence of this transition was the reduction of the average friction coefficient of the valve train from (0.12) to (0.07) which corresponded to the decrease in friction coefficient of the cam/follower interface from (0.09) down to (0.04) as the speed increased from (440 rpm) up to (2070 rpm).

9.4 Comparison of Theoretical and Experimental Results

A series of comparisons have been made between the theoretical predictions and experimental results to examine the validity of the present theoretical model. These comparisons include; quantitative comparisons of the friction torque and friction coefficient at different camshaft rotational speeds and different bulk temperatures and qualitative comparisons of the oil film thickness with the voltage across the contact and the talysurf trace of the wear track on the surface of the follower.

9.4.1 The Friction Torque

The average friction torques of the valve train measured in both the increasing and the decreasing speed loops are presented in Figure (9.7) as a function of the camshaft rotational speed. The solid line represents a least square curve fit to these experimental data pairs while the broken line shows the curve fit to theoretically predicted data pairs. The two curves show the same decreasing trend of average friction torque with the camshaft rotational speed increased from (440 rpm) to (2070 rpm). Furthermore, within a very wide speed range between (650 rpm) and (2070 rpm), the difference between the two curves was less than (5%). More encouragingly, the two curves overlapped within the speed range (800 rpm) to (1800 rpm). In the case of very low test speeds the theoretical prediction underestimated the friction torque. This was thought to be due to the limitation adopted in the present model for the friction coefficient of the boundary lubrication being (0.08). However, the instantaneous friction coefficient at (440 rpm) camshaft speed plotted in Figure (9.5) (a) showed that the cam and follower operated under boundary and severe mixed lubrication conditions with the friction coefficient of the valve train varying between (0.24) and (0.10) which corresponds to the variation of the friction coefficient of the cam/follower interface between (0.12) and (0.10) in the majority of the cam lift portion.

In addition, the theoretical predictions were compared to average friction torques which were measured at different bulk temperatures for a camshaft speed of (1240 rpm). The experimental results were taken from the time averaged value of the friction torque in the last (60 hours) of a (100 hour) duration test. Both theoretical and experimental results are presented in Figure (9.8) as a function of the bulk temperature. The two curves, which are fitted to experimental and theoretical data pairs respectively, showed the same increasing trend of the friction torque as the bulk temperature increased. A very good agreement between the theoretical predictions and the experimental results was obtained, with the maximum difference between the two curves being less than (10%).

The theoretically predicted and experimentally measured instantaneous torques at different camshaft rotational speeds are compared in Figure (9.9) as a function of cam angle. The detailed discussion on these comparisons will be given in the discussion section of this chapter.

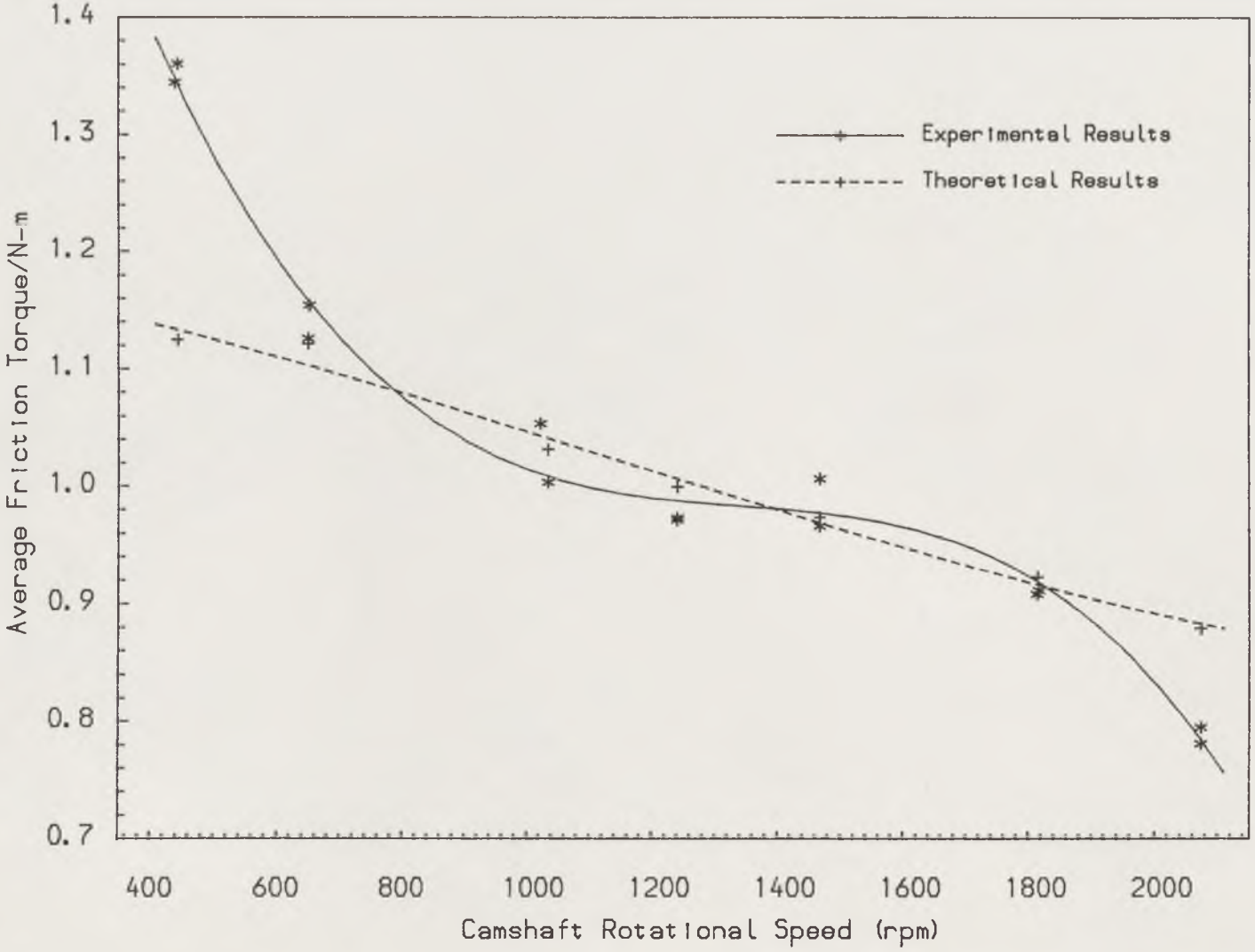

Figure (9.7) The comparison of the theoretical and experimental results of the average frictional torque at different speeds.

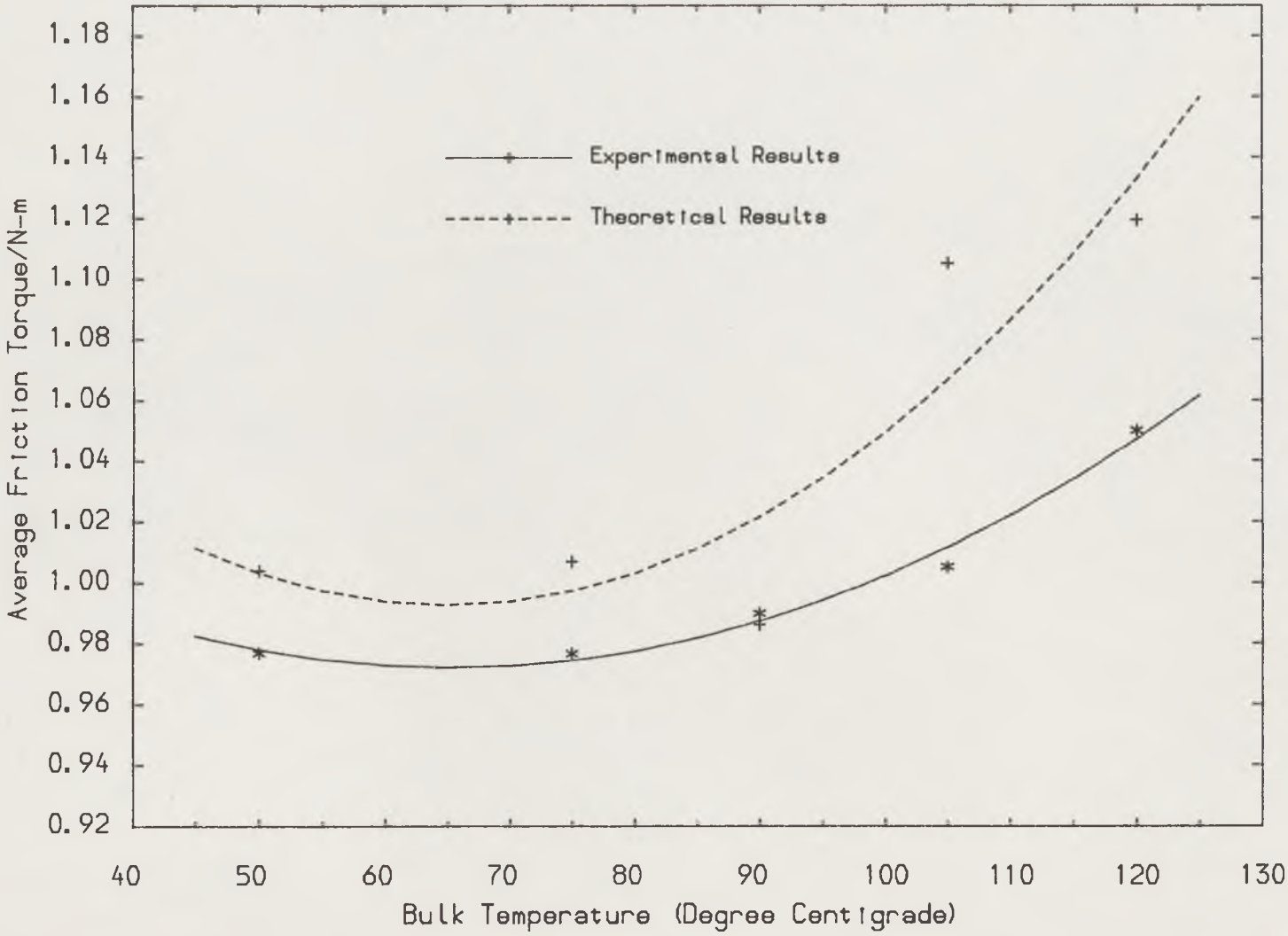

Figure (9.8) The comparison of the theoretical and experimental results on the average friction torque at different bulk temperatures.

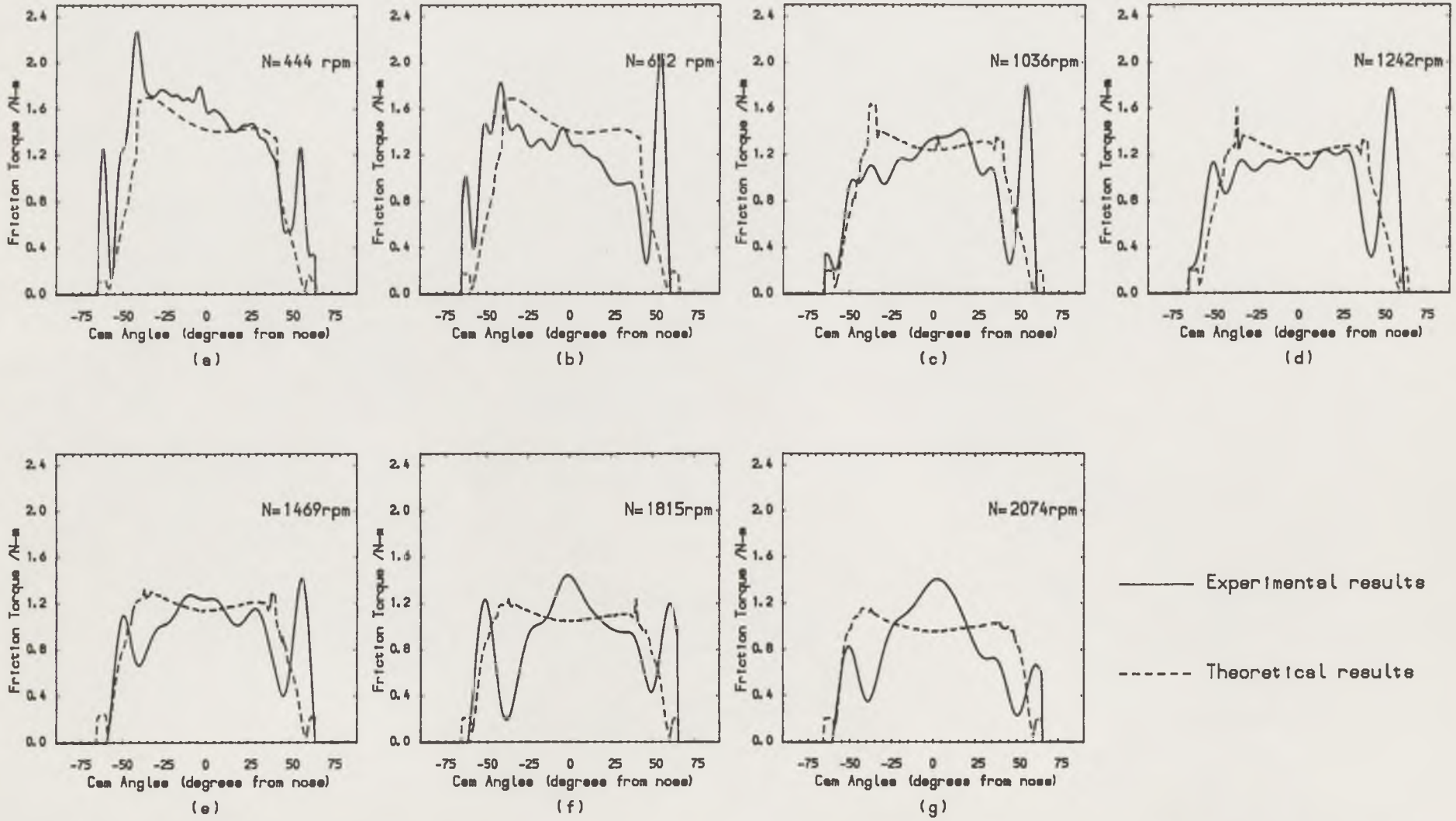

Figure (9.9) The comparison of theoretical and experimental friction torques in the cam lift cycle at different camshaft rotational speeds with (105°C) bulk temperature.

9.4.2 The Friction Coefficient

The average friction coefficients estimated by the theoretical analysis at different camshaft speeds has been presented in Figure (9.6) together with the experimental results. The two curves fitted to these data pairs show the similar trend and deviations to the situation found in the comparison of the average friction torque (see Figure (9.7)).

9.4.3 The Oil Film Thickness

The oil film thicknesses predicted by the transient elastohydrodynamic lubrication theory associated with rough surfaces can be related to the wear marks found on the surface of the follower at the end of the test. The wear track which was found on the surface of the follower corresponded to the points during the cam cycle where the film thicknesses predicted by the lubrication theory were small. Figure (9.10) shows a comparison of the predicted film thickness across the follower (S) and a talysurf trace of the follower wear track. The deeper groove at the right hand end of the trace corresponded to the small entraining velocity region near the cam falling flank. The shallower groove located at the left hand end of the trace related to the other small entraining velocity region near the cam rising flank. Interestingly, the variation of the oil film thickness showed the same tendency as the wear track on the surface of the follower with not only the position but also the depth of the wear track being in harmony with the predicted oil film thickness. The two grooves observed in the middle of the wear track corresponded to the two points at which the cam initiated and completed contact with the follower respectively.

A comparison between predicted film thickness and the voltage across the contact between the cam and follower is shown in Figure (9.11). As discussed in Chapter (8), the voltage drop across the contact represented the separation between the cam and follower and the asperity contact within the conjunction, therefore, the higher voltage drops implied a smaller separation with more asperity contact, and vice versa. Three interesting voltage drops were found; one existed in the cam nose contact region and the other two occurred in the extremely small oil film thickness regions on the cam rising and falling flanks. Again, a very close correlation between the theoretically predicted oil film thickness and the measured voltage drop was found in Figure (9.11). The qualitative coincidence of the position and the

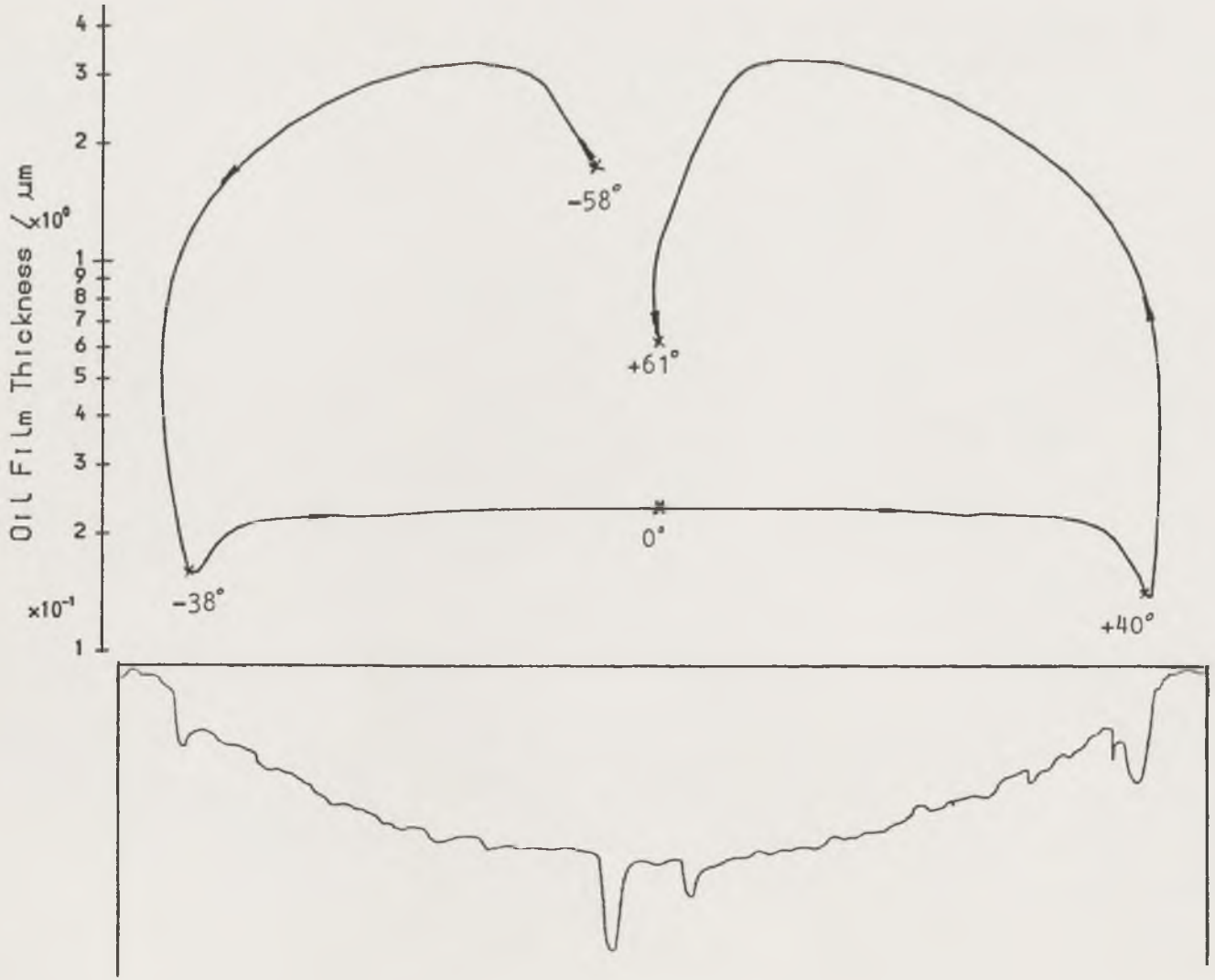

Figure (9.10) Comparison of the talysurf trace of wear tracks on the follower with the oil film thickness predicted by the lubrication analysis.

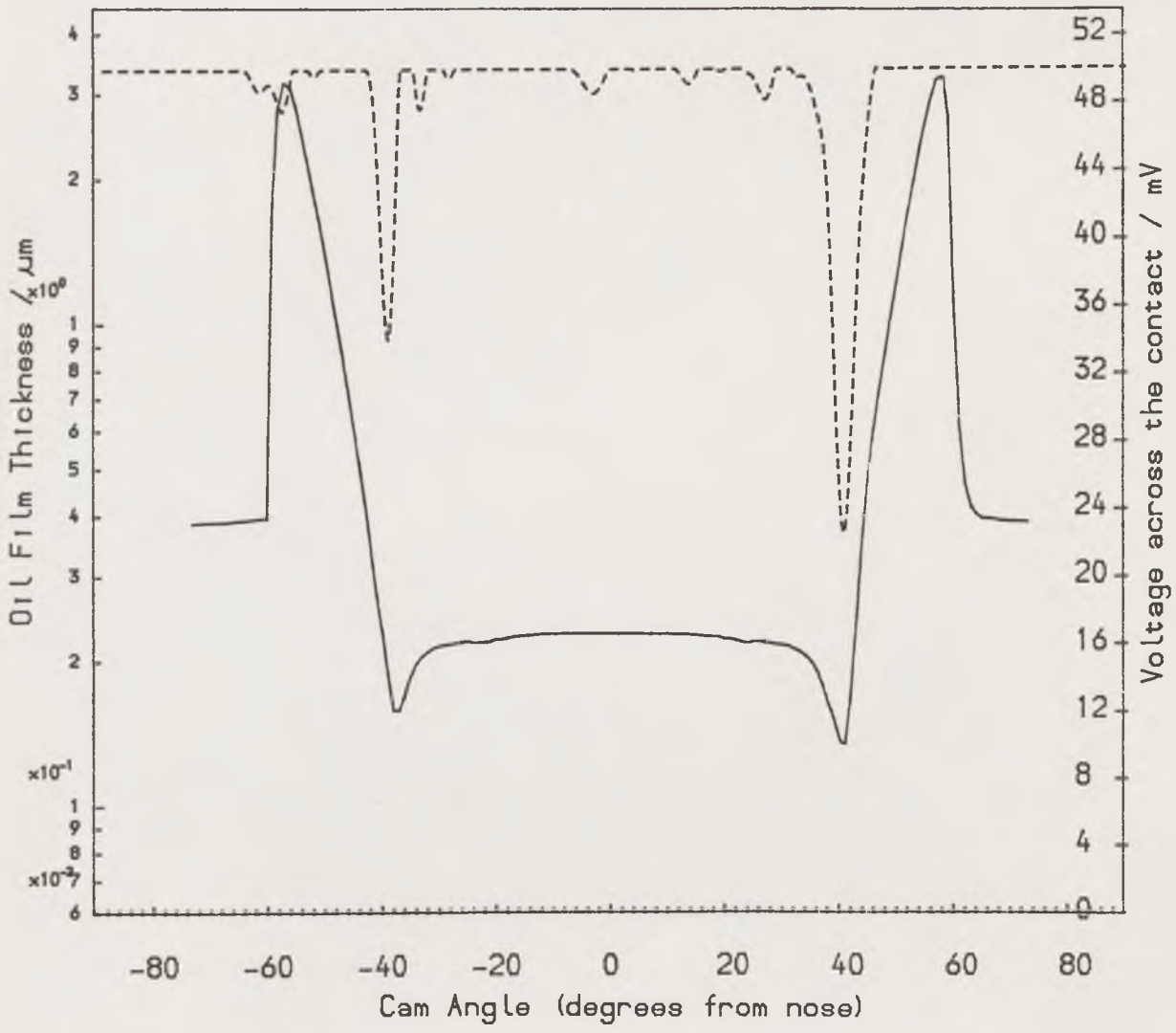

Figure (9.11) The comparison of the voltage across the contact with the oil film thickness predicted by the lubrication analysis.

——— Predicted oil film thickness

------- Measured voltage across the contact

amplitude of the voltage drop with theoretically predicted oil film thicknesses was excellent, although the figure showed a high voltage over the cam nose region where small oil film thickness was predicted by the lubrication analysis. This was thought to be due to the formation of the chemical film on the boundary surfaces. Indeed, in the beginning of the test at low bulk temperature at which the influence of the surface film on the measurement of the electrical resistivity was small, low voltage in the cam nose region was found (see Figure (8.9a)).

In summary, the qualitative comparison of the oil film thicknesses predicted by the lubrication analysis and the experimental results including the voltage drop across the contact and the talysurf trace of the wear track on the surface of the follower confirmed an important finding from the lubrication analysis that two extremely small film thickness regions existed in the vicinity of the zero entraining velocity points near the cam rising and falling flanks respectively. The minimum separation between the cam and follower occurred on the cam falling flank near the zero entraining velocity position.

9.5 Discussion

A brief discussion of the theoretical results and a further discussion of the experimental results have been given in previous sections of this chapter. In the present section the discussion is mainly focused on the comparison of theoretical and experimental results.

The comparison of the friction torque in terms of cam angle has proved to be most interesting. The instantaneous friction torques of the valve train, both theoretical and experimental, are presented in Figure (9.9). The figure showed a fairly good agreement between the theoretical predictions and the experimental results, although the positions at which peaks or valleys occurred were not exactly coincident. This was thought to be due to not employing a camshaft encoder. The cam angle was only located by a trigger impulse generated on the cam base circle by a photo cell. The cam angle corresponded to each of the pieces of sampled data being equally distributed between the two trigger impulses. Thus, the oscillation of the camshaft between the two trigger impulses was omitted. Even so, both the theoretical and experimental results showed the same trends in the variation of the friction torque in the whole cam lift portion. The substantial decrease of the

friction torque on the two cam flanks indicated the great improvement of the lubrication condition in these two regions in which the lubrication analysis predicted that full elastohydrodynamic lubrication was achieved.

In the case of high camshaft rotational speed the comparison showed that the theoretical analysis overestimated the friction torque on the cam flanks and in parts of the nose region. On the contrary, underestimation of the friction torque on the cam nose was found. This is a direct consequence of the lack of consideration of the vibration of the valve spring in the present theoretical model. Beard and Hempson (1962) pointed out that the vibration of the valve spring would play an important role in the actual load applied on the cam if the camshaft rotational frequency exceeded one twelfth of the natural frequency of the valve spring. According to the formula recommoneded by the authors the natural frequency of the valve spring in the present apparatus was approximately (284 Hz). So, one twelfth of this frequency was about (24 Hz). Therefore, if the camshaft rotational speed exceeded (1440 rpm), the instantaneous friction torque predicted by the present theoretical model would deviate from the experimental one. The higher the camshaft rotational speed the more the deviation of the theoretical prediction. However, the average values of the experimental results in the whole cam cycle was not affected by the spring vibration.

If there were no (0.4 mm) clearance between the follower and the cam base circle the two peaks of the friction torque on the two cam ramps would not appear in the experimental results (see Figure (9.9)). Then, the substantial decrease of the friction torque on two cam flanks would not be detected. Consequently, the friction torque would show an increasing trend as the contact of the cam and follower moved towards the nose. Interestingly, the experimental results given by Sun and Rosenberg (1987) did show a similar trend in the variation of the friction torque as anticipated above. Based upon their experimental results the authors concluded that the observed lack of friction reduction over any part of the contact cycle and the large coefficient of friction in the case of conventional lifters ruled out the possibility of elastohydrodynamic lubrication and generation of a squeeze film lubrication mechanism at the contact. This conclusion now seems to be somewhat doubtful. According to the present theoretical and experimental investigations, the substantial increase in the oil film thickness and considerable reduction of the friction coefficient on the cam flanks were due to the entraining velocity of the lubricant into the contact

and the effective radius of curvature of the contact being large, but not the effect of squeeze film action. On the contrary, in the vicinity of zero entraining velocity points where the squeeze film action predominated, extremely small film thicknesses were predicted. As a result of these extremely small film thicknesses, instead of showing a reduction in the friction coefficient in these two regions, a substantial increase of the friction coefficient was observed.

Sun and Rosenberg (1987) measured the spring load by inserting a sensor between the valve spring and the follower. The friction torque was worked out by subtracting the geometric torque, which is the product of the eccentricity and the load measured by the sensor, from the global camshaft torque. Thus, besides the friction torque caused by the cam/follower interface, an additional friction torque arising from the friction of the follower/guide interface was also included in the friction torque presented in their paper. In accordance with the theoretical prediction of this additional friction torque which has been detailed in section (9.2.2b) and Figure (9.4), the friction torque on the cam flanks must be lower than that presented in their paper, and consequently the friction coefficient is lower.

9.6 Conclusions

A theoretical model has been developed for predicting the valve train tribological performance which includes the oil film thickness, asperity contact and the friction forces arising from the cam/follower interface, follower/guide interface and support bearings. It is the first time that a theoretical model for evaluating the friction force arising from the follower and its guide, by taking into account the tilting of the follower, has been presented.

With a comprehensive dynamic analysis including the measurement of the damping coefficient and natural frequency of the camshaft system, the instantaneous friction torque has been obtained with camshaft rotational speeds exceeding (2000 rpm). According to current learned literature this is the highest test speed reached so far.

Furthermore, a multi-aspect comparison between the theoretical predictions and the experimental results has been undertaken. The main conclusions which can be obtained from these theoretical and experimental

results and theoretical comparisons are summarized below;

(1) The good agreement between the theoretical predictions and experimental results in many aspects shows that the theoretical model developed in this chapter provides a good basis for the prediction of tribological characteristics of the cam/flat faced follower and associated mechanism.

(2) Both experimental observation and the theoretical analysis predict that the friction force arising from the contact of the follower and its guide has a significant influence not only on the actual load on the cam but also on the friction torque of the valve train. Whilst the cam/follower interface has a major influence on the power loss of the valve train, the effects of the follower/guide contact can also be important and must be taken into consideration.

(3) By comparing the oil film thickness predicted by the lubrication analysis with experimental results which include the voltage drop across the contact of the cam and follower, talysurf traces of the wear track on the surface of the tested follower and the instantaneous friction coefficients, it has been confirmed that three critical portions of the cycle can be identified – one over the cam nose and the other in the vicinity of the two zero entraining velocity regions. The minimum separation between the cam and follower occurs on the falling flank of the cam.

(4) Both theoretical and experimental results show that the camshaft rotational speed has a significant effect on the lubrication of the cam and follower. At low camshaft rotational speeds boundary or mixed lubrication dominates the lubrication condition of the cam and follower, while at high camshaft rotational speed mixed lubrication predominates with full elastohydrodynamic lubrication being achieved on the cam flanks.

(5) The average friction coefficient for the valve train varied between (0.12) and (0.07) as the camshaft rotational speed increased from (440 rpm) to (2070 rpm) at (105°C) bulk temperature.

(6) At high camshaft rotational speed, it is necessary to take account of the dynamics of the valve spring. It may not have such an effect when a proper dynamic analysis is undertaken.

CHAPTER 10

OVERALL CONCLUSIONS AND SUGGESTIONS FOR FUTURE RESEARCH

10.1 Introduction

The work presented in this thesis has been concerned with both theoretical and experimental studies of the tribology of a four-power polynomial cam and non-rotating flat faced follower. The research has included three main parts: (a) theoretical studies of the tribological performance of the cam and follower, (b) an experimental investigation of the tribological characteristics of the cam and follower and (c) comparisons of theoretical predictions and experimental results.

Firstly, as an initial consideration of surface roughness effects, a mixed lubrication analysis of the cam and follower has been carried out with the assumption that the bounding solids were rigid (elastic deformation of the asperities is of course considered). Recognizing that the lubrication conditions encountered in an automotive cam and follower contact involve significant bulk elastic distortion of the bounding surfaces, a complete numerical analysis of a transient elastohydrodynamic line contact problem with variable squeeze film velocity along the conjunction has been developed for a modified cam and follower arrangement. This is the first time that such an analytical procedure has been applied to a cam and follower mechanism. Furthermore, a technique for estimating the minimum film thickness of a transient elastohydrodynamic line contact associated with rough surfaces has been developed and applied to the mixed lubrication analysis of the practical cam and follower arrangement. This is the first published analysis of the transient elastohydrodynamic line contact with rough surfaces. The computing time required for the lubrication analysis of the cam and follower is minimal.

Secondly, existing experimental apparatus was improved and equipped with thermostatic control facilities. A carefully designed and comprehensive experimental programme consisting of a series of tests at different bulk temperatures and camshaft rotational speeds has been undertaken to investigate the tribological performance of the cam and follower. Several important factors including the friction torque, power loss, electrical resistivity across the contact of the cam and follower and temperatures at the cam nose and in the valve stem guide have been monitored in each test. By adopting advanced techniques for data acquisition and data processing including an ADC data sampling system, a spectrum

analyser and a digital filter and through undertaking a comprehensive dynamic analysis of the camshaft system in the present tests, the instantaneous friction torque has been successfully obtained with camshaft rotational speeds exceeding (2000 rpm). According to current learned society literature, this is the highest speed achieved at the present time for such measurements. The wear characteristics have been examined by measuring the surface roughness values, surface profiles and material hardness of the cam and follower prior to and subsequent to each test.

Finally, based upon the theoretical analyses and experimental findings, a theoretical model for evaluating the tribological performance of the valve train including the cam/follower interface, follower/guide interface and support bearings has been accomplished. A theoretical model for estimating the friction force arising from the conjunction between the follower and its guide, taking into account the tilting of the follower, has been developed. Moreover, a multi-aspect comparison between the theoretical and experimental results has been made. Quantitative comparisons of the average friction torque and associated power loss of the valve train in the cam lift cycle at different bulk temperatures and different camshaft rotational speeds have been undertaken. Qualitative comparisons have been made between the theoretically predicted oil film thickness and the measured voltage across the contact of the cam and follower together with the talysurf trace of the wear track on the surface of the tested follower.

The overall conclusions and suggestions for future research which have emerged from the study described in this thesis are now summarized.

10.2 Overall Conclusions

(1) The excellent agreement between the theoretical predictions and experimental results in relation to many aspects has shown that the theoretical model developed provides a reliable prediction of the tribological characteristics of the cam/flat faced follower and associated mechanism.

(2) The prediction of the cyclic variation of the nominal minimum film thickness has been developed by including the effects of surface elastic deformation, surface roughness and the variation of lubricant viscosity with pressure. The general features of the cyclic variations of the nominal minimum film thickness between the cam and follower were similar to those

predicted by the rigid-isoviscous solution for rough surfaces and the full numerical transient elastohydrodynamic solution for smooth surfaces.

(3) Surface roughness exerted an important influence upon the lubrication performance of the cam and follower. An increase of the composite surface roughness height caused an increase of the nominal minimum film thickness but a decrease in the film parameter. The effect of the distribution of surface roughness between the cam and follower upon the nominal minimum film thickness varied in different parts of the cam profile. The results may be compared with those for the case of the same roughness on both the cam and follower; in the cam nose region a smooth follower and rough cam generated a higher predicted film thickness, whilst a smooth cam and rough follower produced a lower film thickness. By contrast, on the cam ramps the effects were reversed.

(4) Consideration of the local squeeze film velocity relating to the elastic deformation of the surfaces provided an increased damping effect which contributed to the persistence of the minimum film thickness in the two critical parts of the cam cycle where the entraining velocity dropped to zero.

(5) The bulk temperature showed a mild effect on the wear characteristics of the cam and follower as it was increased from (75°C) to (105°C). However, the wear characteristics were considerably affected by further increasing the bulk temperature from (105°C) to (120°C). Furthermore, the tests at different bulk temperatures revealed that increasing the bulk temperature resulted in an increase in both the friction torque and power loss of the valve train, but this was not considerable.

(6) Both theoretical and experimental results showed that the camshaft rotational speed had a significant effect on the lubrication of the cam and follower. At low camshaft rotational speed boundary or mixed lubrication dominated the lubrication condition of the cam and follower, while at high camshaft rotational speed mixed lubrication predominated with full elastohydrodynamic lubrication being achieved on the cam flanks. It was evident that increasing the camshaft rotational speed led to a decrease of the average friction torque and an increase of the power loss.

(7) By comparing the oil film thickness predicted by the lubrication

analysis with experimental results which included the voltage drop across the contact of the cam and follower, talysurf traces of the wear track on the surface of the follower and the instantaneous friction coefficients, it has been confirmed that three critical portions of the cycle can be identified - one over the cam nose and two in the vicinity of the zero entraining velocity regions. The minimum separation between the cam and follower occurred near the falling flank of the cam.

10.3 Suggestions for Future Research

(1) In practical service the follower is free to rotate in its guide. The theoretical models developed in the present research can be extended to include the influence of the rotation of the follower. In parallel with such a theoretical analysis, experimental investigations could be performed on the test apparatus which has been developed.

(2) The technique for predicting the minimum film thickness of a transient elastohydrodynamic line contact associated with rough surfaces is applicable to the lubrication analysis of other types of cam mechanism. This would require details of the kinematics and dynamics of the contact between the cam and follower to be ascertained. On the other hand, this technique may be used to derive an empirical formula for estimating the minimum film thickness in line contact under non-steady state elastohydrodynamic lubrication with rough surfaces. This would be a very useful aid to design.

(3) According to a recent paper by Ai and Yu (1988), a full numerical analysis of the transient elastohydrodynamic line contact associated with rough surfaces in the whole operating cycle of a practical cam and follower arrangement is possible. This would be of value both practically and theoretically in order to gain a greater fundamental knowledge of the tribological performance of the cam and follower.

(4) At high camshaft rotational speed the dynamic characteristics of the valve train including the follower, valve and valve spring can have a significant influence on the actual load acting on the cam and consequently the tribological performance of the cam and follower. In a more comprehensive theoretical model these influences should be considered. Likewise, in the experimental investigation of tribological characteristics of the valve train at high rotational speed, the actual load on the cam must be

recorded simultaneously with the torque signal. In addition, a shaft encoder is required with the present apparatus to monitor the cam angle with great precision.

(5) An experimental investigation at different bulk temperatures and different camshaft rotational speeds with a straight mineral oil lubricant will be necessary to identify the influence of the chemical additives in the multigrade oil used.

(6) It has been found that the variation of camshaft rotational speed and bulk temperature have substantial effects on the tribological performance of the cam and follower. In practical service the cam and follower work under conditions of continuingly fluctuating speed. Thus, the performance of the cam and follower may be greatly affected by this and a laboratory test simulating the actual operating conditions of the cam and follower in a motor car may be required.

REFERENCES

AI, X. and YU, H. (1988), "A Full Numerical Solution for General Transient Elastohydrodynamic Line Contact and Its Application", *Wear*, Vol. 121, pp. 143-159.

ALLEN, C.W., TOWNSEND, D.P. and ZARETSKY, E.V. (1970), "Elastohydrodynamic Lubrication of a Spinning Ball in a Non-Conforming Groove", *Trans. ASME, J.Lub.Tech.*, Vol. 92, No. 1, pp. 89-96.

ANDREW, S., TAYLOR, R.G. and LOVE, R.J. (1962), "A Testing Machine for Cams and Followers", *MIRA Report*, No. 7.

ANDREW, S., WYKES, F.C. and TAYLOR, R.G. (1965), "The Influence of Some Material and Lubricant Variables on the Surface Deterioration of Cams and Cam Followers", *MIRA Report*, No. 4.

ARMSTRONG, W.B. and BUUCK, B.A. (1981), "Valve Gear Energy Consumption: Effect of Design and Operation Parameters", *SAE Technical Paper* series 810787.

BAIR, S., GRIFFIOEN, J.A. and WINER, W.O. (1986), "The Tribological Behaviour of an Automotive Cam and Flat Lifter System", *Trans. ASME, J.Trib.*, Vol. 108, No. 3, pp. 478-486.

BARWELL, F.T. and ROYLANCE. B.J. (1978), "Tribological Considerations in the Design and Operation of Cams – A Review of the Situation", *Cam and Cam Mechanisms, J. Rees-Jones*, MEP, pp. 99-105.

BEARD, C.A., HEMPSON, J.G.G. (1962), "Problems in Valve Gear Design and Instrumentation", *S.A.E. National Powerplant Meeting, Philadelphia.*

BEAUCHAMP, K. and YUEN, C. (1979), "Digital Methods for Signal Analysis", *George Allen & Unwin.*

BEDEWI, M.A. (1985),"Non-Steady State Lubrication of Counterformal Contacts", *Ph. D. Thesis, Leeds University.*

BEDEWI, M.A., DOWSON, D. and TAYLOR, C.M. (1985), "Elastohydrodynamic Lubrication of Line Contact Subjected to Time Dependent Loading with Particular Reference to Roller Bearings and Cams and Followers", *Mechanisms and Surface Distress, 12th Leeds-Lyon Symposium on Tribology*, pp. 289-304, Butterworths.

BELL, J. (1978), "Discussion on Paper of BARWELL and ROYLANCE (1978)" *Cams and Cam Mechanisms*, J. Rees-Jones, MEP, p. 107.

BISHOP, J.L.H. (1950-51), "An Analytical Approach to Automobile Valve Gear Design", *Proc.Instn.Mech.Eng., (A.D.)*, pp. 150-157.

BONA, C.F. and GHILARDI, F.G. (1965), "Influence of Tappet Rotation on Cam and Tappet Surface Deterioration", *Proc.Inst.Mech.Eng.*, Vol. 180, Pt. A, pp.269-278.

BRITISH TECHNICAL COUNCIL OF THE MOTOR AND PETROLEUM INDUSTRIES, (1972), "Cam and Tappets: A Survey of Information".

CHEN, F.Y. (1982), "Mechanics and Design of Cam Mechanism", Pergamon Press.

CHATTERLY, T.C. (1981), "Surface Deterioration of Cams and Cam Followers", *Brit.Tech.Conc.Mot.Petr.Ind., BTC/LI/81.*

CHRISTENSEN, H. (1979), "A Simplified Model of Elastohydrodynamic Lubrication of Rollers – The Central and Exit Solution", *Trans. ASLE*, Vol. 22, No. 4, pp. 323-332.

COY, R.C. and DYSON, A. (1981), "A Rig to Simulate the Kinematics of the Contact Between Cam and Finger Follower", *ASLE/ASME Conf.* as 81-LC-2B-1.

DOWSON, D., HARRISON, P. and TAYLOR, C.M. (1985), "The Lubrication of Automobile Cams and Followers", *Mechanisms and Surface Distress, 12th Leeds-Lyon Symposium on Tribology*, pp. 305-322, Butterworths.

DOWSON. D. and HIGGINSON, G.R. (1966), "Elastohydrodynamic Lubrication", *Pergamon Press.*

DOWSON, D., RUDDY, B.L. and ECONOMMU, P.N. (1983), "The Elastohydrodynamic Lubrication of Piston Rings", *Proc.Roy.Soc.Lond.*, A386, pp. 409-430.

DOWSON, D., TAYLOR, C.M. and ZHU, G. (1986), "Mixed Lubrication Analysis of A Cam and Flat Faced Follower", *Fluid Film Lubrication - Osborne Reynold Centenary, 13th Leeds-Lyon Symposium on Tribology*, pp 599-609, Butterworths.

DUDLEY, W.M. (1948), "New Methods in Valve Cam Design", *S.A.E. Quarterly Trans.*, Vol 2, No. 1, pp. 19-33.

DYSON, A. and NAYLOR, H. (1960-61), "Application of the Flash Temperature Concept to Cam and Tappet Wear Problems", *Prco.Instn.Mech.Eng., (A.D.)*, No. 8, pp. 225-280.

FAIRMAN, A.G.C. and DUFF-BARCLAY, I. (1961), "A Test Rig for the Evaluation of Cam and Follower Design, Metallurgy, and Lubrication", *MIRA Report*, No. 15.

GREENWOOD, J.A. (1972), "An Extension of the Grubin Theory of Elastohydrodynamic Lubrication", *J.Phys., D:Appl. Phys.*, Vol. 5, pp. 2195-2211.

GREENWOOD, J.A. and TRIPP, J.H. (1970-71), "The Contact of Two Nominally Flat Rough Surfaces", *Proc.Instn.Mech.Eng.*, Vol. 185, pp. 625-633.

GRUBIN, A.N. (1949), Central Scientific Research Inst. of Tech. and Mech. Eng. Moscow, Book No.30. DSIR Transl. No.337.

HAMILTON, G.M. (1980), "The Hydrodynamics of a Cam Follower", *Tribology International.*, Vol. 13, No. 3, pp. 113-119.

HARRIS, S.W. and ZAHALKA, T.L. (1983), "A Field Test Study of Camshaf Wear in a 2.3L OHC Engin and Its Correlation to the Sequence V–D Test", *SAE Technical Paper* series 831758.

HARRISON, P. (1985), "A Study of the Lubrication of Automotive Cams", *Ph. D. Thesis, Leeds University.*

HERREBRUGH, K. (1970), "Elastohydrodynamic Squeeze Films Between Two Cylinders in Normal Approach", *Trans. ASME, J.Lub.Tech.*, Vol. 92, No. 2, pp. 292-302.

HOLLAND, J. (1978), "Die Instationare Elastohydrodynamik", Konstruktion, Vol. 30, No. 8, pp. 363-369.

HOLLAND. J. (1978), "Zur Aubildung Eines Tragfahigan Schmierfilm Zwishen Nocken und StoBel", *MTZ.* Vol. 39, No. 5, pp. 225-231.

LIN, Z.G. and MEDLEY, J.B. (1984), "Transient Elastohydrodynamic Lubrication of Involute Spur Gear under Isothermal Conditions", *Wear*, Vol. 95, pp. 143-165.

MACHONOCHIE, B. and CAMERON, A. (1960), "The Measurement of Oil Film Thickness in Gear Teeth", *Trans. ASME*, Series D, Vol. 82, pp. 29-35.

MEDLEY, J.B. and DOWSON, D. (1984), "Lubrication of Elasto-Isoviscous Line Contacts Subject to Cyclic Time–Varying Loads and Entrainment Velocities", *Trans. ASLE*, Vol. 27, pp. 243-251.

MULLER, R. (1966), "The Effect of Lubrication on Cam and Tappet Performance", *MTZ.* Vol. 27, Pt. 2, pp. 58-61. *MIRA Translation*, No. 27/66.

NAYLOR, H. (1967-68), "Cams and Friction Drives", Conf. on Lubrication and Wear *Proc.Inst.Mech.Eng.*, Paper 15, pp. 237-247.

NINOMIYA, K., KAWAMORA M. and FUJI, K. (1978), "Electrical Observation of Lubricant Film Between Cam and Lifter of an O.H.V. Engine", *SAE Technical Paper* series 780093.

PATIR, N. and CHENG, H.S. (1978), "An Average Flow Model for Determining Effects of Three-Dimensional Roughness on Partical Hydrodynamic Lubrication", *Trans. ASME, J.Lub.Tech.*, Vol. 100, No. 1, pp. 12-17.

PATIR, N. and CHENG, H.S. (1979), "Application of Average Flow Model to Lubrication between Rough Sliding Surfaces", *Trans. ASME, J.Lub.Tech.*, Vol. 101, No. 2, pp. 220-231.

PRAKASH, J. and CHRISTENSEN, H. (1981), "A Simplified Model of Elastohydrdynamic Lubrication of Rollers – The Complete Solution", *Trans. ASLE*, Vol. 24, No. 3, pp. 362-370.

PRAKASH, J. and CZICHOS, H. (1983), "Influence of Surface Roughness and Its Orientation on Partial Elastohydrodynamic Lubrication of Rollers", *Trans. ASME. J.Trib.*, Vol. 105, No. 4, pp. 591-597.

ROHDE, S.M. (1981), "A Mixed Friction Model for Dynamically Loaded Contacts with Application to Piston Ring Lubrication", *Friction and Traction, 7th Leeds-Lyon Symposium on Tribology*, pp. 262-278, Butterworths.

RUDDY, B.L., DOWSON, D. and ECONOMOU, P.N. (1982), "The Influence of Running-In of the Twin Land Type of Oil Consumption", *The Running-In Process in Tribology, 8th Leeds-Lyon Symposium on Tribology*, pp. 162-169, Butterworths.

SMALLEY, R.J. and GARIGLIO, R. (1982), "The Role of Tappet Surface Morphology and Metallurgy in Cam/Tappet Life", *Tribology of Reciprocating Engines, 9th Leeds-Lyon Symposium on Tribology*,

pp. 263-272, Butterworths.

STARON, J.T. and WILLERMET, P.A. (1983), "An Analysis of Valve Train friction in Terms of Lubrication Principles", *SAE Technical Paper* series 830165.

SUN, D.C. and ROSENBERG, R.C. (1987), "An Experimental Study of Automotive Cam–Lifter Interface Friction", *Trans. ASLE*, Vol. 30, No. 2, pp. 167-176.

TAYLOR, R.G. and ANDREW, S. (1963), "Surface Deterioration of Cams and Cam Followers: the Influence of Follower Rotation and Contact Stress", *MIRA Report*, No. 5.

TONDER, K. and CHRISTENSEN, H. (1981), "A Unified Numerical Approach to the Lubrication of Roller", *Proc. of European Tribology Congress*, pp. 177-191.

VAN HELDEN, A.K., VAN DER-MEER, R.J., VAN SFAADEN, J.J. and VAN GELDEREN, E. (1985), "Dynamic Friction in Cam/Tappet Lubrication", *SAE Technical Paper* series 850441.

VAN VALKENBURG, M.E. (1982), "Analog Filter Design", *CBS College Publishing*.

VICHARD, J.P. (1971), "Transient Effects in the Lubrication of Herzian Contacts", *J.Mech.Eng.Sci.*, Vol. 13, No. 3, pp. 173-189.

VICHARD, J.P. and GODET, M. (1967-68), "Simultaneous Measurement of Load, Friction and Film Thickness in a Cam and Tappet System", *Symposium on Experimental Methods in Tribology, Proc.Inst.Mech.Eng.*, Vol. 182, Pt. 3G, pp. 109-113.

WADA, S. and TSUKIJIHARA, M. (1978), "Elastohydrodynamic Squeeze Problem of Two Rotating Cylinders (Part I, Newtonian Fluid) and (Part II, Bingham soild)", *Bull. JSME*, Vol. 24, No. 192, pp. 737-783 and pp. 1072-1077.

WANG, K.L. and CHENG, H.S. (1981), "A Numerical Solution to the Dynamic Load Film Thickness and Surface Temperature in Spur Gears PartI Analysis; PartII Results", *Trans. ASME, J.Mech.Design*, Vol. 103, pp. 177-194.

WU, Y.W. and YAN, S.M. (1986), "A Full Numerical Solution for the Non-Steady State Elastohydrodymanic Problem in Nominal Line Contacts", *Fluid Film Lubrication - Osborne Reynolds Centenary, 13th Leeds-Lyon Symposium on Tribology*, pp. 291-298, Butterworths.

APPENDICES

A1 NEW CURVE FITTED FORMULAE FOR THE ASPERITY CONTACT FUNCTIONS

A2 AN EIGHTH–ORDER BUTTWORTH LOWPASS DIGITAL FILTER

APPENDIX A1 NEW CURVE FITTED FORMULAE FOR THE ASPERITY CONTACT FUNCTION

New curve fitted formulae for the asperity contact functions (F_n) for a Gaussian distribution of asperity heights.

Let $H = \frac{h}{\sigma}$

$$F_2(H) = \begin{cases} d_1 \exp(d_2 \ln(H_1 - H) + d_3 [\ln(H_1 - H)]^2) & \text{for } H < 2.0 \\ d_4 \exp(d_5 \ln(H_2 - H) + d_6 [\ln(H_2 - H)]^2) & \text{for } 2.0 \le H < 3.5 \\ d_7 (H_3 - H)^{d8} & \text{for } 3.5 \le H < 4.0 \\ 0.0 & \text{for } 4.0 \le H \end{cases}$$

$$F_{5/2}(H) = \begin{cases} f_1 \exp(f_2 \ln(H_1 - H) + f_3 [\ln(H_1 - H)]^2) & \text{for } H < 2.0 \\ f_4 \exp(f_5 \ln(H_2 - H) + f_6 [\ln(H_2 - H)]^2) & \text{for } 2.0 \le H < 3.5 \\ f_7 (H_3 - H)^{f8} & \text{for } 3.5 \le H < 4.0 \\ 0.0 & \text{for } 4.0 \le H \end{cases}$$

$H_1 = 9.0 \qquad H_2 = 8.0 \qquad H_3 = 4.0$

$d_1 = 0.14704 \times 10^{-40}$	$f_1 = 0.11755 \times 10^{-39}$
$d_2 = 0.70373 \times 10^{2}$	$f_2 = 0.67331 \times 10^{2}$
$d_3 = -0.12696 \times 10^{2}$	$f_3 = -0.11699 \times 10^{2}$
$d_4 = 0.74104 \times 10^{-21}$	$f_4 = 0.15827 \times 10^{-20}$
$d_5 = 0.30813 \times 10^{2}$	$f_5 = 0.29156 \times 10^{2}$
$d_6 = -0.36470 \times 10^{1}$	$f_6 = -0.29786 \times 10^{1}$
$d_7 = 0.88123 \times 10^{-4}$	$f_7 = 0.11201 \times 10^{-3}$
$d_8 = 0.21523 \times 10^{1}$	$f_8 = 0.19447 \times 10^{1}$

The table below compares the values of (F_n) according to the numerical results, Rhode's curve fits (1981) and the new formulae.

H	Numerical		Rohde (1981)		New Formulae	
	F_2	$F_{5/2}$	F_2	$F_{5/2}$	F_2	$F_{5/2}$
0.0	0.50000	0.61664	0.65501	0.54874	0.50217	0.61831
0.5	0.20978	0.24038	0.23519	0.20579	0.20934	0.23956
1.0	0.07544	0.08055	0.07661	0.07040	0.07559	0.08060
1.5	0.02289	0.02285	0.02212	0.02149	0.02307	0.02300
2.0	0.00578	0.00542	0.00547	0.00568	0.00578	0.00542
2.5	0.00120	0.00106	0.00111	0.00124	0.00120	0.00106
3.0	0.00020	0.00017	0.00017	0.00021	0.00020	0.00017
3.5	0.00003	0.00002	0.00002	0.00003	0.00003	0.00002
4.0	0.00000	0.00000	0.00000	0.00000	0.00000	0.00000

APPENDIX A2 AN EIGHTH-ORDER BUTTWORTH LOWPASS DIGITAL FILTER

```
      SUBROUTINE FILTER(VOL,FVOL,FFVOL,TTS,FC,NPTS)                    FIL01
      IMPLICIT REAL*16 (A-H,O-Z)                                       FIL02
      DIMENSION VOL(NPTS),FVOL(NPTS),FFVOL(NPTS)                       FIL03
      PAI=3.141592653589793Q0                                          FIL04
      WA=1.0Q0/QTAN(PAI*TTS*FC)                                        FIL05
      PSAI1=0.5Q0*PAI/8.0Q0                                            FIL06
      PSAI2=1.5Q0*PAI/8.0Q0                                            FIL07
      PSAI3=2.5Q0*PAI/8.0Q0                                            FIL08
      PSAI4=3.5Q0*PAI/8.0Q0                                            FIL09
      A1=QCOS(PSAI1)                                                   FIL10
      A2=QCOS(PSAI2)                                                   FIL11
      A3=QCOS(PSAI3)                                                   FIL12
      A4=QCOS(PSAI4)                                                   FIL13
      A=2.0Q0*(A1+A2)                                                  FIL14
      B=2.0Q0*(1.0Q0+2.0Q0*A1*A2)                                      FIL15
      C=2.0Q0*(A3+A4)                                                  FIL16
      D=2.0Q0*(1.0Q0+2.0Q0*A3*A4)                                      FIL17
      AE=(A+C)*WA                                                      FIL18
      AF=(B+A*C+D)*WA**2                                               FIL19
      AG=(A+B*C+A*D+C)*WA**3                                           FIL20
      AH=(2.0Q0+2.0Q0*A*C+B*D)*WA**4                                   FIL21
      AI=(A+A*D+B*C+C)*WA**5                                           FIL22
      AJ=(B+A*C+D)*WA**6                                               FIL23
      AK=(A+C)*WA**7                                                   FIL24
      AL=1.0Q0*WA**8                                                   FIL25
      P=1.0Q0/(1.0Q0+AE+AF+AG+AH+AI+AJ+AK+AL)                          FIL26
      Q=(8.0Q0+6.0Q0*AE+4.0Q0*AF+2.0Q0*AG-2.0Q0*AI-4.0Q0*AJ-6.0Q0*AK   FIL27
     * -8.0Q0*AL)*P                                                   FIL28
      R=(28.0Q0+14.0Q0*AE+4.0Q0*AF-2.0Q0*AG-4.0Q0*AH-2.0Q0*AI+4.0Q0*   FIL29
     * AJ+14.0Q0*AK+28.0Q0*AL)*P                                       FIL30
      S=(56.0Q0+14.0Q0*AE-4.0Q0*AF-6.0Q0*AG+6.0Q0*AI+4.0Q0*AJ-14.0Q0   FIL31
     * *AK-56.0Q0*AL)*P                                               FIL32
      T=(70.0Q0-10.0Q0*AF+6.0Q0*AH-10.0Q0*AJ+70.0Q0*AL)*P              FIL33
      U=(56.0Q0-14.0Q0*AE-4.0Q0*AF+6.0Q0*AG-6.0Q0*AI+4.0Q0*AJ+14.0Q0   FIL34
     * *AK-56.0Q0*AL)*P                                               FIL35
      V=(28.0Q0-14.0Q0*AE+4.0Q0*AF+2.0Q0*AG-4.0Q0*AH+2.0Q0*AI+4.0Q0*   FIL36
     * AJ-14.0Q0*AK+28.0Q0*AL)*P                                       FIL37
      W=(8.0Q0-6.0Q0*AE+4.0Q0*AF-2.0Q0*AG+2.0Q0*AI-4.0Q0*AJ+6.0Q0*AK   FIL38
      *-8.0Q0*AL)*P                                                    FIL39
      X=(1.0Q0-AE+AF-AG+AH-AI+AJ-AK+AL)*P                              FIL40
      DO 10 I=9,NPTS                                                   FIL41
      FVOL(I)=(VOL(I)+8.0Q0*VOL(I-1)+28.0Q0*VOL(I-2)+56.0Q0*VOL(I-3)   FIL42
      *+70.0Q0*VOL(I-4)+56.0Q0*VOL(I-5)+28.0Q0*VOL(I-6)+8.0Q0*VOL(I-7) FIL43
      *  +VOL(I-8))*P-Q*FVOL(I-1)-R*FVOL(I-2)-S*FVOL(I-3)-T*FVOL(I-4)  FIL44
      *  -U*FVOL(I-5)-V*FVOL(I-6)-W*FVOL(I-7)-X*FVOL(I-8)              FIL45
   10 CONTINUE                                                         FIL46
      NPTT=NPTS-8                                                      FIL47
      DO 20 I=NPTT,1,-1                                                FIL48
      FFVOL(I)=(FVOL(I)+8.0Q0*FVOL(I+1)+28.0Q0*FVOL(I+2)+56.0Q0*       FIL49
     * FVOL(I+3)+70.0Q0*FVOL(I+4)+56.0Q0*FVOL(I+5)+28.0Q0*FVOL(I+6)     FIL50
     * +8.0Q0*FVOL(I+7)+FVOL(I+8))*P-Q*FFVOL(I+1)-R*FFVOL(I+2)         FIL51
     * -S*FFVOL(I+3)-T*FFVOL(I+4)-U*FFVOL(I+5)-V*FFVOL(I+6)            FIL52
     * -W*FFVOL(I+7)-X*FFVOL(I+8)                                      FIL53
   20 CONTINUE                                                         FIL54
      RETURN                                                           FIL55
      END                                                              FIL56
```